THE UNIVERSITY OF CALGARY

# Simulation of Contact Melting of Sulphur

by

**Cheng Yan Wu**

A DISSERTATION

SUBMITTED TO THE FACULTY OF GRADUATE STUDIES

IN PARTIAL FULFILMENT OF THE REQUIREMENTS FOR THE

DEGREE OF DOCTOR OF PHILOSOPHY

DEPARTMENT OF CHEMICAL AND PETROLEUM ENGINEERING

CALGARY, ALBERTA

February, 1995

© Cheng Yan Wu 1995

THE UNIVERSITY OF CALGARY

FACULTY OF GRADUATE STUDIES

The undersigned certify that they have read, and recommend to the Faculty of Graduate Studies for acceptance, a dissertation entitled "Simulation of Contact Melting of Sulphur" submitted by Cheng Yan Wu in partial fulfilment of the requirements for the degree of Doctor of Philosophy.

Dr. A. A. Jeje, Supervisor, Chairman
Department of Chemical and Petroleum Engineering

Dr. R. A. Heidemann
Department of Chemical and Petroleum Engineering

Dr. R. D. Rowe
Department of Mechanical Engineering

Dr. K. Nandakumar, External Examiner
Department of Chemical Engineering
University of Alberta

Dr. S. R. Sreenivasan
Department of Physics and Astronomy

Sept. 21, 1995

Date

# Abstract

An industrial process for liquifying sulphur deposited in mounds which serve as long-term repositories for the element after its recovery from $H_2S$ in sour natural gas has been investigated through numerical modelling. In the operation using the Ellithorpe remelter, staggered banks of vertical tubes in two rows are heated internally with saturated steam and pressed against a vertical wall of sulphur. The melt is squeezed azimuthally out of the gap between the solids and drained by gravity to collection headers. This is a close-contact melting problem with the additional characteristics that the liquid's thermophysical properties are temperature dependent. The objective of this study is to model the early stage of the development of a melting front after the hot tubes are suddenly brought in contact with the surface of sulphur which was initially flat.

The actual model is an isolated heating element which is a cylinder of infinite length maintained at a constant temperature. This is contacted with the surface of a semi-infinite block of sulphur maintained at its melting point. As the melting occurs, the surface is indented. Proximity between the two solid surfaces is maintained by a force applied on the cylinder. The transient outline of the melting interface is unknown *a priori* and it therefore has to be determined as part of the solution.

The algorithm developed involved solving the finite difference forms of the continuity, Navier-Stokes and energy equations simultaneously with the boundary

conditions and closure criteria at the melting interface. The SIMPLE technique was employed to discretize the equations. The technique involves 5-point computational molecules and the staggered grid points around control volumes in a fixed grid domain. A fractional volume of fluid (VOF) method was used to track the advancement of the melting interface.

A simplified pseudo-steady state model was developed to obtain the parameters that affect the melting process. The Stefan number and the ratio of liquid gap thickness at the closest approach $\delta_o$ to the radius of the hot tube were found to be the primary dimensionless quantities. In the numerical simulation of the transient process, these parameters were varied over a wide range. The results for the temperature and velocity fields, gap width and external force required to maintain close contact between the surfaces were compared.

Numerical results are reported on the early development of the outline of the melting boundary, the evolving temperature and velocity fields within the melt inside the gap, and the displacement rate of the hot tube. Calculations were carried out for a set of parameters typical of field conditions. The results show an initial rapid increase in the migration rate of the heat source followed by a near steady rate even when the surface has only been indented a little. The gap width increased in the azimuthal direction. The shape of the melting front, the liquid temperature and the velocity profiles become nearly stationary soon after the melting zone has been established around a sector of the heating tubes.

# Acknowledgments

It is a pleasure to express my sincere thanks to those individuals from whom I have benefited throughout the course of this study.

I would especially like to thank my supervisor, Dr. A. Jeje for his continuous support, guidance, encouragement and invaluable assistance through numerous discussions which made this work possible.

Special thanks go to Dr. R. A. Heidemann for his invaluable criticism, understanding, steadfast support and interests that were so important for the hard times during the course of this work.

I am indebted to Dr. R. Rowe for his numerous valuable suggestions in the initial stages of the numerical modeling and programming development, and also for providing several source codes which were employed as useful references developing the simulation package. It is highly appreciated that Dr. Sreenivasan reviewed the equations in this work. Especially he found another analytical solution to an equation in Chapter 3 which is physically correct and he also gave valuable comments on the analytical model.

My special thanks also go to Dr. J. Belgrave for his invaluable discussions for numerical model and numerical techniques, also his understanding, encouragement and support during this course study. I am grateful to Dr. Moore for his encouragement and interest throughout all stages of this study.

I would like to thank Dr. D. Phillips from ACS High Performance Computing Service, for his assistance and extensive collaboration in using High Performance Computing Fujitsu VPX/240 system. HPC scholarship awarded by HPC Centre is greatly appreciated.

Finally, I would like to offer my sincere thanks to my husband, Jian, for his patience, encouragement, support and understanding during this endeavour. And thanks to my Creator, the source of all knowledge.

*I dedicate this dissertation to my family.....*

**My husband: Jian Liu**

My father and mother: Wu Shulai and Liu Kezhen

My brothers: Deng Liqiang, Xiao Linqiu, Wu Chengming, Xu Zhenhua

My sisters: Wu Chenglan, Wu Chenghong, Zhou Hongying, Wu Chengying

My grandmother: Zhang Silian

My father and mother-in-law: Liu Zhengxian and Gu Yazhen

# Table of Contents

**Approval Sheet** ..... **ii**

**Abstract** ..... **iii**

**Acknowledgements** ..... **v**

**Dedication** ..... **vi**

**Table of Contents** ..... **vii**

**List of Tables** ..... **xi**

**List of Figures** ..... **xii**

**Nomenclature** ..... **xxiii**

**1 Introduction** **1**

1.1 Close-Contact Melting with Migrating Heat Source ..... 1

1.2 Ellithorpe Process for Sulphur Melting ..... 4

1.3 Scope and Objectives of the Study ..... 5

1.4 Dissertation Format ..... 6

**2 Background and Literature Review** **8**

2.1 Industrial Background ..... 8

2.1.1 The Remelter in operation ..... 10

2.1.2 Pertinent sulphur properties ..... 12

2.1.3 The Flow of Melt ..... 18

2.2 Close-Contact Melting . . . . . 20

2.2.1 Moving heat source problems . . . . . 22

2.2.2 Theoretical analysis and experimental investigations on close-contact melting problems . . . . . 24

2.2.3 Numerical simulation of transient close-contact melting . . 39

**3 Analysis** **43**

3.1 Formulation of the Problem . . . . . 43

3.1.1 The Physical model . . . . . 43

3.1.2 Transport Equations . . . . . 45

3.2 Analytical Solution . . . . . 49

3.2.1 A Simplified Mathematical Model . . . . . 49

3.2.2 Order of Magnitude Analysis . . . . . 53

3.2.3 Analytical Solution . . . . . 55

3.2.4 Results and Discussions . . . . . 63

3.3 Closing Remarks . . . . . 84

**4 Numerical Simulation of the Transient Process** **87**

4.1 Literature Review on Numerical Techniques . . . . . 87

4.1.1 Introduction . . . . . 87

4.1.2 Varied and Fixed grids Methods . . . . . 88

4.1.3 Temperature-dependent Properties in Phase-change Process . 90

4.2 Numerical Analysis . . . . . 92
4.2.1 Governing Equations in a Cylindrical Coordinate System . . . 92
4.2.2 Calculation Domain and Mesh Generation . . . . . 99
4.2.3 String Intersected Boundaries . . . . . 101
4.2.4 Discretization of the PDEs . . . . . 110
4.2.5 Treatment of Temperature-dependent Properties . . . . . 114
4.3 Tracking of the Melting Front . . . . . 117
4.3.1 Calculation of Radii of the Interface . . . . . 117
4.3.2 VOF Method . . . . . 119
4.3.3 Determining the Interface Within a Cell . . . . . 119
4.4 The Solution algorithm . . . . . 123
4.4.1 The Speed of Motion of the Hot Tube and the Critical Angle $\theta_c$ . . . . . 123
4.4.2 Calculation Procedures . . . . . 124
4.4.3 Stability of the Finite Difference Scheme . . . . . 127
4.4.4 Validation of the Numerical Algorithm . . . . . 128

**5 Results and Discussion** **137**

5.1 An Illustrative Example . . . . . 137
5.2 Parametric Results . . . . . 166
5.2.1 The Effect of Heating Temperature $T_w$ . . . . . 166
5.2.2 The Effect of Gap Width at $\theta = 0$, $\delta_o$ . . . . . 181

5.2.3 The Effect of Radius of the Hot Tube $r_o$ . . . . . 200

5.3 Computer Efficiency . . . . . 210

**6 Conclusions and Recommendations 215**

6.1 Conclusions . . . . . 215

6.2 Recommendations . . . . . 219

**References 221**

**Appendix 232**

A-1 Governing Equations in Non-inertial Coordinate System . . . . . 232

A-2 Melt Velocity at the Solid-liquid Interface . . . . . 239

A-3 Local Energy Balance Equation at the Interface . . . . . 241

B-1 Curvature of the Melting Interface $G(r_i,\theta,t) = 0$ . . . . . 242

B-2 Expression of Local Energy Balance Equation at the Melting Interface With Gap Width $\delta(\theta,t)$ . . . . . 246

# List of Tables


| Table | Description | Page |
|---|---|---|
| 2.1 | Some important properties of sulphur | 13 |
| 4.1 | Prime variables and their corresponding dimensionless counterparts | 93 |
| 4.2 | Expressions for $\Gamma_\Phi$, $S_p$ and $S_\Phi$ for any general Variable | 111 |
| 5.1 | Parameters for example solutions | 138 |
| 5.2 | The local maximum velocity values at different melting times $T_w$ = 150°C, $u_o$ = 4.4($10^{-5}$) m/s at t = 10 s, and 4.7($10^{-5}$) m/s when t ≥ 30 s | 155 |
| 5.3 | Comparison of maximum velocity values at various angles, t = 60 s, unit for velocity, m/s, $\delta_o$ = 1.5($10^{-4}$)m, $r_o$ = 2.5($10^{-2}$)m | 180 |
| 5.4 | Comparison of maximum velocity values at various angles t = 300 s, unit for velocity, m/s, $\delta_o$ = 1.5($10^{-4}$)m, $r_o$ = 2.5($10^{-2}$)m | 181 |
| 5.5 | Comparison of migration rates at different $\delta_o$ Values | 185 |
| 5.6 | Comparison of maximum velocity values at various angles t = 10 s, $T_w$ = 130°C, unit for velocity, m/s, for $\delta_o$, m | 198 |
| 5.7 | Comparison of maximum velocity values at various angles t = 10 s, $T_w$ = 130°C, unit for velocity, m/s, for $\delta_o$, m | 200 |
| 5.8 | Comparison of maximum velocity values at various angles t = 60 s, $T_w$ = 130°C, unit for velocity, m/s, for $r_o$, m | 210 |

# List of Figures


| Figure | Description | Page |
|---|---|---|
| 2.1 | Schematic of the Ellithorpe remelter | 11 |
| 2.2 | Temperature relationship between the various forms of liquid sulphur (Hatch, 1972) | 15 |
| 2.3 | Phase diagram of sulphur (Findlay, 1945) | 16 |
| 2.4 | Viscosity of liquid sulphur as function of temperature (Bacon & Fanelli, 1943), (a) lower temperature range, (b) high temperature range | 17 |
| 2.5 | Heat capacity of liquid sulphur as function of temperature (Lewis & Randall, 1911) | 19 |
| 2.6 | Schematic of molten sulphur flow between two solid surfaces | 21 |
| 3.1 | Cross-sectional view of model | 44 |
| 3.2 | Physical model for quasi-steady state analysis | 51 |
| 3.3 | Comparison of f(Ste) from eq.(3.48a&b) (dotted line) and eq.(3.48c) (solid line), (a) at small Ste ranges; (b) Ste from 0 to 8 | 60 |
| 3.4 | Critical sector angle as function of Ste at different $p_f^*$ values | 64 |
| 3.5 | Migration rate of heat source $u_o$ as function of Ste at different $p_f^*$ values | 66 |
| 3.6 | Gap width at $\theta = 0$, $\delta_o^*$ as function of $p_f^*$ at different Ste values | 67 |
| 3.7 | Gap width at $\theta = 0$, $\delta_o^*$ as function of Ste at different $p_f^*$ values | 69 |

| Figure | Description | Page |
|---|---|---|
| 3.8(a) | Gap width $\delta^*$ development along azimuthal direction at different Ste values; $p_f^* = 2.70(10^7)$ | 70 |
| 3.8(b) | Gap width $\delta^*$ development along azimuthal direction at different Ste values; $p_f^* = 2.70(10^8)$ | 71 |
| 3.8(c) | Gap width $\delta^*$ development along azimuthal direction at different Ste values; $p_f^* = 2.70(10^9)$ | 72 |
| 3.9(a) | Average heat flux of $q_s^*$ as function of Ste at different $p_f^*$ values | 73 |
| 3.9(b) | Average heat flux of $q_I^*$ as function of Ste at different $p_f^*$ values | 74 |
| 3.10(a) | Heat flux at heating surface $q^*$ as function of polar angle position at different Ste values; $p_f^* = 2.70(10^7)$ | 75 |
| 3.10(b) | Heat flux at heating surface $q^*$ as function of polar angle position at different Ste values; $p_f^* = 2.70(10^8)$ | 76 |
| 3.10(c) | Heat flux at heating surface $q^*$ as function of polar angle position at different Ste values; $p_f^* = 2.70(10^9)$ | 77 |
| 3.11(a) | Pressure $p^*$ as function of polar angle position at different Ste values; $p_f^* = 2.70(10^7)$ | 78 |
| 3.11(b) | Pressure $p^*$ as function of polar angle position at different Ste values; $p_f^* = 2.70(10^8)$ | 79 |
| 3.11(c) | Pressure $p^*$ as function of polar angle position | |

| Figure | Description | Page |
|---|---|---|
| | at different Ste values; $p_f^* = 2.70(10^9)$ | 80 |
| 3.12(a) | Pressure gradient $dp^*/d\theta$ as function of polar angle position at different Ste values; $p_f^* = 2.70(10^7)$ | 81 |
| 3.12(b) | Pressure gradient $dp^*/d\theta$ as function of polar angle position at different Ste values; $p_f^* = 2.70(10^8)$ | 82 |
| 3.12(c) | Pressure gradient $dp^*/d\theta$ as function of polar angle position at different Ste values; $p_f^* = 2.70(10^9)$ | 83 |
| 3.13 | Production rate of the melt $V^*$ as function of Ste at different $p_f^*$ values | 85 |
| 4.1 | Definition of $\phi$ and velocity component at the melting interface | 97 |
| 4.2 | Initial calculation domain | 100 |
| 4.3(a) | Schematic of main grid point, staggered grid points and control volume for T and p | 102 |
| 4.3(b) | Control volume for u | 103 |
| 4.3(c) | Control volume for v | 104 |
| 4.4 | A surface cell bisected by the solid-liquid interface | 105 |
| 4.5(a) | Schematic of string intersected boundary in one direction | 107 |
| 4.5(b) | Schematic of string intersected boundary in two directions | 108 |
| 4.6 | Illustration of the grid cell used in the interpolation of variable properties in a main-staggered grid net. Temperature, pressure and properties ($\eta$, $C_p$ etc.) are defined at the grid points a-d, the $\theta$-component velocity u is | |

| Figure | Description | Page |
|---|---|---|
| | defined at the staggered points by solid squares, and the r-component velocity v is defined at the grid points represented by empty squares. . . . . | 116 |
| 4.7 | Examples of interface shapes used in the advection of F. The donor-acceptor arrangement is shown in (a), where the dashed line indicates the left boundary of the total volumes being advected. The cross-hatched regions shown in (b-d) are the actual amounts of F fluxed. . . . . | 121 |
| 4.8 | Flow diagram for the numerical algorithm . . . . . | 126 |
| 4.9 | Numerical simulation of ice thickness versus time, compared with analytical solution by Ozisik(1980) . . . . . | 129 |
| 4.10 | Numerical simulation of migration rate of the hot tube $u_o$ when $T_w$ = 120°C, compared with steady state solution obtained from chapter 3 | 131 |
| 4.11 | Migration rate of the horizontal hot tube $u_o$ for n-octadecane melting when $T_w$ = 40°C and $T_\infty = T_m$ = 27.5°C, compared with the experimental results (•) of Moallemi and Viskanta (1986) . . . . . | 132 |
| 4.12 | Migration rate of the horizontal hot tube $u_o$ for n-octadecane melting when $T_w$ = 36°C and $T_\infty$ = 23°C, compared with the experimental results of (▽) Moallemi and Viskanta (1986) . . . . . | 133 |
| 4.13 | Migration rate of the horizontal hot tube $u_o$ for n-octadecane melting when the hot tube wall heat flux q" = 2630 W/m$^2$, $T_\infty$ = 21°C (Ste = 2.326), compared with the experimental results of (○) Moallemi and Viskanta | |

| Figure | Description | Page |
|---|---|---|
| | (1985b) . . . . . | 135 |
| 4.14 | Variation of heat-source surface temperature with time for n-octadecane melting when the hot tube wall heat flux q" = 2630 W/m$^2$, $T_\infty$ = 21°C (Ste = 2.326), compared with the experimental results of ($\Delta$ for 0°) Moallemi and Viskanta (1985b) . . . . . | 136 |
| 5.1 | Migration rate of the hot tube $u_o$ as function of time, $T_w$ = 150°C (Ste = 0.77), $\delta_o = 1.5(10^{-4})$m, $r_o = 2.5(10^{-2})$m . . . . . | 139 |
| 5.2 | External applied force $F_e^*$ as function of time, $T_w$ = 150°C (Ste = 0.77), $\delta_o = 1.5(10^{-4})$m, $r_o = 2.5(10^{-2})$m . . . . . | 141 |
| 5.3(a) | Radial temperature profiles across the melt gap at different angles, t = 10s, $T_w$ = 150°C (Ste = 0.77), $\delta_o = 1.5(10^{-4})$m, $r_o = 2.5(10^{-2})$m . . . . . | 142 |
| 5.3(b) | Radial temperature profiles across the melt gap at different angles, t = 30s, $T_w$ = 150°C (Ste = 0.77), $\delta_o = 1.5(10^{-4})$m, $r_o = 2.5(10^{-2})$m . . . . . | 143 |
| 5.3(c) | Radial temperature profiles across the melt gap at different angles, t = 60s, $T_w$ = 150°C (Ste = 0.77), $\delta_o = 1.5(10^{-4})$m, $r_o = 2.5(10^{-2})$m . . . . . | 144 |
| 5.3(d) | Radial temperature profiles across the melt gap at different angles, t = 300s, $T_w$ = 150°C (Ste = 0.77), $\delta_o = 1.5(10^{-4})$m, $r_o = 2.5(10^{-2})$m . . | 145 |
| 5.4 | Angular variation of heat flux ratio $q_l/q_S$ as function of melting times $T_w$ = 150°C (Ste = 0.77), $\delta_o = 1.5(10^{-4})$m, $r_o = 2.5(10^{-2})$m . . . . . | 147 |
| 5.5 | Comparison of radial temperature profiles at $\theta$ = 0, from simulation and eq.(5.4), $T_w$ = 150°C (Ste = 0.77), $\delta_o = 1.5(10^{-4})$m, $r_o = 2.5(10^{-2})$m | |

| Figure | Description | Page |
|---|---|---|
| | . . . . . 150 | |
| 5.6(a) | Tangential velocity profiles across the melt gap at different angles, t=10s, $T_w$ = 150°C (Ste = 0.77), $\delta_o = 1.5(10^{-4})$m, $r_o = 2.5(10^{-2})$m . . . . . | 151 |
| 5.6(b) | Tangential velocity profiles across the melt gap at different angles, t=60s, $T_w$ = 150°C (Ste = 0.77), $\delta_o = 1.5(10^{-4})$m, $r_o = 2.5(10^{-2})$m . . . . . | 152 |
| 5.6(c) | Tangential velocity profiles across the melt gap at different angles, t=180s, $T_w$ = 150°C (Ste = 0.77), $\delta_o = 1.5(10^{-4})$m, $r_o = 2.5(10^{-2})$m . . . . . | 153 |
| 5.6(d) | Tangential velocity profiles across the melt gap at different angles, t=300s, $T_w$ = 150°C (Ste = 0.77), $\delta_o = 1.5(10^{-4})$m, $r_o = 2.5(10^{-2})$m . . . . . | 154 |
| 5.7 | Angular variation of bulk mean temperature as function of melting times $T_w$ = 150°C (Ste = 0.77), $\delta_o = 1.5(10^{-4})$m, $r_o = 2.5(10^{-2})$m . . . . . | 157 |
| 5.8 | Radial velocity profiles across the melt gap at different angles, t = 60 s $T_w$ = 150°C (Ste = 0.77), $\delta_o = 1.5(10^{-4})$m, $r_o = 2.5(10^{-2})$m . . . . . | 159 |
| 5.9(a) | Gap width development as function of time ( time = n×60 s), $T_w$ = 150°C (Ste = 0.77), $\delta_o = 1.5(10^{-4})$m, $r_o = 2.5(10^{-2})$m . . . . . | 160 |
| 5.9(b) | Interface development with melting time (gap width was enlarged 100 times), time interval between two contours is 60 seconds, $T_w$ = 150°C (Ste = 0.77), $\delta_o = 1.5(10^{-4})$m, $r_o = 2.5(10^{-2})$m . . . . . | 161 |
| 5.10 | Curvature of $G(r_i,\theta,t)$ as function of melting time, $T_w$ = 150°C (Ste = 0.77), $\delta_o = 1.5(10^{-4})$m, $r_o = 2.5(10^{-2})$m . . . . . | 162 |
| 5.11(a) | Critical sector angle $\theta_c$ as function of melting time at $t \leq 5$ s, $T_w$ = 150°C | |

| Figure | Description | Page |
|---|---|---|
| | (Ste = 0.77), $\delta_o = 1.5(10^{-4})$m, $r_o = 2.5(10^{-2})$m . . . . . | 164 |
| 5.11(b) | Critical sector angle $\theta_c$ as function of melting time , $T_w$ = 150°C (Ste = 0.77), $\delta_o = 1.5(10^{-4})$m, $r_o = 2.5(10^{-2})$m . . . . . | 165 |
| 5.12 | Migration rate of the hot tube $u_o$ as function of Ste number, $\delta_o = 1.5(10^{-4})$m, $r_o = 2.5(10^{-2})$m . . . . . | 168 |
| 5.13 | Comparison of the applied force as function of Ste number, $\delta_o = 1.5(10^{-4})$m, $r_o = 2.5(10^{-2})$m . . . . . | 169 |
| 5.14 | Comparison of gap width development as function of Ste number, $T_w$ of 150°C (Ste = 0.77)(-) and 120°C(Ste = 0.15)(---), $\delta_o = 1.5(10^{-4})$m, $r_o = 2.5(10^{-2})$m . . . . . | 170 |
| 5.15(a) | Interface shape development as function of angle position; gap width was enlarged 100 times; time interval between two contours is 60 seconds, $T_w$ = 120°C (Ste = 0.15), $\delta_o = 1.5(10^{-4})$m, $r_o = 2.5(10^{-2})$m . . . . . | 171 |
| 5.15(b) | Interface shape development as function of angle position; gap width was enlarged 100 times; time interval between two contours is 60 seconds, $T_w$ = 130°C (Ste = 0.36), $\delta_o = 1.5(10^{-4})$m, $r_o = 2.5(10^{-2})$m . . . . . | 172 |
| 5.15(c) | Interface shape development as function of angle position, gap width was enlarged 100 times; time interval between two contours is 60 seconds, $T_w$ = 140°C (Ste = 0.56), $\delta_o = 1.5(10^{-4})$m, $r_o = 2.5(10^{-2})$m . . . . . | 173 |
| 5.16 | Comparison of critical sector angle development as function of Ste number, | |

| Figure | Description | Page |
|---|---|---|
| | $\delta_o = 1.5(10^{-4})$m, $r_o = 2.5(10^{-2})$m . . . . . | 174 |
| 5.17 | Comparison of radial temperature profiles, at t = 10s, $T_w$ of 150°C (Ste = 0.77)(-) and 120°C(Ste = 0.15)(---), $\delta_o = 1.5(10^{-4})$m, $r_o = 2.5(10^{-2})$m . . . . . | 176 |
| 5.18 | Comparison of radial temperature profiles, at t = 60s, $T_w$ of 150°C (Ste = 0.77)(-) and 120°C(Ste = 0.15)(---), $\delta_o = 1.5(10^{-4})$m, $r_o = 2.5(10^{-2})$m . . . . . | 177 |
| 5.19 | Comparison of tangential velocity profiles, at t = 60s, $T_w$ of 150°C (Ste = 0.77)(-) and 120°C(Ste = 0.15)(---), $\delta_o = 1.5(10^{-4})$, $r_o = 2.5(10^{-2})$m . . . . . | 178 |
| 5.20 | Comparison of tangential velocity profiles, at t = 300s, $T_w$ of 150°C (Ste = 0.77)(-) and 120°C(Ste = 0.15)(---), $\delta_o = 1.5(10^{-4})$m, $r_o = 2.5(10^{-2})$m . . . . . | 179 |
| 5.21 | Migration rate of the hot tube $u_o$ as function of gap width at $\theta = 0$, $\delta_o$, $T_w$ = 130°C (Ste = 0.36), $r_o = 2.5(10^{-2})$m . . . . . | 182 |
| 5.22 | Migration rate of the hot tube $u_o$ as function of gap width at $\theta = 0$, $\delta_o$, $T_w$ = 140°C (Ste = 0.56), $r_o = 2.5(10^{-2})$m . . . . . | 183 |
| 5.23 | Migration rate of the hot tube $u_o$ as function of gap width at $\theta = 0$, $\delta_o$, $T_w$ = 150°C (Ste = 0.77), $r_o = 2.5(10^{-2})$m . . . . . | 184 |
| 5.24(a) | Comparison of applied force as function of $\delta_o$, $T_w$ = 130°C (Ste = 0.36), $r_o = 2.5(10^{-2})$m . . . . . | 186 |

| Figure | Description | Page |
|---|---|---|
| 5.24(b) | Comparison of applied force as function of $\delta_o$, $T_w$ = 140°C (Ste = 0.56), $r_o = 2.5(10^{-2})$m | 187 |
| 5.24(c) | Comparison of applied force as function of $\delta_o$, $T_w$ = 150°C (Ste = 0.77), $r_o = 2.5(10^{-2})$m | 188 |
| 5.25(a) | Comparison of gap width development as function of $\delta_o$, $\delta_o = 1.5(10^{-4})$m(-), $2.0(10^{-4})$m(---) and $2.5(10^{-4})$m(.....), $T_w$ = 130°C (Ste = 0.36), $r_o = 2.5(10^{-2})$m | 190 |
| 5.25(b) | Comparison of gap width development as function of $\delta_o$, $\delta_o = 1.5(10^{-4})$m(-), $2.0(10^{-4})$m(---) and $2.5(10^{-4})$m(.....), $T_w$ = 140°C (Ste = 0.56), $r_o = 2.5(10^{-2})$m | 191 |
| 5.25(c) | Comparison of gap width development as function of $\delta_o$, $\delta_o = 1.5(10^{-4})$m(-), $2.0(10^{-4})$m(---) and $2.5(10^{-4})$m(.....), $T_w$ = 150°C (Ste = 0.77), $r_o = 2.5(10^{-2})$m | 192 |
| 5.26(a) | Comparison of critical sector angle development as function of $\delta_o$, $T_w$ = 130°C (Ste = 0.36), $r_o = 2.5(10^{-2})$m | 193 |
| 5.26(b) | Comparison of critical sector angle development as function of $\delta_o$, $T_w$ = 140°C (Ste = 0.56), $r_o = 2.5(10^{-2})$m | 194 |
| 5.26(c) | Comparison of critical sector angle development as function of $\delta_o$, $T_w$ = 150°C (Ste = 0.77), $r_o = 2.5(10^{-2})$m | 195 |
| 5.27 | Comparison of radial temperature profiles, at t = 10s, $\delta_o = 1.5(10^{-4})$m(-), $2.0(10^{-4})$m(---) and $2.5(10^{-4})$m(.....), $T_w$ = 130°C (Ste = 0.36), | |

| Figure | Description | Page |
|---|---|---|
| | $r_o = 2.5(10^{-2})$m . . . . . | 196 |
| 5.28 | Comparison of radial temperature profiles, at t = 60s, $\delta_o = 1.5(10^{-4})$m(-), $2.0(10^{-4})$m(---) and $2.5(10^{-4})$m(.....), $T_w$ = 130°C (Ste = 0.36), $r_o = 2.5(10^{-2})$m . . . . . | 197 |
| 5.29 | Comparison of tangential velocity profiles, at t = 60s, $\delta_o = 1.5(10^{-4})$m(-), $2.0(10^{-4})$m(---) and $2.5(10^{-4})$m(.....), $T_w$ = 130°C (Ste = 0.36), $r_o = 2.5(10^{-2})$m . . . . . | 199 |
| 5.30 | Migration rate of the hot tube $u_o$ as function of tube radius $r_o$ (1.25, 2.5, $5.0\times10^{-2}$ m), $T_w$ = 130°C (Ste = 0.36), $\delta_o = 1.5(10^{-4})$m . . . . . | 201 |
| 5.31 | Comparison of applied force as function of $r_o$, normalized by corresponding $r_o$ values $T_w$ = 130°C (Ste = 0.36), $\delta_o = 1.5(10^{-4})$m . . . . . | 202 |
| 5.32 | Comparison of applied force as function of $r_o$, $r_o$ (1.25, 2.5, $5.0\times10^{-2}$ m),normalized by the same $r_o$ value ($2.5\times10^{-2}$ m), $T_w$ = 130°C (Ste = 0.36), $\delta_o = 1.5(10^{-4})$m . . . . . | 204 |
| 5.33 | Comparison of gap width development as function of $r_o$, $r_o = 2.5(10^{-2})$m(-), $1.25(10^{-2})$m(---) and $5.0(10^{-2})$m(.....), $T_w$ = 130°C (Ste = 0.36), $\delta_o = 1.5(10^{-4})$m . . . . . | 205 |
| 5.34 | Comparison of critical sector angle development as function of $r_o$, $T_w$ = 130°C (Ste = 0.36), $\delta_o = 1.5(10^{-4})$m . . . . . | 206 |
| 5.35 | Comparison of radial temperature profiles, at t = 10s, $r_o = 2.5(10^{-2})$m(-), $1.25(10^{-2})$m(---) and $5.0(10^{-2})$m(.....), $T_w$ = 130°C (Ste = 0.36), | |

| Figure | Description | Page |
|---|---|---|
| | $\delta_o = 1.5(10^{-4})$m . . . . . | 207 |
| 5.36 | Comparison of radial temperature profiles, at t = 60s, $r_o = 2.5(10^{-2})$m(-), $1.25(10^{-2})$m(---) and $5.0(10^{-2})$m(.....), $T_w$ = 130°C (Ste = 0.36), $\delta_o = 1.5(10^{-4})$m . . . . . | 208 |
| 5.37 | Comparison of tangential velocity profiles, at t = 60s, $r_o = 2.5(10^{-2})$m(-), $1.25(10^{-2})$m(---) and $5.0(10^{-2})$m(.....), $T_w$ = 130°C (Ste = 0.36), $\delta_o = 1.5(10^{-4})$m . . . . . | 209 |
| 5.38 | Comparison of CPU time on both systems, AIX(-) and Fujitsu(---) | 212 |
| 5.39 | Comparison of elapsed time on both systems, AIX(-) and Fujitsu(---) . . . . . | 213 |
| A-1 | Schematic of inertial and moving frames of reference . . . . . | 233 |
| B-1 | Expression of a point on the interface at both cartesian and polar systems . . . . . | 243 |

# Nomenclature

| | |
|---|---|
| a | coefficients in discretization equations |
| Ar | Archimedes number $(\Delta\rho/\rho_s)(gr_o^3/\kappa^2)$ |
| b | source term in discretization equations |
| $C_p$ | specific heat capacity |
| $C_{pm}$ | specific heat capacity at the melting point of sulphur |
| $f_{r\,ij}$ | fraction coefficient in r-direction |
| $f_{t\,ij}$ | fraction coefficient in θ-direction |
| f(Ste) | function of Ste defined in eq.(2.4) |
| F | cell flag defined in eq.(4.39) |
| $\mathbf{F}_e$ | externally applied force |
| F(Ste) | function of Ste defined in eq.(2.9) |
| $F_d$ | applied force defined in eq.(2.5) |
| g | gravity acceleration |
| $G(r_i,\theta,t)$ | surface and interface position function |
| G(θ) | pressure gradient defined in eq.(3.33) |
| h | enthalpy |
| $h_{sl}$ | latent heat of fusion |
| $H_o$ | initial height of the PCM block |
| k | curvature |
| L | vertical length of the hot tube |
| M | mass of heat source |
| **n** | direction vector |
| $N,N_2$ | constant defined in eq.(5.5) |
| $N_j$ | number of grid points in r-direction |
| $r_o$ | radius of heat source |
| p | pressure |
| $p_{av}$ | average pressure in eq.(2.2) |

$P_n$ instantaneous average pressure in eq.(2.19)

Pr Prandtl number ($\eta C_p/\lambda$)

$\dot{q}$ heat flux vector

$(r,\theta)$ polar coordinates

$S_p$ pressure term defined in eq. (4.22)

$S_\Phi$ source term defined in eq. (4.22)

Ste Stefan number ($C_p\Delta T_w/h_{sl}$)

t time

T temperature

(u,v) velocity components in (x,y) directions

**U** velocity vector

$u_o$ velocity of heat source

$(V_r, V_\theta)$ velocity components in $(r,\theta)$ directions

(x,y) cartesian coordinates

(X,Y) cartesian coordinates defined in fig. 3.2

## GREEK SYMBOLS

$\beta$ constant defined in eq.(2.11)

$\beta'$ constant defined in eq.(2.14)

$\Gamma_\Phi$ exchange coefficient

$\Delta r$ grid size in r-direction

$\Delta T_{bm}$ bulk-mean temperature of the melt

$\Delta T_w$ temperature difference between the hot surface and the melting interface

$\Delta V$ volume of a control cell

$\Delta\theta$ grid size in $\theta$-direction

$\delta$ melt thickness

$\delta_o$ melt thickness at $\theta = 0°$

$\delta'$ $d\delta/dx$

$\varepsilon$ constant defined in eq.(5.5)

| | |
|---|---|
| $\eta$ | viscosity |
| $\theta$ | polar angle |
| $\theta_c$ | critical polar angle |
| $\kappa$ | thermal diffusivity |
| $\kappa_m$ | thermal diffusivity at the melting point of sulphur |
| $\lambda$ | thermal conductivity |
| $\xi$ | $\alpha/\alpha_r$ |
| $\rho$ | density |
| $\rho_h$ | density of heat source |
| $\Phi$ | general variable defined in eq.(4.22) |
| $\phi$ | interface position angle |
| $\Psi$ | $\theta - \phi$ |

**SUBSCRIPTS**

| | |
|---|---|
| E | east grid point next to P |
| I | solid - liquid interface |
| m | fusion |
| N | north grid point next to P |
| o | at $\theta = 0°$ |
| P | grid point P |
| s | solid |
| S | south grid point next to P |
| w | hot surface |
| W | west grid point next to P |
| (x,y) | in coordinate (x,y) directions |

**SUPERSCRIPTS**

| | |
|---|---|
| * | dimensionless variable |
| o | previous time step variable |

# Chapter 1

# Introduction

## 1.1 Close-Contact Melting with Migrating Heat Source

Close-contact melting in a domain of fixed coordinates, or under transient conditions, is a moving boundary problem. It is characterized by a thin gap between a solid to be liquefied and a body warmer than the melting point of the solid. This gap, from which the liquid produced is continuously displaced, is usually maintained by a force acting on one of the bodies. Under time-dependent conditions, at least a segment of one of the apposed surfaces is in relative motion to the other surface. When the heating surface has an arbitrary shape and the initial boundary of the melting solid is described by a different geometric form, the melting surface would undergo changes in shape within a stationary coordinate frame of reference. The evolving contour or the outline of the surface is not known *a priori*. Typically, the rate of relative movement between the heat source and the melting boundary has to be regarded as a function of time and space and considered as an integral part of obtaining simultaneous solutions to the energy and hydrodynamic equations which describe the system.

In close-contact melting, either the solid melts and slides around a stationary heat source as in latent heat storage systems (Saito et al. 1985a, 1985b, 1986, 1988) or the heat source migrates through the solid. For the latter, the movement occurs in the

direction of forces such as gravity, buoyancy, shear forces (Emerman and Turcotte, 1983, Moallemi and Viskanta, 1985a & 1985b) or along an external applied force (Lea and Stegall, 1973). Such forces are not large enough to induce regelation at temperatures lower than the solid's melting point.

The problem of current interest involves the application of an external force while melting occurs. Because of decreased spacing between the solids, the heat flux density is much higher than for a phase change process in which the heat source position is fixed and the thickness of liquid layer progressively increased, i.e. the thermal resistance increases with time (Sparrow and Myrum, 1985). Since the liquid production rate is enhanced with close-contact melting, it has been applied in the latent heat thermal storage systems (Saito et al. 1985a, 1986, 1988), utilized in industrial processes such as metallurgy and welding (Jacson, 1965), and observed during the migration of hot zones in geophysics (Emerman and Turcotte, 1983) and nuclear technology (Tong, 1965).

In close-contact melting process, the liquid layer between the heat source and the phase change material (PCM) is normally very thin due to the applied force which continuously squeezes the liquid produced out of the gap. Consequently, the melting rate of the PCM and energy transfer to the PCM are greatly increased. The gap width is usually less than 1 mm. For direct-contact melting involving a flat heating surface impressed on a planar PCM, Saito et al. (1985a, 1985b) reported that the liquid layer width ranged between 0.014 and 0.16 mm. The PCM used in their experiment was ice and the force applied to maintain close contact varied from 0.42 N to 42.7 N. The heat flux was reported to increase about 1.5 - 1.8 times when the contact pressure was

increased 10 times. The maximum velocity of the melt in the gap between the surfaces was reported to vary between $5.1(10^{-3})$ and $4.7(10^{-2})$ m/s when the applied force was increased about 200 times, from 0.234 N to 42.7 N. In a different study, melting was observed for a PCM inside a horizontal tube. Close-contact melting was maintained by gravity force on the PCM heated by the enclosing wall. The rate of melting was higher by 50-100% compared to a system where the surfaces were kept separated (Sparrow and Myrum, 1985). For example, when 30% of the PCM had melted for the non-contact case, about 52% of solid was liquefied in the direct-contact operation over the same length of time. For larger periods, the corresponding fractions of melt were 0.45 and 0.85. It is also shown that about 88-94% of the total volume of melt was produced in the region of close contact which means that melting was more efficiently carried out where the solid separation was narrow. In view of the high energy transport rates and rapid phase change, there is an economic incentive to encourage industrial application of direct-contact of melting.

The motivation for this study is an industrial scheme which involves the use of hot tubes for liquefying sulphur ($T_m \sim 113°C$) which is piled in above-ground blocks. A commercial equipment called the Ellithorpe remelter is of current interest. This is described in the following section. The problem is interesting and complex because the thermophysical properties of liquid sulphur vary strongly with temperature over the range maintained across the narrow gap. To the author's knowledge, there has not been any previous analysis or numerical investigation of this problem.

## 1.2 Ellithorpe Process for Sulphur Melting

The Ellithorpe remelter is a contraption, the heart of which is a steam-heated array of tubes forced against the sulphur block in the horizontal direction. This contrasts with the Frasch direct-contact hot water process for underground mining. In the Frasch process, the sulphur is melted in situ by direct contact through injection of superheated steam. Molten sulphur is air lifted to the surface (Kirk and Othmer, 1978, Mollere, 1989). As an alternative to melting, elemental sulphur deposited near the top of the soil may be recovered by open pit mining. This is an operation which involves scraping and hauling and a considerable amount of dust is generated. Apart from the detrimental effects on human health and the environmental impact problems posed by such airborne articles, the dust may lead to explosions and conflagrations. The Ellithorpe remelter was designed to avert such hazards.

The basic element of the remelter is a series of vertical steel tubes, approximately 3 m in length and 5 cm in diameter (12 BWG). Eight-five (85) tubes are arranged per set in a staggered 2-row pattern. A particular unit has four sets of tubes stacked one on the top of the other and the entire set is driven against the sulphur mound by a motor-driven rig. Saturated steam is fed through the tubes in one pass. The force applied to the tubes serves to maintain close contact between the sulphur and the heat source. The sulphur is judged to be predominantly in the rhombic allotropic form. Molten sulphur is squeezed out primarily in the azimuthal ($\theta$) direction through the gap between the surfaces. As it emerges at the back side of the tubes, it runs down into the collection trays. The gap width between the tube surface and solid-liquid interface appears, from visual observation,

to be less than 0.5 mm for a substantial region around each tube. Thus both conduction and convection of heat occur in the narrow channel. The dynamics and stability of the process can be complex. The field operation shows significant variations in melting rates under apparently constant process conditions. There is currently little theoretical guidance for optimizing the equipment and its performance.

## 1.3 Scope and Objectives of the Study

This study was motivated by the need to establish theoretically the rates at which the liquid can be produced under varying operating conditions and geometry of the equipment. The model is an isolated hot tube impressed upon a semi-infinite body of solid sulphur which initially had a flat surface. Although this model does not allow for interactions between the thermal fields of closely spaced tubes, it nonetheless sets the lower bounds for the system performance. The goals are to describe the velocity and thermal fields, monitor the evolution of the contour of the interface between solid and liquid sulphur and obtain estimates for the migration rates of the hot tube.

Specifically, the current work is aimed at the following tasks:

1. Develop a numerical model and its algorithm.

2. Derive equations for an approximate analytical solution to provide and identify important parameters. Dimensionless parameter groups which describe the process are to be explored through an analysis based on a simplified case under quasi-steady state condition.

3. Carry out a parametric study to find out the dominant critical parameters for

the melting process.

## 1.4 Dissertation Format

The content of each section in this dissertation is briefly summarized as follows.

In chapter 2, the field process for sulphur melting and the unique thermophysical properties of sulphur are described. Theoretical analysis, experimental studies and numerical treatment carried out in previous studies on close contact melting are reviewed. Focus has been placed especially on transient analyses and numerical simulations. Finally, the features to be considered in this work are identified.

The physical model is described in chapter 3. Equations are formulated to describe the flow and energy transport. Constraints which need to be satisfied are determined. A preliminary analysis involving assumptions of steady state and the lubrication approximation was performed to identify the relevant dimensionless parameter groups.

In chapter 4, the full set of transport equations, without simplifications, are formulated in a cylindrical coordinate system. The problem was translated into a non-inertial frame through fixing the origin along the axis of the hot tube. An algorithm was developed to discretize the system of equations. The technique was a combination of a discritization method developed by Patankar (1981) (SIMPLE method) and a melting interface tracking method developed by Hirt and Nicols (1981) (VOF method) which together determined the temperature and velocity field and the moving interface boundary contour.

Results and discussions are presented in chapter 5. Numerical results for a typical

set of parameters are reported which include the temperature and velocity profiles, migration rates of the hot tube, melting interface shape changes and the applied force. Effects of variations of the parameters on the melting process are also investigated and the results are presented.

In the final chapter, the most important findings of the present study are summarized. Recommendations for future research are made.

# Chapter 2

# Background and Literature Review

## 2.1 Industrial Background

Sulphur is an important industrial commodity used for the manufacture of sulphuric acid, fertilizers, petrochemicals and structural materials (Vroom, 1972, Platou, 1972). In Alberta, when the market is not favourable, it is typically stockpiled in open mounds near sour natural gas plants after its recovery from hydrogen sulphide ($H_2S$) in the produced gas (Hatch, 1972). One of the ways to transport the sulphur from such a site involves making sulphur beads or pellets from the liquid sulphur produced by the solid. The current research is focused on liquefying the solid sulphur in situ. An equipment for this operation is the Ellithorpe remelter. Of industrial interest are the rates at which liquid sulphur can be produced (by the Ellithorpe remelter and its variants), the costs of the operation and the "involuntary" expenses associated with pollution abatement, or the clean-up of block pads.

The production rate of liquid sulphur has been observed to vary significantly with time and from one block to another even under similar operating conditions. The melting pattern may be determined in part by the physical characteristics and composition of the solid medium. Typical features for the solid are as follows: 1) pure sulphur exists as a mixture of allotropes in monoclinic, orthorhombic and amorphous structures in relative

proportion which vary with solidification conditions, 2) a sulphur block cast from melt in layers contains different amounts, types and concentrations of insoluble impurities (like sand, leaves, moisture etc.) and bubbles and 3) sulphur derived from the base of sulphur blocks is contaminated by organic substances and inorganic particles. How these conditions affect the efficiency and the cost of sulphur remelting are poorly established.

To the knowledge of the author, little or no systematic experimental data or theoretical analysis which would serve as the basis and guidance for industrial operations exist. Comprehensive investigations of many problems associated with sour gas processing and sulphur handling have been carried out at the Alberta Sulphur Research Ltd. (ASR) and other organizations. These include describing the interconversion between allotropic forms of sulphur and the time-dependent change in the mechanical properties of solid sulphur (Currell et al., 1975, Roberts et al., 1987) and the forming, handling and transportation of elemental sulphur (Raymont and Hyne, 1983; Hyne, 1989). Problems on fugitive dust generation and measurement during the handling of formed solid sulphur (Wassink and Hyne, 1993), establishment of protocols to recover sulphur from pads (Hyne, 1981/2, Hyne and Schwalm, 1982/3, Hyne and Schwalm, 1983, Schwalm and Hyne, 1984), the production and friability of prills (Schwalm and Hyne, 1983), and hydrogen sulphide ($H_2S$) release during remelt (Schwalm et al. 1987/8) have also been examined. Finding large-scale uses for sulphur (West, 1975) and explorations on a variety of sulphur recovery techniques as alternatives or complementary schemes to the Claus process (Pfeiffer, 1975, Hyne, 1990) have also been of interest. The foregoing indicates that thermodynamic aspects, i.e the chemistry of the processes and phase equilibria as

related to species concentrations and crystal habits (Hatch, 1972), have been the dominant areas of the extensive studies to date.

### 2.1.1 *The Remelter in operation*

As a prelude to describe the problem to be investigated, it is useful to briefly consider the geometric and operational aspects of an industrial equipment currently used to remelt sulphur stockpiled in mounds outside sour gas processing plants. The Ellithorpe remelter illustrated in Fig. 2.1 has been described in chapter 1 (tube diameter and length, number of tubes in one set, etc.). The tubes in each set are staggered with centre-to-centre spacing of 6 cm. That means the minimum separation between two tube surfaces in the same row is ~1 cm. Effectively, each set of tubes covers a 3m × 3m area. The assembly is driven against the sulphur mound with a minimum pressure of ~ 3 kPa.

Saturated steam (at 200°C, ~15.4 atm) is fed into the tubes at a rate between 2500 and 3500 kg/hr. This corresponds to 29.5 and 41 kg/hr per tube. The latent heat content of the steam supply is hence 4.8 to 6.8 GJ/hr. Liquid sulphur is produced at an average rate of up to ~22.5 tons/hour when tubes move between 0.254 and 0.352 m/hr. Since the solid will be mostly in the orthorhombic crystalline habit ($S_\alpha$ , $\Delta H_f$ = 49.8 kJ/kg), about 1.1 GJ/hr of heat is utilized for melting. The sensible heat to bring the solid sulphur, at an average temperature of 5°C, to the melting temperature of ~113°C is ~1.7 GJ/hr. A conclusion from the foregoing is that between 40 and 60% of the energy supplied is lost to the ambient. In some operations, the tubes migrated, without significant changes in steam input rates and other processing conditions, at speeds reaching 0.66 m/hr. A higher

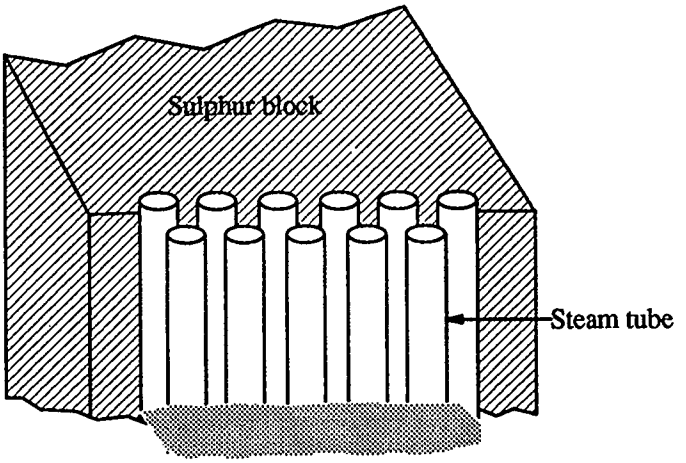


(a) Schematic view of the remelter

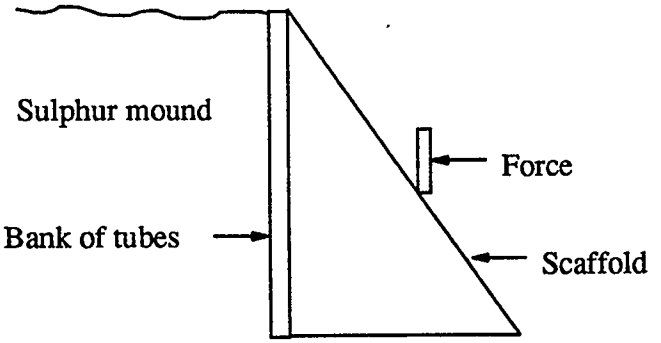


(b) Side view of the remelter

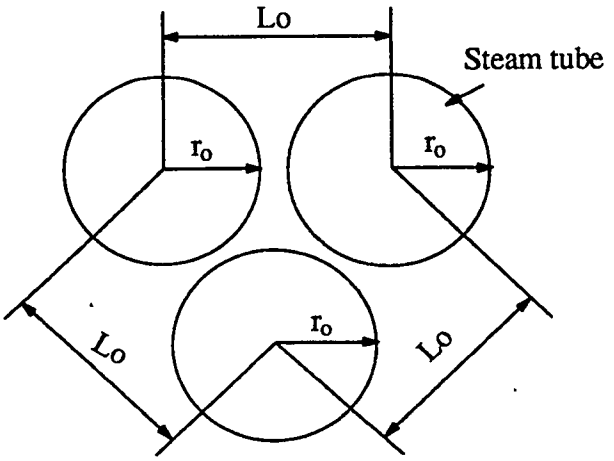


(c) Top view of the remelter (enlarged compared with (a) and (b))

Fig. 2.1 Schematic of the Ellithorpe remelter

steam utilization efficiency is thus realized. It is obvious that the nature of the solid, the geometry of the remelter and the process conditions influence the production rate of the liquid.

### 2.1.2 *Pertinent sulphur properties*

The properties of solid sulphur of importance in the remelt process are the relative quantities of crystalline and amorphous sulphur, heterogeneities caused by molecular aggregates, fractions of solid spaces and insoluble impurities, and the thermophysical properties associated with heat conduction and phase transformation. For the liquid, the density, viscosity and heat capacity are important because of the strong coupling between the dynamics of melt flow and the rates of heat conduction through the liquid layer or film to the multi-solid interface. Thermophysical properties of sulphur are summarized in Table 2.1 (Kirk and Othmer, 1978).

The physical characteristics of the solid in a mound may be determined by the following factors:

(a) When the liquid sulphur (density, $\rho$~1800 kg/m$^3$) at a temperature below 159°C (lambda sulphur or $S_\lambda$) is cooled down slowly, the volume contracts as fusion occurs to form monoclinic sulphur($S_\beta$, $\rho$~1960 kg/m$^3$). Sulphur $S_\beta$ is however unstable and a substantial fraction of the crystals change in hours to the orthorhombic habit ($S_\alpha$) which has a density of 2070 kg/m$^3$. The maximum possible volume reduction of 5% in the crystals is incorporated in the matrix structure.

Table 2.1 Some Important Properties of Sulphur (Kirk and Othmer, 1978)

| | | | | |
|---|---|---|---|---|
| Freezing point, °C | | | | |
| | | rhombic | | 110.2 (112.8, ideal) |
| | | monoclinic | | 114.5 (119.3, ideal) |
| Density, kg/m$^3$ | | | | |
| | solid | rhombic | | 2070 |
| | | monoclinic | | 1960 |
| | | amorphous | | 1920 |
| | liquid | 125 °C | | 1799 |
| Specific heat | kJ/kgK | | | |
| | solid | rhombic | 60 °C | 0.732 |
| | | | 95.4 °C | 0.754 |
| | | monoclinic | 100 °C | 0.754 |
| | | | 115.2°C | 0.790 |
| | liquid | (see Fig. 2.5) | | |
| Heat of fusion | kJ/kg | | | |
| | rhombic | → S (liquid) | | 498 (at 112.8°C) |
| | monoclinic | → S (liquid) | | 385 (at 118.9°C) |
| | monoclinic | → Equilibrium mixture (liquid) | | 536 (at 115.2°C) |
| Thermal conductivity, W/mK | | | | |
| | solid | rhombic | 20 °C | 0.272 |
| | | | 60 °C | 0.243 |
| | | | 95 °C | 0.226 |
| | | monoclinic | 100 °C | 0.161 |
| | | amorphous | 20 °C | ≈0.09 |
| | liquid | | | 0.1399 |

(b) The batch way that the original melt was poured into the mound may cause the block to be anisotropic.

(c) When liquid sulphur is rapidly cooled from a temperature above 159°C (μ sulphur or $S_\mu$), a solid mixture of polymeric ($S_w$) and $S_8$ ring molecules is amorphous. This is unstable and becomes friable after a while. At elevated temperatures, the liquid's octatomic ring structure is broken and sulphur polymerizes into long chain. The liquid finally becomes octatomic linear molecules when the temperature exceeds 300°C. Rapid cooling at these temperatures give the amorphous solid. These transitions between molecular forms is shown in Fig. 2.2 (Hatch, 1972).

Properties of the liquid are presented with reference to the phase diagram in Fig. 2.3. (Findlay, 1945; Hatch, 1972). Conditions for the 3 stable triple points are indicated. At atmospheric pressure, $S_\alpha$ to $S_\beta$ transition occurs at 112.8°C while the monoclinic crystals melt at 119.5°C. In the natural state, rhombic sulphur contains other allotropic forms and the melting point is depressed to 110.2°C. With the monoclinic habit predominant, the melting point is also depressed to 114.5°C. Between 120°C and 157°C, the liquid ($S_\lambda$) consists essentially of $S_8$ ring molecules. As shown in Fig. 2.4, the liquid sulphur viscosity decreases from 11 mPa.s to 6.7 mPa.s. Some of the ring molecules undergo scission at around 159°C to produce straight molecules with (reactive) free radicals at either end. Hence the molecules can polymerize by addition. The liquid ($S_\mu$) hence contains $S_8$ rings and straight sulphur molecules in equilibrium. Large polymer molecules and lower $S_8$ ring concentrations are present at higher temperatures. The liquid viscosity consequently rises to 8.0 mPa.s(cP) at 158°C, 30 mPa.s at 160°C and attains a

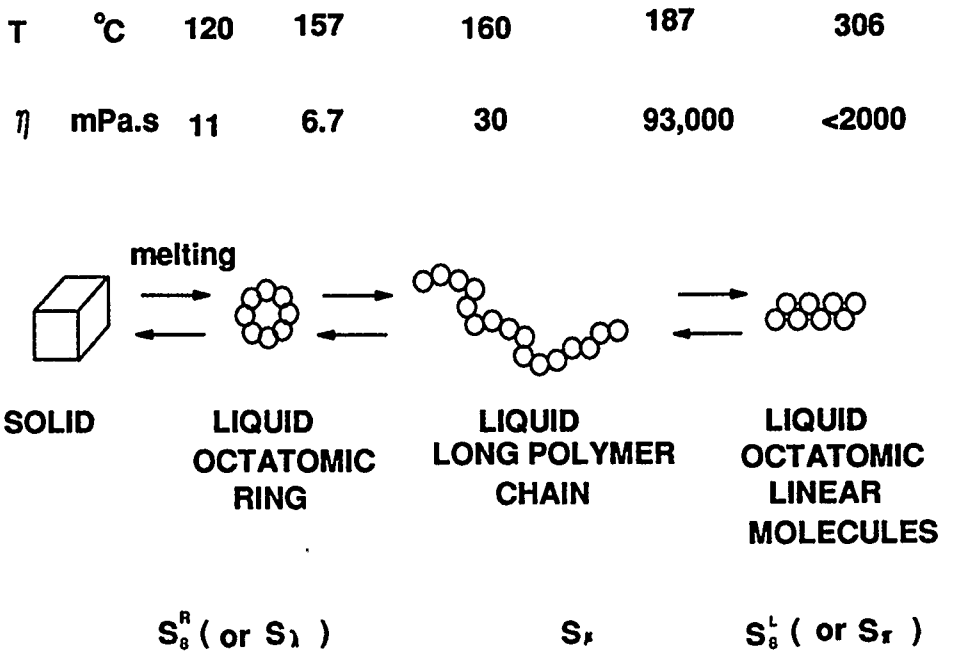


Fig. 2.2 Temperature relationship between
the various forms of liquid sulphur (Hatch, 1972)

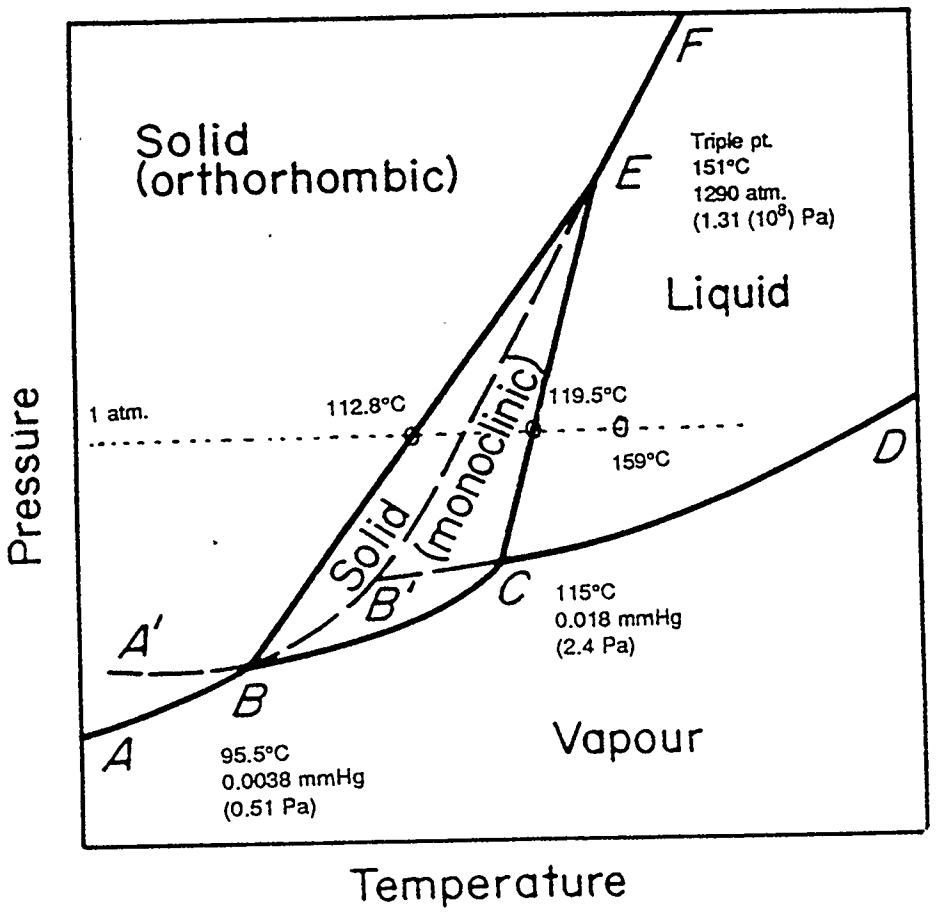


Fig. 2.3 Phase diagram of sulphur (Findlay, 1945)

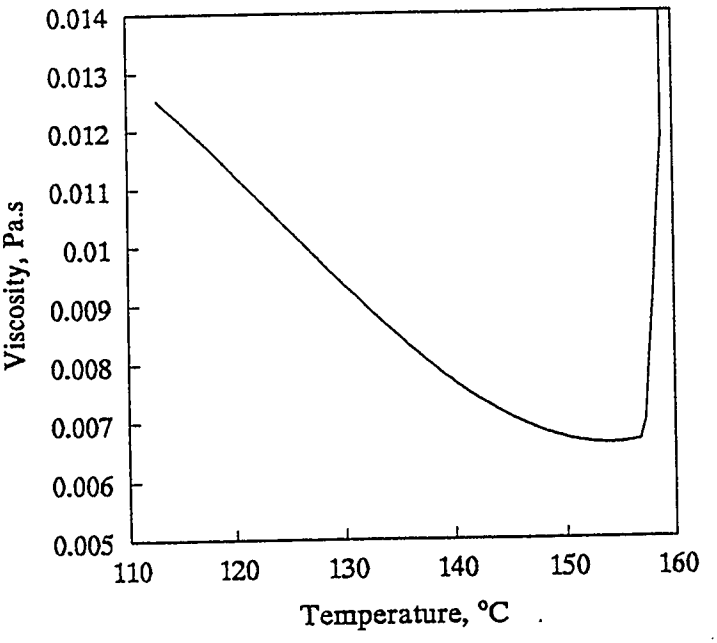


(a)

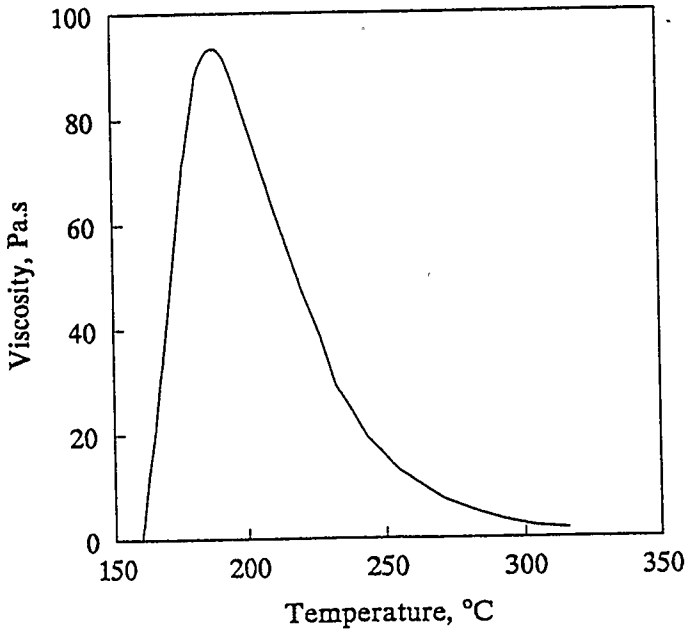


(b)

Fig. 2.4 Viscosity of liquid sulphur as function of temperature (Bacon & Fanelli, 1943), (a) lower temperature range, (b) high temperature range

maximum of 93,000 mPa.s at 187°C, i.e. approximately 8000 times the value at 120°C. The viscosity decreases beyond this temperature by a factor of 60 until 315°C (Bacon and Fanelli, 1943). The heat capacity plotted in Fig. 2.5 also increases 1.8 times from 1.02 kJ/kgK at 130°C until a maximum is attained ~158°C (Lewis and Randall, 1911). Approximately 75% of the rise in $C_p$ value occurs at ~157°C. That is both $\eta$ and $C_p$ rise sharply at effectively the same temperature but attain maximum values at different points and show different trends as the temperature is increased. At ~188°C at which $\eta$ is close to maximum, $C_p$ had already decreased to 1.17 kJ/kgK.

### 2.1.3 *The Flow of Melt*

As sulphur melts, the liquid is expelled from the gap between the two boundaries by an applied force. The liquid film width is normally very narrow. It is within 1 mm as discussed in chapter 1 and it increases along the azimuthal direction. The flow of liquid in contact melting is usually laminar (Moallemi and Viskanta, 1985a). Velocities, however, can reach up to $4.7(10^{-2})$ m/s (Saito et al., 1985a, 1985b) depending on the magnitude of the applied force. This continuous flow affects the heat transfer rates which in turn promotes the melting process. The relationship between the heat transport and the fluid flow is non-linear and can be complex due to the following reasons: a) the surface contour is unknown *a priori* and is expected to vary with time and depend on factors such as applied force, separation between tubes and size of tube; b) the migration rate of the hot tube depends on the process driving force ($\Delta T_w$), the gap width and flow patterns around the tube and c) changes in viscosity ($\eta$) over the range 113 ~ 200 °C (since

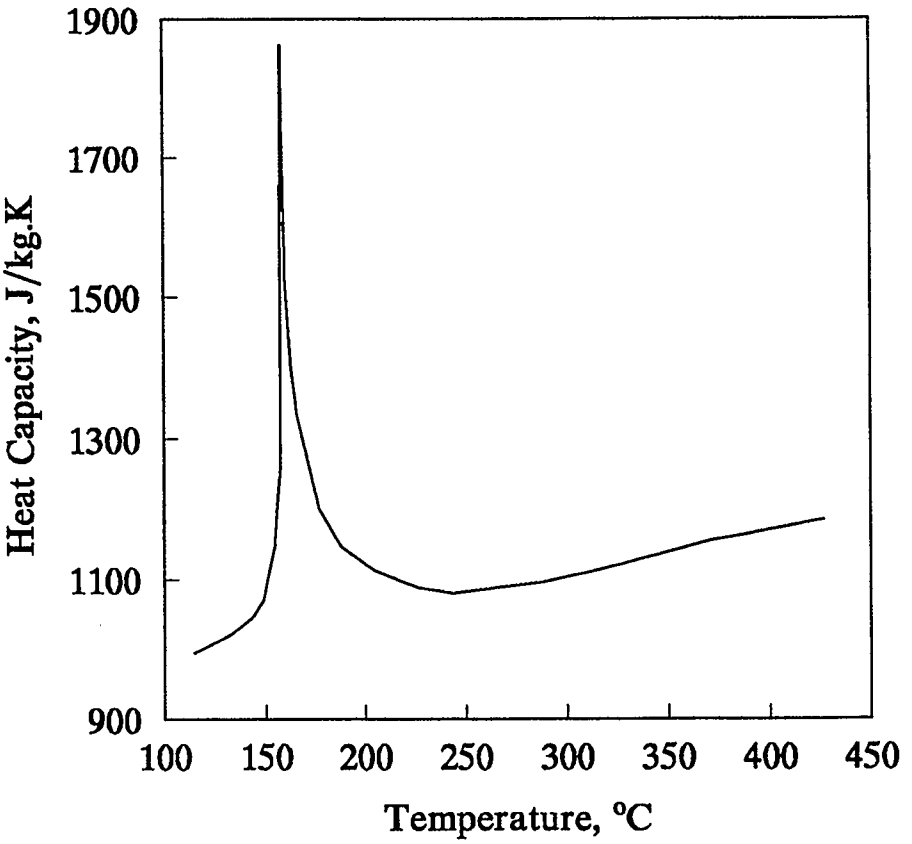


Fig. 2.5 Heat capacity of liquid sulphur as function of temperature
(Lewis & Randall, 1911)

operators prefer to keep the hot tube at ~200°C) may mean that the velocity profile will be complicated and different from Couette flow ( as shown in Fig. 2.6).

## 2.2 Close-Contact Melting

The "classical" phase change problem, known as the Stefan problem (Stefan, 1890), has been widely studied during the past century. In the traditional approach to the melting process, it was assumed that the conduction across the liquid melt was the sole means by which heat was carried from the heating source to the interface. Thus the heat transfer rate decreases monotonically as the melting surface receds. Such a problem can be solved analytically with a prediction for the movement of the melting front.

In more recent work, encompassing both experiment and analysis, it has been demonstrated that a key role is played by natural convection in the melt layer. The cases of melting above or below a heated horizontal plate and at vertical surfaces have been studied by Hale and Viskanta (1978, 1980). The melting inside vertically oriented cylindrical enclosures has also been studied experimentally by Bareiss and Beer (1980). Melting within horizontal tubes has been the subject of studies which are numerical simulations (Saitoh and Hirose, 1982), experimental observations (Katayama et al., 1981) and both (Rieger et al. 1983). Melting outside a stationary vertical tube, with natural convection present, was numerically simulated by Sparrow et al.(1977). Features common to the aforementioned investigations are: (a) the demonstrated importance of natural convection unlike in Stefan's formulation and (b) there is no relative movement between

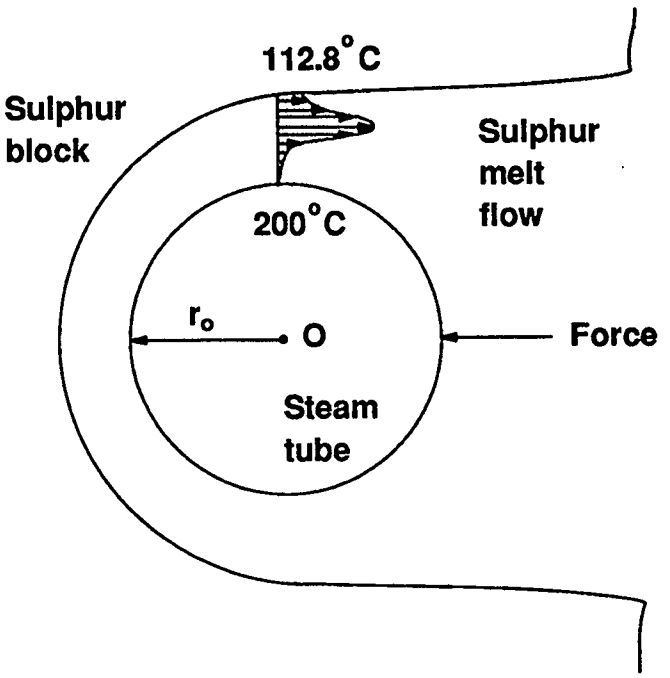


Fig. 2.6 Schematic of molten sulphur flow between two solid surfaces

the solid and the heating source during melting. For example, in Sparrow et al.'s (1977) numerical study on the melting of a solid at its fusion point by an embedded vertical tube which was heated, natural convection caused variations in the heat rate. The rate decreased at early times and reached a minimum when heat transport was controlled only by heat conduction. With the onset of convection, the rate increased and achieved a maximum before decreasing again as the melting surface receded. With pure conduction, however, the heat transfer rate would have continued to decrease monotonically. The width of the region occupied by the melt was found to vary along the length of the tube, with the greatest thickness near the top. These findings indicate that flow effects are of importance in enhancing melting rates.

In close-contact melting, the phase change material (PCM) and the heating source are pressed against each other. Heat transfer occurs through a very thin layer to enable high heat fluxes. Studies involving close contact melting are reviewed in the following sub-sections. The problem has the following features. A heat source is in relative motion with the domain in which it is embedded or with which it comes in contact. The melt is produced and thus flows over the surface of the source. The heat input by the source is distributed between warming up the domain, supplying latent heat for melting and storage in the melt produced as sensible heat.

### 2.2.1 *Moving heat source problems*

Analytical solutions for problems with moving heat sources have been obtained for simple configurations such as slabs and half-infinite plates (Rosenthal, 1946; Landau,

1950; Carslaw and Jaeger, 1959). The heat source was assumed to be infinitesimal in size such as a hot spot in the medium. In Carslaw and Jaeger's (1959) model, the hot spot was represented as a point source of heat in an infinite half space. The heat source moved vertically with a constant rate $u_o$. The hot zone locally melted the PCM, but as it passed through, the liquid formed re-froze. Heat was conducted from the source to the surrounding region. The temperature distribution was derived as

$$T(x,y,z) = (s/4\pi\lambda)\left(\frac{\exp\left[-(R_1 - x)\,u_o/2\kappa\right]}{R_1} - \frac{\exp\left[-(R_2 - x)\,u_o/2\kappa\right]}{R_2}\right) \quad (2.1)$$

where s is the strength of the source, $\lambda$ is the thermal conductivity, $\kappa$ is the thermal diffusivity, $R_1$ and $R_2$ are the distances to the source and the image source.

Jackson (1965) extended the work of Carslaw and Jaeger (1959) to the case of a thin rod geometry. Temperature distributions were determined subject to a constant migration rate of the heat source. Here again, the heat source was considered to be infinitesimal in size as a hot spot. No convective interaction between the melt and the heat source was included. The melt was simply assumed to re-solidify into its original solid shape after the passage of the heat source due to some external cooling.

Logan (1974) attempted to account for the convection effect on a process in which phase change occurred around a moving heat source. The process described was a deep self-burial of radioactive wastes by rock-melting capsules which are normally spherical containers. The heat generated inside the capsule brought the surface of the sphere to a temperature which was higher than the melting point of the surrounding rock. Formation of a melt rock-layer occurred. The melt was displaced and the capsule continuously

descended under its own weight. The descent rate was determined by the rate of energy exchange between the capsule and the rock melt with the consideration of conduction losses by using an empirical estimation. The displacement rate, therefore, was only a function of the heat generation rate. No convective heat transport due to the upward movement of the "squeezed" melt was considered in the model, and the rock melt layer thickness between the source surface and the rock interface was not determined.

For these set of studies, the motion of the melt is ignored. Heat used to produce a small amount of melt is withdrawn by the medium. The net effect is that the hot body moves and the surrounding is heated.

### 2.2.2 *Theoretical analyses and experimental investigations on close-contact melting problems*

Lea and Stegall (1973) analyzed the steady melting of an ice wall with a hot plate impressed under a constant pressure. The plate was assumed to move at a constant rate. A thin film of water separated the two solids. In their analysis of the flow of water within the film, the governing Navier-Stokes equation was linearized by neglecting the inertial terms. The density and viscosity of the melt were assumed constant. They suggested that a relationship exists between the film thickness, the contact pressure and the melting rate of ice, which can be expressed as

$$\delta = \left[ \frac{v_m \, \eta \, L^2}{p_{av}} \right]^{\frac{1}{3}} \qquad (2.2)$$

In their equation, $p_{av}$ is the average pressure within the fluid in the gap, $L$ is the vertical length of the melting surface, $v_m$ is the velocity at which the melting surface moved and $\eta$ is the melt viscosity. Equation (2.2) is consistent with the trends one would anticipate since the film thickness decreases as the contact pressure is elevated. The energy balance equation in two dimensions is

$$u \frac{\partial T}{\partial x} + v \frac{\partial T}{\partial y} = \lambda \left( \frac{\partial^2 T}{\partial x^2} + \frac{\partial^2 T}{\partial y^2} \right)$$

The scalar orders of the heat conduction terms in the energy equation are $\Delta T/L^2$ and $\Delta T/\delta^2$ along the flow direction (i.e. x direction) and across the film (i.e. y direction), respectively. Since $\delta << L$ and $\partial^2/\partial x^2 << \partial^2/\partial y^2$, the first term on RHS, or the conduction term in the melt flow direction can be neglected (The orders of magnitude for convection terms are respectively $\Delta T \, u_o/L$ and $\Delta T \, v_m/\delta$). Only if $(v_m/\delta)(L^2/\lambda) << 1$ can the convection terms in LHS be omitted.

In their analysis, all convection terms were neglected without verifying the above condition. Therefore, a linear temperature profile was obtained across the film.Moreover, another relationship between $v_m$ and $\delta$ should be determined such that $v_m$ and $\delta$ can be predicted from eq.(2.2).

A more realistic model was developed by Emerman and Turcotte (1983). They studied the migration of a hot sphere under gravity as it melts the surrounding medium. The liquid between two solid surfaces was a thin film. Behind the sphere was a molten

wake. The liquid gap thickness, $\delta$, varied with the longitudinal angle $\theta$. the layer was thin compared to the radius of the sphere $r_o$ ($\delta/r_o << 1$). A coordinate system (x,y) was curvilinear with x along the spherical surface and y across the film. The lubrication approximation (Schlichting, 1979) was applied. This involves neglecting the inertial terms in the equations of motion. In the energy equation, conduction along the x direction was neglected. The convection term along the y direction was retained. The energy equation was solved by an integral method. The gap thickness was then found to satisfy

$$\delta = \frac{\kappa f(Ste)}{u_o \cos \theta} \tag{2.3}$$

In eq.(2.3), Ste is the Stefan number defined as $C_p(T_w-T_m)/h_{sl}$, where $h_{sl}$ is the heat of fusion, $T_m$ is the melting point of the PCM, $T_w$ is the temperature of the heat source and $C_p$ is the heat capacity of the melt. Also $\kappa$ is thermal diffusivity and $u_o$ is the migration speed of the sphere, $\theta$ is the azimuthal angle from the direction of migration of the heat source. The function f(Ste) is written explicitly as:

$$f(Ste) = \frac{1}{2}\left( -\frac{3}{2} Ste - 10 + \left[\frac{9}{4} Ste^2 + 70\, Ste + 100\right]^{1/2} \right) \tag{2.4}$$

An obvious limitation for eq.(2.3) is that $\delta$ becomes infinite when $\theta = \pi/2$. In eq.(2.3), neither of $\delta$ and $u_o$ is known. The additional relationship required was obtained from a force balance. This related the migration rate $u_o$ to the pressure forces. The shear stress, of the order of $\eta u_o r_o/\delta^2$, is negligible compared to the pressure grdient which is of the order $\eta u_o r_o/\delta^3$. The force, $F_d$, is expressed as:

$$F_d = \frac{\pi\eta R^4 u_o^4}{2\kappa^3 f^3(Ste)} \tag{2.5}$$

Moallemi and Viskanta (1985a) extended the above analysis to the case of a horizontal cylinder migrating through a solid block under gravity. Their assumptions and the solution technique were similar to those by Emerman and Turcotte (1983). They also carried out experiments using the same geometry and n-octadecane as the phase change material. The temperature of the cylindrical surface was kept constant at a value above n-octadecane's melting point. Parameters varied were the density (and hence gravity forces) of the heat source, its surface temperature and where the source was initially located in the PCM. The velocity of the heat source was empirically correlated with the Stefan number from the experimental data as:

$$u_o^* = 161.3\ (Ste)^{1.095} \tag{2.6}$$

In eq.(2.6), $u_o^*$ is the dimensionless displacement rate of the heat source, defined as $u_o r_o/\kappa$. This relationship did not agree well with the results from the analytical model which suggested that (for Ste < 0.2)

$$u_o^* = 146.5\ (Ste)^{0.75} \tag{2.7}$$

Eq.(2.7) was derived from an expression similar to eq.(2.5). The measured velocities are between 64 percent to 47 percent lower than those predicted by the analysis. For instance, when Ste = 0.1, $u_o^*$ values calculated form eq.(2.6) and (2.7) are 12.96 and 26.05 respectively, or the measured velocity is ~50.2 percent smaller than prediction.

From the experimental investigation of Moallemi and Viskanta (1985a), two

conclusions can be drawn: (a) conduction was the dominant heat transfer mechanism around the lower stagnation point of the source where the surfaces are in closest approximation. The migration velocity of the heat source is essentially determined by the heat transfer in this region. (b) The shape of the melting interface near the stagnation point stops changing quickly while other points continue to deform. Experiments involving the same geometry and under constant surface heat flux conditions were undertaken by Moallemi and Viskanta (1985b). Their findings were similar to those obtained by Moallemi and Viskanta (1985a).

In Saito et al.'s (1985a) experiments on contact melting, molten liquid was squeezed out of a thin layer between a flat solid and the melting interface by an imposed force. Parameters varied were the contact area of the surface of the disk, the force applied and the surface temperature. The heat flux increased by about 1.5 ~ 1.8 times for a contact pressure rise by a factor of 10. The correlation derived was

$$q^* = A\ (P^*)^m\ (Ste)^{-n} \qquad (2.8)$$

where $q^*$ is the non-dimensional heat flux ($q\ r_o/\lambda\Delta T$ ), $P^*$, the dimensionless contact pressure ($F/\pi\eta\kappa$), and A, m and n are constants with m and n estimated to be 0.2 ~ 0.3.

The actual mean liquid layer thickness was 0.014 and 0.16 mm as dimensionless pressure decreased 100 times from $5.85(10^{10})$ to $5.88(10^{8})$ for melting ice. The maximum velocities along the flow direction at approximately the middle plane of the liquid gap were reported to increase nearly 10 fold from $5.1(10^{-3})$ to $47(10^{-3})$ m/s at ($P^*$, Ste) values of ($2.25(10^{8})$, $2.51(10^{-2})$) and ($5.85(10^{10})$, $1.59(10^{-2})$) respectively. Maximum velocities in the vertical direction were attained at the melting boundary with values between $1.9(10^{-5})$

and $9.8(10^{-5})$ m/s for ($P^*$, Ste) values with ranges ($5.85(10^{10})$, $3.78(10^{-3})$) and ($2.25(10^{8})$, $1.59(10^{-1})$) respectively. For the Ste range of $10^{-3}$ to 0.1, heat fluxes were correlated against pressure and Stefan number, using the least square approximation, to give values of A = 0.94, both m and n with 0.25. For Ste less than 0.1, the thickness of the liquid film was almost uniform and convection due to the flow of melt did not appear to enhance the rates of heat transfer between the two surfaces.

This problem was numerically simulated (Saito et al., 1985b) with neglect of the inertial terms in the hydrodynamic equations. The analysis involved a steady state. Parameters were varied over a wide range, i.e. Ste = $10^{-3}$ ~ 2.5 and $P^*$ = 10 ~ $10^{11}$. The liquid gap thickness was calculated and shown to vary along the flow direction. Nevertheless, only average gap widths were reported in the results.

In further studies on the subject, Saito et al. (1986) provided an expression valid for wider ranges of Ste ($10^{-3}$ ~ 4.0) and $P^*$ (10 ~ $10^{11}$). The parameter A in eq.(2.8) was replaced by a function F(Ste) determined as:

$$F(Ste) = 0.915 + 0.168\ Ste - 0.00608\ Ste^{2.64} \qquad (2.9)$$

F(Ste) or A equals 0.94 when Ste ~ 0.15. The experiments from which this relationship was generalized involved melting in an enclosed capsule. Heat was supplied from the bottom and the melt produced was expelled by gravity forces on the mass of solid left. The liquid flowed to the side and accumulated over the solid.

The height of the solid block decreased with time according to the relationship:

$$H^* = ( 1 - 0.75\ \beta\ t^* )^{4/3} \tag{2.10}$$

where

$$\beta = \left[ \frac{g\ r_o^2\ \Delta\rho\ H_o}{\eta\ \kappa} \right]^{0.25} (Ste)^{-0.25}\ F(Ste) \tag{2.11}$$

In eq.(2.10), $H^*$ has been scaled by the initial height $H_o$, $t^*$ is the dimensionless time scaled by $(Ste\ \kappa/r_o\ H_o)(\rho/\rho_s)$. $\Delta\rho$ is the density difference between the solid and its melt $(\rho_s - \rho)$ and g is the gravitational acceleration.

Moallemi et al.(1986) also conducted similar experiments with n-octadecane employed as PCM. The solid was not enclosed in a capsule and the melt was expelled. The study included a steady state analysis in which the following assumptions and approximations were made: a) the energy transport as sensible heat by the melt was not negligible compared with latent heat; b) temperature distribution in the liquid layer was obtained by an integral method and c) the liquid layer thickness was prescribed as an exponential function. A relationship for the height of the solid left versus time was obtained as:

$$H^{*'} = \left[ H_o^{*'\ 3/4} - \frac{3}{4}\ t^{*'}\ \left(\frac{\rho^*\ g^*\ Ste}{C\ Pr}\right)^{1/4} \right]^{4/3} \tag{2.12}$$

where $H_o^{*'}$ is the dimensionless initial height of solid $H/r_o$, $t^{*'}$ is the dimensionless time $(\kappa/r_o^2)\ t$, $g^* = gr_o^3/\kappa^2$ and $\rho^* = \rho_s/\rho$. Eq.(2.12) can be re-arranged to yield

$$H^* = [\ 1 - 0.75\ \beta'\ t^*\ ]^{4/3} \tag{2.13}$$

where

$$\beta' = \left[\frac{g\, r_o^2\, \rho_s\, H_o}{\eta\, \kappa}\right]^{0.25} (Ste)^{-0.75}\, C^{-0.25}\, (\frac{\rho_s}{\rho}) \qquad (2.14)$$

The constant C has value of 3/2 for a circular area of close contact and 4 for a rectangular surface.

Predictions of $H^*$ from eq.(2.13) were always lower than the measured values and the difference increased with elapsed time. The foregoing is the reverse of the trends obtained by Saito et al. (1986) with the melt contained. Moallemi et al.(1986) obtained that

$$\delta^* = \frac{f(Ste)}{u_o^*} \qquad (2.15)$$

where $\delta^*$ is the dimensionless thickness of liquid film defined as $\delta/r_o$. The function f(Ste) was given as:

$$f(Ste) = \frac{\left(\sqrt{400 + (200 + 80n)\, Ste + 9\, Ste^2}\right) - 3\, Ste - 20}{2\,(n+1)} \qquad (2.16)$$

In eq.(2.16), n has value 0 for rectangular and 1 for circular cross sections of the PCM. The rate of migration of the solid depended on the instantaneous weight of the solid, i.e.

$$u_o^* = \left[\frac{g^*\, \rho^*\, Ste}{C\, Pr}\right]^{0.25} (H^{*\prime})^{0.25} \qquad (2.17)$$

Pr in the denominator is the Prandtl number ($\eta C_p/\lambda$).

In a relatively recent study, Hirata et al. (1991) investigated melting of ice and n-octadecane inside horizontal rectangular capsules at three aspect ratios ($H_o/L$ = 3, 1 and

1/3, L is the length of the capsule). Close contact between the heated and melting surfaces was maintained by gravity. Sensible heat in the melt was neglected and the width of the liquid gap was held constant along the flow direction. The film thickness was derived as,

$$\delta^* = \left[ \frac{Ste}{g^* (1-\rho^*) Pr (H_o/L)} \frac{1}{H^*} \right]^{1/4} \qquad (2.18)$$

In eq.(2.18), $\delta^*$ depends on time elapsed through $H^*$. Hirata et al. (1991) obtained $\delta$ values in the ranges between 0.1 and 0.4 mm at the bottom of the capsule. These values are much larger than values of 0.014 and 0.16 mm reported by Saito et al.(1985a, 1985b), but forces were different by an order of magnitude of ~1000.

Bejan (1993) commented on the work of Hirata et al. (1991) and suggested that the thin film analysis was a special case of the more general theory earlier derived by Bejan (1989). In the latter, Bejan described melting on a rectangular surface with or without relative motion (sliding) between the solids and with or without heat generation by viscous dissipation in the liquid film. He noted that the film thickness formula (eq.2.18) was essentially the same as

$$\delta^* = \left[ \frac{Ste}{P_n/(\kappa\eta/L^2)} \right]^{1/4} \qquad (2.19)$$

where $P_n$ is the instantaneous average pressure maintained between a melting solid and a flat hot surface. He also pointed out that, because contact melting was quasi-steady, the presence of $H^*$ as a time-dependent variable on the right-hand side of eq.(2.18) is misleading: the time-dependence entered that expression only through the instantaneous

average pressure, which changed slowly with time. However, we can see the systems described by Hirata et al. (1991) and Bejan (1989) are different. Hirata et al.'s (1991) problem is subject to buoyancy and therefore the actual pressure on the film is H $(\rho_s-\rho)g$. For the latter case, the liquid was squeezed out of the film and the contact pressure is $H\rho_s g$.

In the following, studies involving melting inside the horizontal cylindrical capsules and spherical enclosures are reviewed. Bareiss and Beer (1984) were the first to investigate the case of a horizontal cylinder. They monitored photographically changes in the contours of the enclosed solid as it melted. The rate of liquid production and the heat flux densities were determined. An analysis was carried out with assumptions which include: a) the fluid flow within the gap is quasi-steady and laminar; b) pressure gradients across the liquid film were negligible; c) there was no flow along the radial direction, d) the density of the solid is greater than that of the liquid and natural convection at the upper region was non existent and e) the temperature profile across the gap was linear. The downward velocity of the centroid of the solid bulk was correlated with Stefan number ( $Ste = C_p(T_w-T_m)/h_{sl}$), Prandtl number ( $Pr = C_p\,\eta/\lambda$ ) and Archimedes number ( $Ar = (\Delta\rho/\rho_s)(gr_o^3/\kappa^2)$ ). The expression obtained was:

$$u_o^* = 0.4\left(\frac{Pr\ Ar}{Ste}\right)^{0.25} \rho^{*\,0.75}\,(\,1 + CC\,) \qquad (2.20)$$

where

$$CC = 0.25 \left( \frac{Ste}{Pr\ Ar}\ \rho^*\ Ra \right)^{0.25} \qquad (2.21)$$

The dimensionless time required for completely melting the solid $t_a^*$ is the inverse of eq.(2.20). Therefore $t_a^* = 1/u_o^*$. The shift distance $s_o$ was defined as the distance of the upper most point on the melting solid contour to the upper most point of the enclosure. The relationship between $s_o$ and the elapsed time was given as:

$$t^* = \frac{0.805}{u_o^*} \left( s_o^* + 0.167\ s_o^{*2} + 0.074\ s_o^{*3} \right) \qquad (2.22)$$

In eq.(2.22), $t^*$ is dimensionless elapsed time (Ste $\kappa/r_o^2$) t, $s_o^*$ is the dimensionless shift distance as $s_o/2r_o$. When $t^* = t_a^*$, $s_o^* = 1$.

The experimental results agreed with the theoretical predictions at early times in the melting process. The data ($s_o^*$ and $t^*$) deviated significantly from analytical solutions in the final stages of the liquefaction. They suggested that the limit of validity of the analytical solution can be defined by means of following expression

$$\frac{Ste}{Pr\ Ar}\ \rho^*\ Ra < 1.4 \qquad (2.23)$$

Eq.(2.23) suggests that the CC value (in eq.(2.21) would be less than 0.27. The melting which occurred at the upper surface of the cylinder was estimated as ~ 10 - 15% of the total. This was ignored in their analysis. One can, however conclude that the melt conveyed sensible heat to the wake of the PCM to cause some of the phase change.

Prasad and Sengupta (1987) extended Bareiss and Beer's (1984) work by including the effect of natural convection in the governing equations and they solved the problem

numerically. Calculated Nusselt numbers ($Nu = h\ d/\lambda$) along the upper surface of the tube and at the rear side of the PCM are indicated to strongly depend on the Rayleigh number ($Ra = \beta\ g\ r_o^3\ (T_w - T_m)/(\kappa\ \nu)$ ). Their results were in close agreement with Bareiss and Beer's (1984) prediction up to $Ra = 5(10^5)$. It was suggested that, at higher Rayleigh numbers, Bareiss and Beer's (1984) results underestimate the heat flux.

Saito et al. (1988) also studied a similar problem with the difference that the tube was not closed. That is, the heat transfer surface was a sector covered on the upper surface of a copper block. The radius of the surface was, $r_o = 17.5$ mm, its length was 240 mm and the sector angle was $2 \cdot \pi/3$ (120°). The system was symmetric about a vertical plane through the axis of the circle circumscribed. The melting solid was ice. A steady force was applied to the top of the ice. The water produced was squeezed azimuthally out of the gap and over the edge at an angle of 60° to the vertical. The analysis performed had similar assumptions to those previously given by Saito et al.(1985b, 1986). The average heat flux on the heat transfer surface was found to depend on three non-dimensional parameters: Stefan number Ste, contact pressure $P^*$ and the contact angle $\theta_c$. Melting was controlled by pure conduction across the liquid gap for Ste $< 0.1$. For Ste $> 0.1$, the flow of the melt significantly enhanced the rate of phase change. Their experimental results were in good agreement with the numerical solutions.

The effect of inclining the tube which contained a melting solid was studied experimentally by Sparrow and Myrum (1985). The circular tube was of copper and the PCM was high purity paraffin (99 percent pure n-eicosane). The length-diameter ratio of the tube was ~5. Melting was first investigated with the tube axis vertically oriented. Then

the tube was inclined successively at angles of 5, 10 ,15, 20, 25 deg to the vertical. It was found that natural convection determined the melting rates until an angle 15° was reached. Thereafter, close-contact was established. With close contact, enhancements up to a factor of two in the rate at which melt was produced were achieved compared to when natural-convection dominated the melting process.

In the experiments performed by Sparrow and Geiger (1986) to study the melting of a solid encapsulated in a horizontal tube, a comparison of heat transfer rates was made for cases of the solid constrained to be stationary and allowed to fall freely to the bottom of the tube under gravity. The results showed that for a fixed duration, the melt produced in the unconstrained mode exceeded that in the constrained mode by 50-100%. For the unconstrained mode, 90% of the melting occurred at the lower region of the solid.

Webb et al. (1987) similarly investigated a melting process of unconstrained ice in a horizontal cylindrical capsule to determine the interaction of "forced" flow induced by the solid squeezing out the melt and natural convection. The PCM, ice, was lifted by buoyancy to the top of the heated cylinder where close-contact melting occurred. Three distinct flow regimes were identified as the cylinder wall temperature was changed. When the wall was below the density inversion point of ~ 4°C, water was squeezed out of the gap by the solid, to form weak recirculation cells at the lower edges of the ice near the wall. With increasing time, the separation point on the cylinder wall moved upward such that the recirculation cells remained approximately the same size. At wall temperatures far above 4°C, the flow exhibited two-dimensional recirculation cells near the edge of ice, and strong three-dimensional rolls and plumes in the cavity below. At intermediate wall

temperatures, the flow pattern was in transition, characterized by multiple two-dimensional cells in the melt.

The melting of solids confined within spherical enclosures has also been studied. Moore and Bayazitoglu (1982) were the first to carry out an experimental study and undertake a numerical analysis of the problem. Results of their study showed good agreement with their experimental data for Ste = 0.05 and 0.1 with a maximum deviation of about 10 percent for the predicted interface position. Roy and Sengupta (1987) extended Bareiss and Beer's (1984) analysis of the melting process in a cylindrical enclosure to the one with spherical geometry. They employed the same assumptions. The solutions were in good agreement with the experimental data of Moore and Bayazitoglu (1982). The maximum deviation of the predicted interface position from the experimental results was about 16 percent. The two main parameters found to affect the melt rates were the temperature difference across the film and the ratio of the net gravity to viscous forces in the film. The latter is defined as the Archimedes number. Babrami and Wang (1987) also applied an analytical technique similar to that of Bareiss and Beer (1984) in considering melting inside a sphere. The theories of lubrication (Schlichting 1979) and film condensation (Nusselt, 1916) were applied. The energy equation was solved using an integral technique similar to the one employed by Emerman and Turcotte (1983). In their findings, the centroid of the solid bulk descended at a relatively constant speed. The dimensionless melting time was expressed as a function of Ste, Pr, Ar and dimensionless travel distance. The functions relating melting time to distance travelled by the centroid were different for spheres and for cylinders ( as in eqs.(2.20) to (2.22) ). For complete

melting of a sphere, $t_a^*$ was derived as (Babrami and Wang, 1987)

$$t_a^* = 2.03\ \rho^* \left( \frac{Ste}{Pr\ Ar} \right)^{1/4} \tag{2.24}$$

From the foregoing review, the major findings from analytical and experimental studies on close-contact melting are summarized as follows.

From the theoretical analysis:

1. The dimensionless parameters affecting the close-contact melting are found to be the Stefan number Ste, the applied force $P^*$ (if there is one), Archimedes number Ar (when there is buoyancy) and critical sector angle $\theta_c$ (in cylindrical or surface curved geometry).
2. The liquid film thickness between two contact surfaces is very thin, normally less than 0.5 mm. Its value can be estimated from analysis.
3. The rates of relative motion between the melting solid and the heating source are inversely proportionally to the liquid gap width. The migration rates are also increased at higher driving potential (i.e. larger Ste) and larger imposed pressure;

From experimental observations:

1. The process is transient at least in the early stages of melting;
2. The heat transfer rate is much higher for close contact melting compared with the phase change problems in which there are no relative motions between the

heating source and the melting solid;

3. Conduction is the principal mode for heat transfer in this process when Ste numbers are small. Fluid flow enhances melting at high Ste. When the heat transfer surfaces are curved as with cylinders and spheres, conduction determines the rate of melting at the stagnation point and hence the displacement rate of the heat source.

### 2.2.3 *Numerical simulation of transient close-contact melting*

Literature on numerical solution of transient close-contact melting problem is very sparse. In the following section, the related studies are reviewed.

In the analysis of steady or quasi-steady melting problem, numerical calculations have been undertaken to solve simplified transport equations (Saito et al.,1985b, Saito et al., 1986, Saito et al., 1988). Moore and Bayazitoglu (1982) were the first to simulate a transient close-contact melting process within a spherical enclosure. The density of the solid was greater than that of the liquid so that the solid continually dropped towards the bottom of the shell as melting progressed. The model was developed in polar coordinates and the origin was placed at the centre of the sphere and was thus valid as long as the origin is within the solid region. The interface contour could be predicted only up to the time when the point at the most upper front (at $\theta = 0$) of the contour coincided with the origin. It was also assumed that the gap width changed slowly with time and the velocity field was quasi-steady. The radial velocity was neglected. The energy and interface equations were solved by the Crank-Nicolson procedure which employed finite difference

techniques. Numerical results were reported for the instantaneous interface positions of the solid and the temperature distributions in the melt. The interface position was found to be in good agreement with their experimental results in the early stages of melting and at small Stfan numbers. About a ~10% deviation was observed when Ste became larger ($> 0.1$).

Moallemi (1985), Moallemi and Viskanta (1986) formulated a general mathematical model for unsteady contact melting by a migrating horizontal cylinder. One difficulty associated with the problem, as formulated, is that at time zero, the two surfaces touch and cause a singularity. They then simplified the problem according to their experimental observations which suggested that the melt domain can be divided into two distinct and different regions. Two regions were distinguished by the thickness of the melt layer, $\delta(\theta)$, separating the source and the solid. The first region referred to the melt layer under the heat source bounded by the solid where $\delta(\theta)$ was much smaller than the radius of the source (i.e. $\delta(\theta) << r_o$). The second region was then the remaining of the melt domain or the melt wake left behind the source. They then set up two sets of formulations for two the regions. In the first region, a quasi-steady state was assumed and the migration rate of the heat source was independent of time. Due to $\delta(\theta) << r_o$, the momentum equations and energy balance equations were further simplified by neglecting the second derivatives along the flow direction (i.e. $\partial^2/\partial x^2 << \partial^2/\partial y^2$ ). To this point, their simplified transport equations in this region were similar to those of Emerman and Turcotte (1983) and Moallemi and Viskanta (1985a, 1985b) for steady analyses. In the second region, $u_o$ was also assumed constant. For the numerical approach, a new

parameter $\delta_o$ was introduced which was the minimum separation gap width (at $\theta = 0$). The displacement rate of the heat source was then determined by the melting interface energy balance at $\theta = 0$. The transport equations in the first region were solved via a marching-integration procedure along the dominant flow direction. Based on the solutions from the first region, the transport equations in the second region were solved by equating the profiles of velocity and temperature at the interface between the two regions. The irregular flow domain was transferred to a regular one through an adaptive grid generation method. The numerical results showed that the heat source velocity was only a function of Ste, as it was independent of $\delta_o$ and the density difference between the source and the melt. The simulation, however, underestimated the heat source velocity compared with experimental observations.

Hong and Saito (1993) recently undertook a numerical simulation for a transient close-contact melting. An algorithm was developed for a solid pressed against a flat heating surface in rectangular coordinates. The usefulness and effectiveness of their algorithm were tested by two problems. The first one involved imposing a constant temperature at the heating surface. The second one was a copper block with an initial temperature higher than 0° and being cooled by ice in which the copper block was used as the heat source. The copper block was insulated except at the surface contacting ice. The algorithm employed the SIMPLE method (Patankar, 1980) in a fixed grid domain. Transport equations were formulated using the primitive variables in two-dimensional Cartesian coordinates. For the first problem, steady state was attained after ~15 seconds. The gap width gradually increased along the direction of liquid flow, but the difference

between the minimum near the centre line and the maximum near the exit was less than 0.1%. The liquid-solid interface was reported to be planar and parallel to the heating plate at smaller Stefan number ( less than 0.1). The average thickness of the liquid layer calculated from their simulation was in good agreement with that of the steady state analysis conducted by Moallemi and Webb et al.(1986) and Saito et al. (1986). The velocity profile was almost parabolic with its maxima located at the middle of the gap and its value increasing along the flow direction. In their second problem, the calculations were carried out for different initial temperatures and heights of the copper block. Results were presented for only one specification of the copper block: 0.2 m in length, 0.05 m in height and initially at 20°C. Ice was 0.1 m in height and at melting point 0°C. The velocity profiles were also parabolic, similar to those in the first problem. Nevertheless, the thickness of the liquid layer increased significantly along the flow direction. The thickness difference between the minimum and maximum was much greater than that in the first problem and amounted up to 4.5%. The surface temperature of the copper block and heat fluxes varied along the surface. The non-uniformity of surface temperature increased with time.

In closing, one can state that the numerical simulation for unsteady close-contact melting problem is now still at an early stage. Moore and Bayazitoglu (1982), Moallemi and Viskanta (1986) and Hong and Saito (1993) are the three papers so far found in the literature that deal with transient contact melting phenomena. There has been no attempt to obtain a fundamental understanding of the transient behaviour of direct-contact melting with a moving cylindrical or spherical heat source, at least in the early phases of melting.

# Chapter 3

# Analysis

## 3.1 Formulation of the Problem

A physical model of close-contact melting with an isolated vertical hot tube is proposed in this section. Governing equations which describe the hydrodynamics of fluid flow and energy transfer within the melt domain are derived in a non-inertial frame with its origin fixed with respect to the axis of the cylinder. The model is different from the commercial melting device described in chapter 1 which consists of two staggered arrays of tubes. Normally the thermal fields of an array of tubes will interact if the spacing between the tubes is small. With large spacing, and because of low thermal conductivity ($\lambda$) for sulphur, each tube may be treated as isolated.

### 3.1.1 *The Physical Model*

The model, as illustrated in Fig. 3.1, is a hot, vertical tube suddenly brought in contact with the flat surface of a solid sulphur block to be melted. In the schematic diagram, changes in the contour of the melting surface relative to an origin located at the axis of the hot tube are shown. At the start of the melting, saturated steam is suddenly passed through the tube and a constant temperature $T_w$ is rapidly attained and maintained on the tube surface. The tube is kept in close contact with the surface of the solid sulphur

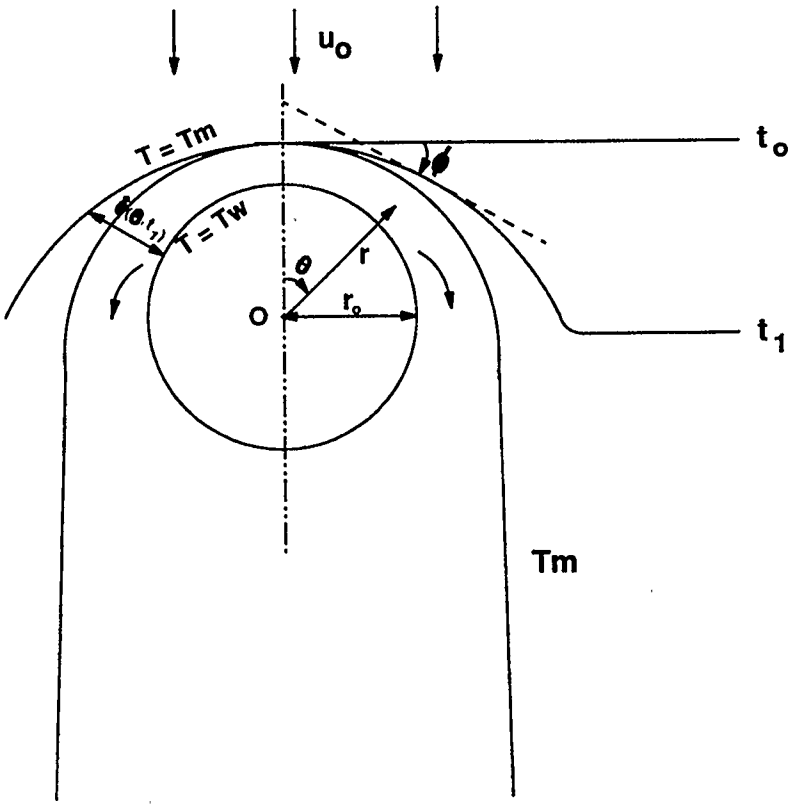


Fig. 3.1 Cross-sectional view of model

by an externally applied force. Molten sulphur produced is squeezed in the azimuthal direction out of the gap that develops and it runs down at the rear side of the tubes into a catchment basin located at the bottom of the tubes. The cylinder is assumed long enough such that the end effects can be neglected. The flow of melt is assumed to be 2-dimensional, i.e. in the radial and azimuthal directions within the gap which is the primary domain of interest. The sites of drainage due to gravity, where velocities may be 3-dimensional, were assumed sufficiently displaced away from the gap and ignored.

The following conditions are imposed on the problem.

1. The solid sulphur is composed of pure rhombic crystals, always at its melting point;

2. The melt is an incompressible and Newtonian fluid;

3. The density and thermal conductivity of the liquid are assumed constant, i.e. $\rho$ = 1790 kg/m$^3$ and $\lambda$ = 0.1399 W/mK (from experiments, $\rho$ varies by 15 kg/m$^3$ in the 120-160°C range). The density of the solid is 2070 kg/m$^3$. The density can thus decrease by a maximum ~ 16% on melting. This density difference is ignored in the current analysis.

4. The flow is laminar and viscous dissipation is negligible.

### 3.1.2 *Transport Equations*

The equations which describe the flow and the temperature fields for the melt in the inertial frame are respectively the continuity, momentum and energy equations (Bird, Stewart and Lightfoot, 1960)

$$\nabla \cdot \boldsymbol{U} = 0 \tag{3.1}$$

$$\frac{D\boldsymbol{U}}{Dt} = -\frac{1}{\rho}\nabla p + \frac{1}{\rho}\nabla\cdot(\eta\nabla\boldsymbol{U}) \tag{3.2}$$

$$\frac{Dh}{Dt} = -\frac{1}{\rho}\nabla\cdot\boldsymbol{q} + T\frac{DC_p}{Dt} \tag{3.3}$$

In Eqs. (3.1) -(3.3), **U** is the velocity vector, h equals $C_pT$ and **q** is the heat flux defined as $-\lambda\nabla T$.

With the origin fixed with respect to the axis of the cylinder and its displacement rate time dependent, the Navier-Stokes equations and the energy equation have to be transformed into a non-inertial frame when the tube is held stationary and melting solid moves with velocity $\mathbf{u}_o$ (The transformation is shown in Appendix A.1). The governing equations become (Jeje and Wu, 1994):

$$\nabla \cdot \boldsymbol{u} = 0 \tag{3.4}$$

$$\frac{D\boldsymbol{u}}{Dt} = -\frac{1}{\rho}\nabla p + \frac{1}{\rho}\nabla\cdot(\eta\nabla\boldsymbol{u}) - \frac{\partial \boldsymbol{u}_o}{\partial t} \tag{3.5}$$

$$\frac{Dh}{Dt} = -\frac{1}{\rho}\nabla\cdot\boldsymbol{q} + T\frac{DC_p}{Dt} \tag{3.6}$$

where **u** is the velocity vector in the moving coordinate system relative to $\mathbf{u}_o$. Its components are u and v in the $\theta$ - and r-directions respectively. Eq.(3.6) is expanded as, with $\kappa$ symbolizing the thermal diffusivity ($\lambda/\rho C_p$) and density $\rho$ = constant,

$$\frac{Dh}{Dt} = \nabla \cdot \kappa \nabla h + \nabla \cdot T\kappa \nabla C_p + T\frac{DC_p}{Dt} \tag{3.7}$$

The equations are subject to the following boundary conditions.

On the hot tube surface, $r = r_o$, there is no slip and temperature is uniform and constant,

$$\boldsymbol{u} = 0 \quad and \quad T = T_w \tag{3.8}$$

At the solid-melt boundary, $r = r_i$ (see Appendix A-2, eq.(A-29));

$$\boldsymbol{u} = -\frac{\partial G/\partial t - \boldsymbol{u}_o \cdot \nabla G}{|\nabla G|} \quad and \quad T = T_m \tag{3.9}$$

where $r_i$ is the radial distance from the melting interface to the centre of the tube. $G(r_i,\theta,t)$ is an implicit function which describes the shape of the melting boundary,

$$G\,(r_i,\ \theta,\ t\,) = 0 \tag{3.10}$$

Along the line of symmetry $\theta = 0$,

$$u = 0 \quad and \quad \frac{\partial \boldsymbol{u}}{\partial \theta} = \frac{\partial T}{\partial \theta} = 0 \tag{3.11}$$

The initial conditions are:

$$t = 0;\ \boldsymbol{u} = 0 \quad and \quad T = T_m \tag{3.12}$$

Eqs. (3.4) to (3.7) with the boundary and initial conditions are to be solved in a domain whose boundary at $r_i$ is not known *a priori*. Since $\mathbf{u}_o$ is a function of time, the

velocity at the melting front is also unknown. Consequently, two more constraints have to be imposed on the system so that the number of equations may match the number of unknowns. These are the local energy balance equation at the melting front and a balance on the force to maintain close contact.

At the melting surface, the energy balance equation is (Arpaci, 1966; Ozisik, 1978)

$$\lambda_s \frac{\partial T_s}{\partial n} - \lambda \frac{\partial T}{\partial n} = \rho\, h_{sl} u_n \tag{3.11}$$

where **n** is the normal vector inwards to the melting interface. Eq.(3.11) yields, in the non-inertial frame (see appendix A.3),

$$\nabla G \cdot \nabla T = \frac{\rho\, h_{sl}}{\lambda} \left[ \frac{\partial G}{\partial t} - \boldsymbol{u}_o \cdot \nabla G \right] \tag{3.12}$$

The relative motion between the hot tube and the sulphur block is governed by Newton's second law of motion

$$M \frac{d\boldsymbol{u}_o}{dt} = \Sigma \boldsymbol{F} \tag{3.13}$$

where M is the mass of the heat source, **F** is the net force acting on the body. The latter includes the externally applied force, the normal force due to pressure and the drag force due to shear stress.

The system of equations are time-dependent, non-linear and highly-coupled. Therefore, a numerical computational scheme was developed to obtain a solution. An analytical solution based on a simplified model was also examined to determine the principal parameters which affect the melting process. In the following subsections, the simplified model and the analytical solutions are presented.

## 3.2 Analytical Solution

### 3.2.1 *A Simplified Mathematical Model*

An approximate solution for the melting problem, after a long time has elapsed from the start, is here presented. Its purpose is to determine the relevant parameters and the steady state solution for the displacement rate of the heat source, the temperature and the flow fields for the melt. In the analytical solutions of Emerman and Turcotte (1983) and Moallemi and Viskanta (1985a) for spherical and cylindrical heat sources respectively, they assumed that the thin film of the melt terminated at 90° degrees from the plane of symmetry. That is, they set the critical angle $\theta_c$ to be $\pi/2$. This is the angle beyond which the curvature of the melting surface would remain constant. In their numerical simulation, Moallemi and Viskanta (1985a) found that the critical angle could be different as the melting conditions varied . It was 66.7° degrees , for example, for the melting of octadecane when the heat flux was constant and the closest approach between the surface, $\delta_o$, = $7.5(10^{-4})$ m. Saito et al. (1988) used a critical angle of 60° degrees in their experimental set-up. Since the critical angle is a parameter which defines the domain, the task is to find out how it relates to the other parameters of the system.

In addition to the assumptions stated in the previous section, the temperature range for the melting is chosen to be narrow such that the properties of liquid sulphur: viscosity and heat capacity ($\eta$ and $C_p$) can be considered constant and the liquid film separating the hot tube and solid sulphur is very thin ($\delta/r_o << 1$).

It is convenient, for the analysis, to introduce a local cartesian coordinate system

(x,y) on the cylindrical boundary (Morega et al. 1993) as shown in Fig. 3.2, which is related in the cylindrical geometry to (θ,r) as

$$x = r_o\,\theta\,, \qquad y = r - r_o \tag{3.14}$$

The Jacobian of this transformation (with respect to the rectangular coordinates (X,Y))can be written as (X = r cosθ and Y = r sinθ)

$$-\left(1 + \frac{y}{r_o}\right) = \frac{\partial\,(X,Y)}{\partial\,(x,y)} = 1 + \frac{x}{r_o} = 1 + O(\frac{\delta}{r_o}) \tag{3.15}$$

For a thin gap, eq.(3.15) shows that it is possible to consider (x,y) coordinates as if they were orthogonal coordinates with no local curvatures and constant metric. The transport equations under steady state conditions can be transformed into the (x,y) coordinate system as:

(a) mass continuity:

$$\frac{\partial u}{\partial x} + \frac{\partial v}{\partial y} = 0 \tag{3.16}$$

(b) momentum equations for velocity component u and v:

$$u\frac{\partial u}{\partial x} + v\frac{\partial u}{\partial y} = -\frac{1}{\rho}\frac{\partial p}{\partial x} + \nu\,(\frac{\partial^2 u}{\partial x^2} + \frac{\partial^2 u}{\partial y^2}) \tag{3.17}$$

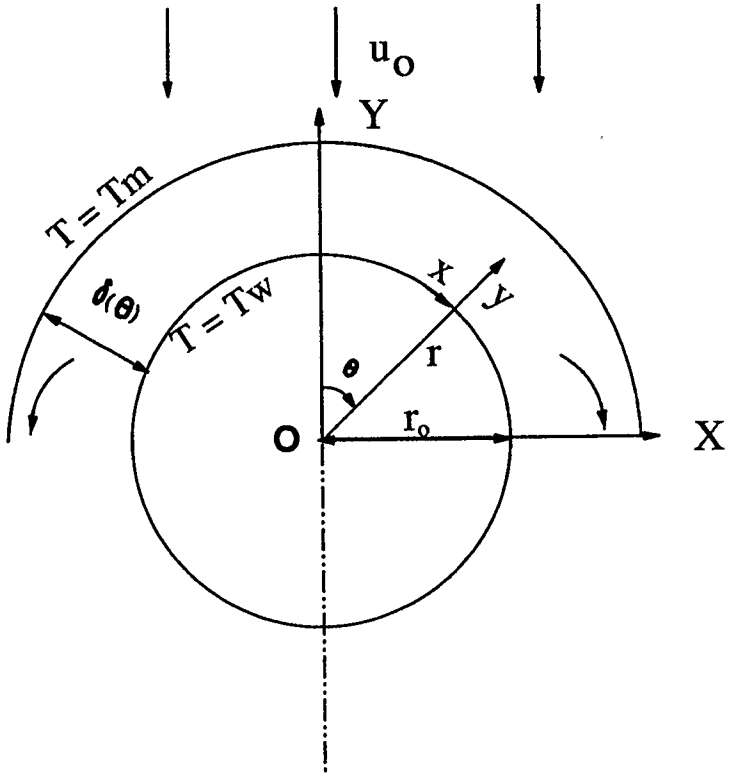


Fig. 3.2 Physical model for quasi-steady state analysis

$$u\frac{\partial v}{\partial x} + v\frac{\partial v}{\partial y} = -\frac{1}{\rho}\frac{\partial p}{\partial y} + \nu\left(\frac{\partial^2 v}{\partial x^2} + \frac{\partial^2 v}{\partial y^2}\right) \tag{3.18}$$

(c) energy conservation:

$$u\frac{\partial T}{\partial x} + v\frac{\partial T}{\partial y} = \kappa\left(\frac{\partial^2 T}{\partial x^2} + \frac{\partial^2 T}{\partial y^2}\right) \tag{3.19}$$

with constant fluid properties $\kappa$ ($\lambda/\rho C_p$) and $\upsilon$ ($= \eta/\rho$).

The order of magnitude for the two terms in eq.(3.16) are $\frac{u}{r_o}$ and $\frac{v}{\delta}$ respectively. Since

$\delta/r_o << 1$, one obtains that $v << u$. Eq.(3.18) can thus be neglected as the pressure is considered to be constant in the y direction. For the same reason, $\frac{\partial u}{\partial x} << \frac{\partial u}{\partial y}$ and

$\frac{\partial^2}{\partial x^2} << \frac{\partial^2}{\partial y^2}$, terms with $\frac{\partial^2}{\partial x^2}$ can be neglected compared with terms of $\frac{\partial^2}{\partial y^2}$.

With the above approximations, equations (3.17) to (3.18) simplify to:

$$\frac{\partial p}{\partial x} = \eta \frac{\partial^2 u}{\partial y^2} \tag{3.22}$$

and

$$u\frac{\partial T}{\partial x} + v\frac{\partial T}{\partial y} = \kappa \frac{\partial^2 T}{\partial y^2} \tag{3.23}$$

The boundary conditions to be applied are:

$$\begin{array}{lll} y = 0; & u = v = 0; & T = T_w \\ y = \delta(\theta); & u = 0; \quad v = -u_o \cos\theta; & T = T_m \\ x = 0; & \dfrac{\partial \delta}{\partial x} = 0 & \end{array} \tag{3.24}$$

Since $u_o$ and $\delta(\theta)$ are unknown *a priori*, one more constraint is needed to solve the problem. An energy balance at the melting boundary is appropriate. With the negligible sensible heat in the melt as produced and displaced into the gap, the balance equation can be expressed as:

$$-\lambda \frac{\partial T}{\partial y}\Big|_{y=\delta(\theta)} = \rho_s \, u_o \, h_{sl} \cos\theta \tag{3.25}$$

### 3.2.2 *Order of Magnitude Analysis*

Before solving the above set of equations subject to the boundary conditions, a dimensionless analysis is presented to show the relationship between the migration rate

$u_o$ and other parameters relevant to the melting process. The length and velocity scales are $r_o$ and $u_o$ respectively. The angle scale is chosen as critical contact angle $\theta_c$ ($< \pi/2$). Eq.(3.16) suggests that

$$\frac{u_{max}}{r_o} \sim \frac{u_o}{\delta}$$

or

$$u_{max} \sim \frac{r_o}{\delta} u_o \tag{3.26}$$

For the momentum equation (3.22), the order of magnitude is,

$$\frac{\Delta P}{r_o} \sim \eta \frac{u_{max}}{\delta^2} \tag{3.27}$$

Eliminating $u_{max}$ from equation (3.27) by substituting equation (3.26), results in

$$\delta \sim \left( \frac{\eta r_o^2 u_o}{\Delta P} \right)^{1/3} \tag{3.28}$$

The order of magnitude for the local energy balance equation (3.25), is

$$\lambda \frac{\Delta T}{\delta} \sim \rho_s h_{sl} u_o \cos\theta_c \tag{3.29}$$

Equation (3.29) can be re-organized with substitution of equation (3.28) to give

$$\eta r_o^2 u_o^4 \sim \Delta P \left( \frac{\lambda \Delta T}{\rho_s h_{sl} \cos\theta_c} \right)^3$$

or

$$\frac{u_o r_o}{\kappa} \sim \left( \frac{Ste}{\cos\theta_c} \right)^{3/4} \left( \frac{\Delta P r_o^2}{\eta \kappa} \right)^{1/4} \tag{3.30}$$

where Stefan number (Ste) is defined as

$$Ste = \frac{C_p (T_w - T_m)}{h_{sl}} \tag{3.31}$$

The left side of equation (3.30) is the dimensionless migration rate $u_o^*$ of the hot tube. The ratio involving $\Delta P$ is the dimensionless contact pressure $p_f^*$.

### 3.2.3 *Analytical Solution*

The analytical solution to equations (3.16), (3.22) and (3.23) subject to the boundary conditions eqs.(3.24) and (3.25) is derived in this sub-section. When equation eq.(3.22) is integrated, one obtains,

$$u = -\frac{G(\theta)}{2\,\eta\, r_o}\, y\,(y - \delta) \tag{3.32}$$

where

$$G(\theta) = -\frac{dp}{d\theta} \tag{3.33}$$

The continuity eq.(3.16) can be integrated with respect to y by substituting eq.(3.32) and using the conditions in eq.(3.24) to produce

$$\frac{\partial}{\partial\theta}\left(\frac{G(\theta)\,\delta^3}{12\,\eta\, r_o^2}\right) = u_o \cos\theta \tag{3.34}$$

Eq.(3.34) can be further integrated respect to $\theta$ to obtain

$$\frac{dp}{d\theta} = -G(\theta) = -\frac{12\,\eta\, u_o\, r_o^2}{\delta^3(\theta)} \sin\theta \tag{3.35}$$

Combining eq.(3.32) and (3.35) yields

$$u = -\frac{6\, u_o\, r_o}{\delta^3}\, y\,(y - \delta)\sin\theta \tag{3.36}$$

Temperature distribution across the liquid gap can be obtained under two different situations according to the melting rate of the process.

*At Low Melting Rates*

The left side of eq.(3.23) presents the convection term whose representative scale is $u_o\Delta T/\delta$. The scale of the diffusion effect is $\kappa\Delta T/\delta^2$. Comparing these scales, one can conclude that the effect of convection is negligible if $u_o\delta/\kappa << 1$. If this inequality is satisfied, only the conduction term is retained in the energy equation (3.23). Temperature distribution in the melt layer is then linear, i.e.,

$$T = T_w - \frac{T_w - T_m}{\delta} y \tag{3.37}$$

The local balance equation eq.(3.25), with the temperature distribution eq.(3.37) can be re-organized to obtain a relationship between the migration velocity and liquid gap thickness,

$$u_o\ \delta(\theta)\ \cos\theta = \kappa\ Ste \tag{3.38}$$

*At High Melting Rates*

When the condition $u_o\delta/\kappa < 1$ is not satisfied, the flow effects on heat transfer can not be neglected. Eq.(3.23) is then solved by an integral method. The temperature profile may be approximated with a quadratic polynomial in y as:

$$T = C_1 + C_2\ y + C_3\ y^2 \tag{3.39}$$

where $C_1$, $C_2$ and $C_3$ are constants determined from the boundary conditions, eq.(3.24) and (3.25):

$$C_1 = T_w$$

$$C_2 = -(T_w - T_m)\left(\frac{2}{\delta} - \frac{u_o \cos\theta}{\kappa Ste}\right) \qquad (3.40)$$

$$C_3 = \frac{(T_w - T_m)}{\delta}\left(\frac{1}{\delta} - \frac{u_o \cos\theta}{\kappa Ste}\right)$$

Up to this point, the temperature distribution is not yet determined since $C_2$ and $C_3$ include the unknown gap width $\delta$ and the migration rate of the tube $u_o$. The relationship between $\delta$ and $u_o$ can be obtained through integrating eq.(3.23) across the melt layer and substituting Eqs. (3.24), (3.25), (3.39) and (3.40). The mathematical manipulations are similar to those carried out by Emerman and Turcotte (1983) and Moallemi and Viskanta (1985a). They are summarized as follows. Integration of eq.(3.23) yields,

$$\frac{\partial}{\partial x}\int_0^{\delta} (u\,T)\,dy - u_o\,T_m\cos\theta = \kappa\left[\frac{\partial T}{\partial y}\Big|_{y=\delta} - \frac{\partial T}{\partial y}\Big|_{y=0}\right] \qquad (3.41)$$

where

$$\int_0^{\delta} u\,T\,dy = u_o\,r_o\sin\theta\,\left(C_1 + \frac{1}{2}C_2\,\delta + \frac{3}{10}C_3\,\delta^2\right)$$

and

$$\frac{\partial}{\partial x}\int_0^{\delta} u\,T\,dy - u_o\,T_m\cos\theta = u_o\,(T_w - T_m)\left(\frac{3}{10}\cos\theta + \frac{1}{10}\frac{u_o}{\kappa Ste}\frac{d}{d\theta}(\delta\sin 2\theta)\right)$$

$$\kappa\left[\frac{\partial T}{\partial y}\Big|_{y=\delta} - \frac{\partial T}{\partial y}\Big|_{y=0}\right] = 2\,(T_w - T_m)\left(\frac{\kappa}{\delta} - \frac{u_o\cos\theta}{Ste}\right)$$

So that eq.(3.41) can be arranged as

$$\frac{d}{d\theta}\left(\frac{\delta}{r_o}\sin 2\theta\right) + (20 + 3Ste)\frac{\kappa}{u_o r_o}\cos\theta - 20\frac{Ste}{\delta/r_o}\left(\frac{\kappa}{u_o r_o}\right)^2 = 0 \qquad (3.42)$$

With the boundary condition $d\delta/d\theta = 0$ at $\theta = 0$, the first term in Eq.(3.42) has a zero value. If Ste $\ll$ 20/3, an initial solution for the term of $(\delta/r_o)\cos\theta$ can be obtained from eq.(3.42),

$$\frac{\delta}{r_o}\cos\theta = \frac{\kappa\, Ste}{u_o r_o} \qquad (3.43a)$$

Inserting eq.(3.43a) into (3.42), one obtains

$$\frac{d}{d\theta}\left(\frac{\delta}{r_o}\sin 2\theta\right) = -\frac{3\, Ste\, \kappa}{u_o r_o}\cos\theta \qquad (3.44)$$

The integration of eq(3.44) gives,

$$\frac{\delta}{r_o}\cos\theta = -\frac{3}{2}\frac{\kappa\, Ste}{u_o r_o} \qquad (3.43b)$$

The integration constant is zero as at $\theta = 0$, both sides of the equation have to be equal.

In each of the above cases, eqs.(3.43a) and (3.43b) are substituted into eq.(3.44), it then becomes,

$$\frac{d}{d\theta}\left(\frac{\delta}{r_o}\sin 2\theta\right) = -3\frac{\delta}{r_o}\cos^2\theta \qquad (3.45a)$$

and

$$\frac{d}{d\theta}\left(\frac{\delta}{r_o}\sin 2\theta\right) = 2\frac{\delta}{r_o}\cos^2\theta \qquad (3.45b)$$

respectively.

By substitution of eqs.(3.45a) and (3.45b) into eq.(3.42), one obtains

$$-3\left(\frac{u_o\delta\cos\theta}{\kappa}\right)^2 + (20+3Ste)\left(\frac{u_o\delta\cos\theta}{\kappa}\right) - 20\, Ste = 0 \qquad (3.46a)$$

and

$$2\left(\frac{u_o\delta\cos\theta}{\kappa}\right)^2 + (20+3Ste)\left(\frac{u_o\delta\cos\theta}{\kappa}\right) - 20\,Ste = 0 \qquad (3.46b)$$

respectively.

The roots of eqs.(3.46a) and (3.46b) can be found and expressed as

$$u_o\,\delta(\theta)\cos\theta = \kappa\, f(Ste) \qquad (3.47)$$

where f(Ste) is a function of Ste and has the following forms:

$$f(Ste) = \frac{20}{3} \qquad (3.48a)$$

or

$$f(Ste) = Ste \qquad (3.48b)$$

from eq.(3.46a) and

$$f(Ste) = -\frac{3}{4}Ste - 5 + \left(\frac{9}{16}Ste^2 + \frac{70}{4}Ste + 25\right)^{1/2} \qquad (3.48c)$$

or

$$f(Ste) = -\frac{3}{4}Ste - 5 - \left(\frac{9}{16}Ste^2 + \frac{70}{4}Ste + 25\right)^{1/2} \qquad (3.48d)$$

from eq.(3.46b).

Eq.(3.48d) is not physically realistic and therefore is eliminated. It is interesting to notice that eqs.(3.48a) and (3.48b) are consistent in that they have the same value when Ste = 20/3. A comparison of eqs.(3.48a), (3.48b) and (3.48c) is shown in Fig. 3.3. The function f(Ste) in eq(3.48c) approaches Ste as Ste $\rightarrow$ 0. For Ste $\leq$ 0.0132, f(Ste) of eq.(3.48b) and eq.(3.48c) equals Ste (from Fig.3.3(a)). At Ste = 0.1, since f(Ste) = 0.0976 (from eq.(3.48c), for example, the error is 1% and heat transfer rates may be considered negligibly affected by the flow of the melt. The f(Ste) value difference between eq.(3.48b)

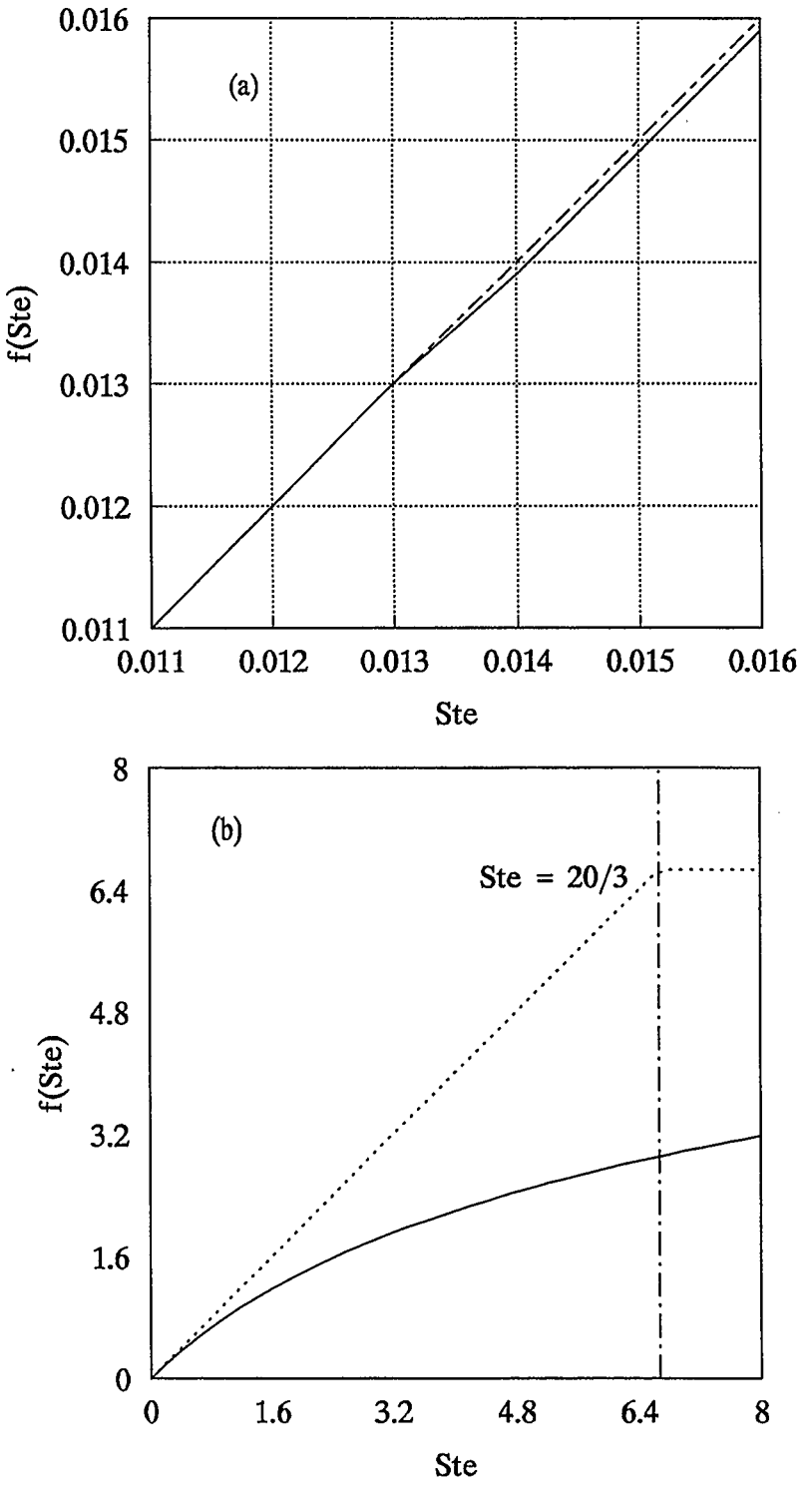


Fig. 3.3 Comparison of f(Ste) from eq.(3.48a&b) (dotted line) and eq.(3.48c) (solid line), (a) at small Ste ranges; (b) Ste from 0 to 8

and (3.48c) increases as Ste increases. At Ste = 20/3, for example, since f(Ste) = 3.1774 (from eq.(3.48c), a 52% difference can be noticed. Nevertheless, since the analytical model is only valid at lower Ste range, the solutions from eqs. (3.48b) and (3.48c) are still in consistence. In the following presentation and discussion, both the eqs.(3.48b) and (3.48c) are included and compared. In all the plots, solid lines refer to eqs.(3.48c) whereas the dotted lines to eq.(3.48b). We will discuss in more detail the consequences of the solutions (3.48b) in a subsequent publication.

The pressure gradient can be determined by using eq.(3.47) to substitute for $\delta(\theta)$ in eq.(3.35),

$$\frac{dp}{d\theta} = - \frac{12\ \eta\ r_o^2\ u_o^4\ \cos^3\theta\ \sin\theta}{\kappa^3\ f^3(Ste)} \tag{3.49}$$

Eq.(3.49) can be further integrated with respect to $\theta$, from 0 to a critical contact angle $\theta_c$ after which the criteria $\delta/r_o << 1$ will be invalid. The result is, with the zero pressure at $\theta_c$,

$$p = 3\frac{\eta\ r_o^2\ u_o^4}{\kappa^3\ f^3(Ste)} \left( \cos^4\theta - \cos^4\theta_c \right) \tag{3.50}$$

The force balance acting on the hot tube can be written as:

$$F_e = 2\ L\ r_o \int_o^{\theta_c} \left( p\ \cos\theta + \tau\ \sin\theta \right) d\theta \tag{3.51}$$

The shear stress is considered negligible compared to pressure for $\delta/r_o << 1$. When eq.(3.50) is substituted into eq.(3.51), the integration result is:

$$F_e = \frac{8}{5}\ L\ \frac{r_o^3\ \eta\ u_o^4}{\kappa^3\ f^3(Ste)}\ \sin^3\theta_c\ \left( 5 - 3\ \sin^2\theta \right) \tag{3.52}$$

Through the application of the following non-dimensional variables,

$$y^* = \frac{y}{r_o} \qquad \delta^* = \frac{\delta}{r_o}$$
$$u_o^* = \frac{u_o\, r_o}{\kappa} \qquad V_m^* = \frac{V_m\, r_o}{\kappa} \tag{3.53}$$
$$p_f^* = \frac{(\frac{F_e}{L})\, r_o}{\eta\kappa} \qquad p^* = \frac{p\, r_o^2}{\eta\, \kappa} \quad ,$$

Eq.(3.52) can be arranged to obtain the non-dimensional migration velocity:

$$u_o^* = p_f^{*\,1/4} \left( f(Ste) \right)^{3/4} \left( \frac{8}{5} \sin^3\theta_c \left( 5 - 3 \sin^2\theta_c \right) \right)^{-1/4} \tag{3.54}$$

The non-dimensional liquid gap width is found to be

$$\delta^* = \frac{1}{\cos\theta} \left( \frac{\frac{8}{5} f(Ste) \sin^3\theta_c \left( 5 - 3 \sin^2\theta_c \right)}{p_f^*} \right)^{1/4} \tag{3.55}$$

The heat flux at the hot tube surface can be obtained from eq.(3.39) and it is equal to $C_2$. That is

$$q_s = \lambda\, (T_w - T_m) \left( \frac{2}{\delta} - \frac{u_o \cos\theta}{\kappa Ste} \right) \tag{3.56}$$

Eq.(3.25) can be re-arranged to obtain the heat flux at the melting interface:

$$q_I = \lambda\, (T_w - T_m)\, \frac{u_o \cos\theta}{\kappa Ste} \tag{3.57}$$

If the non-dimensional heat flux is defined as

$$q^* = q\, \frac{r_o}{\lambda\, (T_w - T_m)} \tag{3.58}$$

Then the non-dimensional heat fluxes at the hot tube surface and the melting interface $q_s^*$ and $q_I^*$ are given as

$$q_s^* = u_o^* \left( \frac{2}{f(Ste)} - \frac{1}{Ste} \right) \cos\theta \tag{3.59}$$

$$q_l^* = u_o^* \frac{1}{Ste} \cos\theta \tag{3.60}$$

### 3.2.4 *Results and Discussions*

The above results are now used for the specific case of melting a block of sulphur with a hot vertical tube. The values for the thermophysical properties of the sulphur are presented in Table 2.1. The radius of the tube, $r_o$, is chosen as $2.5(10^{-2})$ m and the length of the cylinder L is chosen as 3 m. The thermal diffusivity is found to be $\kappa = 7.3133(10^{-8})$ $m^2/s$, Stefan number is related to the temperature difference $\Delta T$ as $Ste = 0.01995\ \Delta T$.

The critical melting sector angle $\theta_c$ is first determined at different Ste and $p_f^*$ values. It is noted that $\delta/r_o$ is not $<< 1$ when $\theta \geq \theta_c$. $\theta_c$ is determined from eq.(3.53) by replacing $\theta$ value with $\theta_c$ and $\delta$ value with $\delta_c$ which is chosen as 1 percent of the tube radius. A function for $\theta_c$ is then obtained as:

$$f(\theta_c) = \frac{8}{5} f(Ste) \sin^3\theta_c \left( 5 - 3 \sin^2\theta_c \right) - (\delta_c^* \cos\theta_c)^4 p_f^* = 0 \tag{3.61}$$

To find $\theta_c$, a Newton-Raphson iteration procedure is employed to find the roots of eq.(3.61). A plot of $\theta_c$ against Ste is shown in Fig. 3.4 for three different $p_f^*$ values: $2.70(10^7)$, $2.70(10^8)$ and $2.70(10^9)$. These values correspond to the applied force $F_e$ (N) and contact pressure $F_e/2\pi r_o L$ ($N/m^2$) of (0.3, 0.645), (3, 6.45) and (30, 64.5) respectively. The solutions with solid and dotted lines are those from eqs.(3.48c) and (3.48b) respectively. $\theta_c$ value calculated from eq.(3.48a) does not change with Ste. It is not considered here since the result discussion is confined in lower Ste range where the

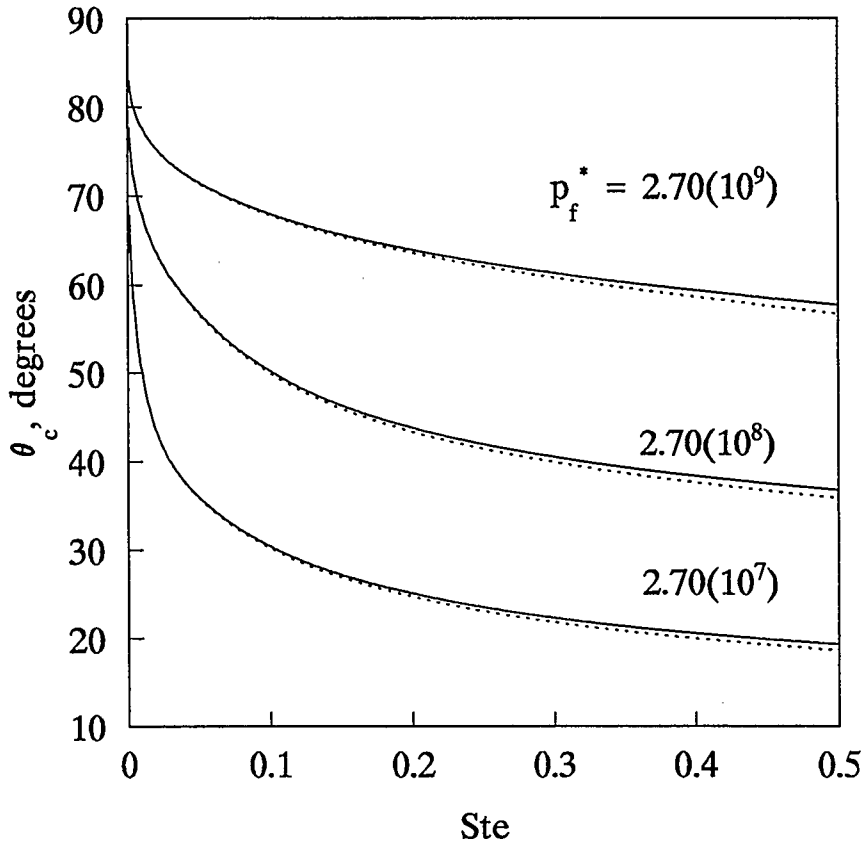


Fig. 3.4 Critical sector angle as function of Ste at different $p_f^*$ values

analytical solution is valid. The critical contact angle is noted in the plot to decrease with increasing Stefan number. It also increased with increasing applied force. The critical contact angle declined sharply at low Ste. That is, when two surfaces have nearly the same temperatures, the melting surface closely matches the contour of the heating surface and the critical contact angle approaches 90° deg. The gap width will be small and nearly constant along the azimuthal direction. As the hot surface temperature is increased, the gap width increases from its smallest value at $\theta = 0$ along the azimuthal direction. As the contact pressure is increased, more liquid sulphur is squeezed out and the melt layer becomes narrower. Since $\theta_c$ increases, the channel length becomes longer. The solution for f(Ste) from eq.(3.48b) is the same as from eq.(3.48c) when Ste is small (<0.05). The critical angle value then tends to be lower from eq.(3.48b) with a difference of 1% from that of eq.(3.48c).

With the knowledge of $\theta_c$, the migration velocity of the tube was calculated from eq.(3.54) and plotted at different $p_f^*$ values. The results in Fig. 3.5 show that the migration rate of the hot tube $u_o$ is higher as $p_f^*$ is increased. At Ste = 0.1, for example, the contact angles, with f(Ste) from eq.(3.48b), are 30.2°, 50.0° and 67.9°, and with f(Ste) from eq.(3.48c), 30.4°, 50.2° and 68.0°, when $p_f^* = 2.70(10^7)$, $2.70(10^8)$, $2.70(10^9)$ respectively, the velocities are $3.37(10^{-6})$, $4.68(10^{-6})$ and $7.76(10^{-6})$ m/s and $3.30(10^{-6})$, $4.59(10^{-6})$ and $7.62(10^{-6})$ m/s. The dimensionless gap width at $\theta = 0°$, $\delta_o^*$, a function of Ste, $p_f^*$ and $\theta_c$, can be obtained from eq.(3.55). The relationship between $\delta_o^* * 10^2$ and $p_f^* * 10^{-9}$ at different Ste values is presented in Fig. 3.6. $\delta_o^*$ first decreased most rapidly at low values for $p_f^*$. When $p_f^*$ exceeded $1.0(10^9)$, the decline was slower.

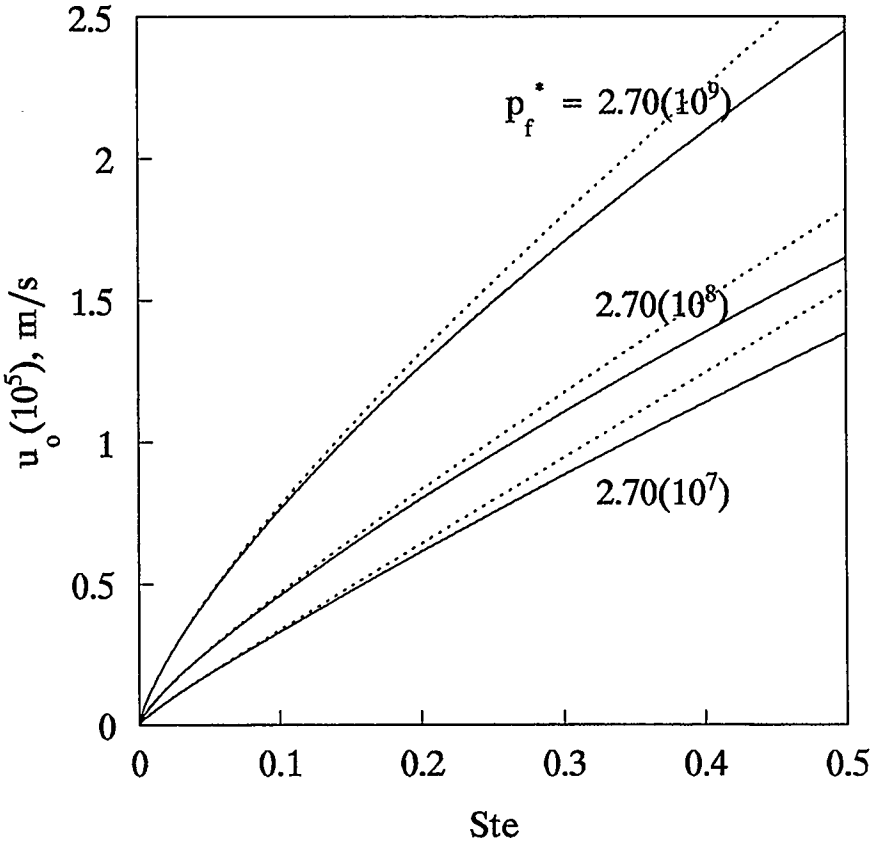


Fig. 3.5 Migration rate of heat source $u_o$ as function of Ste at different $p_f^*$ values

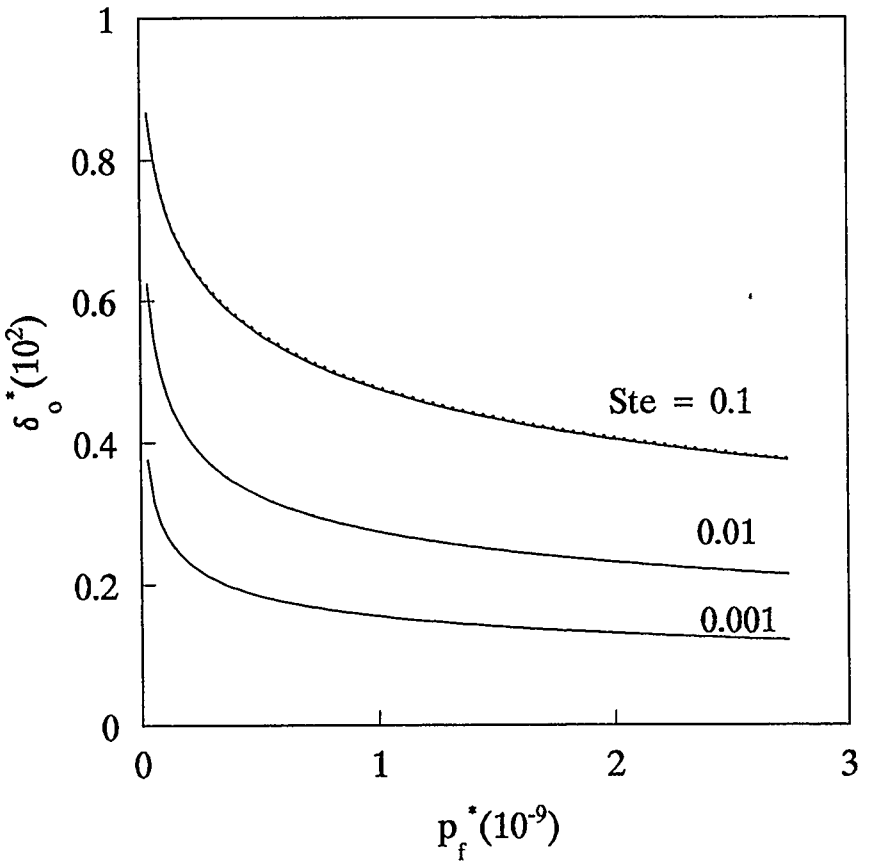


Fig. 3.6 Gap width at $\theta = 0$, $\delta_o^*$ as function of $p_f^*$ at different Ste values

Fig. 3.7 shows $\delta_o^* * 10^2$ plotted as function of Ste at different $p_f^*$ values. When the applied force is small, $\delta_o^*$ becomes independent of Ste for Ste > 0.1. $\delta_o^*$ decreased from 0.2044 mm to 0.026 mm when $p_f^*$ was increased 100 times at Ste = 0.1. From Saito et al.'s (1985b) work, the average liquid gap width for the flat heating surface was reported to change from 0.16 mm to 0.014 mm when the dimensionless contact pressure decreased 100 times from $5.85(10^{10})$ to $5.85(10^8)$ when ice was melted.

In Figs. 3.8(a-c), variations in the liquid gap thickness $\delta^*$ along the azimuthal direction are presented at various Ste and $p_f^*$ values. The gap width initially increased gradually. Beyond $\theta_c$, when $\delta/r_o << 1$ is not satisfied, the liquid gap thickness increased very sharply and the channel diverged.

The average dimensionless heat flux at the hot tube surface $q_S^*$ and the interface $q_I^*$ are plotted in Figs. 3.9a and 3.9b at different $p_f^*$. When Ste exceeds 0.1, $q_S^*$ and $q_I^*$ attain different values and $q_S^*$ is greater than $q_I^*$. This is due to the sensible heat carried by the flow of the melt. The heat flux from the hot tube $q_S^*$ at lower Ste values are plotted in Fig. 3.10 (a), (b) and (c). The larger the applied force, the higher the heat flux achieved at the same Ste.

The pressure distribution patterns are shown in Figs. 3.11(a-c) ($p^* * 10^{-7}$, $p^* * 10^{-8}$, $p^* * 10^{-9}$ versa $\theta$ for (a), (b) and (c) respectively) for the same condition as in Fig. 3.8. The pressure is almost independent of Ste when $p_f^*$ becomes large. The pressure gradients calculated from eq.(3.38) are presented in Figs. 3.12(a-c) ($dp^*/d\theta * 10^{-7}$, $dp^*/d\theta * 10^{-8}$, $dp^*/d\theta * 10^{-9}$ versa $\theta$ for (a), (b) and (c) respectively) for the same conditions as in Fig. 3.8. They approach maximum values around 30° degrees under all the different conditions.

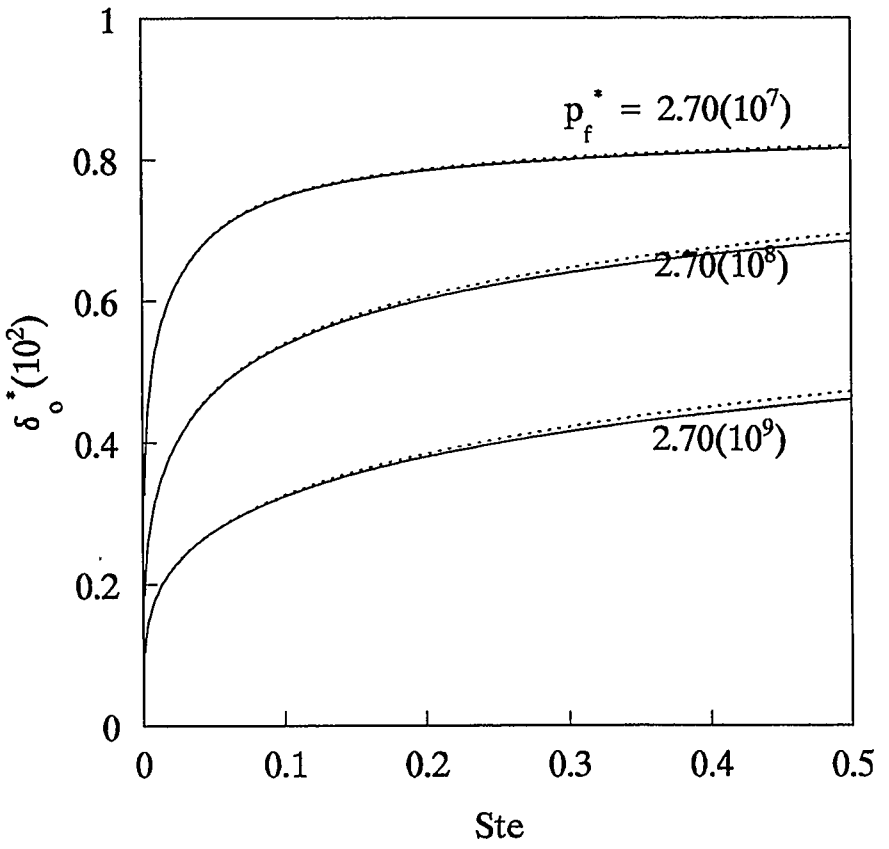


Fig. 3.7 Gap width at $\theta = 0$, $\delta_o^*$ as function of Ste at different $p_f^*$ values

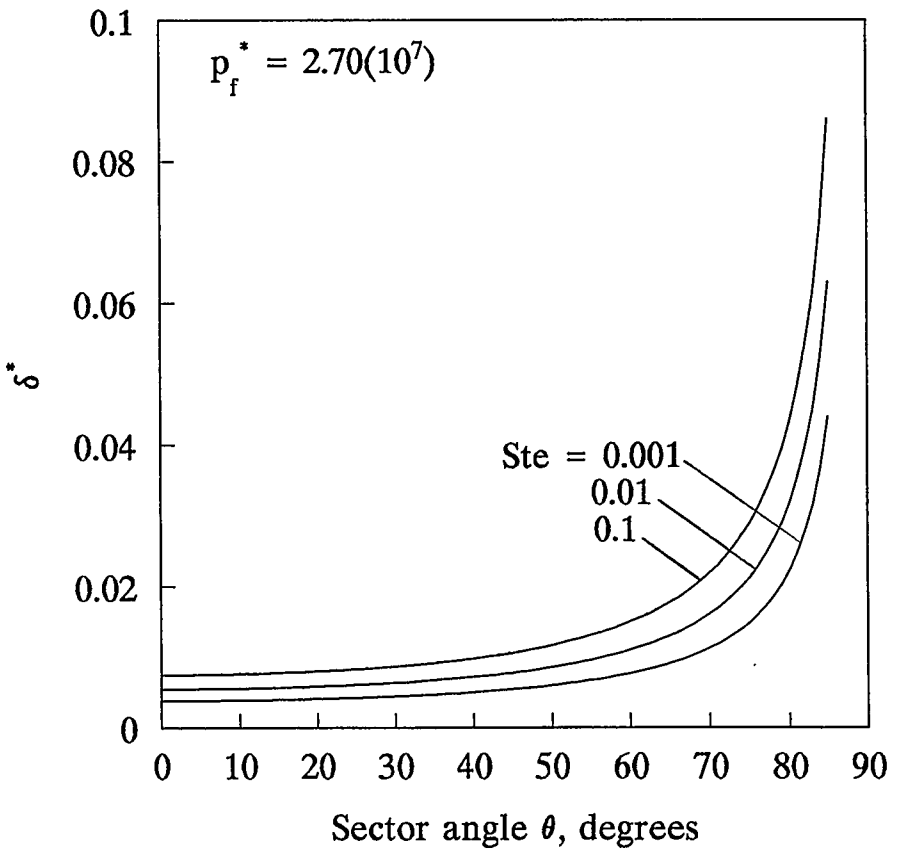


Fig. 3.8 (a) Gap width $\delta^*$ development along azimuthal direction at different Ste values; $p_f^* = 2.70(10^7)$

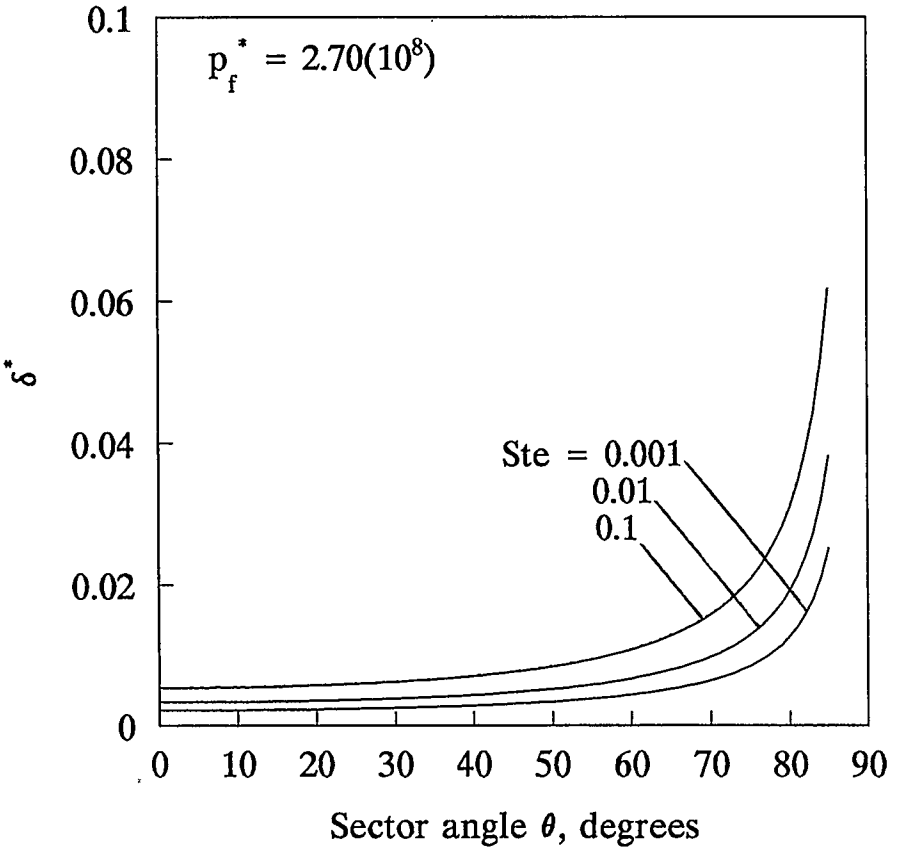


Fig. 3.8 (b) Gap width $\delta^*$ development along azimuthal direction at different Ste values; $p_f^* = 2.70(10^8)$

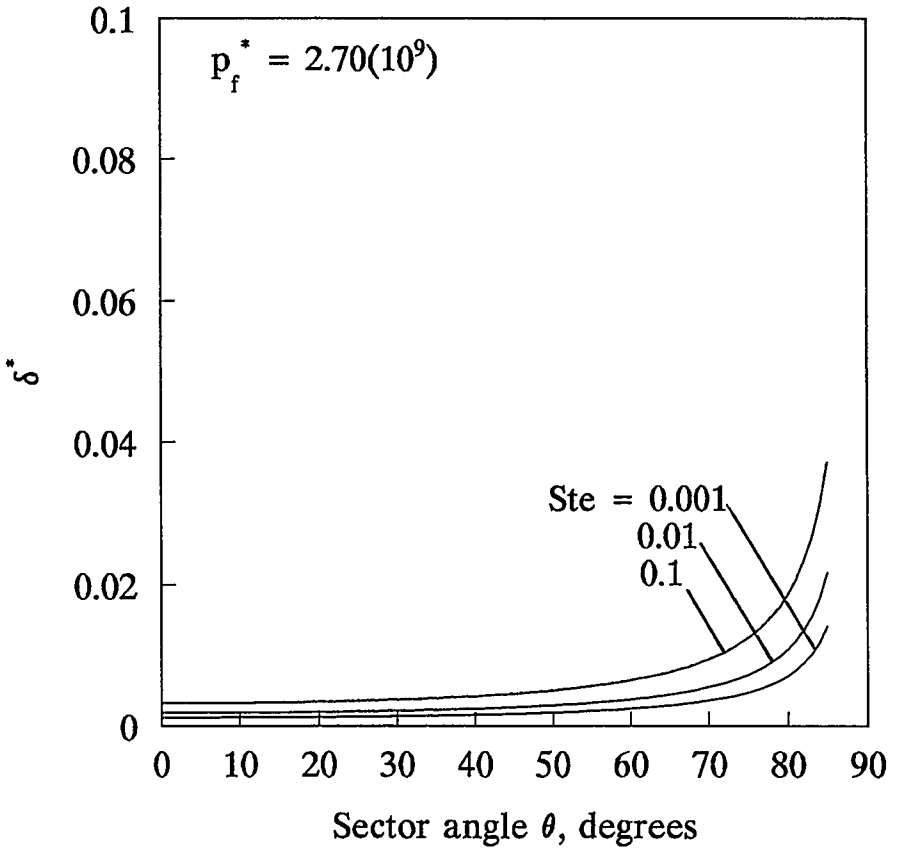


Fig. 3.8 (c) Gap width $\delta^*$ development along azimuthal direction at different Ste values; $p_f^* = 2.70(10^9)$

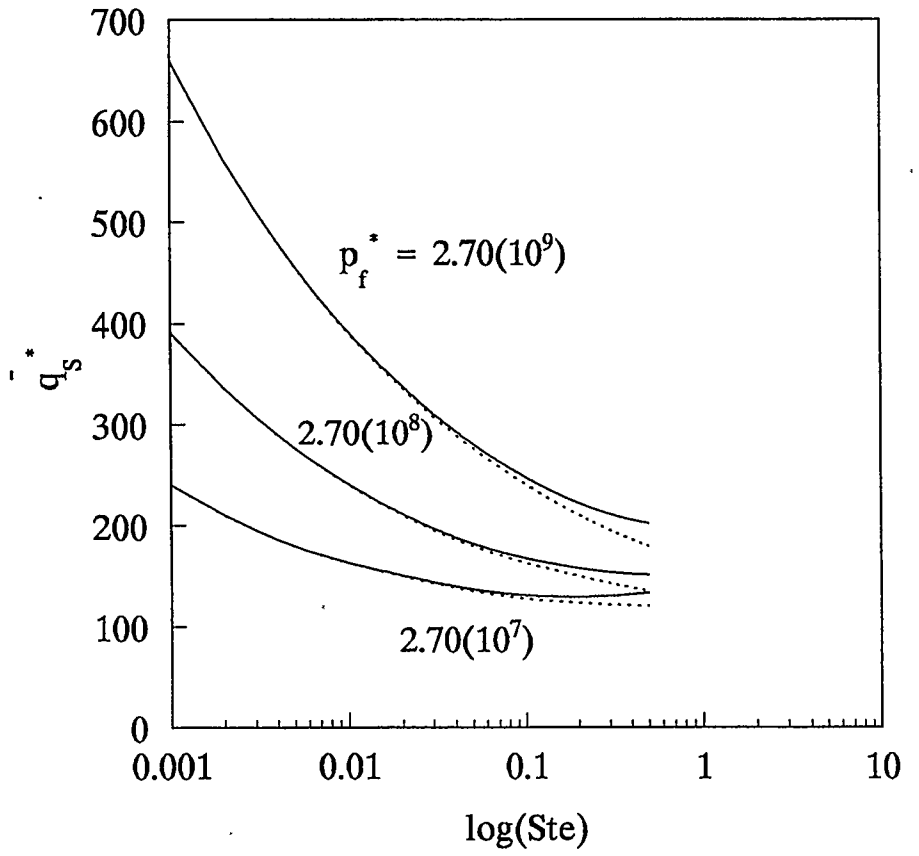


Fig. 3.9(a) Average heat flux of $q_s^*$ as function of Ste at different $p_f^*$ values

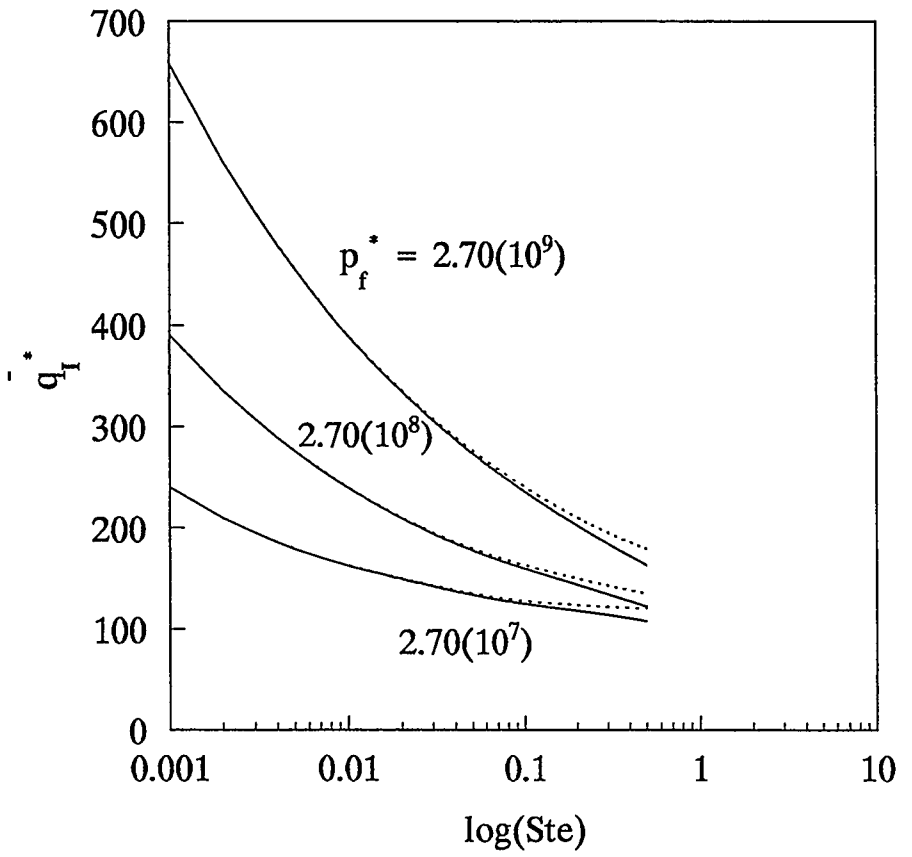


Fig. 3.9(b) Average heat flux of $q_I^*$ as function of Ste at different $p_f^*$ values

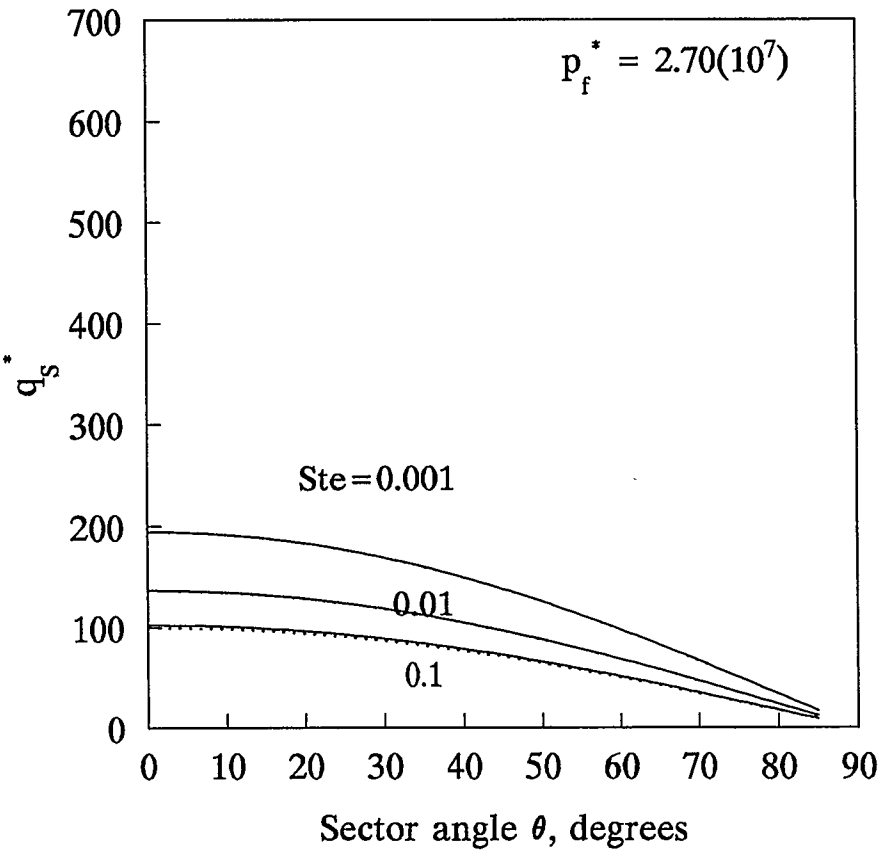


Fig. 3.10 (a) Heat flux at heating surface $q^*$ as function of polar angle position at different Ste values; $p_f^* = 2.70(10^7)$

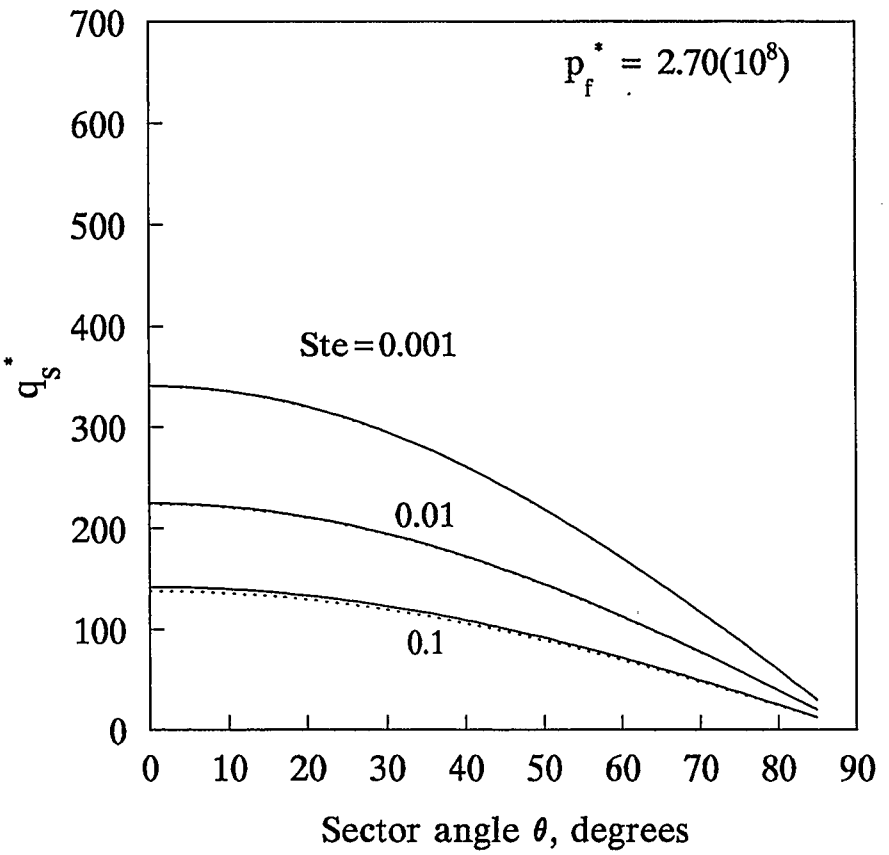


Fig. 3.10 (b) Heat flux at heating surface $q^*$ as function of polar angle position at different Ste values; $p_f^* = 2.70(10^8)$

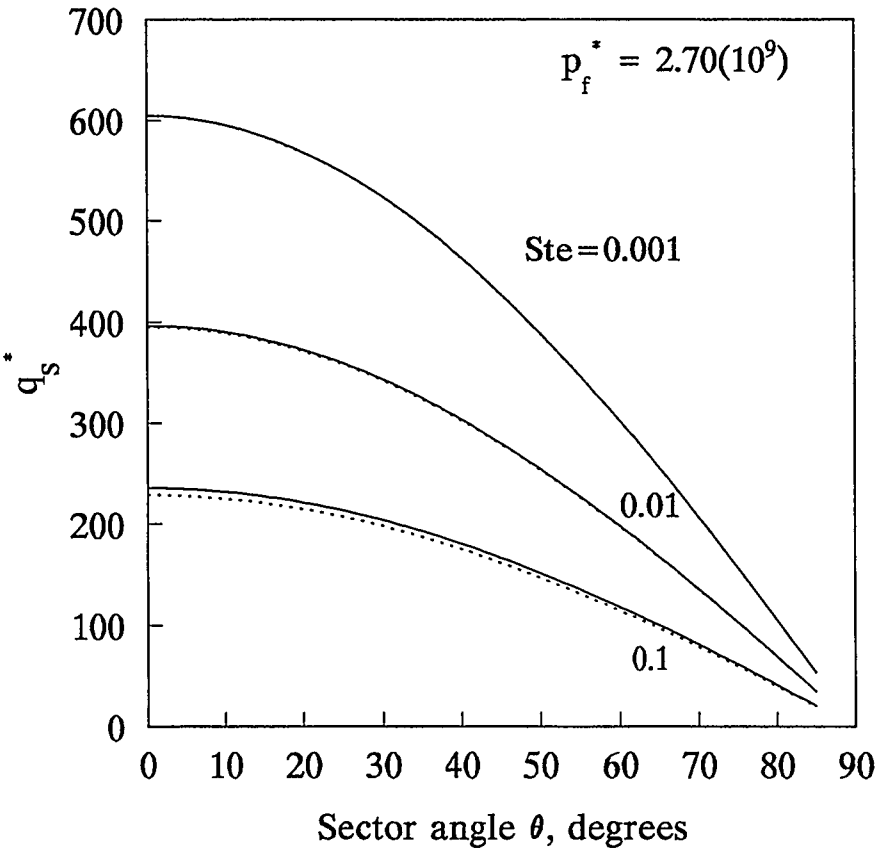


Fig. 3.10 (c) Heat flux at heating surface $q^*$ as function of polar angle position at different Ste values; $p_f^* = 2.70(10^9)$

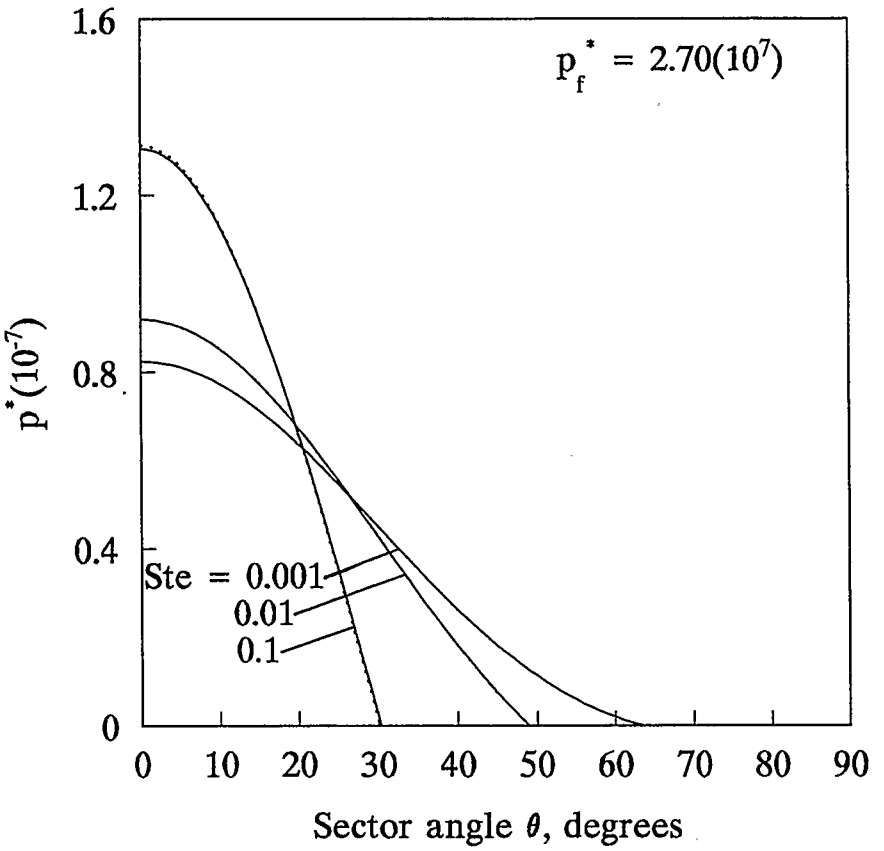


Fig. 3.11 (a) Pressure $p^*$ as function of polar angle position at different Ste values; $p_f^* = 2.70(10^7)$

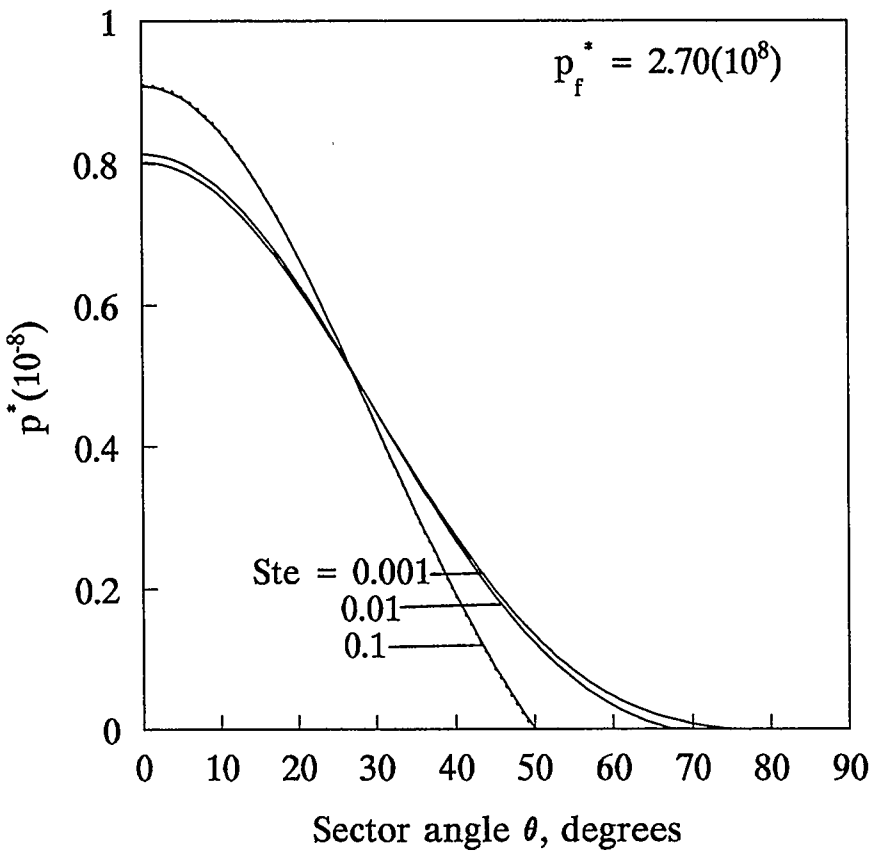


Fig. 3.11 (b) Pressure $p^*$ as function of polar angle position at different Ste values; $p_f^* = 2.70(10^8)$

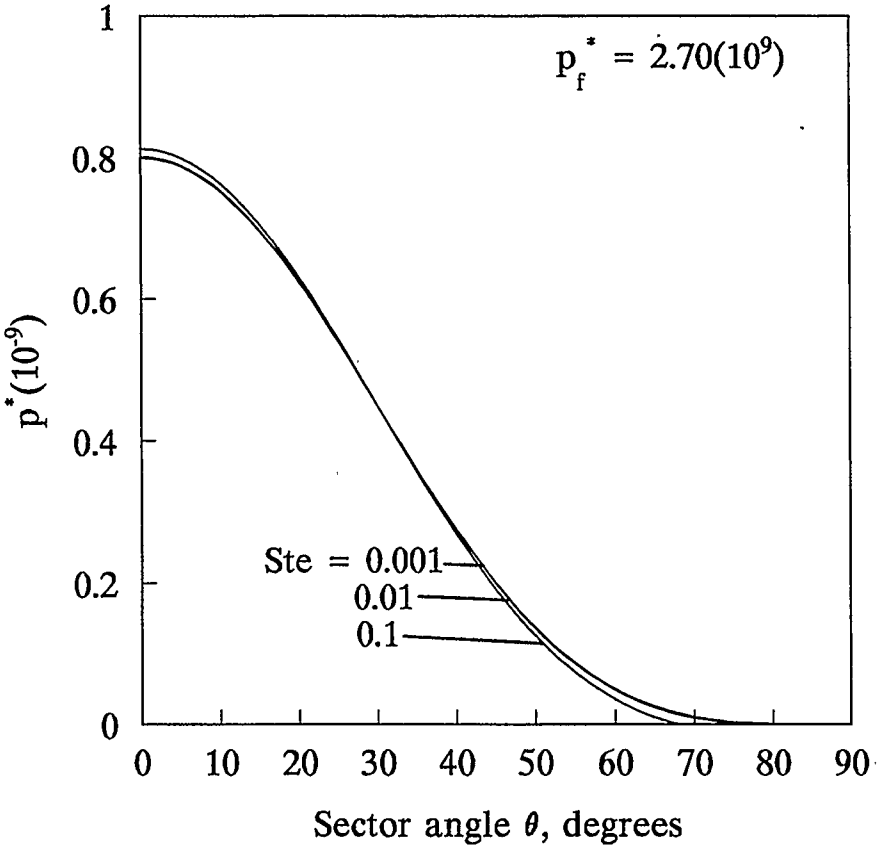


Fig. 3.11 (c) Pressure $p^*$ as function of polar angle position at different Ste values; $p_f^* = 2.70(10^9)$

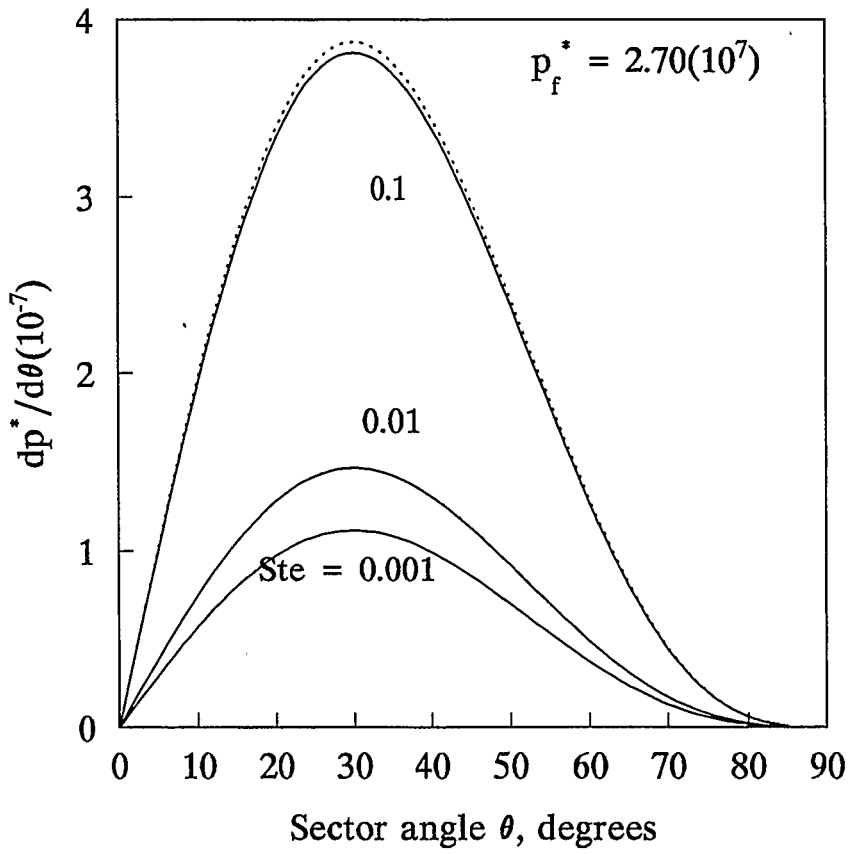


Fig. 3.12 (a) Pressure gradient $dp^*/d\theta$ as function of polar angle position at different Ste values; $p_f^* = 2.70(10^7)$

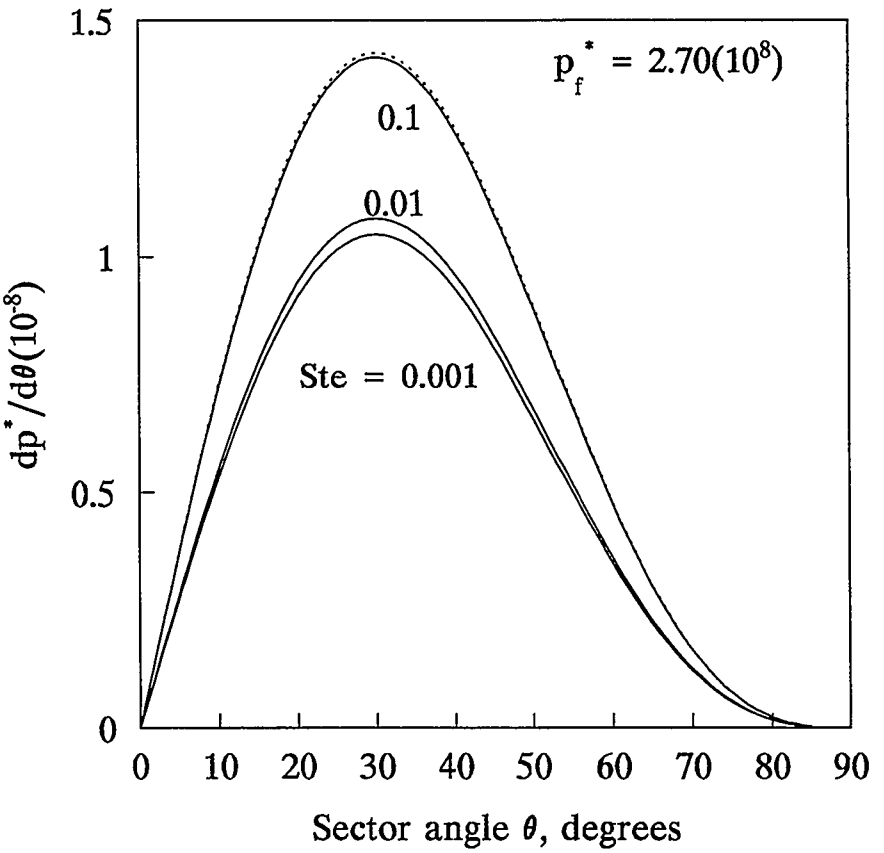


Fig. 3.12 (b) Pressure gradient $dp^*/d\theta$ as function of polar angle position at different Ste values; $p_f^* = 2.70(10^8)$

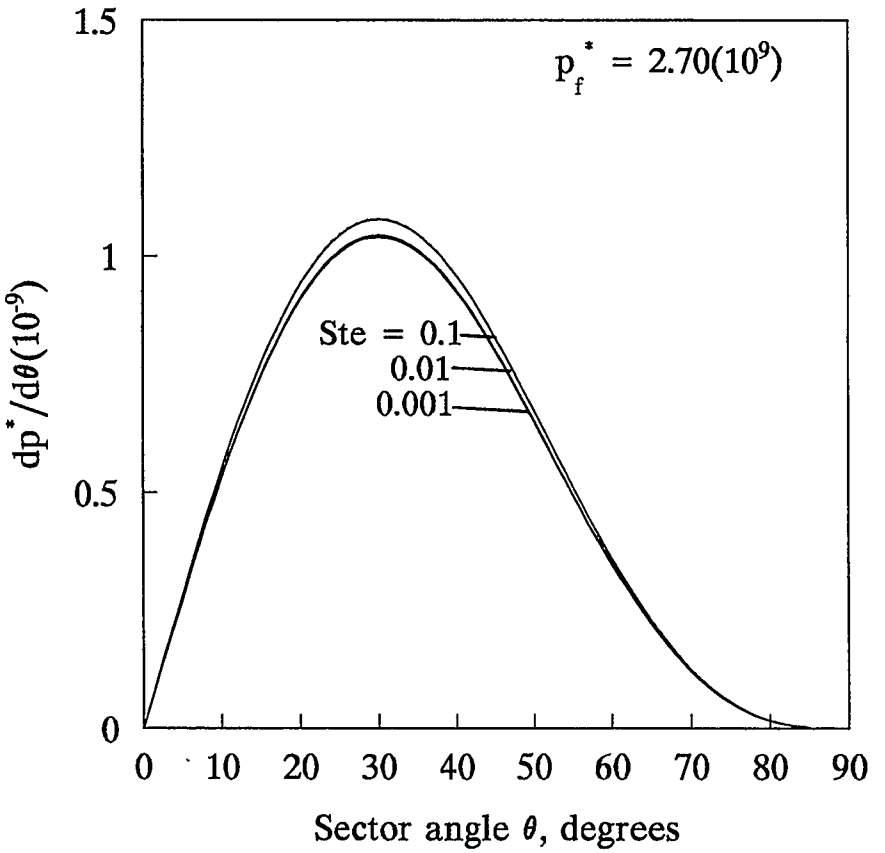


Fig. 3.12 (c) Pressure gradient $dp^*/d\theta$ as function of polar angle position at different Ste values; $p_f^* = 2.70(10^9)$

The tangential magnitude eq.(3.36) can be re-arranged to give,

$$\frac{u}{u_o} = \frac{6 \sin\theta \left(\frac{y}{\delta}\right) \left(1 - \frac{y}{\delta}\right)}{\frac{\delta}{r_o}} \tag{3.61}$$

The $u/u_o$ profiles are parabolic across the liquid gap, with maximum value increasing along azimuthal direction.

When eq.(3.16) is integrated with the substitution of eq.(3.61), one obtains the normal velocity component as,

$$\frac{v}{u_o} = \left(\frac{y}{\delta}\right)^2 \left( \left(2 \frac{y}{\delta} - 3\right) \cos\theta + 6 \left(1 - \frac{y}{\delta}\right) \frac{\sin^2\theta}{\cos\theta} \right) \tag{3.62}$$

The volumetric production rate of melt is obtained by evaluating the tangential velocity eq. (3.53) at sector angle $\theta_c$. The result is, in dimensionless form,

$$V_m^* = u_o^* \sin\theta_c \,/\, \delta_c^* \tag{3.63}$$

Plots of $V_m^*$ versus Ste at different $p_f^*$ are shown in Fig. 3.13. Under same applied force, the $V_m^*$ increases with increasing Ste number. The production rate is also higher when $p_f^*$ is increased under the same driving potential $\Delta T_w$ or Ste.

## 3.3 Closing Remarks

In this chapter, a physical model was proposed and the general equations were formulated with respect to the coordinate system fixed at the centre of the heat source. These provide the foundation on which the numerical computational scheme was developed.

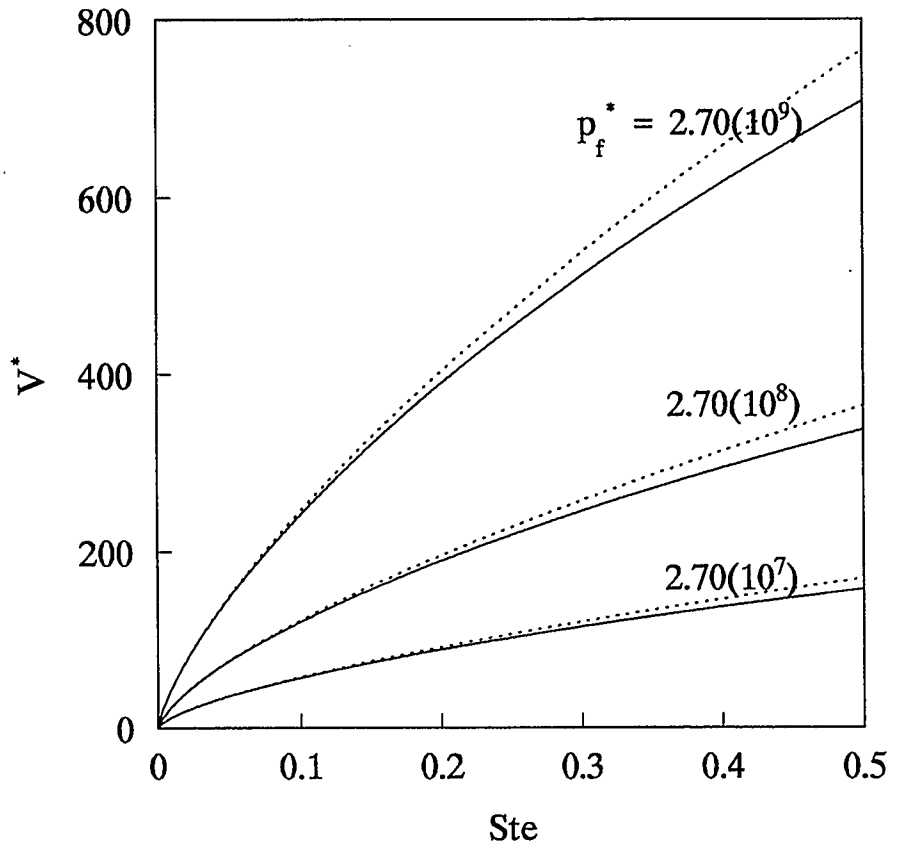


Fig. 3.13 Production rate of the melt $V^*$ as function of Ste at different $p_f^*$ values

A simplified quasi-steady state model was developed under a local curvilinear coordinate system (x,y) based on the general physical model. Approximate analytical results were presented for the migration rate of the heat source. The intent of the analysis was to obtain the dimensionless parameters that could affect the melting process. The results show that the primary parameters are the Stefan number and a dimensionless applied force $p_f^*$. The critical sector angle $\theta_c$ is a parameter related to the applied force and surface temperature and it also influences the process. The migration velocity was found to vary from $7.7814(10^{-8})$ m/s to $2.415(10^{-5})$ m/s while Ste and $p_f^*$ varied from $(0.001, 2.70(10^7))$ to $(0.5, 2.70(10^9))$, respectively. The gap width at angle $\theta = 0$ changes from 0.026 mm to 0.204 mm as $p_f^*$ was decreased by a factor of a 100 from $2.70(10^9)$ to $2.70(10^7)$. The result also shows that at very small Ste number ( $Ste < 0.015$), the heat transfer is controlled by conduction. Sensible heat transport can not, however, be neglected at large Ste number. The differences between two f(Ste) solutions (3.48b and 3.48c) become more critical as Ste value increases. Most of the disccussion in this chapter pertains to consequences of eq.(3.48c) while the conclusions do not change for very low Stefan number. The follow-up change due to the other solution (3.48b) will be done in subsequent research.

# Chapter 4

# Numerical Simulation of the Transient Process

In this chapter, numerical techniques used in solving a moving boundary problem with a phase change event are reviewed. The grid generation method, how irregular-shaped boundaries are treated, how temperature-dependent physical properties of the melt are handled, and the procedure for tracking the moving interface are briefly summarized. Discretization of the PDEs is carried out and an algorithm was developed to solve the resulting algebraic equations.

## 4.1 Literature Review on Numerical Techniques

### 4.1.1 *Introduction*

The problem of a phase change with a moving heat source involves both the conduction as well as convection of thermal energy. The resulting transport equations are nonlinear for three reasons. One type of non-linearity is due to the convective terms in

the momentum and energy equations. The second is because the thermophysical properties of the melt vary strongly with temperature. The third kind of non-linearity is caused by the existence of a moving boundary; the melting interface whose loci is not known *a priori* and has to be determined simultaneously as a part of the system solution. The shape of the boundary may not match or follow the coordinate directions. For treating such problems by numerical techniques, there are basically two approaches. The first one is connected with interface-fitting algorithms (varied grid or mesh methods), and the second one with interface-smearing (fixed grid) methods. Samarskii et al. (1993) have recently reviewed these two numerical techniques in relation to solving moving-boundary problems. Lacroix and Voller (1990) have also suggested that both varied and fixed grids can be applied with success to a wide variety of problems, including solving phase change problems.

### 4.1.2 *Varied and Fixed grid Methods*

The varied grid method is based on a transformation of the irregular physical domain under consideration into a regular rectangular one through the introduction of new independent variables. If the process is transient (or time-dependent) with a moving boundary, the transformation has to be repeated continually since the system geometry changes. Although the domain thus transformed is regular, the mapping from the physical domain to each new regular domain is demanding. It is necessary to solve a coupled system of PDEs at every time-level as the grid is constructed (Thompson, 1982; Warsi and Thompson, 1982). This procedure may require more computational effort than solving

the transport equations directly. If the relationship between an irregular domain and the transformed regular one can be expressed analytically, the mapping would be straightforward and the PDEs may not have to be solved. The work is simplified if the new coordinate variables can be defined explicitly by using the old ones. Sparrow et al. (1977) and Hsu et al. (1981) employed the varied grid method to transform the physical domain to a rectangular one without solving the transformation PDEs. Under their specific conditions, a vertical hot tube was embedded at a fixed location in a solid to be melted. The melting interface formed a truncated cone wider at the top. The cone angle varied with elapsed time. Natural convection involving the melt in this space is two dimensional, i.e. in r- and z- directions. During any given computational interval, the shape was assumed unchanged. As a consequence, when this geometry was transformed into a rectangular one, the new coordinate variables were defined explicitly as functions of the interface radius (i.e. $\chi = (r-r_o)/(r_i-r_o)$ and $\psi = z/z_o$). Solutions of PDEs for the grid transformation were thus avoided. This transformation was also used by Moore and Bayazitoglu (1982) for investigating close-contact melting inside a spherical enclosure. Moallemi (1985) and Moallemi and Viskanta (1986) employed an adaptive grid generator to create a curvilinear coordinate in their simulation of a horizontal tube melting its way through a phase-changing solid.

The varied grid method removes the difficulties which arise from the presence of irregular boundaries. However, new difficulties arise. The transformed governing equations are more complicated than the untransformed ones and the execution of the algorithm consumes a large amount of CPU time. The alternative fixed grid method is

thus in more common use. In the fixed grid technique, the mesh established at the start is not altered during the entire calculation process. The calculation domain is the physical one which is usually irregular. Discretizations of PDEs can be done using a general approach which is known as the fictitious regions method (FRM). The energy equation can be formulated using temperature (Hong and Saito, 1993) or enthalpy (Shamsunder and Sparrow, 1975; Voller and Prakash, 1987; Brent, Voller and Reid, 1988, Date, 1991). For defining the velocity field, the fixed grid method can be employed using either primitive variables (velocity-pressure) or a stream function-vorticity formulation. In terms of the primitive variables formulation (u,v,p), the governing equations are the Navier-Stokes equations. The stream function-vorticity formulation involves a fourth-order equation derived from the Navier-Stokes equations through eliminating the pressure terms.

For the present study, the fixed gird method was chosen and the numerical simulation involved the primitive variables formulation (u,v,p). The transformed grids method or varied grid method is an efficient method to solve a phase change problem in some cases, but it was difficult to apply to the present problem. For the transformed grids method, the calculation domain must be mapped from the real region for each time step. This requires extensive calculations and, therefore, is costly. The unknown migration rate of the heat source must also be re-calculated whenever the assumed velocity is updated at each time step.

### 4.1.3 *Temperature-dependent Properties in Phase-change Process*

In the process of melting and solidification, media properties sometimes vary with

process temperature. Cho and Sunderland (1974) analyzed a phase-change heat conduction problem into a semi-infinite slab in which thermal conductivity was assumed to be a linear function of temperature. Oliver and Sunderland (1987) extended the above problem to the situation where both the thermal conductivity and heat capacity of the melt varied linearly with temperature. A semi-analytical solution was obtained by using modified error functions to predict the heat transfer rates. A Runge-Kutta scheme was used to evaluate the modified error functions. Heat conduction with phase change and varied properties have also been investigated by Sheen and Hayakawa (1991) in a food freezing process which involves volumetric changes. To overcome the convergence problem in their analysis due to the temperature-dependent food properties (both the thermal conductivity and heat capacity were functions of temperature), the internal temperatures were solved numerically by an implicit finite difference method while a finite volume heat balance method was applied at the boundary nodes. They, however, did not elaborate on how to handle the varied properties when discretizing the PDEs.

Patankar(1980) introduced an "effective" thermal conductivity for the case of varied thermophysical properties. Ogawa et al. (1991) employed a similar technique to handle the situation in which viscosity was expressed as an exponential function of temperature. Similar treatments were used by Hong and Saito (1993) for the viscosity and Voller and Swaminathan (1993) for the thermal conductivity at the phase change boundaries.

## 4.2 Numerical Analysis

The governing equations are expanded and normalized in the cylindrical coordinate system as described in subsection 4.2.1. The calculation domain and the technique to generate the grid mesh is described in 4.2.2. The treatment of the string intersected boundary and the discretization of the partial differential equations (PDE) are then presented respectively in 4.2.3 and 4.2.4.

### 4.2.1 *Governing Equations in a Cylindrical Coordinate System*

In chapter 3, a mathematical model was described with respect to a coordinate system fixed at the centre of the hot tube. In this section, detail expressions of the governing equations will be developed for the cylindrical coordinate along the θ- and r-directions as in Fig.3.1. The boundary conditions are elaborated upon. The constraints are presented as expressions to be solved simultaneously with the governing equations.

Equations (3.4), (3.5) and (3.7) are expressed in the cylindrical coordinate system. The properties of the melt (e.g. $\eta$, $C_p$) are not constant but temperature-dependent. A reference temperature was chosen to be the melting point $T_m$. The variables were normalized with respect to the following scales: length, $r_o$; velocities, $\kappa_m / r_o$; pressure, $\rho\kappa_m^2/r_o^2$; time, $\kappa_m^{-1} r_o^2$; energy content, $h_w - h_m$; and temperature, $T_w - T_m$. The prime variables and the corresponding dimensionless ones with scales are listed in Table 4.1.

Table 4.1 Prime variables and their corresponding dimensionless counterparts

| Dimensionless Variable | Definition |
|---|---|
| $r^*$ | $r/r_o$ |
| $\delta^*$ | $\delta/r_o$ |
| $u^*$ | $u/(\kappa_m r_o^{-1})$ |
| $v^*$ | $v/(\kappa_m r_o^{-1})$ |
| $u_o^*$ | $u_o/(\kappa_m r_o^{-1})$ |
| $u_{or}^*$ | $u_o \cos\theta/(\kappa_m r_o^{-1})$ |
| $u_{o\theta}^*$ | $u_o \sin\theta/(\kappa_m r_o^{-1})$ |
| $p^*$ | $p/(\rho\kappa_m^2 r_o^{-2})$ |
| $t^*$ | $t/(r_o^2 \kappa_m^{-1})$ |
| $h^*$ | $(h - h_m)/(h_w - h_m)$ |
| $T^*$ | $(T - T_m)/(T_w - T_m)$ |
| $M^*$ | $M/(\rho r_o^2 L)$ |
| $F_e^*$ | $F_e/(\rho\kappa_m^2 L r_o^{-1})$ |
| $C_p^*$ | $C_p/C_{pm}$ |

The governing equations, in dimensionless form, are

(a) continuity:

$$\frac{1}{r^*}\frac{\partial}{\partial r^*}(r^* v^*) + \frac{1}{r^*}\frac{\partial u^*}{\partial \theta} = 0 \tag{4.1}$$

(b) r- component

$$\begin{aligned}
&\frac{\partial v^*}{\partial t^*} + v^*\frac{\partial v^*}{\partial r^*} + \frac{u^*}{r^*}\frac{\partial v^*}{\partial \theta} = -\frac{\partial p^*}{\partial r^*} \\
&+ \frac{2}{r^*}\frac{\partial}{\partial r^*}\left(Pr\, r^*\frac{\partial v^*}{\partial r^*}\right) + \frac{1}{r^*}\frac{\partial}{\partial \theta}\left(\frac{Pr}{r^*}\frac{\partial v^*}{\partial \theta}\right) \\
&+ \frac{1}{r^*}\frac{\partial}{\partial \theta}\left[Pr\left(\frac{\partial u^*}{\partial \theta} - \frac{u^*}{r^*}\right)\right] \\
&- \frac{2\,Pr}{r^{*2}}\left(\frac{\partial u^*}{\partial \theta} + v^*\right) + \frac{u^{*2}}{r^*} - \frac{\partial u^*_{or}}{\partial t^*}
\end{aligned} \tag{4.2}$$

(c) θ- component

$$\begin{aligned}
&\frac{\partial u^*}{\partial t^*} + v^*\frac{\partial u^*}{\partial r^*} + \frac{u^*}{r^*}\frac{\partial u^*}{\partial \theta} = -\frac{1}{r^*}\frac{\partial p^*}{\partial \theta} \\
&+ \frac{1}{r^*}\frac{\partial}{\partial r^*}\left(Pr\, r^*\frac{\partial u^*}{\partial r^*}\right) + \frac{1}{r^*}\frac{\partial}{\partial \theta}\left(\frac{Pr}{r^*}\frac{\partial u^*}{\partial \theta}\right) \\
&+ \frac{1}{r^*}\frac{\partial}{\partial r^*}\left[Pr\left(\frac{\partial v^*}{\partial \theta} - u^*\right)\right] + \frac{1}{r^*}\frac{\partial}{\partial \theta}\left[\frac{Pr}{r^*}\left(\frac{\partial u^*}{\partial \theta} + 2v^*\right)\right] \\
&+ \frac{Pr}{r^*}\left(\frac{\partial u^*}{\partial r^*} + \frac{1}{r^*}\frac{\partial v^*}{\partial \theta} - \frac{u^*}{r^*}\right) - \frac{u^* v^*}{r^*} - \frac{\partial u^*_{o\theta}}{\partial t^*}
\end{aligned} \tag{4.3}$$

(c) energy

$$\frac{\partial h^*}{\partial t^*} + v^* \frac{\partial h^*}{\partial r^*} + \frac{u^*}{r^*} \frac{\partial h^*}{\partial \theta} =$$

$$\frac{1}{r^*} \frac{\partial}{\partial r^*} \left( r^* \zeta \frac{\partial h^*}{\partial r^*} \right) + \frac{1}{r^*} \frac{\partial}{\partial \theta} \left( \frac{\zeta}{r^*} \frac{\partial h^*}{\partial \theta} \right)$$

$$- \frac{1}{r^*} \frac{\partial}{\partial r^*} \left( r^* h^* \zeta \frac{\partial \ln C_p^*}{\partial r^*} \right) - \frac{1}{r^*} \frac{\partial}{\partial \theta} \left( \frac{h^* \zeta}{r^*} \frac{\partial \ln C_p^*}{\partial \theta} \right) \qquad (4.4)$$

$$+ h^* \left( \frac{\partial \ln C_p^*}{\partial t^*} + v^* \frac{\partial \ln C_p^*}{\partial r^*} + \frac{u^*}{r^*} \frac{\partial \ln C_p^*}{\partial \theta} \right)$$

where $Pr = \eta_m C_{pm}/\lambda$ is the Prandtl number and $\zeta = \kappa/\kappa_m$ is the ratio of the thermal diffusivity at temperature T relative to the value at the melting point $T_m$. The reference diffusivity, $\kappa_m$, is defined as $\frac{\lambda}{\rho C_{pm}}$ where $C_{pm}$ is heat capacity at the melting temperature. $C_p^* = C_p/C_{pm}$.

The boundary conditions to be applied are

$$r^* = 1 \; ; \quad u^* = v^* = 0 \quad and \quad h^* = 1 \tag{4.5}$$

$$r^* = 1 + \delta^* \; ; \; u^* = u_o^* \cos\theta \sin(\theta - \phi)$$
$$v^* = - u_o^* \cos\theta \cos(\theta - \phi); \quad and \quad h^* = 0 \tag{4.6}$$

$$\theta = 0; \; \frac{\partial u^*}{\partial \theta} = \frac{\partial v^*}{\partial \theta} = \frac{\partial h^*}{\partial \theta} = 0 \tag{4.7}$$

where angle $\phi$ (Fig. 4.1) is subtended by the tangent to the curve defined by G ($r_i$, $\theta$, t) and the horizontal, i.e.

$$\phi = \theta - \tan^{-1} \left\{ \frac{1}{1 + \delta^*(\theta, t)} \frac{\partial \delta^*}{\partial \theta} \right\} \tag{4.8}$$

The curvature at any point on the melting surface is given as:

$$k = \frac{(1 + \delta^*) \frac{\partial^2 \delta^*}{\partial \theta^2} - 2 \left( \frac{\partial \delta^*}{\partial \theta} \right)^2 - (1 + \delta^*)^2}{\left[ (1 + \delta^*)^2 + \left( \frac{\partial \delta^*}{\partial \theta} \right)^2 \right]^{3/2} \cdot r_o} \tag{4.9}$$

Derivations of eqs.(4.8) and (4.9) are in Appendix B.1.

The initial conditions for the problem are

$$t^* = 0; \; u^* = 0 \; , \; v^* = 0 \quad and \quad h^* = 0 \tag{4.10}$$

So far, eight unknowns are identified, i.e. u, v, h, p, $u_o$, $\delta$, $\phi$ and k. However, only six equations are available (eqs.(4.1) to (4.4), (4.8) and (4.9). Two constraint equations are needed for closure. The constraint expression eq.(3.14), is simplified using the

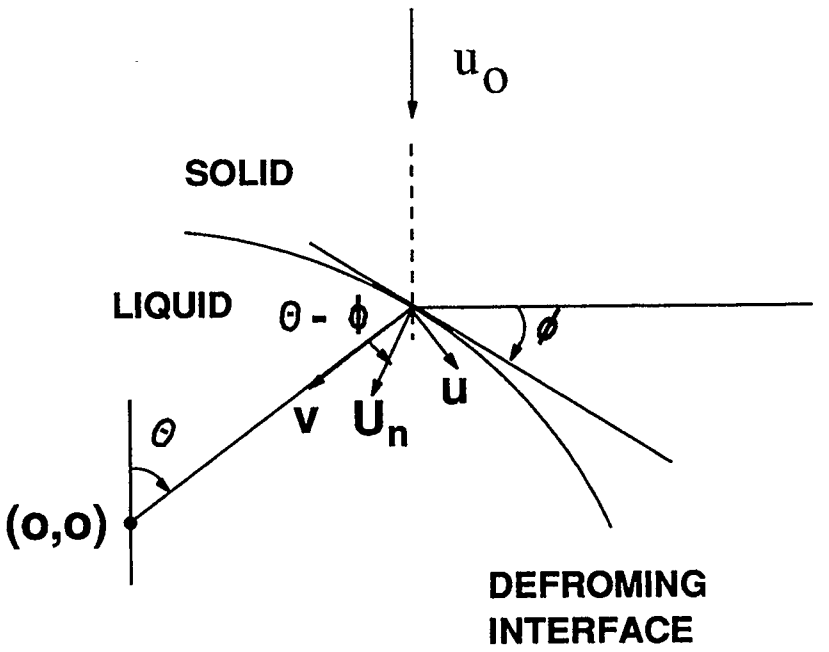


Fig. 4.1 Definition of $\phi$ and velocity component at the melting interface

approach suggested by Patel (1968). The details are presented in Appendix B.2. Some important formulas are summarized as follows:

Since

$$\boldsymbol{u}_o = - u_o ( \cos\theta \, \hat{i} - \sin\theta \, \hat{j} ) ;$$

$$\nabla G = \hat{i} \frac{\partial G}{\partial r} + \hat{j} \frac{1}{r} \frac{\partial G}{\partial \theta} ;$$

$$G = r - r_o - \delta (\theta, t) = 0 ;$$

$$and \quad \frac{\partial G}{\partial r} = 1, \quad \frac{\partial G}{\partial \theta} = - \frac{\partial \delta}{\partial \theta}, \quad \frac{\partial G}{\partial t} = - \frac{\partial \delta}{\partial t}$$

Eq. (3.14) can then be expanded as

$$\frac{\partial \delta^*}{\partial t^*} = u_o^* \left( \cos\theta + \frac{1}{r^*} \frac{\partial \delta^*}{\partial \theta} \sin\theta \right) - Ste \left( 1 + \frac{1}{r^{*2}} \left( \frac{\partial \delta^*}{\partial \theta} \right)^2 \right) \frac{\partial T^*}{\partial r^*} \Big|_{r^* = 1 + \delta^*} \tag{4.11}$$

An external force is applied on the hot tube to maintain a close contact of two solid surfaces for the operation. The force balance for the heat source in dimensionless form is formulated as :

$$M^* \frac{du_o^*}{dt^*} = F_e^* - 2 \int_0^{\theta_c} \left( p^* \cos\theta + \tau_w^* \sin\theta \right) d\theta \tag{4.12}$$

where $F_e^*$ denotes the dimensionless applied force per tube length. $\tau_w^*$ is the dimensionless shear stress, $\theta_c$ is the critical sector angle.

For the present problem, the boundary at $\theta = 0°$ has a stagnation point on the

surface of the tube. The surfaces also have the closest approach at this boundary. In order to find a solution to the problem, either the force applied or the minimum spacing $\delta_o^*$ has to be specified. $\delta_o^*$ was chosen as the prescribed parameter. The energy balance at $\theta$ = 0 can be obtained directly from eq.(4.11) as:

$$|u_o^*| = Ste \left.\frac{\partial T^*}{\partial r^*}\right|_{r^*=1+\delta_o^*} \tag{4.13}$$

### 4.2.2 *Calculation Domain and Mesh Generation*

The origin of the system, as illustrated in Fig.3.1, is fixed at the centre of the hot tube. Only one half plane is considered due to the symmetry about the vertical line through the origin. The solid wall being melted is assumed initially flat. The domain, as shown in Fig. 4.2, is a rectangular block upon which a cylindrical grid pattern is superposed (Hastaoglu, 1987, Negiz, 1991). The indices i and j are for $\theta$ and r directions respectively. It is important to note that the sketch is not scaled as the $\delta_o$ value has been exaggerated and is not proportional to the radius $r_o$. The initial grid domain is much larger than the region where melting occurs. The latter expands as the melting progresses. The lateral side of the computational domain, R, is 5 $r_o$. The mesh is non-uniform but $\Delta r$ and $\Delta\theta$ are constant. The sizes are $1.5(10^{-5})$m and $\pi/180$ for $\Delta r$ and $\Delta\theta$ respectively. The grid is 181×101.

System variables such as temperature and pressure are determined at the nodes of the principal grids (e.g. points N E S W in Fig. 4.3(a)). The velocity components u and

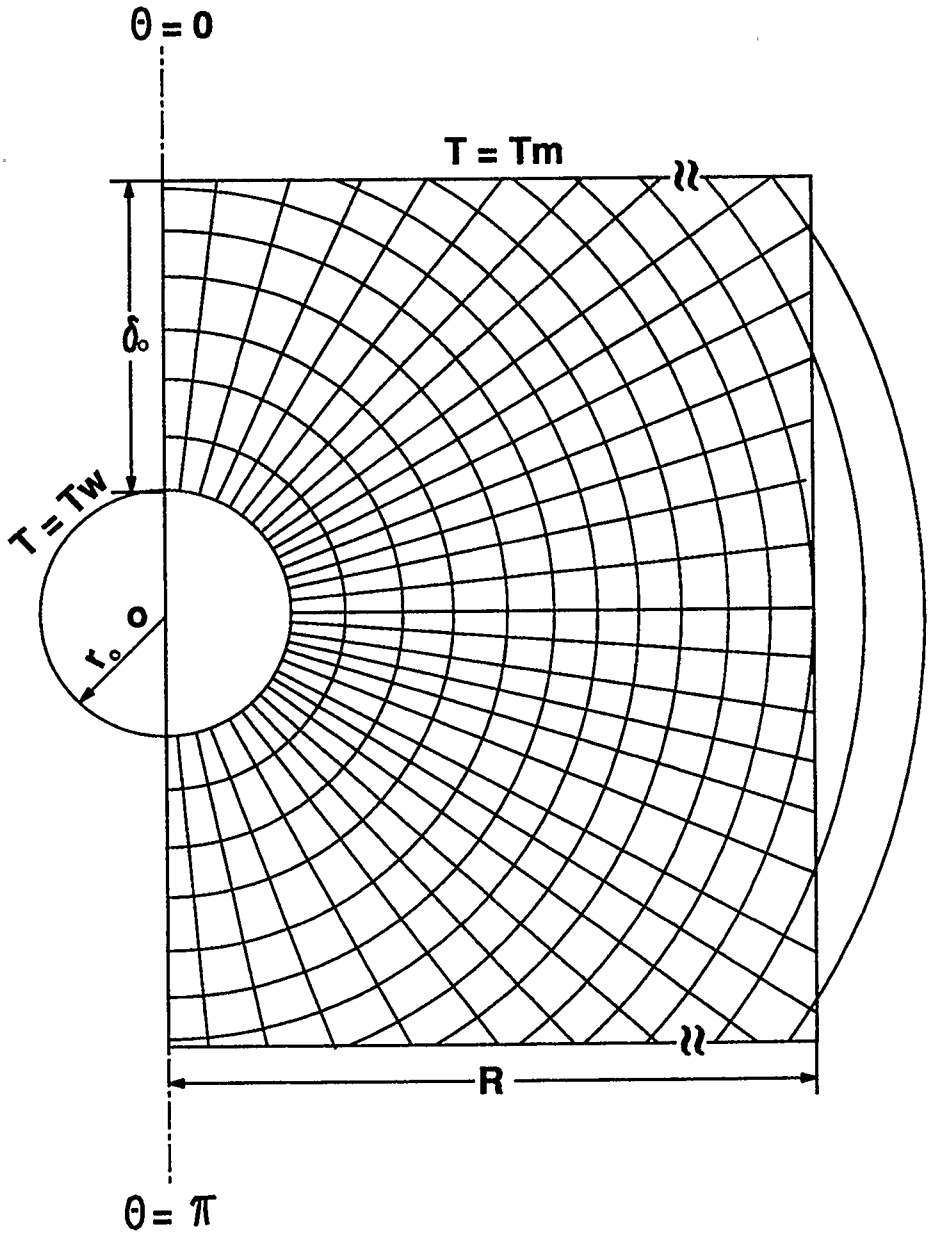


Fig. 4.2 Initial calculation domain

v are evaluated at the staggered secondary grid points (n e s w) located midway between the main grid points in the θ- and r- directions. As noted by Patankar (1980, 1988), this keeps the continuity equation consistent and unrealistic pressure and velocity fields, which may also satisfy the continuity equation and Navier-Stokes equations, are avoided. A control volume is illustrated as in the shaded area in Fig.4.3(a) for the variables such as temperature and pressure. Similar control volumes are constructed for the staggered grid points where the momentum equations are discretized. Fig. 4.3(b) and (c) illustrate the control volumes for the u and v components both of which shift halfway along the θ and r directions respectively.

### 4.2.3 *String Intersected Boundaries*

As close-contact melting progresses, the solid-liquid interface is continuously deformed and the melt envelops the hot tube surface. It is possible that the curved boundary intersects the grid mesh at the points which are not located at the mesh nodes. String intersected boundaries arise in our problem due to the fact that the interface contour may not coincide with the grid line of the mesh. The melting interface may traverse a cell bounded by a set of computational molecules as illustrated in Fig. 4.4. Such cells are called surface or partial cells as compared full cells which fully locate inside the flow domain. Under this condition, "short legs" arise when string(s) are intersected by the curved boundary. That means the distance ($f_{r\,ij}\ \Delta r$) between the node and the interface (shown in Fig. 4.4), where $f_{r\,ij} \leq 1$, is less than the mesh size $\Delta r$. The

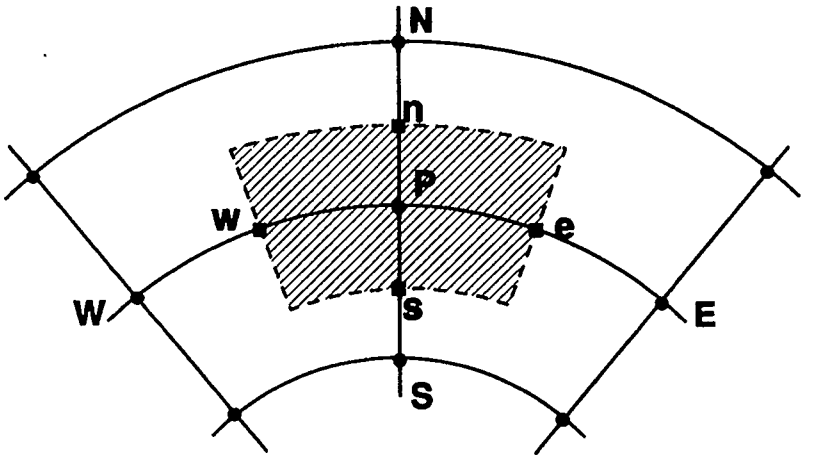


Fig. 4.3(a) Schematic of main grid point, staggered grid points and control volume for T and p

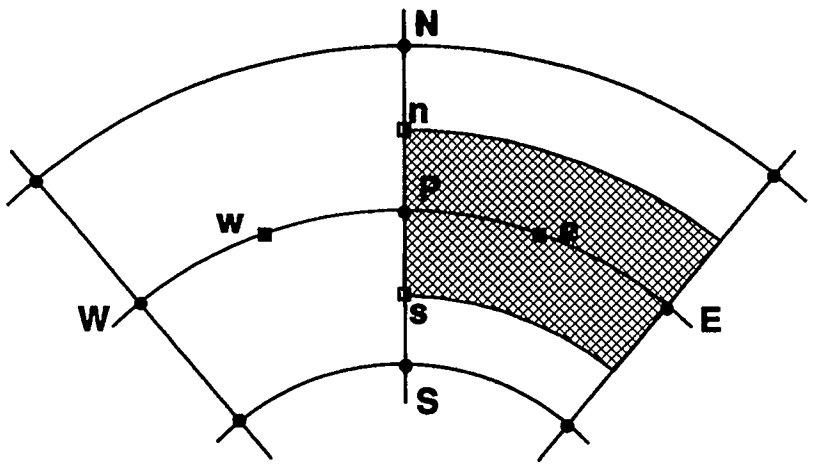


Fig. 4.3(b) Control volume for u

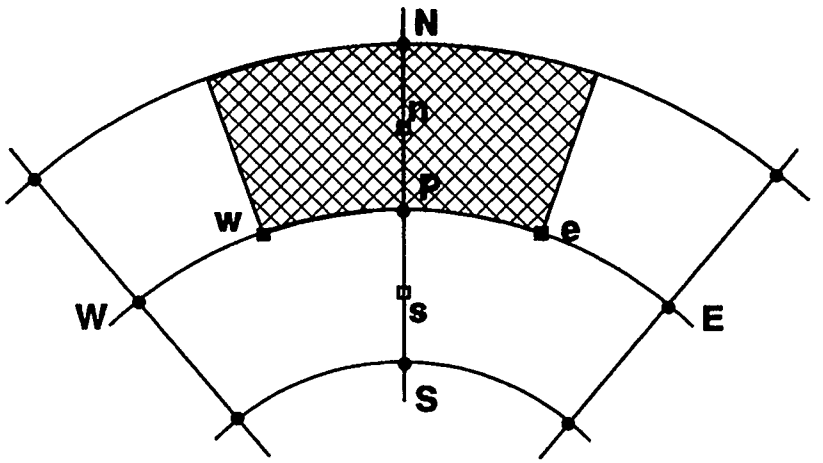


Fig. 4.3(c) Control volume for v

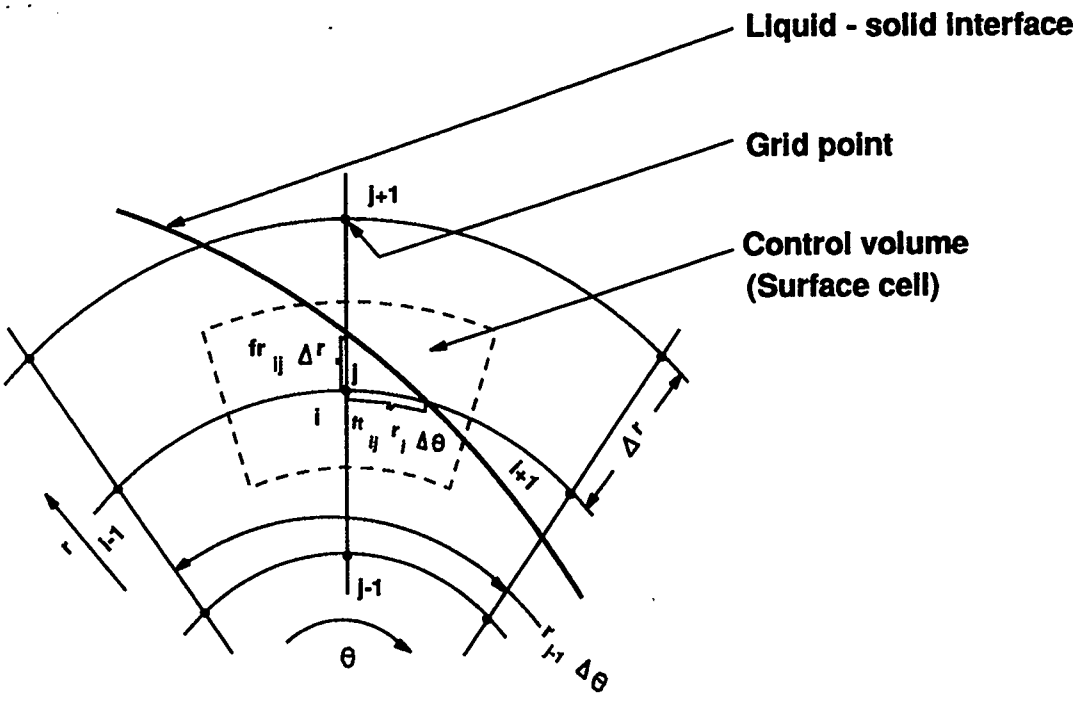


Fig. 4.4 A surface cell bisected by the solid-liquid interface

number of grid points in r direction is not the same at the different angles, θ. When the value for $\delta_o$ is prescribed, the number of grid points in the r- direction, at each angle θ, can be calculated from

$$N_j(\theta) = \left\lfloor \frac{r_i - r_o}{\Delta r} \right\rfloor = \left\lfloor \frac{\delta(\theta)}{\Delta r} \right\rfloor + 1 \qquad (4.14)$$

The symbol ⌊ ⌋ means the integral values of the quotient. These numbers are updated once the melting interface shape is established at each time step. The coefficient $f_{r\,ij}$ for the r-direction can be determined from the formula

$$f_{r\,ij} = [\ \delta(\theta) - (\ N_j(\theta) - 1\ )\ \Delta r\ ]\ \frac{1}{\Delta r} \qquad (4.15)$$

Coefficient $f_{t\,ij}$ in θ- direction can be calculated from:

$$f_{t\,ij} = \frac{(i-1)\ \Delta\theta - \Phi_j}{\Delta\theta} \qquad (4.16)$$

where $\Phi_j$ is the root of the equation

$$G(r_i\ ,\ \Phi_j\ ,\ t) = 0 \qquad (4.17b)$$

at $r_i = r_o + \Delta r\ (\ N_j(\theta) - 1\ )$.

Special treatment is required to incorporate these coefficients into the derivatives in the system of equations, instead of using the standard forms (Thom and Apelt, 1961; Ozisik, 1980, Vemuri and Karplus, 1981). For a partial cell, it can happen under two situations: either one or two of its strings may be intersected by the boundary. Fig. 4.5(a) shows a situation in which only one of the strings from the node(i,j) is intersected by the

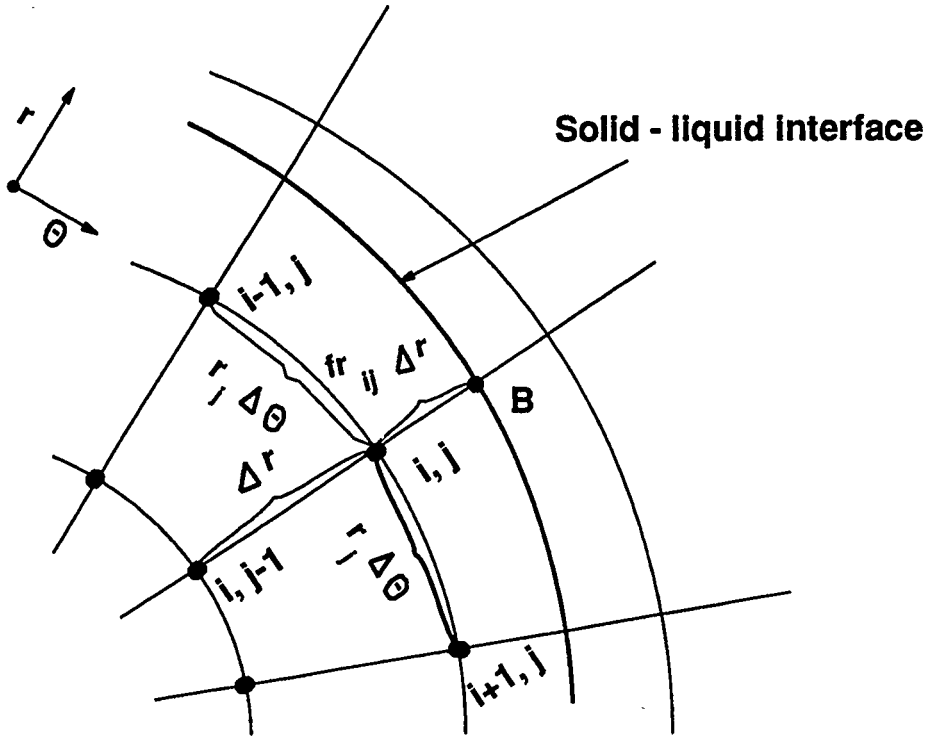


Fig. 4.5(a) Schematic of string intersected boundary in one direction

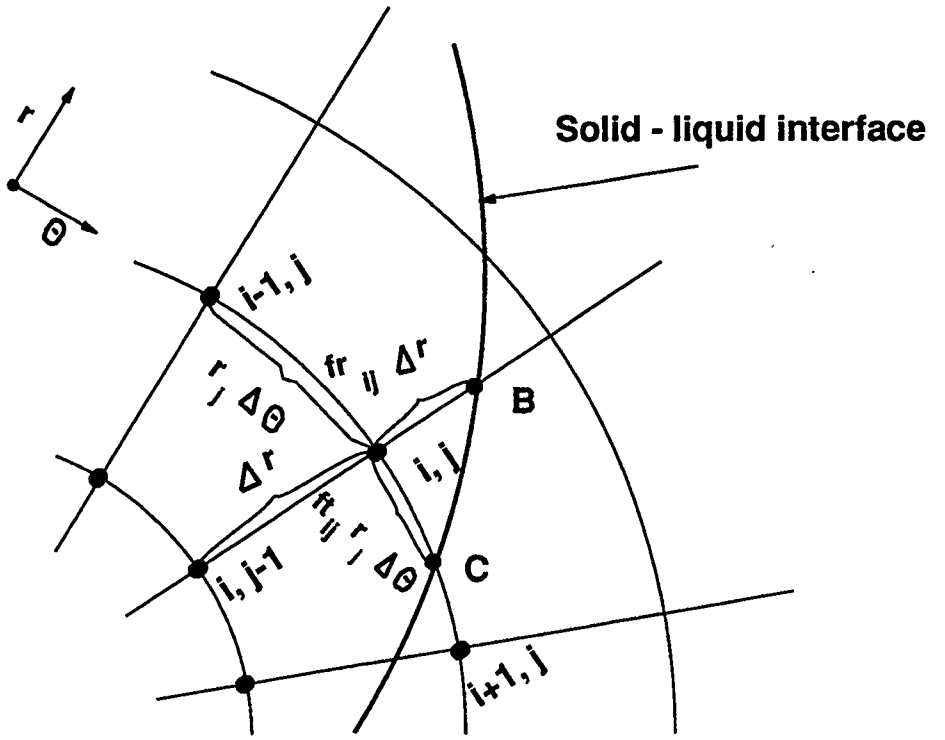


Fig. 4.5(b) Schematic of string intersected boundary in two directions

curved boundary at point B. The distance between the nodes (i,j) and B is $f_{r\,ij}\ \Delta r$. Fig. 4.5(b) illustrates a situation in which two of the strings from the node(i,j) are intersected by the curved boundary at points B and C. The distances between the nodes (i,j) and B and C are $f_{r\,ij}\ \Delta r$ and $f_{t\,ij}\ r_j\ \Delta\theta$ respectively. The representation of $\partial h/\partial r$ at node (i,j) can be obtained from (Ozisik, 1980)

$$\frac{\partial h}{\partial r}\Big|_{i,j} = \frac{1}{\Delta r}\left[\frac{h_m}{f_{r\,ij}\,(1+f_{r\,ij})} - \frac{f_{r\,ij}}{1+f_{r\,ij}}\,h_{i,j-1} - \frac{1-f_{r\,ij}}{f_{r\,ij}}\,h_{i,j}\right] \tag{4.18}$$

For the second order finite difference approximation, one obtains

$$\frac{\partial^2 h}{\partial r^2}\Big|_{i,j} = \frac{2}{(\Delta r)^2}\left[\frac{h_m}{f_{r\,ij}\,(1+f_{r\,ij})} + \frac{h_{i,j-1}}{1+f_{r\,ij}} - \frac{h_{i,j}}{f_{r\,ij}}\right] \tag{4.19}$$

A similar expression can be obtained for derivatives with respect to θ as:

$$\frac{\partial h}{\partial \theta}\Big|_{i,j} = \frac{1}{r_j\,\Delta\theta}\left[\frac{h_m}{f_{t\,ij}\,(1+f_{t\,ij})} - \frac{f_{t\,ij}}{1+f_{t\,ij}}\,h_{i-1,j} - \frac{1-f_{t\,ij}}{f_{t\,ij}}\,h_{i,j}\right] \tag{4.20}$$

and

$$\frac{\partial^2 h}{\partial \theta^2}\Big|_{i,j} = \frac{2}{(r_j\,\Delta\theta)^2}\left[\frac{h_m}{f_{t\,ij}\,(1+f_{t\,ij})} + \frac{h_{i-1,j}}{1+f_{t\,ij}} - \frac{h_{i,j}}{f_{t\,ij}}\right] \tag{4.21}$$

where $f_{r\,ij}$ and $f_{t\,ij}$ are coefficients defined in eqs.(4.15) and (4.16) in r- and θ- directions respectively.

Singularity may arise in eqs.(4.18) to (4.21) if the coefficients $f_{t\,ij}$ and $f_{r\,ij}$ are zero or very close to zero. This means that, if the grid point is very close to the solid-liquid

interface, the discretization should be handled differently. When the solid-liquid interface is closer to a grid point than a fixed distance, variables at the node are set to assume the values at the interface. Equations (4.18) to (4.21) can not be applied at such grid points. The criterion implemented was that the distance from the grid point to the surface in any of the two directions be less than $10^{-10}$ m, i.e.

$$f_{r\,ij}\,\Delta r \quad and \quad f_{t\,ij}\,r_j\,\Delta\theta < 10^{-10}$$

### 4.2.4 *Discretization of the PDEs*

#### I Treatment of internal nodes

Equations (4.1) - (4.6) are coupled and non-linear. For the discretization, the finite control volume method developed by Patankar(1980, 1988) was used. This method combines finite difference as well as finite element techniques, and the conservation principle applies at every node point (Li and Durbetaki, 1992, Hong and Saito, 1993).

In this approach, each of the transport equations is expressed, in terms of a general variable $\Phi$, of the form

$$\frac{\partial}{\partial t}(\rho\Phi) + \frac{1}{r}\frac{\partial}{\partial r}(\rho r V_r \Phi) + \frac{1}{r}\frac{\partial}{\partial \theta}(\rho V_\theta \Phi) = \frac{1}{r}\frac{\partial}{\partial r}\left(r\Gamma_\phi \frac{\partial \Phi}{\partial r}\right) + \frac{1}{r}\frac{\partial}{\partial \theta}\left(\Gamma_\phi \frac{1}{r}\frac{\partial \Phi}{\partial \theta}\right) + S_p + S_\phi \tag{4.22}$$

where $\Gamma_\Phi$, $S_\Phi$ and $S_p$ are respectively the exchange coefficient, the source and the pressure terms. The terms $\Phi$, $\Gamma_\Phi$, $S_\Phi$ and $S_p$ are defined for each of the equations (4.1) - (4.4)

through certain manipulations. These results are presented in Table 4.2.

Table 4.2. Expressions for $\Gamma_\Phi$, $S_p$ and $S_\Phi$ for any general Variable $\Phi$

| Equation | $\Phi$ | $\Gamma_\Phi$ | $S_p$ | $S_\Phi$ |
|---|---|---|---|---|
| Continuity | 1 | 0 | 0 | 0 |
| Angular Momentum | $u^*$ | Pr | $-\frac{1}{r^*}\frac{\partial p^*}{\partial \theta}$ | $\frac{1}{r^*}\frac{\partial}{\partial r^*}\left[P_r\left(\frac{\partial v^*}{\partial \theta} - u^*\right)\right] + \frac{1}{r^*}\frac{\partial}{\partial \theta}\left[\frac{P_r}{r^*}\left(\frac{\partial u^*}{\partial \theta} + 2v^*\right)\right] - \frac{u^* v^*}{r^*} - \frac{\partial u^*_{o\theta}}{\partial t^*}$ |
| Radial Momentum | $v^*$ | Pr | $-\frac{\partial p^*}{\partial r^*}$ | $\frac{1}{r^*}\frac{\partial}{\partial r^*}\left(P_r r^* \frac{\partial v^*}{\partial r^*}\right) + \frac{1}{r^*}\frac{\partial}{\partial \theta}\left[P_r\left(\frac{\partial u^*}{\partial \theta} - \frac{u^*}{r^*}\right)\right] - \frac{2P_r}{r^{*2}}\left(\frac{\partial u^*}{\partial \theta} + v^*\right) + \frac{u^{*2}}{r^*} - \frac{\partial u^*_{or}}{\partial t^*}$ |
| Energy | $h^*$ | $\zeta$ | 0 | $-\frac{1}{r^*}\frac{\partial}{\partial r^*}\left(r^* h^* \zeta \frac{\partial \ln C_p^*}{\partial r^*}\right) - \frac{1}{r^*}\frac{\partial}{\partial \theta}\left(\frac{h^*\zeta}{r^*}\frac{\partial \ln C_p^*}{\partial \theta}\right) + h^*\left(\frac{\partial \ln C_p^*}{\partial t^*} + v^*\frac{\partial \ln C_p^*}{\partial r^*}\right) + h^*\left(\frac{u^*}{r^*}\frac{\partial \ln C_p^*}{\partial \theta}\right)$ |

The governing partial differential equations summarized in Table 4.2 are discretized to yield algebraic equations by using a power law difference scheme discussed by Patankar (1980). The grid and the control volume in (r,θ) coordinates have been presented earlier in Fig. 4.3. The z-direction thickness of the control volume is assumed to be unity. To obtain the discretization equation, we integrate eq.(4.22) with respect to r and θ over the control volume. The general discretization equation can be written as

$$a_P\Phi_P = a_E\Phi_E + a_W\Phi_W + a_N\Phi_N + a_S\Phi_S + b \tag{4.23}$$

where

$$a_E = D_e\, A(|P_e|) + [\![-F_e\ ,\ 0]\!] \tag{4.24a}$$

$$a_W = D_w\, A(|P_w|) + [\![-F_w\ ,\ 0]\!] \tag{4.24b}$$

$$a_N = D_n\, A(|P_n|) + [\![-F_n\ ,\ 0]\!] \tag{4.24c}$$

$$a_S = D_s\, A(|P_s|) + [\![-F_s\ ,\ 0]\!] \tag{4.24d}$$

$$b = a_P^{o}\Phi_P^{o} + S_c\,\Delta V \tag{4.24e}$$

$$a_P^{0} = \frac{\Delta V}{\Delta t} \tag{4.24f}$$

$$a_P = a_E + a_W + a_N + a_S + a_P^{o} - S_p\,\Delta V \tag{4.24g}$$

$$A(|P_e|) = [\![0\ ,\ (1 - 0.1|P_e|)^5]\!] \tag{4.24h}$$

$$\Delta V = 0.5 \left( r_s + r_n \right) \Delta r \, \Delta\theta \tag{4.24i}$$

In the foregoing equations, $a_P^\circ$ and $\Phi_P^\circ$ are values known at time level t while all other values refer to values at time level t+$\Delta$t which are unknown. $[\![\ ]\!]$ means the larger of the enclosed components. $S_C$ and $S_P$ are the coefficients of the source term after a linearization by a formula

$$S = S_C + S_P \, \Phi \tag{4.25}$$

F, D and P (Peclet number) are defined as

$$F_e = u_e \, \Delta r \qquad D_e = \frac{\Gamma_e \, \Delta r}{r_e \, (\Delta\theta)_e} \qquad P_e = \frac{F_e}{D_e} \tag{4.26a}$$

$$F_w = u_w \, \Delta r \qquad D_w = \frac{\Gamma_w \, \Delta r}{r_w \, (\Delta\theta)_w} \qquad P_w = \frac{F_w}{D_w} \tag{4.26b}$$

$$F_n = v_n \, r_n \, \Delta\theta \qquad D_n = \frac{\Gamma_n \, r_n \, \Delta\theta}{(\Delta r)_n} \qquad P_n = \frac{F_n}{D_n} \tag{4.26c}$$

$$F_s = v_s \, r_s \, \Delta\theta \qquad D_s = \frac{\Gamma_s \, r_s \, \Delta\theta}{(\Delta r)_s} \qquad P_s = \frac{F_s}{D_s} \tag{4.26d}$$

The momentum equations have been discretized in a way similar to the discretization of the energy equation. The control volumes for $u^*$ and $v^*$ are different from each other and both are different from that for $h^*$, as was shown in Fig. 4.3 (b) and (c). The resulting discretization equations for $u^*$ and $v^*$ can be written as

$$a_e u_e^* = \Sigma a_{nb} u_{nb}^* + b + (p_P^* - p_E^*) A_e \tag{4.27}$$

for the u component, and

$$a_n v_n^* = \Sigma a_{nb} v_{nb}^* + b + (p_P^* - p_N^*)A_n \quad (4.28)$$

for the v component. The terms $A_e$ and $A_n$ are defined as:

$$A_e = \Delta r \quad (4.29a)$$

$$A_n = 0.5(r_P + r_N)\Delta\theta \quad (4.29b)$$

They represent the areas over which the pressure differences act in the radial and azimuthal directions respectively. The neighbour coefficients, $a_{nb}$, account for the combined convection-diffusion transport across the control-volume faces. The terms $a_{nb}$ and b in eqs. (4.27) and (4.28) are defined in the same manner as in eq.(4.24).

II Treatment of boundary nodes

Due to the fact that the calculation domain is irregular, grid cells close to the interface may not be full. As discussed earlier in this section, the fraction values should be considered when discretizing the system of equations. Eqs.(4.14) -(4.17) are employed for the discretization. The resulting algebraic equations are similar to eq.(4.23). However, on the boundary, the values of $\Phi_N$ or/and $\Phi_W$ correspond to the values at the melting boundary.

### 4.2.4 *Treatment of Temperature-dependent Properties*

In the temperature range of industrial interest, from the hot surface to the melting point of solid sulphur (112.8 - 200°C), the viscosity and the heat capacity of liquid

sulphur exhibit almost discontinuous changes as the temperature is increased, as was described in section 2.2.2. These data could not be fitted with simple mathematical formulas. Therefore, values for viscosity and heat capacity were stored in two data files in the program package and retrieved (with interpolation as necessary) at temperatures obtained at the main grid points. When Patankar (1980)'s SIMPLE method is employed to discretize the PDEs, the property values are defined for the conditions at the centre of a grid cell while velocities are defined at points on the cell faces. However, one needs the values of the viscosity $\eta$ at the corners of grid cells (e.g. point e in Fig.4.6) when the viscous terms in the momentum equations are calculated. Special care has to be taken in calculating the viscosity $\eta_e$ from values at the neighbouring grid points by interpolation to avoid numerical instability. The treatment as described in Patankar (1980) for the varied thermal conductivity and its application by Ogawa et al. (1991) to handle the varied viscosity was employed for the $\eta_e$ calculation. In the calculation of the θ-momentum equation, for example, $\eta_e$ was calculated from the following equations (Patankar, 1980, Ogawa et al. 1991)

$$\eta_e = \frac{\eta_1 \, \delta\theta_1 + \eta_2 \, \delta\theta_2}{\delta\theta_1 + \delta\theta_2} \tag{4.30}$$

$$\eta_{1,2} = \frac{2 \, \Delta r}{\dfrac{\delta r_1}{\eta_{d,c}} + \dfrac{\delta r_2}{\eta_{a,b}}} \tag{4.31}$$

here $\eta_i$ is the viscosity at point i in Fig.4.6 such as point 1 or 2. When $\eta_b$, for example, is much larger than the viscosities at the points a, d and c, $\eta_b$ contributes negligibly to the

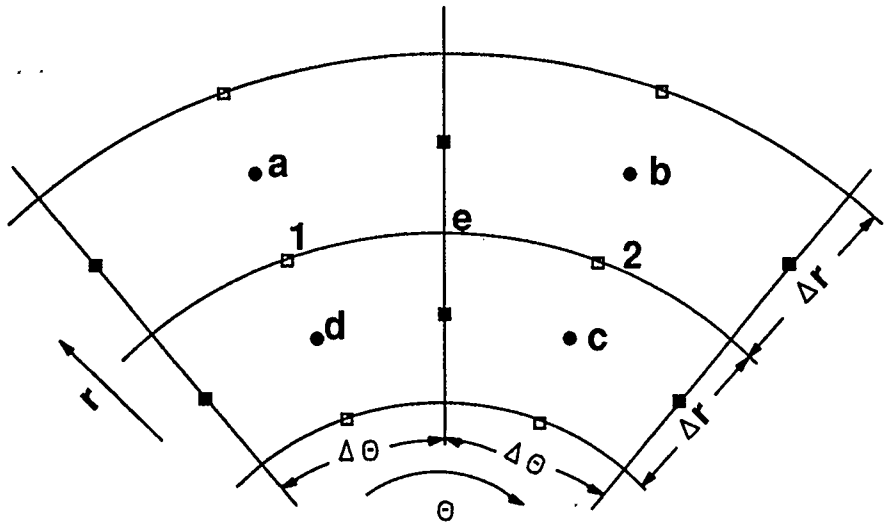


Fig. 4.6 Illustration of the grid cell used in the interpolation of variable properties in a main-staggered grid net. Temperature, pressure and properties ($\eta$, $C_p$ etc.) are defined at the grid points a-d, the $\theta$-component velocity u is defined at the staggered points by solid squares, and the r-component velocity v is defined at the grid points represented by empty squares.

viscosity $\eta_e$. This procedure facilitates computation when large viscosity differences exist even between adjacent grid cells. A similar treatment has been applied to the interpolation of $C_p$ values, when necessary.

## 4.3 Tracking of the Melting Front

### 4.3.1 *Calculation of Radii of the Interface*

The solid-liquid interface location is a function of time as the melting progresses. The interface which is defined by an implicit function $G(r_i,\theta,t)$ in eq.(3.10) can be explicitly expressed, in dimensionless form, as

$$r_i^* = f\,(\,\theta\,,\,t^*\,) \tag{4.32}$$

As discussed in section 4.1.1, the development of the melting contour is determined by the local energy balance equation at the melting interface and the migration rate of the hot tube. The discretization of eq.(4.11) in finite difference form is

$$\frac{r_i^* - r_i^{o\,*}}{\Delta t^*} = u_o^* \left( \cos\theta_i + \frac{\sin\theta_i}{r_i^*} \frac{\partial \delta^*}{\partial \theta} \right) - Ste \left. \frac{\partial T^*}{\partial r^*} \right|_i \left( 1 + \frac{1}{r_i^{2\,*}} \left( \frac{\partial \delta^*}{\partial \theta} \right)^2 \right) \tag{4.33}$$

where

$$\frac{\partial \delta^*}{\partial \theta} = \frac{r_{i+1}^* - r_{i-1}^*}{2\,\Delta\theta} \tag{4.34}$$

Here, $r_{i-1}^*$, $r_i^*$ and $r_{i+1}^*$ indicate the radii of the interface at angle $\theta_{i-1}$, $\theta_i$ and $\theta_{i+1}$,

respectively, and $r_i^{o*}$ is the value of $r_i^*$ at the time t level. Eq.(4.33) can be re-arranged in the following form by substitution of eq.(4.34),

$$a_r\, r_{i-1}^* + b_r\, r_i^* + c_r\, r_{i+1}^* = 0 \tag{3.35}$$

where

$$a_r = \frac{\sin\theta_i}{\Delta\theta} + \frac{Ste}{(\Delta\theta)^2}\,\frac{\partial T^*}{\partial r^*}\Big|_i \tag{4.36a}$$

$$b_r = \frac{r_i^{2*} - r_i^{o*}\, r_i^*}{\Delta\theta} - u_o^*\cos\theta_i\, r_i^* \tag{4.36b}$$

$$c_r = -\frac{\sin\theta_i}{\Delta\theta} + \frac{Ste}{(\Delta\theta)^2}\,\frac{\partial T^*}{\partial r^*}\Big|_i\,(r_{i+1}^* - 2\, r_{i-1}^*) \tag{4.36c}$$

This set of non-linear equations with three bands can be easily solved using the Newton-Raphson iteration method(Burden, 1980).

In the above equation, $u_o^*$ is calculated from eq.(4.13). $\partial T^*/\partial r^*\,|_i$ is the temperature gradient at the solid-liquid interface. It can be numerically evaluated by using the temperature values at the nodes closest to the surface. The evaluation formula for $\partial T^*/\partial r^*\,|_i$ may, due to the irregularity, vary with the interface position: the closest node may be located exactly at the interface or at a position between two grid nodes. If the contour is intersected by the r grid line, at the grid node or very close to the grid node NR (the criterion for which is discussed in section 4.2.1), it can be evaluated using a formula suggested by (Kuehn and Goldstein, 1976)

$$\frac{\partial T^*}{\partial r^*}\Big|_i = \frac{-2\ T^*_{i,NR-3} + 9\ T^*_{i,NR-2} - 18\ T^*_{i,NR-1} + 11\ T^*_{NR}}{6\ \Delta r^*} \qquad (4.37)$$

In this case, $T_{NR} = T_m$. If the boundary intersects r grid line at a distance $f_{t\,ij}\ \Delta r$ above the nearest internal grid node NR, the heat flux can be calculated using a formula which takes the coefficients into account. That is,

$$\frac{\partial T^*}{\partial r^*}\Big|_i = \frac{-2\ T^*_{i,NR-2} + 9\ T^*_{i,NR-1} - 18\ T^*_{i,NR} + 11\ T^*_m}{(11\ f_{r\,ij} - 5)\ \Delta r^*} \qquad (4.38)$$

### 4.3.2 *VOF Method*

Since the melting front becomes indented and its position moves as the melting proceeds, it is necessary to develop a strategy to track this irregular interface in order to compute efficiently the numerical approximations to partial differential equations within a variable calculation domain. Several methods for tracking discontinuous front and interface are reviewed by Hyman (1984). These methods include surface tracking techniques based on connected marker points along the interface, volume tracking methods that track the volume occupied by the solution regions bounded by the interfaces, and moving-mesh methods where the underlying mesh is aligned and moved with the interface.

Among these methods, the fractional volume method (also called the volume of fluid,VOF) developed by Nichols et al. (1980) and Hirt and Nichols (1981) seems suitable for the current interface tracking. VOF is one of the volume tracking methods which

employs the fractional volumes of fluid in a cell as the identification flag for this grid cell. In this technique, a function F(r,θ,t) is defined whose value is unity (1) at any point occupied by fluid and zero (0) elsewhere. When averaged over the cells of a computational mesh, the average value of F in a cell is equal to the fractional volume of the cell occupied by the fluid. Cells with F values between zero and one contain a boundary surface (surface cell or partial cell). This method was initially developed for tracking a free surface, and it is found that it can be applied for a moving boundary tracking with phase change after some modification.

In the (r,θ) coordinates, the time dependence of F is governed by the equation

$$\frac{\partial F}{\partial t^*} + \frac{1}{r^*}\frac{\partial}{\partial \theta}(Fu^*) + \frac{1}{r^*}\frac{\partial}{\partial r^*}(r^*Fv^*) = 0 \qquad (4.39)$$

When eq.(4.39) is integrated over a computational cell, the changes in F within a cell reduce to fluxes of F across the cell faces. Special care must be taken in computing these fluxes to preserve the sharp definition of an interface. The technique used here is a type of donor-acceptor flux approximation (Johnson, 1970). The essential idea is to use information about F downstream as well as upstream of a flux boundary to establish a crude interface shape, and then to use this shape in computing the flux.

As shown in Fig. 4.7, considering the amount of F to flow through the right-hand face of a cell during a time step of duration $\Delta t^*$, the total flux of fluid volume and void volume crossing the right cell face per unit sectional area is $V_x = u^* \Delta t^*$. The sign of $u^*$ determines the donor and acceptor cells, i.e, cells losing and gaining fluid volumes respectively. For example, if $u^*$ is positive, the upstream or left cell is the donor and the

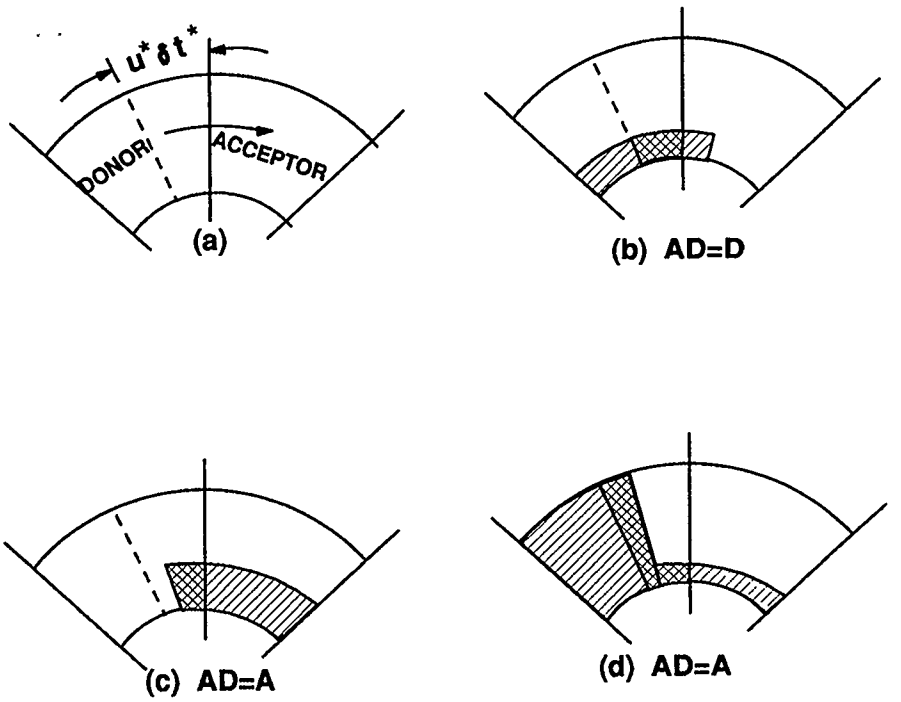


Fig. 4.7 Concept of donor and acceptor cells

down stream or right cell the acceptor. The amount of F flowed across the cell face within one time step is a product of $\delta F_x$ and the face cross-sectional area. $\delta F_x$ is defined as

$$\delta F_x = MIN \left( F_{AD} \, |V_x| + CF, \, F_D \, r^* \, \delta\theta_D \right) \tag{4.40}$$

where

$$CF = MAX \left( (1.0 - F_{AD}) \, |V_x| - (1.0 - F_D) \, r^* \, \delta\theta_D \, , \, 0.0 \right) \tag{4.41}$$

Single subscripts denote the acceptor (A) and donor (D) cells. The double subscript, AD, refers to either A or D, depending on the orientation of the interface relative to the direction of flow: AD = A or acceptor cell is used when the surface is convected mostly normal to itself; otherwise, the donor cell value is used. Briefly, the MIN feature in eq.(4.40) prevents the flowing of more fluid from the donor cell than it has to give, while the MAX feature accounts for an additional fluid, CF, if the amount of void to be flowed exceeds the amount available. Similar treatment can be used to calculate $\delta F_y$ for the lower and upper cells when the total flux of fluid volume and void volume crossing the lower cell face per unit cross sectional area is $V_y = v^* \, \Delta t^*$. Therefore the updated fluid configuration will be

$$F = F^o - \delta F_x \, \Delta r^* - \delta F_y \, r^* \, \Delta\theta \tag{4.42}$$

for a donor cell, and

$$F = F^o + \delta F_x \, \Delta r^* + \delta F_y \, r^* \, \Delta\theta \tag{4.43}$$

for an acceptor cell.

### 4.3.3 *Determining the Interface Within a Cell*

One needs to know the exact location of the interface in surface cells in order to obtain the fraction information. In the VOF approach, it is assumed that the boundary can be approximated by a straight line cutting through the cell. By first determining the slope of this line, it then can be moved across the cell to a position where it intersects the known amount of fluid volume in the cell.

The slope of the intersect line is:

$$\frac{dY}{dX} = \frac{r_i + r_{i+1}}{r_{i-1} + r_i + r_{i+1}} \frac{r_i \cos\theta_i - r_i \cos\theta_{i-1}}{r_i \sin\theta_i - r_{i-1}\sin\theta_{i-1}} + \frac{r_i + r_{i-1}}{r_{i-1} + r_i + r_{i+1}} \frac{r_{i+1}\cos\theta_{i+1} - r_i\cos\theta_i}{r_{i+1}\sin\theta_{i+1} - r_i\sin\theta_i} \tag{4.44}$$

Given the slope of the interface at a location, a line can be drawn through the cell with the correct amount of fluid volume within the fluid side of the volume. This line represents a portion of the actual surface and provides the information necessary to calculate the coefficients for the application of equations for the surface nodes as described in eqs.(4.15) to (4.21).

## 4.4 The Solution algorithm

### 4.4.1 *The Speed of Motion of the Hot Tube and the Critical Angle* $\theta_c$

As mentioned in section 4.2.1, the displacement rate of the heating tube $u_o^*$ can be evaluated from eq.(4.13) since the gap thickness $\delta_o$ at $\theta = 0°$ is assumed as a

parameter for the process. $\partial T^*/\partial r^* \mid_{\theta=0}$ at the interface can be calculated using eq.(4.37) or eq.(4.38) depending on the boundary situation there. The migration rate affects the velocity field and depends explicitly on the temperature field. Since the velocity field is determined on the basis of a guessed migration velocity $u_o$, the procedure of velocity and temperature calculations has to be repeated until convergence is reached. The loop is presented in the flow diagram which is Fig 4.8.

As melting progresses, the polar sector of the flow domain continuously expands and the θ-direction numbering of the grid points varies as a function of time elapsed from the start of the melting. The sector angle subtended by the gap is the instantaneous critical angle $\theta_c$. Beyond $\theta_c$, the flow channel diverges widely and the heat transfer towards the interface at the melting point is negligible. The challenging problems involved are how to determine this angle $\theta_c$ and where to terminate the calculation. As the heating body migrates and the melting surface is indented, the curvature of the melting interface would be observed to change sharply in the plane of the original wall location. This point of curvature change determines the extent of the domain at each time step. The curvature of the melting surface is calculated from eq.(4.9) after the boundary shape is re-determined using eq.(4.11). Consequently the angle $\theta_c$ can be updated.

### 4.4.2 *The Calculation Procedures*

After the relevant technical details have been discussed in the above sections, a solution algorithm can be presented and the sequence of calculations shown for each time step (Wu and Jeje, 1994). A flow diagram of the calculation procedure is shown in Fig.

4.8. The highlights of the key operations in each time step are listed as follows:

1. A semi-implicit technique, the SIMPLE method (Patankar, 1980), is employed to calculate the primitive variables $u^*$, $v^*$ and $p^*$ for the radial and azimuthal components in the equations of motion and continuity.

2. The temperature field is then determined from the energy equation and, from the result, the local values for heat capacity ($C_p$) and viscosity ($\eta$) are evaluated according to the latest temperature field.

3. These updated property values are then substituted into the transport equations and calculations are repeated until convergence is achieved at each time step.

4. The moving rate of heat source is calculated by eq.(4.13).

5. Calculations are returned to step 1 until a constant velocity for the migration rate is obtained.

6. The melting boundary is located and the surface cells are tracked by the VOF technique (Hirt and Nichols, 1981). The fluid configuration is updated and the fraction values are calculated.

7. The curvature of the interface contour is then calculated and the critical angle $\theta_c$ is determined and the numberings of grid points in the r- and $\theta$-directions are re-calculated. The flow domain is then advanced.

The calculation is stopped when a specified simulation time is reached. In this approach, it is assumed that the melting process allows for a small time lag between the heat transfer to the interface and the movement of the interface (due to melting and also motion of the heat source). To explain this treatment: suppose that for a small time

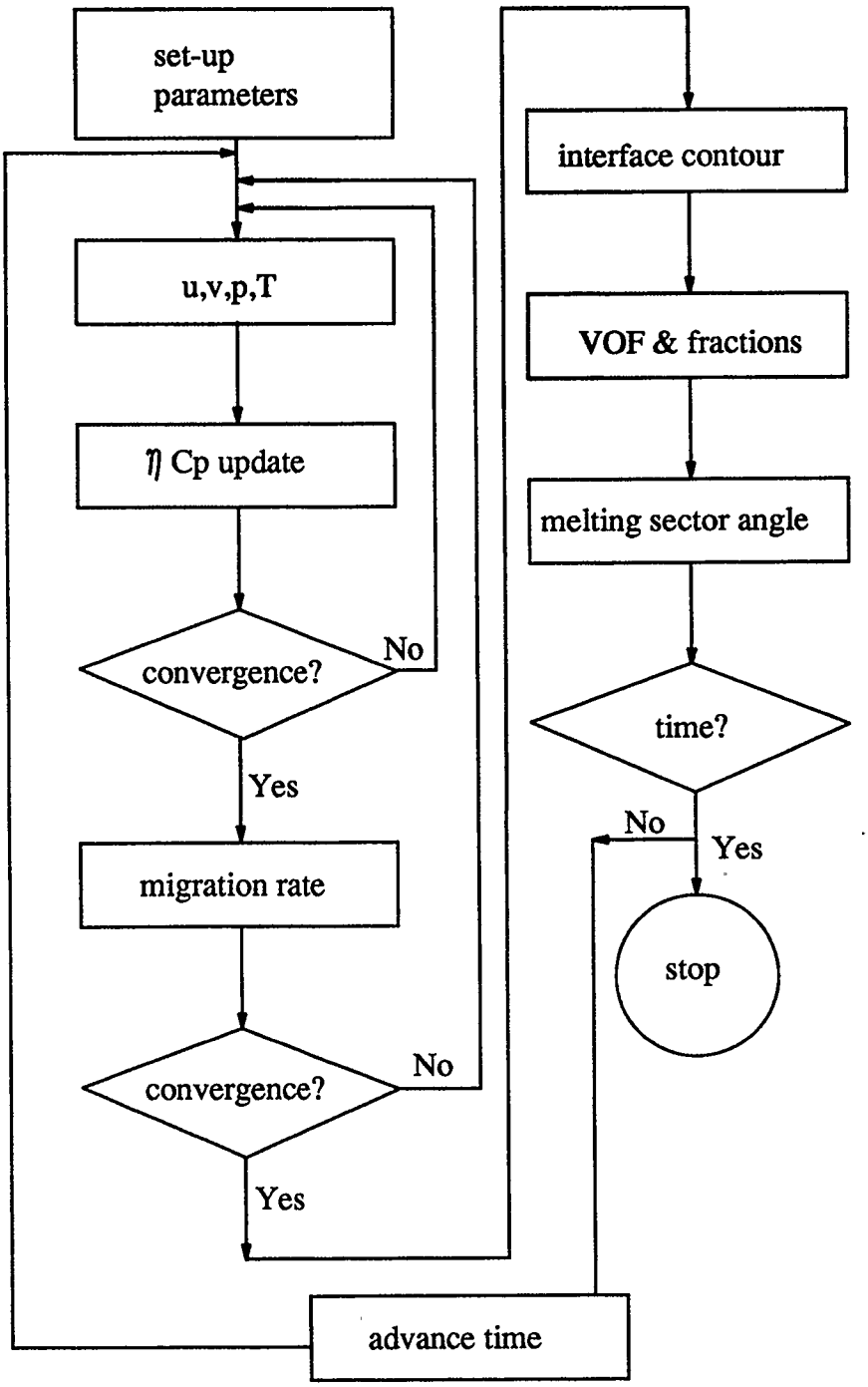


Fig. 4.8 Flow diagram for the numerical algorithm

interval, $\Delta t$, the interface is regarded as fixed. For this fixed calculation domain (with respect to the heat source), the SIMPLE approach is used to solve the discretized system of equations for the velocity and temperature fields, subject to the boundary conditions, to yield the distributions of the field variables for the next time step. The interface contour is then updated using the heat flux through the interface calculated from the distribution of temperature based on the fixed domain throughout the time interval. The heat flux through the interface at $\theta = 0$ is used to evaluate the displacement rate of the hot tube.

### 4.4.3 *Stability of the Finite Difference Scheme*

The effective implementation of the above approach requires that $\Delta t$ be sufficiently small to avoid errors associated with the lag between the heat delivery to the interface and the resultant interface displacement. The value of the time increment has a significant effect on the stability of the solution, particularly for the melting interface contour. After a series of tests, a time increment of $2(10^{-3})$ second was found small enough to ensure stability of the solution. The corresponding dimensionless time increment is $2.261(10^{-5})$.

The effect of varying the grid size ($\Delta r$ and $\Delta\theta$) on the solution was examined. The grid sizes were: 91×51, 181×101 and 361×201. For identical conditions of the calculations, the results obtained were similar to each other. A run with more grid points (i.e. finer grid size) consumed more CPU time (a ~40% increase compared with the intermediate one). For the coarsest grid size, the plotted contours of the melting interface were not very smooth. An intermediate set of the grid sizes provided the best compromise

with respect to both CPU consumption and smoothness of the melting interface contours. This corresponds to the size values of $1.5(10^{-5})$m and $\pi/180$ for $\Delta r$ and $\Delta\theta$ respectively as mentioned earlier in Section 4.2.2.

### 4.4.4 *Validation of the Numerical Algorithm*

Since there were no numerical and/or experimental data available in the literature, no comparisons can be made with previous work. A validation of the numerical algorithm was carried out on a simple ice-making process. The scheme was also tested by comparing the migration rates of the hot tube $u_o$ obtained from transient simulation algorithm and from the steady analytical solution at low Stefan numbers. The analytical solution in Chapter 3 has been demonstrated to be valid when Ste is small. In the following presentation, the solid lines refer to the results from numerical simulation whereas the dashed lines and discrete dots to the analytical solutions and experimental data points.

Growth of ice above a horizontal plate maintained at -20°C and in contact with a semi-infinite body of water was simulated. It was assumed that no convection currents were present in the water and heat transfer with phase change occurred only by conduction. Numerical results obtained for the time-dependent thickness of the ice match the analytical solution presented by Ozisik (1980) as shown in Fig. 4.9.

For the melting of sulphur, when the Stefan numbers are low, the plateau value for $u_o$ (after the initial rapid increase) obtained from the numerical simulation was almost the same as the one calculated from the analytical solution using eq.(3.54) (f(Ste) values

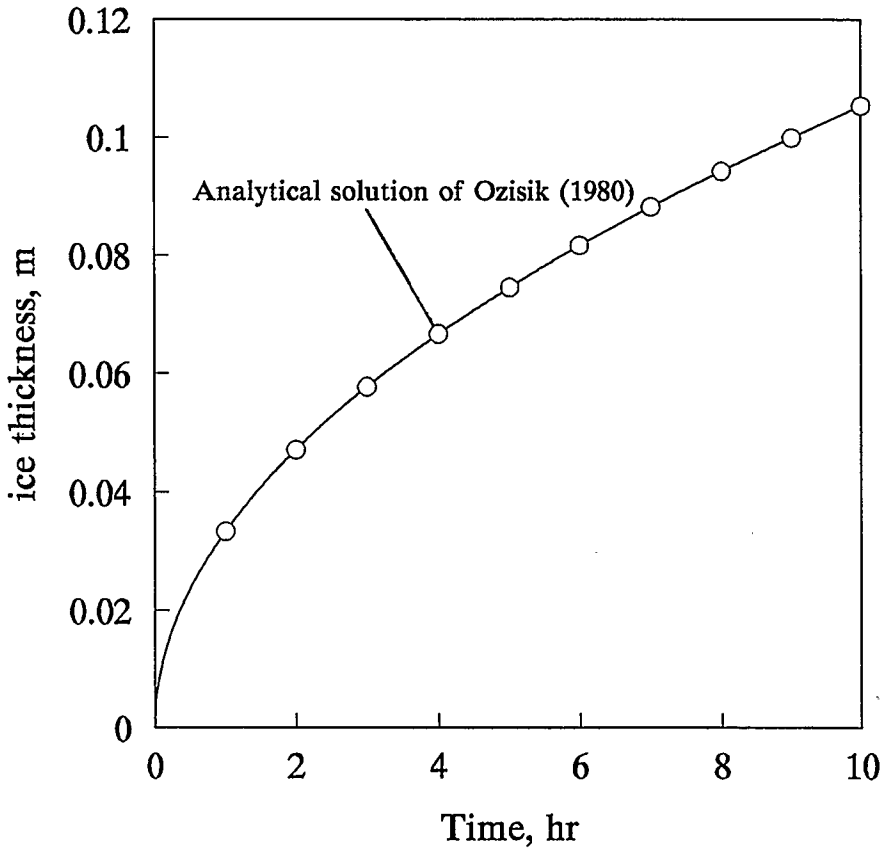


Fig. 4.9 Numerical simulation of ice thickness versus time, compared with analytical solution by Ozisik(1980)

from eqs.(3.48b) and (3.48c) respectively) along the $\theta = 0$ direction. This result is illustrated in Fig. 4.10 for Ste = 0.15 ($T_w$ = 120°C) and $\delta_o = 1.5(10^{-5})$ m. When the temperature of the hot surface was increased, the analytical solution underestimated $u_o$ by ~5% (when Ste<0.5).

The numerical model was also employed to simulate the melting of n-octadecane with a horizontal hot tube migrating through the phase change material under gravity. The thermophysical properties of n-octadecane used are as follows: fusion temperature, 27.5 °C; heat of fusion, 243.5 kJ/kg; specific heat of liquid, 2.23 kJ/kg.K; density of liquid, 768 kg/m$^3$; viscosity of liquid, 3.064 mPa.s.

The calculated migration rate of the hot tube is compared with the experimental data of Moallemi & Viskanta (1986) when the hot tube temperature was set at 40°C and the phase change block was at the melting point of n-octadecane, which is 27.5°C . As shown in Fig. 4.11, the steady displacement rate of the hot tube is in good agreement with the data. The experimental observation for $u_o$ was ~2% higher at the initial melting stage. The difference may be attributed to natural convection occurring in the experimental system. This was neglected in the numerical simulation.

To compare the simulation results with the experimental data when the n-octadecane block is at a temperature lower than its melting point, the algorithm was modified to take into account heat conduction into the block. The migration velocity of the hot tube was obtained for $T_w$ = 36°C and $T_\infty$ = 23°C. The results are plotted in Fig 4.12 and compared with experimental data reported by Moallemi & Viskanta (1986). The results are in close agreement with a maximum difference of 5%.

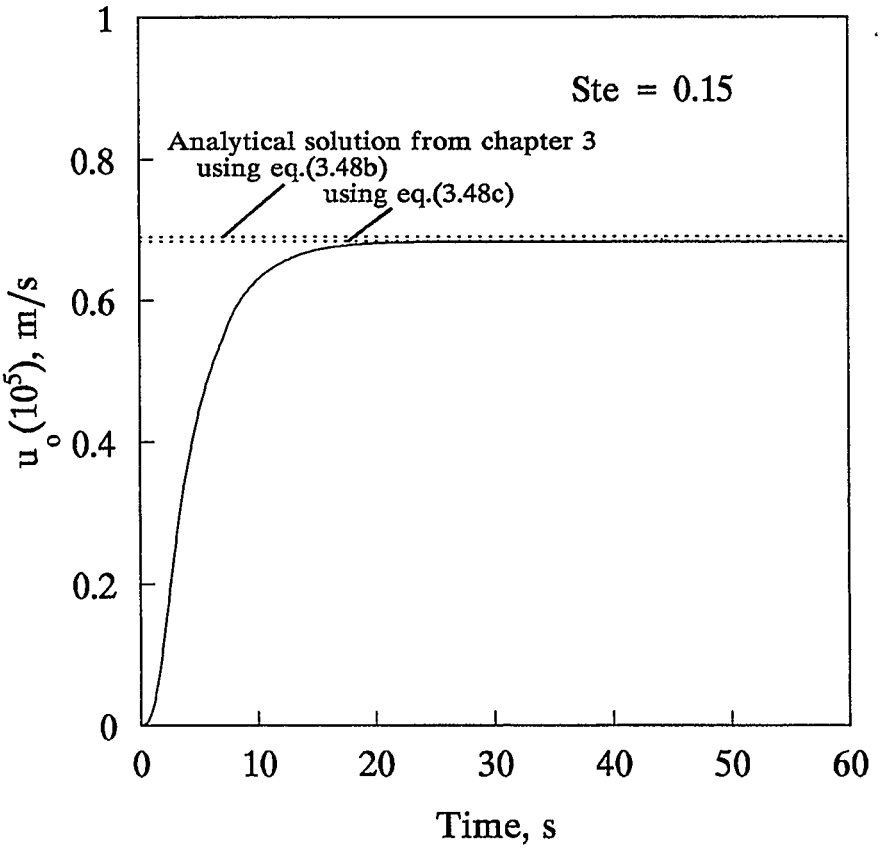


Fig. 4.10 Numerical simulation of migration rate of the hot tube $u_o$ when $T_w$ = 120°C, compared with steady state solution obtained from chapter 3

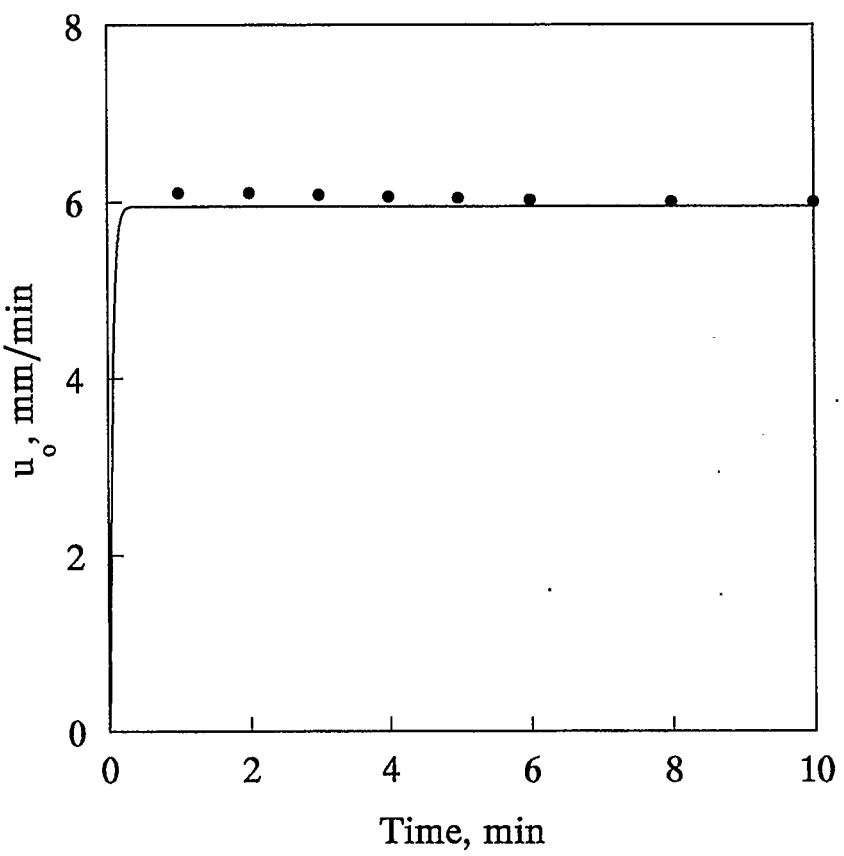


Fig. 4.11 Migration rate of the horizontal hot tube $u_o$ for n-octadecane melting when $T_w = 40°C$ and $T_\infty = T_m = 27.5°C$, compared with the experimental results (•) of Moallemi and Viskanta (1986)

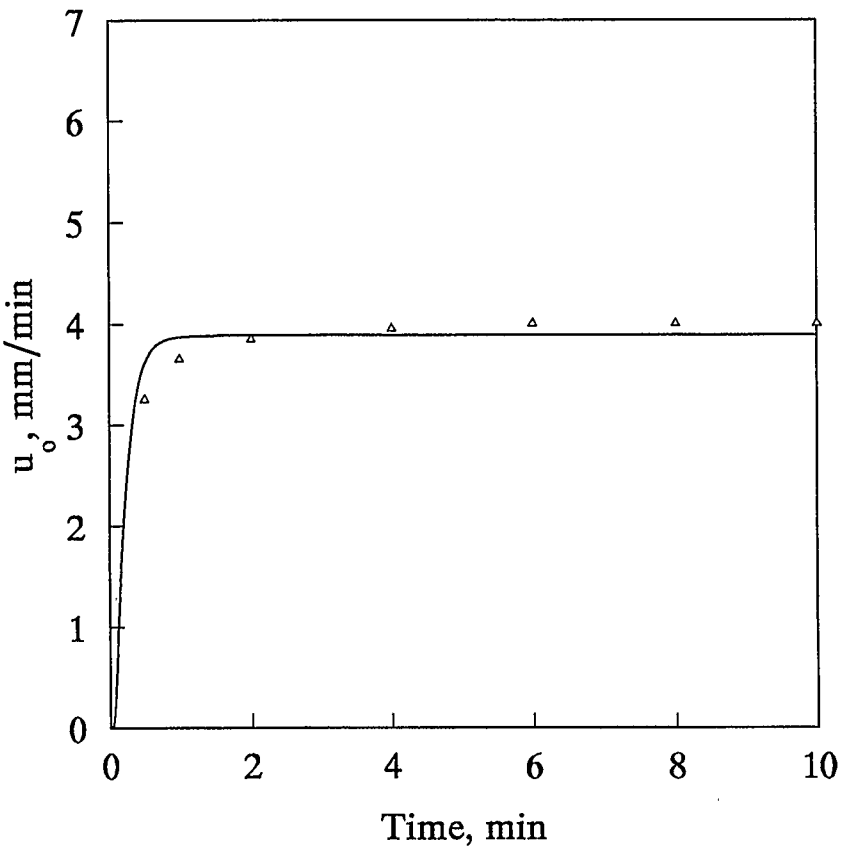


Fig. 4.12 Migration rate of the horizontal hot tube $u_o$ for n-octadecane melting when $T_w$ = 36°C and $T_\infty$ = 23°C, compared with the experimental results (▽) of Moallemi and Viskanta (1986)

Although the melting on the melting sulphur in this study is based on the assumption that the surface of the hot cylinder involved with melting is at the prescribed temperatures, the algorithm has been tested for the situation with a prescribed heat flux, the Neumann boundary condition. The medium, as for the foregoing, is n-octadecane for which the thermophysical properties can be assumed invariant. At a heat flux of 2630 $W/m^2$ which corresponds to a Stefan number ( defined as $Ste = r_o\, q''/[h_{sl} + C_s\,[T_m - T_\infty]$ ) of 2.326 and with the n-Octadecane maintained initially at $T_\infty = 21$ °C, the results for the migration velocity are as presented in Figure 4.13. A definite "overshoot" is predicted in agreement with the experimental data of Moallemi and Viskanta (1985b) which are also shown on the same plot. This overshoot was never predicted from any of the calculations based on specifying a constant temperature at the surface of the hot cylinder. In the present calculations, the simulation was terminated when the azimuthal angle for melting reached 90°.

In Figure 4.14, the variation in temperature with melting time was plotted at angle of 0°. The simulation shows good agreement with the measured data (Moallemi and Viskanta, 1985b). The wall temperature of the hot tube first increased to a peak value before declining with time. The variation of the wall temperature affects the migration rate of the hot tube which demonstrated an "overshooting" in the initial stage as shown in Fig. 4.13.

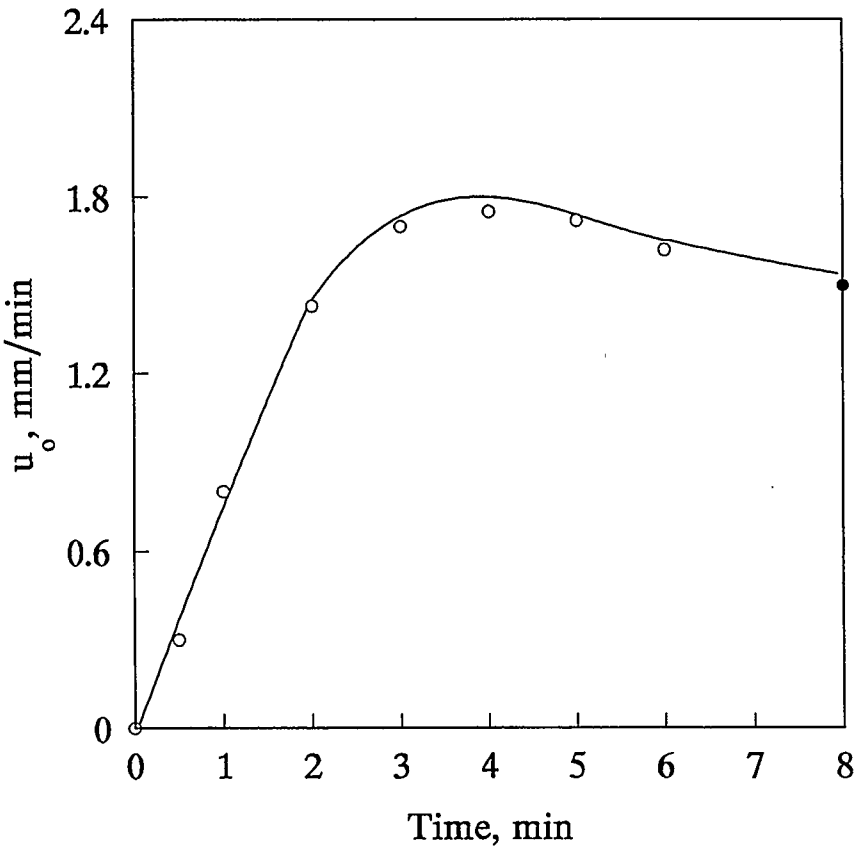


Fig. 4.13 Migration rate of the horizontal hot tube $u_o$ for n-octadecane melting when the hot tube wall heat flux q" = 2630 W/m$^2$, $T_\infty$ = 21°C (Ste = 2.326), compared with the experimental results of (○) Moallemi and Viskanta (1985b)

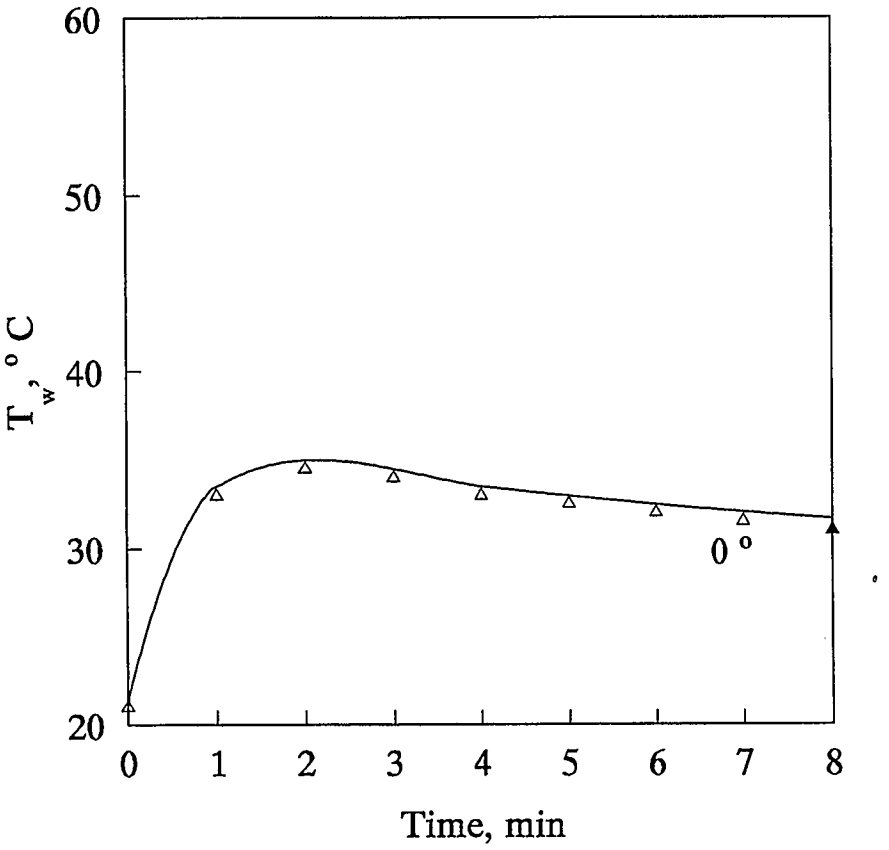


Fig. 4.14 Variation of heat-source surface temperature with time for n-octadecane melting when the hot tube wall heat flux q" = 2630 W/m$^2$, $T_\infty$ = 21°C (Ste = 2.326), compared with the experimental results of (▵ for 0°) Moallemi and Viskanta (1985b)

# Chapter 5

# Results and Discussion

In this chapter, results are presented for the temperature and the velocity fields, the displacement rates of the heating source, and the evolution of the outline of the melting front at early times during close-contact melting. In Section 5.1, the results typical for the process are discussed and interpreted. In the following section, the effects of changes in the variables are presented. These variables had earlier been identified as the surface temperature of the heat source, the gap width $\delta_o$ at $\theta = 0$ and the radius of the hot tube $r_o$.

## 5.1 An Illustrative Example

In this simulation, initial conditions for the solid sulphur block and the cylindrical tube were specified as eq.(4.10). The surface of sulphur was initially flat and the solid block was at its melting point during the entire process. The surface temperature of the tube was also initially at the melting point of sulphur. The temperature of the heat source was then suddenly increased to a temperature $T_w$ ($T_w > T_m$) and melting commenced. The equations to be solved include terms for $\eta$ and $C_p$. Both vary with temperature in a complicated way - both rise rapidly at certain temperatures and the sensitivity of the

solutions to the changes in the parameter increases, i.e., the eqs.(4.2)-(4.4) become ill-conditioned. For this reason, the temperature of the hot tube was maintained at ≤ 158°C such that predominantly the $S_\lambda$ liquid would be present (Fig. 2.2). Under this condition, the viscosity of liquid sulphur decreased monotonically from 12.64 mPa.s at the melting point of 112.8°C for orthorhombic sulphur to a minimum value of 6.63 mPa.s at 153°C. Beyond this temperature, viscosity increased to 11.9 mPa.s at 158°C. The imposed temperature limit reduced the degree of system sensitivity, i.e. the equations are not as wretchedly ill-conditioned as for a larger range of temperature. The heat capacity, however, increased from 0.993 kJ/kg K at the melting point to 1.86 kJ/kg K at 158°C. The latter is slightly beyond the peak of a cusp in the data.

The representative results of calculation are for a typical set of parameters listed in Table 5.1.

Table 5.1 Parameters for the Example Solutions

| Ste (or $T_w$, °C) | $\delta_o$ (m) | $r_o$ (m) |
|---|---|---|
| 0.77 ( 150 ) | $1.5(10^{-4})$ | $2.5(10^{-2})$ |

Results for the migration rate of the hot tube versus time elapsed is shown in Fig.5.1. At the very initial stage of the process, the migration rate $u_o$ increased rapidly as melting started. After a short induction period, the acceleration rate of the tube increased from zero, then reached a maximum value of $1.0(10^{-5})$ m/s$^2$ in the first ~10 seconds. The

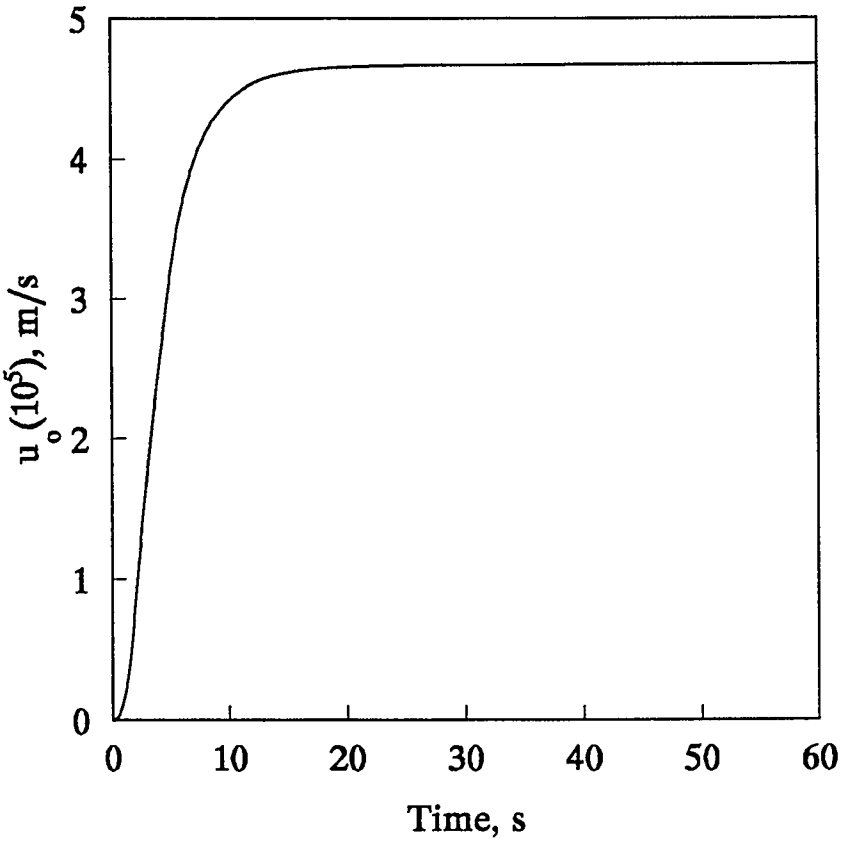


Fig. 5.1 Migration rate of the hot tube $u_o$ as function of time
$T_w$ = 150°C (Ste = 0.77), $\delta_o = 1.5(10^{-4})$m, $r_o = 2.5(10^{-2})$m

velocity attained a near plateau value of $4.7(10^{-5})$ m/s (or 16.8 cm/hr) after ~15 seconds. This $u_o$ value is in agreement with the field operating observation which is from 26 to 34 cm/hr when $T_w$ is set to 200°C.

In calculating the force required to maintain the minimum separation distance $\delta_o$ between the hot tube and the sulphur block, the term $M^* du_o^*/dt^*$ in eq.(4.12) was neglected because its maximum value is $\sim 1.01(10^5)$ while $F_e^*$ is in the range of $10^9 \sim 10^{10}$. A plot of the applied force as function of the melting time is shown in Fig. 5.2. $F_e^*$ of $10^9$ corresponds to an absolute force of 11.1 N for a 3 m long tube. The force increased rapidly in the early phases of the melting process. It then increased at a slower pace after ~60 seconds. The applied force serves two functions in this process: a) to keep a constant moving rate of the tube or to keep close contact of the hot tube with the solid surface, and b) to overcome the drag force due to the melt flow along the surface. Pressure forces are much larger than the viscous forces. The ratio is ~20. As the melting progressed and the melting interface deformed continuously, the close approach area between the melting surface and the hot tube increased with time. Both the pressure and drag forces increased and larger external forces were needed. Even though the migration rate of the heating tube reached a steady state in a short time, the applied force kept increasing. Nevertheless, the force increased only slowly with time after ~420 seconds.

Fig. 5.3(a) - (d) show the dimensionless temperature distributions across the film at various angles and after different elapsed time up to 300 seconds. The abscissa is the radial distance from the heating surface $(r - r_o)$ scaled by the local melt thickness $(r_i - r_o)$ or $\delta(\theta,t)$. The ordinate is the dimensionless temperature defined as

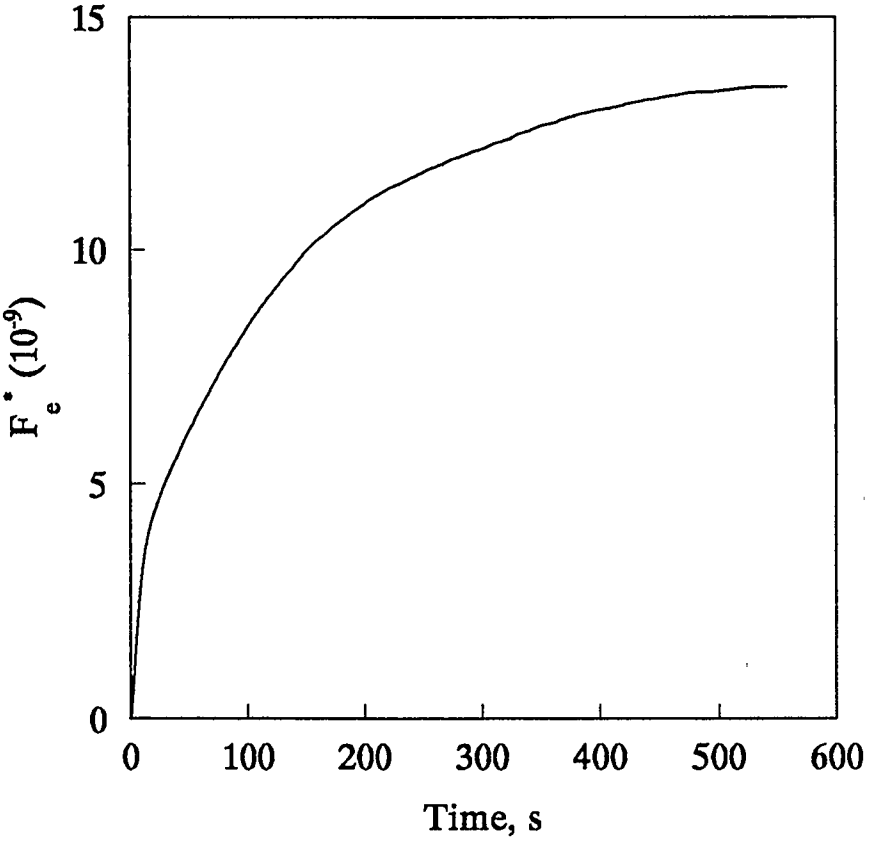


Fig. 5.2 External applied force $F_e^*$ as function of time
$T_w$ = 150°C (Ste = 0.77), $\delta_o = 1.5(10^{-4})$m, $r_o = 2.5(10^{-2})$m

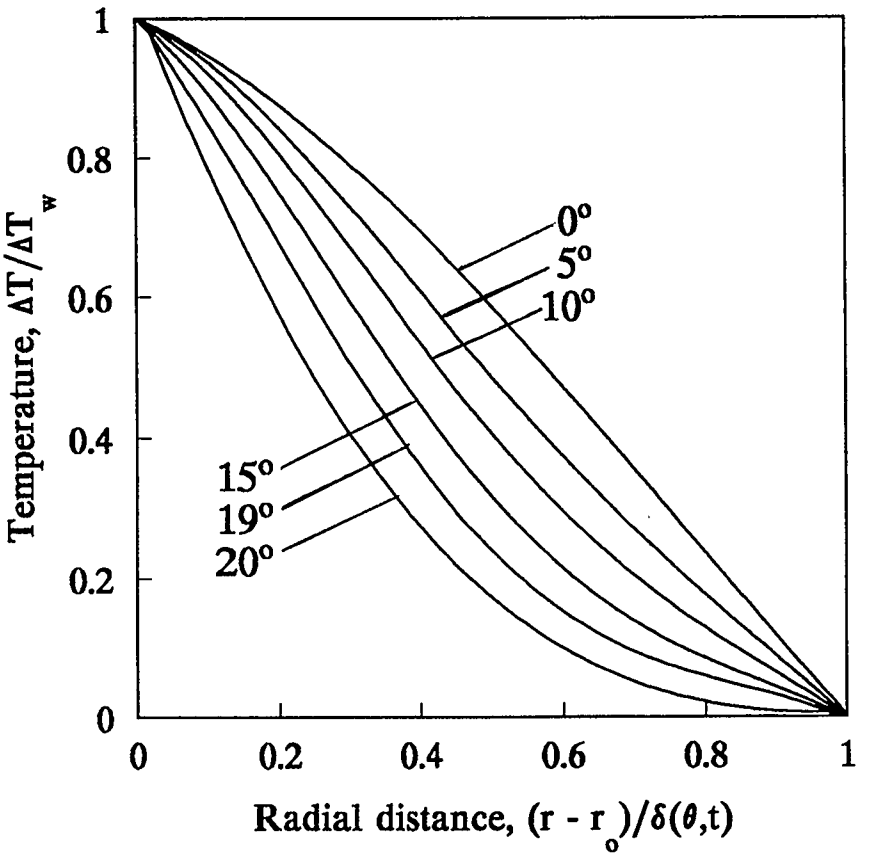


Fig. 5.3(a) Radial temperature profiles across the melt gap at different angles, t = 10 s
$T_w$ = 150°C (Ste = 0.77), $\delta_o = 1.5(10^{-4})$m, $r_o = 2.5(10^{-2})$m

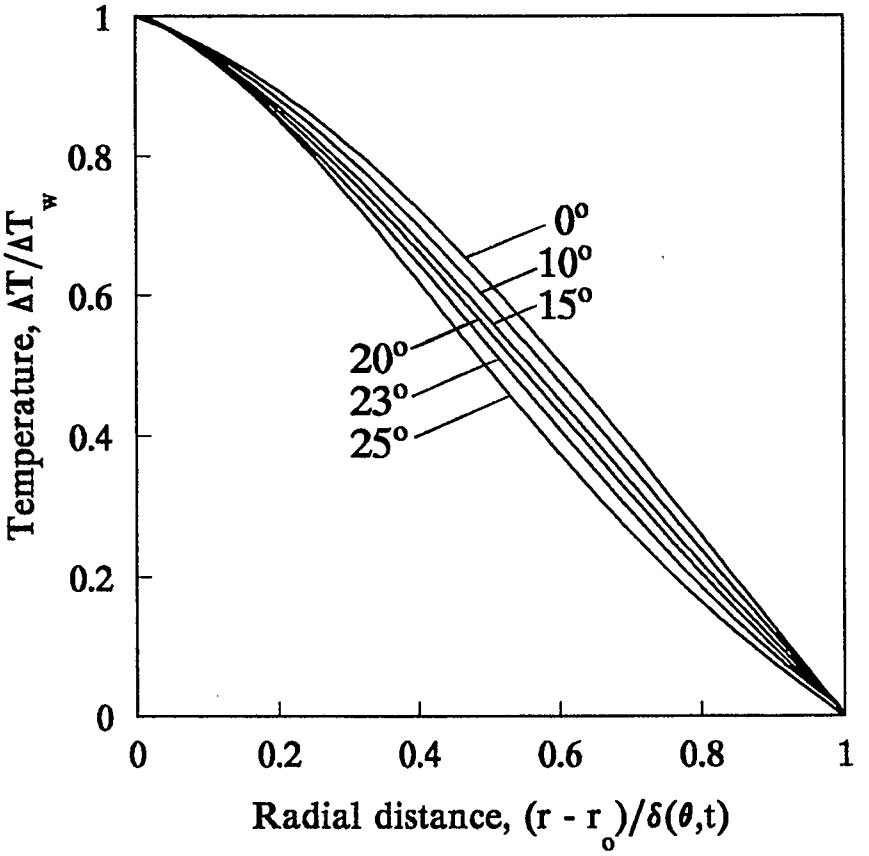


Fig. 5.3(b) Radial temperature profiles across the melt gap at different angles, t = 30 s
$T_w$ = 150°C (Ste = 0.77), $\delta_o = 1.5(10^{-4})$m, $r_o = 2.5(10^{-2})$m

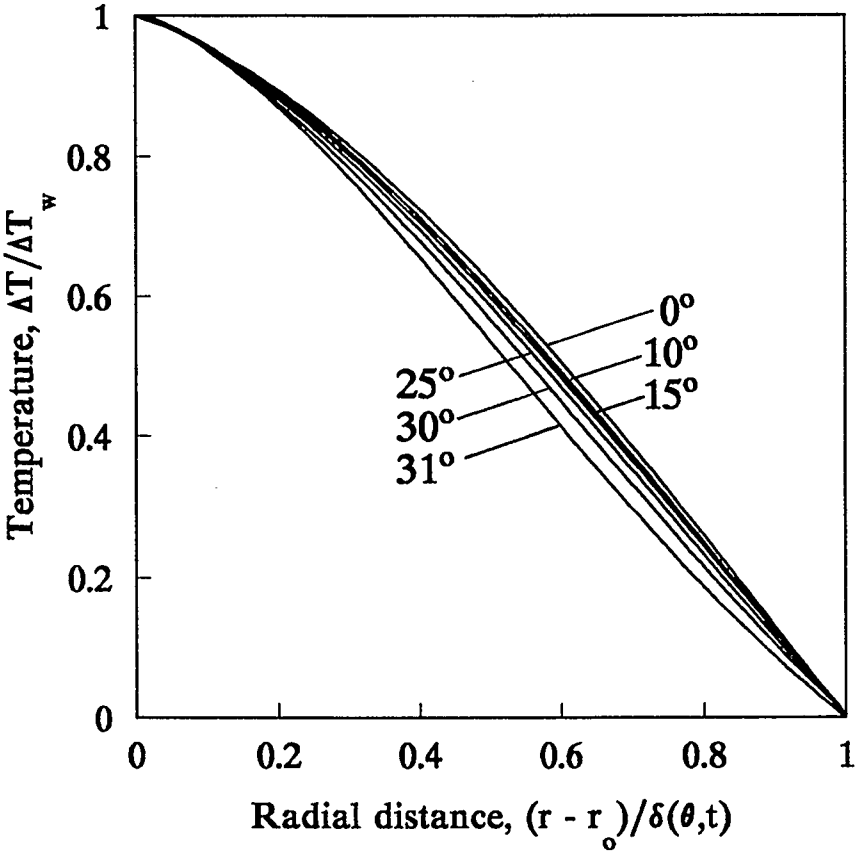


Fig. 5.3(c) Radial temperature profiles across the melt gap at different angles, t = 60 s
$T_w$ = 150°C (Ste = 0.77), $\delta_o = 1.5(10^{-4})$m, $r_o = 2.5(10^{-2})$m

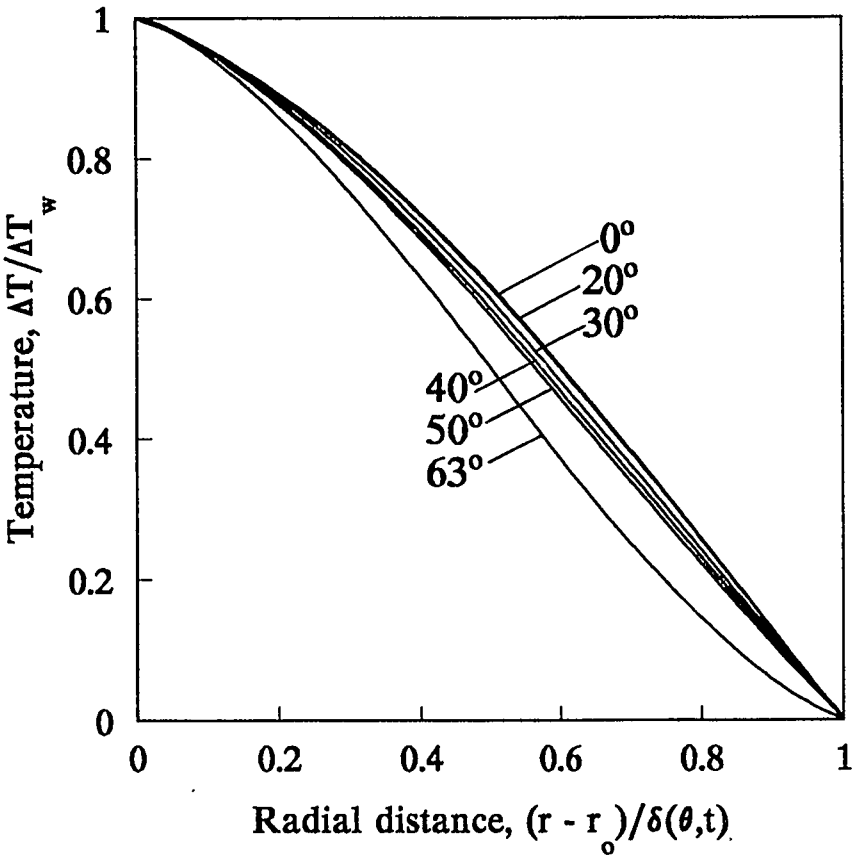


Fig. 5.3(d) Radial temperature profiles across the melt gap at different angles, t=300 s
$T_w$ = 150°C (Ste = 0.77), $\delta_o = 1.5(10^{-4})$m, $r_o = 2.5(10^{-2})$m

$$\frac{\Delta T}{\Delta T_w} = \frac{(T - T_m)}{(T_w - T_m)} \tag{5.1}$$

which varies from 0 at the melting interface to 1 at the heating surface. Temperature T is calculated from the dimensionless heat content, $h^*$:

$$T = \frac{[h^* \cdot (h_w - h_m)] + h_m}{C_p} \tag{5.2}$$

where

$$h_w = T_w \bullet C_{pw}; \qquad h_m = T_m \bullet C_{pm}$$

At the initial stage of the melting, the temperature shows strong non-linear profiles at different angles. The differences among the profiles are large. The melt became cooler as the angle θ increased from 0°. Radial heat transfer occurs over a longer path length at larger polar angles. After ~10 seconds, for example, the heat flux ratio at the melting interface and the hot surface, $q_l/q_s$, at angle 0° is **~0.4**, while at angle 20° ($\theta_c$), it is **~0.1**, as shown in Fig. 5.4. On the melting boundary, the ratio of the temperature gradients at angle 0° and at 20° is **~10**. The temperature profiles at different angles come closer to one another with time. The ratio of the temperature gradients at angle 0° and at 20° at the melting boundary approached **~1.05** after 60 seconds. The average heat flux ratio at the melting interface to the hot surface became **~.45** (Fig. 5.4), or about 45% the heat was utilized for the phase change.

The non-linearities of the temperature profiles are due to the changes in the curvature of the surfaces and the "injection" of the liquid from the melting interface.

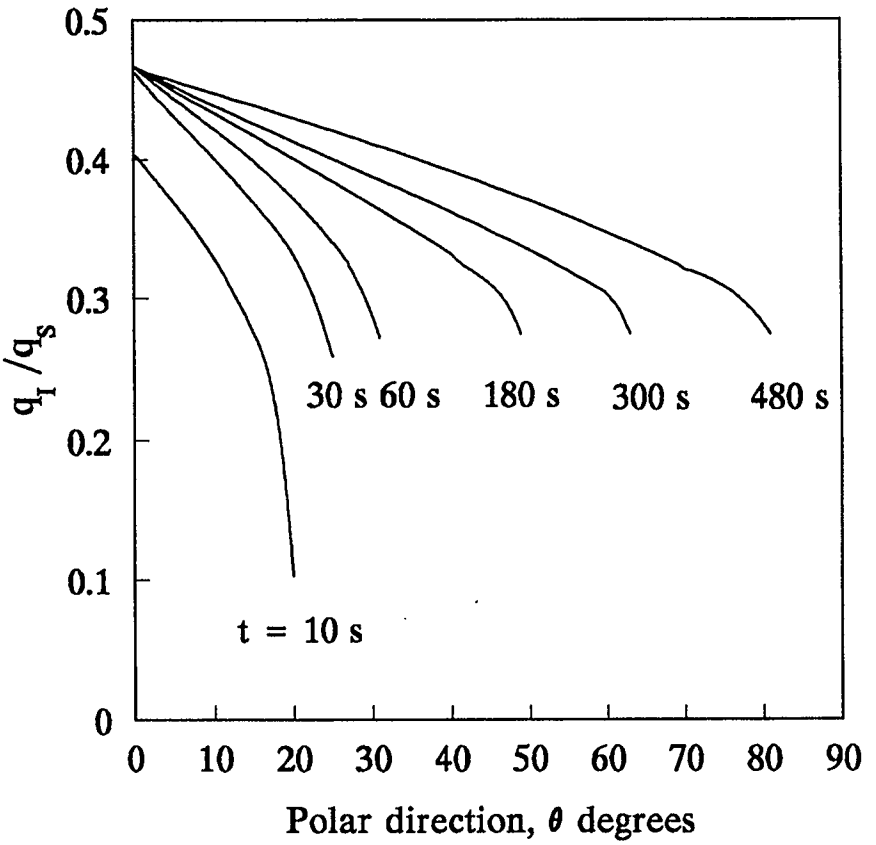


Fig. 5.4 Angular variation of heat flux ratio $q_l/q_s$ as function of melting times $T_w$ = 150°C (Ste = 0.77), $\delta_o = 1.5(10^{-4})$m, $r_o = 2.5(10^{-2})$m

Curvature of the melting surface, from eq. (4.9) is, at $\theta = 0$,

$$k_o = \frac{1}{(r_o + \delta_o)^2} \left.\frac{\partial^2 \delta}{\partial \theta^2}\right|_{\theta = 0} - \frac{1}{(r_o + \delta_o)} \tag{5.3}$$

Along $\theta = 0$, heat transfer is by conduction. When liquid injection from the melting surface into the gap is ignored along $\theta = 0$, the radial temperature profile, may be estimated through the use of the method of heat sources and sinks (Eckert and Drake, 1987):

$$\frac{T - T_m}{T_w - T_m} = \ln\left[\frac{(N/r^+) + \sqrt{(N/r^+)^2 - 1}}{k_o N_2 + \sqrt{(k_o N_2)^2 - 1}}\right] \Bigg/ \ln\left[\frac{(N_1/r_o) + \sqrt{(N_1/r_o)^2 - 1}}{k_o N_2 + \sqrt{(k_o N_2)^2 - 1}}\right] \tag{5.4}$$

where

$$N = \left[k_o^{-2} - r^{+2} - \xi^2\right]/2\xi;\ N_1 = \left[k_o^{-2} - r_o^2 - \varepsilon^2\right]/2\varepsilon;$$

$$N_2 = \left[k_o^{-2} - r_o^2 + \varepsilon^2\right]/2\varepsilon = \left[k_o^{-2} - r^{+2} + \xi^2\right]/2\xi \tag{5.5}$$

$$\varepsilon = k_o^{-1} - r_o - \delta_o\ ;\quad \xi = k_o^{-1} - r^+ - \delta_o + z$$

Curvature at $\theta = 0$ would be a little lower than the theoretical curvature of the isothermal surface if heat transfer was strictly by conduction.

This profile differs from that obtained when heat is conducted between the

surfaces of two concentric cylinders. The latter is given as:

$$\frac{T - T_m}{T_w - T_m} = \frac{\ln ( r / r_o )}{\ln ( r_i / r_o )} \qquad (5.6)$$

As $r_i$ approaches $r_o$, the right side of eq.(5.6) becomes $(r - r_o)/(r_i - r_o)$.

In the numerical calculations shown in Figs. 5.3(a-d), the profile along $\theta = 0$ changed only significantly at the early times, < ~30 seconds, when $k_o$ changed from 0 to $1/r_o$. Thereafter it was nearly invariant. The analytical solution from eq.(5.4) is compared with the limiting profile in Fig.5.5. The temperature obtained from eq.(5.4) is almost linear and the melt is predicted to be cooler at the same radial position as compared with the numerical results. The injection of melt into the gap is suggested to account for the differences. The maximum difference between the two temperatures is ~30%.

The azimuthal velocities at different angular positions are plotted in Fig.5.6 (a) to (d) at different melting times (10, 60, 180 and 300 seconds). The abscissa is the dimensionless distance from the hot surface as defined for Fig. 5.3 while the ordinate is the dimensionless velocity $u/u_o$. The velocity of approach of the sulphur block to the heating surface, $u_o$, is a function of time as presented in Fig. 5.1. At a given instant, the maximum of the normalized velocity profiles initially increased as the polar angle $\theta$ increased. The maximum velocity in the domain is at an angle $\theta < \theta_c$. It is important to note that the volume rate of the melt flow increased monotonically with $\theta$ at each instant and the normalization of velocity with $u_o$ (which varied with time) gives a wrong impression at a first glance at these curves. The highest velocity in the gap is located at a point within the domain and its value and position changed with time. Peak velocities

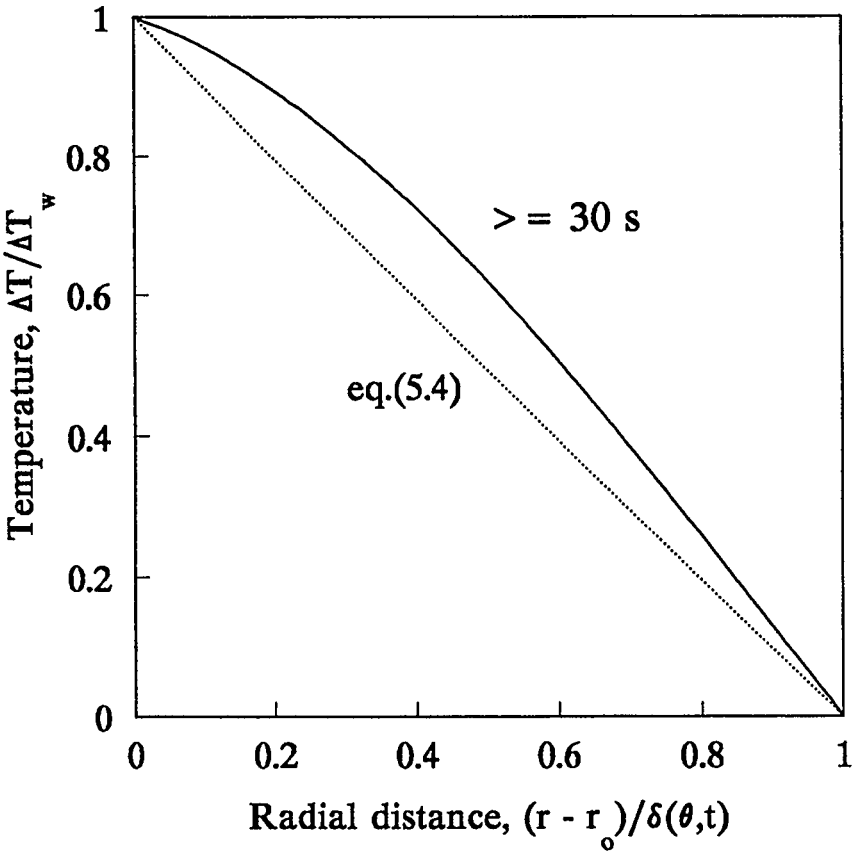


Fig. 5.5 Comparison of radial temperature profiles at $\theta = 0$, from simulation and eq.(5.4), $T_w = 150°C$ (Ste = 0.77), $\delta_o = 1.5(10^{-4})$m, $r_o = 2.5(10^{-2})$m

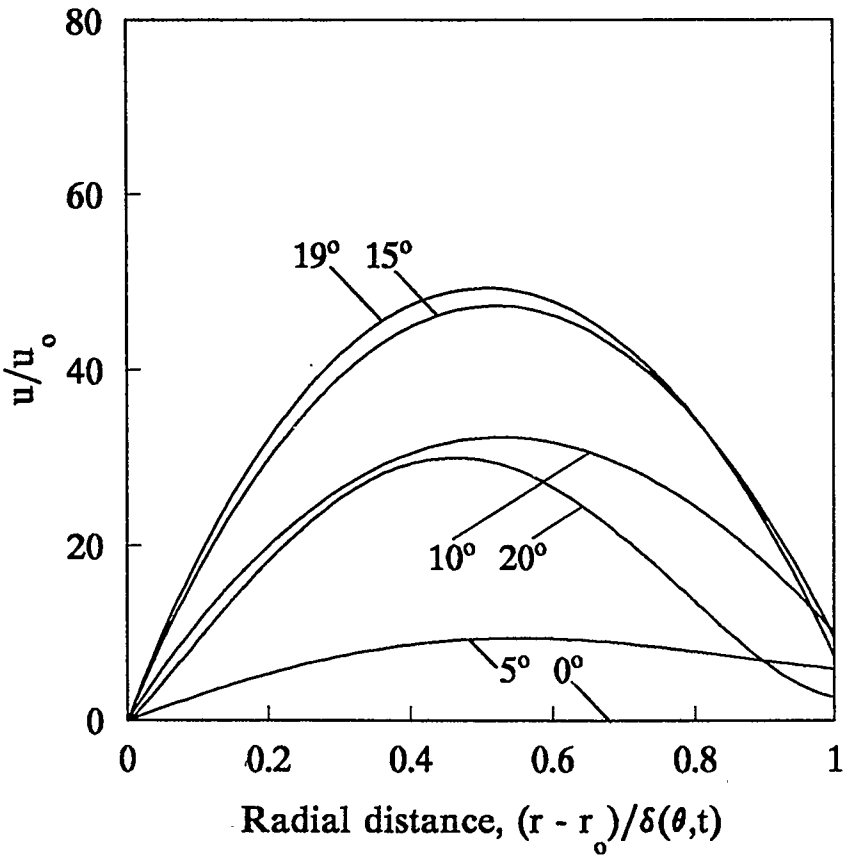


Fig. 5.6(a) Tangential velocity profiles across the melt gap at different angles, t=10 s
$T_w$ = 150°C (Ste = 0.77), $\delta_o = 1.5(10^{-4})$m, $r_o = 2.5(10^{-2})$m

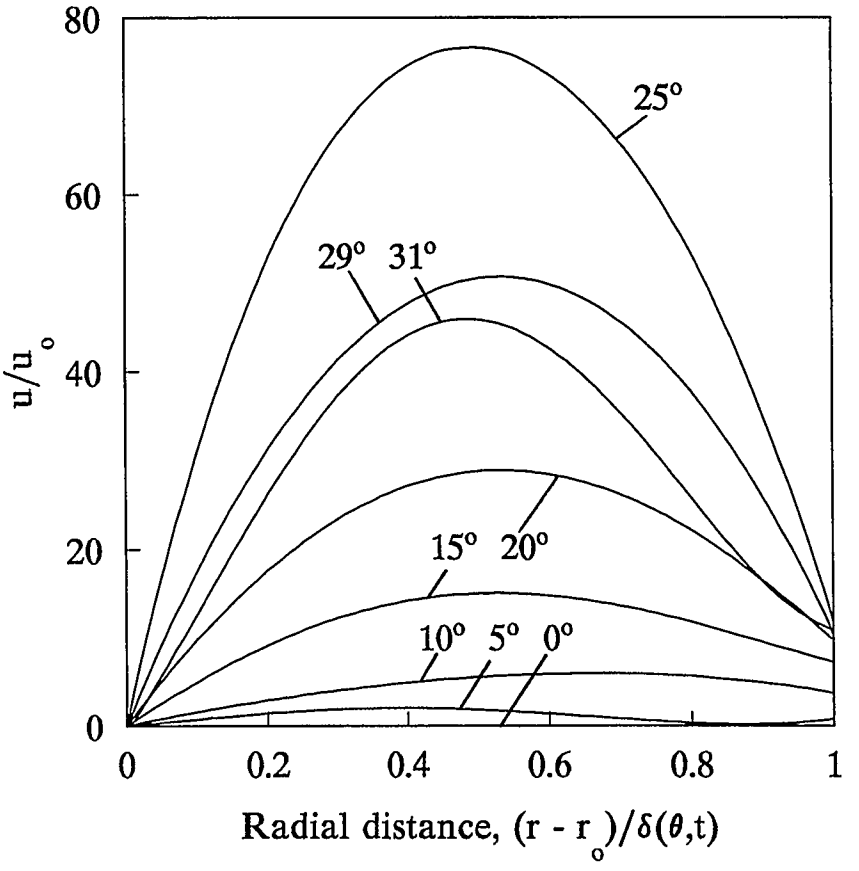


Fig. 5.6(b) Tangential velocity profiles across the melt gap at different angles, t=60 s
$T_w$ = 150°C (Ste = 0.77), $\delta_o = 1.5(10^{-4})$m, $r_o = 2.5(10^{-2})$m

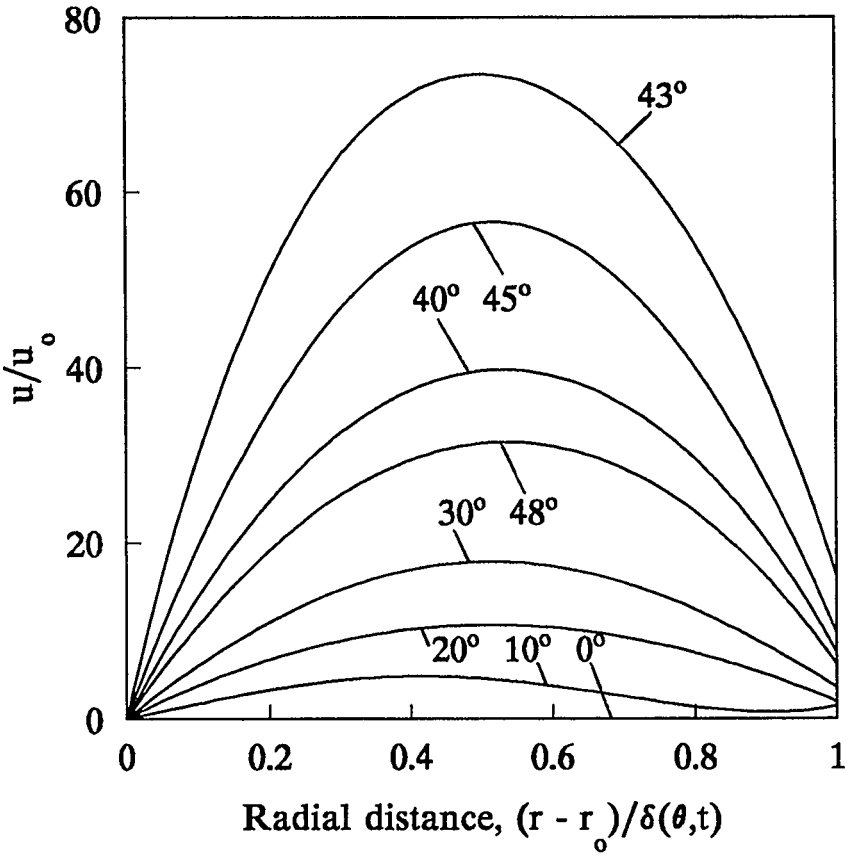


Fig. 5.6(c) Tangential velocity profiles across the melt gap at different angles, t=180 s
$T_w$ = 150°C (Ste = 0.77), $\delta_o = 1.5(10^{-4})$m, $r_o = 2.5(10^{-2})$m

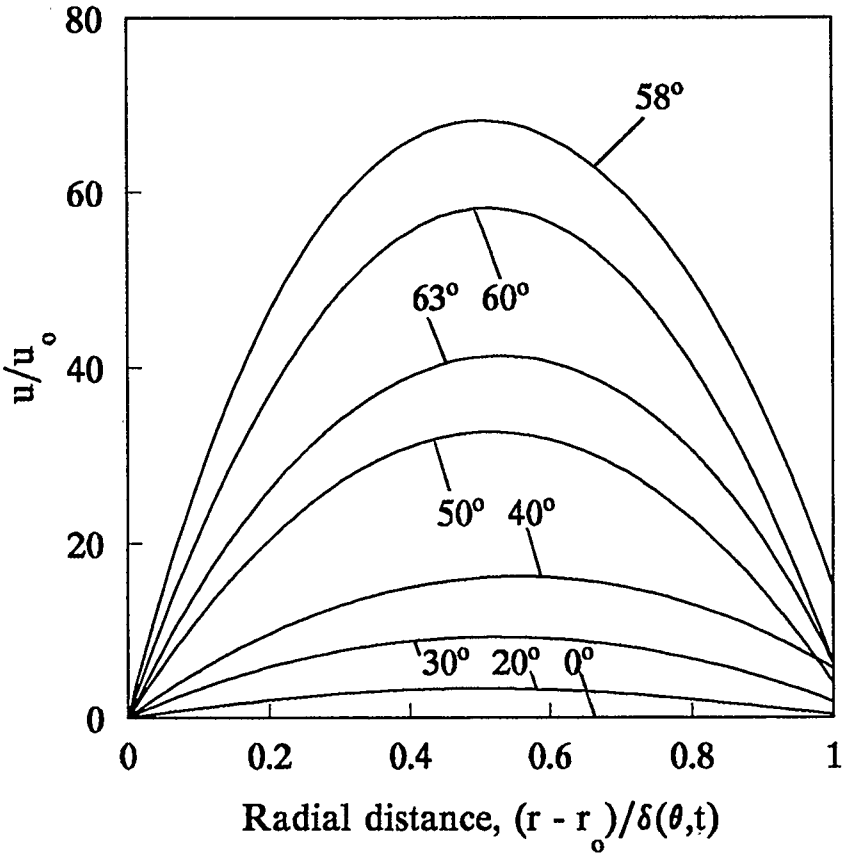


Fig. 5.6(d) Tangential velocity profiles across the melt gap at different angles, t=300 s
$T_w$ = 150°C (Ste = 0.77), $\delta_o = 1.5(10^{-4})$m, $r_o = 2.5(10^{-2})$m

are given in Table 5.2 at the radial distances where they are located. The profiles are not similar since the curves in each plot can not be collapsed into one. Non-zero velocities at $(r - r_o)/\delta = 1$, reflect two things - first, the surface is being deformed and moving at a velocity different from the approach velocity of the block to the hot surface. Secondly, each location on the surface is curling around the tube at different rates.

Table 5.2 The local maximum velocity values at different melting times

$T_w = 150°C$, $u_o = 4.4(10^{-5})$ m/s at t = 10 s, and $4.7(10^{-5})$ m/s when $t \geq 30$ s

| t (s) | $\theta°$ ($\theta_c°$) | $(r-r_o)/\delta$ | Maximum $u(10^{-3})$ (m/s) |
|---|---|---|---|
| 10 | 19 ( 20 ) | .475 | 2.17 |
| 30 | 22 ( 25 ) | .465 | 3.46 |
| 60 | 25 ( 31 ) | .479 | 3.58 |
| 90 | 29 ( 36 ) | .477 | 3.55 |
| 120 | 34 ( 41 ) | .469 | 3.50 |
| 150 | 39 ( 45 ) | .479 | 3.48 |
| 180 | 43 ( 48 ) | .479 | 3.44 |
| 210 | 48 ( 52 ) | .500 | 3.40 |
| 240 | 51 ( 56 ) | .487 | 3.30 |
| 270 | 54 ( 59 ) | .494 | 3.25 |
| 300 | 58 ( 63 ) | .472 | 3.18 |
| 360 | 63 ( 69 ) | .467 | 3.00 |
| 420 | 67 ( 76 ) | .448 | 2.51 |

The velocity profiles show some interesting patterns. In Fig. 5.6(a), the maximum velocities at different angles are located at varying dimensionless radial distances which are progressively (as $\theta$ varies) closer to the heating surface at each instant. In Fig.5.6(b), the profile at $\theta = 5°$ shows almost zero velocity at a radial position of ~0.88 and the local shear stress vanishes. This suggests that the flow could become unstable and flow structures like rolls (cells) could develop. A similar minimum in the velocity pattern appears in Fig. 5.6(c) at $\theta = 10°$. Since such a profile is not seen at larger times in Fig. 5.6(d), any unstable structures may be transient. Hydrodynamic instability has not been examined in this study.

The dimensionless bulk-mean temperature of the melt is defined as $\Delta T_{bm}/\Delta T_w$. The numerator can be evaluated from:

$$\Delta T_{bm} = \frac{\int_{r_o}^{r_o+\delta} u\,(T - T_m)\,C_p\,r\,dr}{\int_{r_o}^{r_o+\delta} u\,C_p\,r\,dr} \qquad (5.7)$$

Fig.5.7 presents the angular variation of the dimensionless bulk-mean temperature at different times. At the initial stage of the melting ($t < 30$ s), the bulk-mean temperature of the melt decreased significantly along the melt channel. The liquid was initially at the melting point $T_m$ and time was required for the melt to gain sensible heat through conduction. At early times, the volume of melt per sector angle between 0 to $\theta_c$ is the largest. Furthermore, temperatures at $\theta \sim 0°$ are rapidly elevated because $\delta$ is minimum. The discharged melt, therefore, has a disproportionate amount of liquid initially present at the temperature of $T_m$. With increasing time, more of the melting surface approaches

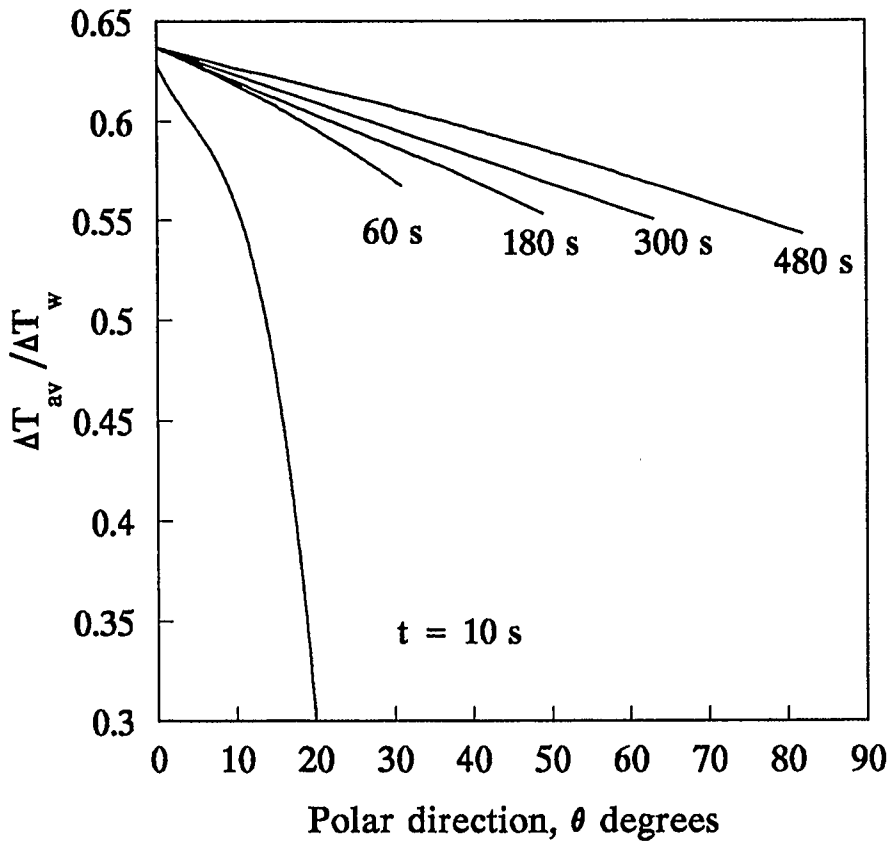


Fig. 5.7 Angular variation of bulk mean temperature as function of melting times $T_w$ = 150°C (Ste = 0.77), $\delta_o = 1.5(10^{-4})$m, $r_o = 2.5(10^{-2})$m

the hot surface. This encourages a more rapid heat accumulation in the gap and the fraction of sensible heat in the melt to latent heat used for the phase change increases. The bulk-mean temperature declined at a slower rate at longer times along the azimuthal direction.

With the production of melt at the interface, there is a radial velocity component. Fig.5.8 shows the profiles at 60 seconds. The radial velocity components are small compared to the azimuthal values and they decayed rapidly away from the interface. The values became low and convergent on one line within 0.15 of the gap width from the melting boundary. Liquid produced is quickly re-directed in the azimuthal direction.

Changes in the gap width, $\delta(\theta,t)$, are illustrated in Fig.5.9(a). The locations for $\theta_c$ values are noted in each curve. The curves are described by a bounding envelope from which each curve diverged at increasing elapsed time. The implication is that as time progresses, larger sectors of the melting surface become fixed in shape. For example, at 240 seconds, only the surface region within the sector $40° < \theta < 60°$ exhibits changes in the gap width. The development of the melting surface contour is illustrated in Fig.5.9(b). The gap width has been enlarged 100 times. It is obvious that only portion of the surface near $\theta_c$ is modified progressively. After 540 seconds, the critical sector angle had reached 81° under the set of parameter used.

Changes in the curvature of the melting surface with time and position are presented in Fig. 5.10. The curves show the instantaneous variations with polar angle up to 420 seconds from the start of melting. As was earlier noted, near $\theta = 0$, a fixed curvature was rapidly achieved. Thereafter, the general pattern shows a slight decrease

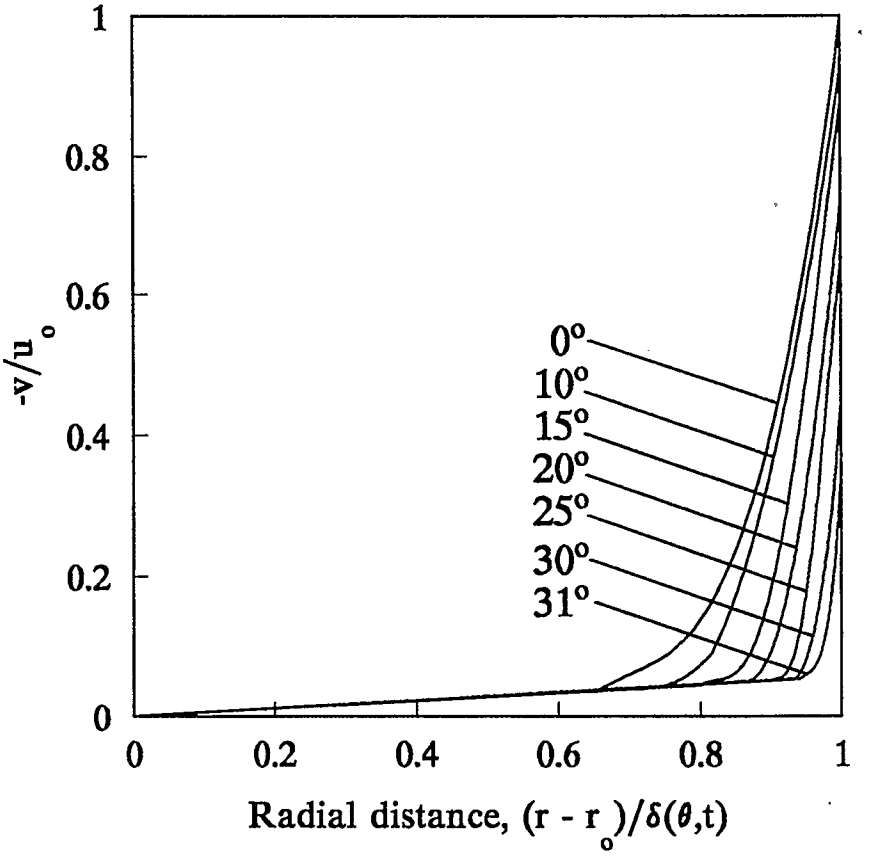


Fig. 5.8 Radial velocity profiles across the melt gap at different angles, t = 60 s
$T_w$ = 150°C (Ste = 0.77), $\delta_o = 1.5(10^{-4})$m, $r_o = 2.5(10^{-2})$m

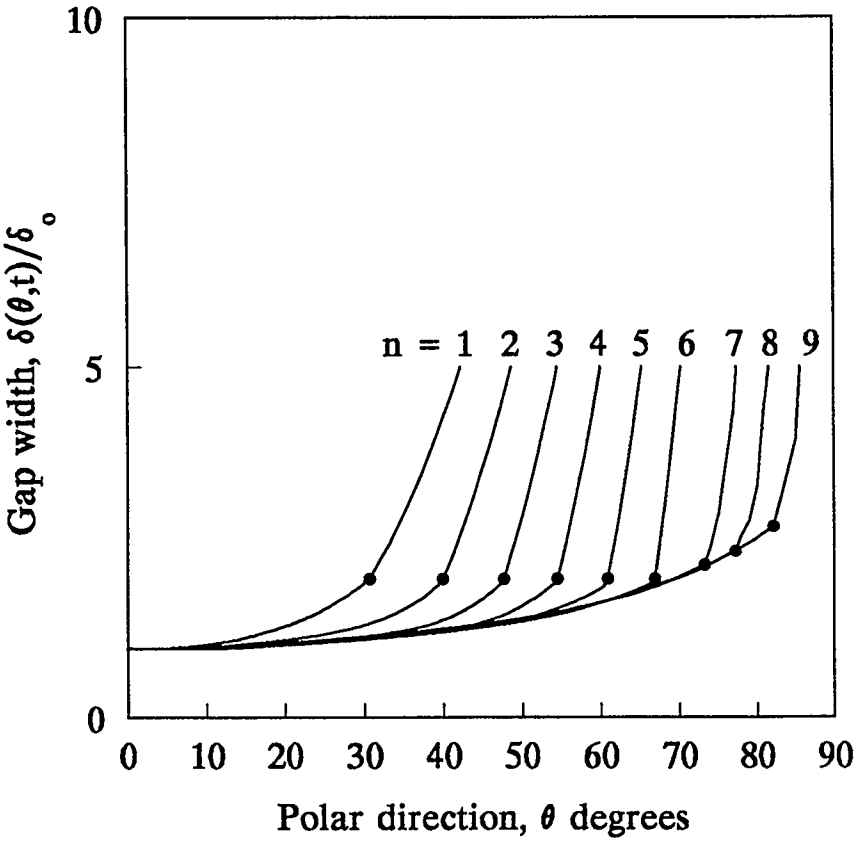


Fig. 5.9(a) Gap width development as function of time ( time = n×60 s)
$T_w$ = 150°C (Ste = 0.77), $\delta_o = 1.5(10^{-4})$m, $r_o = 2.5(10^{-2})$m

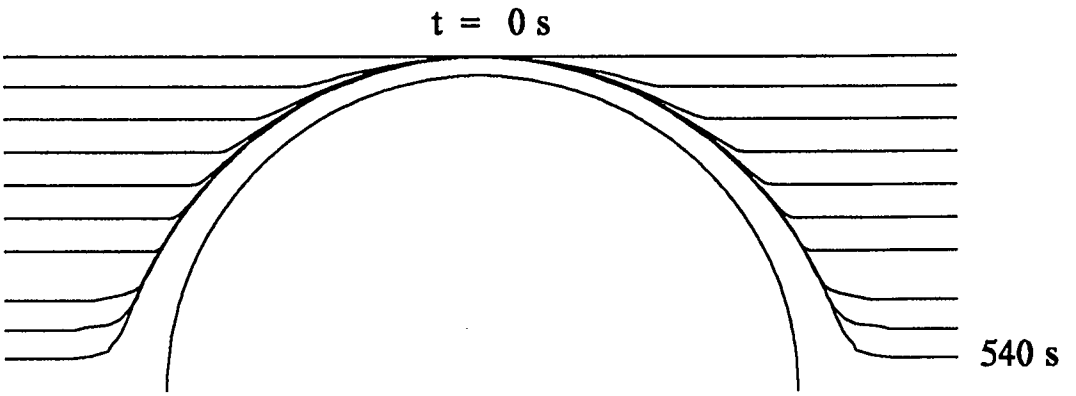


Fig. 5.9(b) Interface development with melting time
time interval between two contours is 60 seconds
$T_w$ = 150°C (Ste = 0.77), $\delta_o$ = 1.5($10^{-4}$)m, $r_o$ = 2.5($10^{-2}$)m

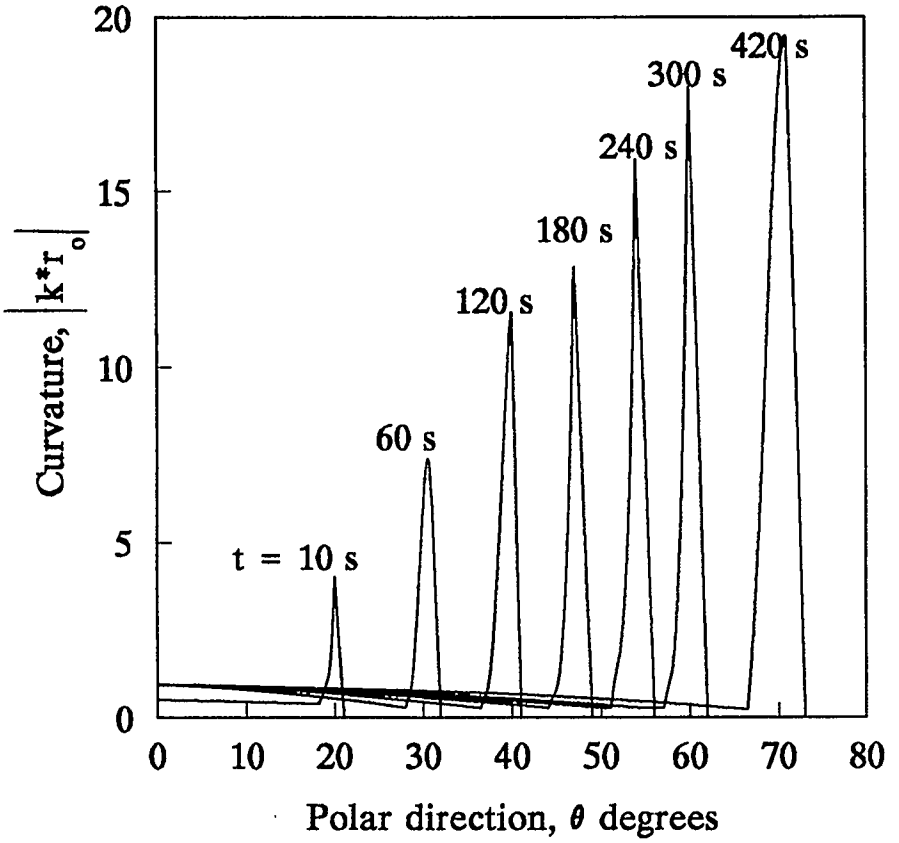


Fig. 5.10 Curvature of $G(r_i,\theta,t)$ as function of melting time
$T_w$ = 150°C (Ste = 0.77), $\delta_o = 1.5(10^{-4})$m, $r_o = 2.5(10^{-2})$m

in curvature form $\theta = 0$ to a minimum close to the melt discharge angle. The curvature decreases sharply and becomes negative at the edge of the melting front. The angles subtended from the axis of the hot tube are $\theta_c$ at the peaks of the curves in the figure in which absolute values of curvature are plotted.

In the Fig. 5.11 (a and b), the changes in $\theta_c$ with time are presented. This reflects the rate at which the sulphur block wraps around the hot tube. The plots suggest that there are two regimes. Within less than 1 second, the melting surface was rapidly indented such that an angle of ~30° was subtended at the hot surface in close contact with the sulphur. Initially, contact was along a line. In this interval, the volume of melt produced is, according to the sketch below,

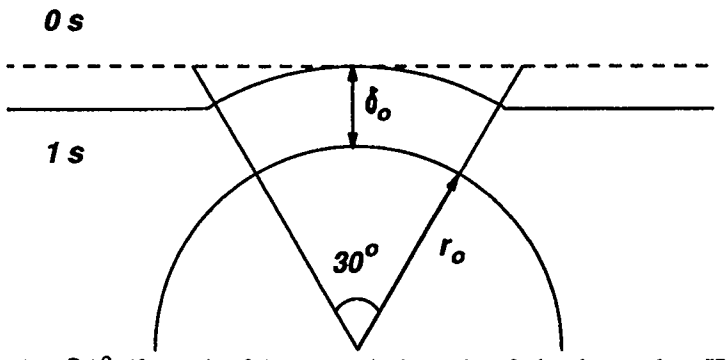


less than $1/2\ (r_o+\delta_o)^2\ (\theta_c - \sin\theta_c)$ per unit length of the hot tube. With $r_o = 2.5(10^{-2})$ m, $\delta_o = 1.5(10^{-4})$ m and $\theta_c = 15°$, the volume of the melt is $\sim 3.8(10^{-3})$ times the volume of the hot tube. This means only a minute quantity of melt would have been expelled with the conformational change. The heat transferred in the interval therefore goes primarily into phase change and $\theta_c$ increases rapidly. It is suggested that when $\theta_c$ reaches ~15°, the curvature in the region of $\theta = 0$ might have stopped changing, i.e. reached its upper limit

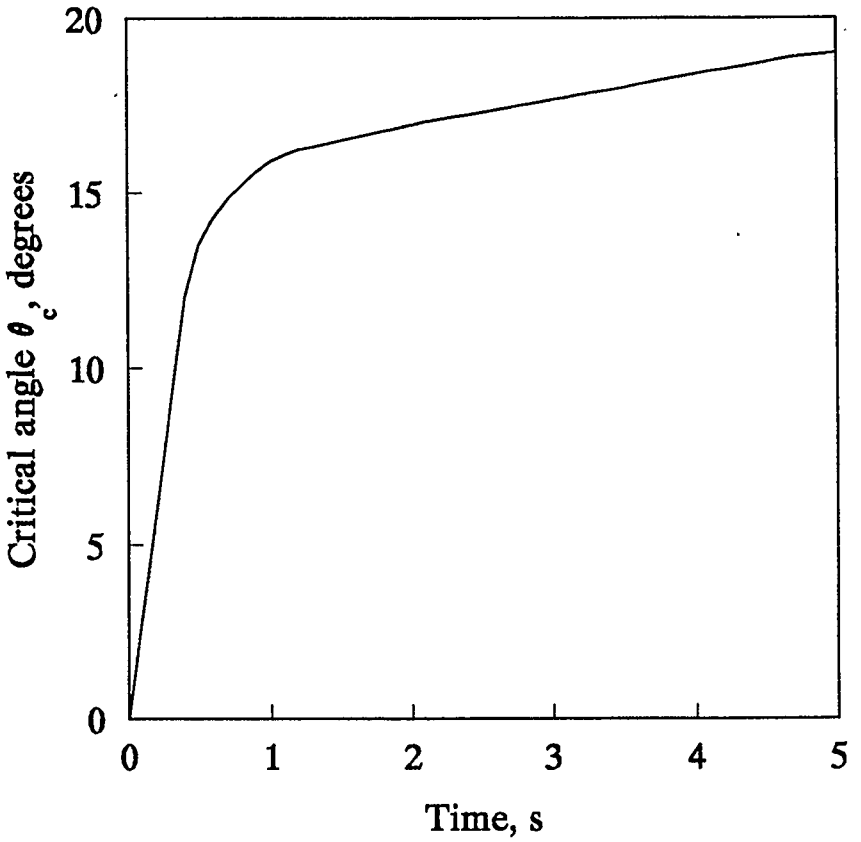


Fig. 5.11(a) Critical sector angle $\theta_c$ as function of melting time at $t \leq 5$ s
$T_w = 150°C$ (Ste = 0.77), $\delta_o = 1.5(10^{-4})$m, $r_o = 2.5(10^{-2})$m

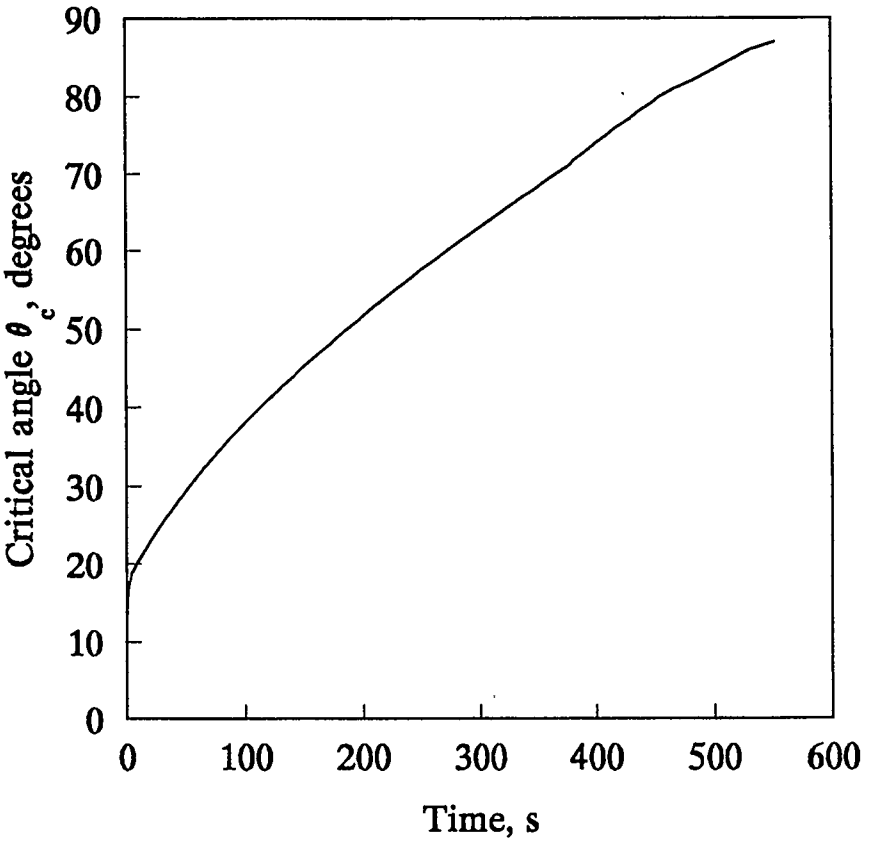


Fig. 5.11(b) Critical sector angle $\theta_c$ as function of melting time
$T_w$ = 150°C (Ste = 0.77), $\delta_o = 1.5(10^{-4})$m, $r_o = 2.5(10^{-2})$m

and thus any further liquid produced in this zone of closest approach needs to be expelled to maintain a constant $\delta_o$. This initiates the motion of the melt and subsequent developments. In the second regime, melt is expelled and a fraction of the heat transferred by the hot tube is carried off as sensible heat not utilized for melting. The corresponding rate of change of $\theta_c$ thus decreases. The plot in Fig. 5.11(b) suggests that, gradually, a higher fraction of the heat supplied per area of contact, is convected as sensible heat with the melt.

## 5.2 Parametric Results

The effects of varying the principal parameters on the melting process are presented and discussed. These parameters are as follows: surface temperature of the hot tube, the gap width at $\theta = 0°$, $\delta_o$, and the radius of the tube $r_o$. Surface temperatures are set at 120, 130, 140 and 150°C which correspond to Ste values of 0.15, 0.36, 0.56, 0.77 respectively. The $\delta_o$ values are chosen to be $1.5(10^{-4})$, $2.0(10^{-4})$, $2.5(10^{-4})$ m and the radii of the tube are $1.25(10^{-2})$, $2.5(10^{-2})$, $5.0(10^{-2})$ m respectively. In the following discussion, just one of these parameters is changed while others are kept constant. The typical values of parameters are: 130°C for the steam temperature, $1.5(10^{-4})$ m for $\delta_o$ and $2.5(10^{-2})$ m for the tube radius.

### 5.2.1 *The Effect of Heating Temperature $T_w$*

The tube temperature has a significant influence on the melting process as shown from the theoretical analysis in chapter 3. The effects of steam temperature on the

migration rates are shown in Fig. 5.12. The migration rates varied significantly with time and Stefan numbers. The velocities first increased sharply and then attained a near plateau values after ~15 seconds. The steady state values were higher as the driving potential $\Delta T_w$ (or $T_w - T_m$) increased. Asymptotic velocities ($u_o$) of $6.8(10^{-6})$, $1.8(10^{-5})$, $3.0(10^{-5})$, $4.7(10^{-5})$ m/s ( or 2.4, 6.5, 10.6, 15.7 cm/hr ) were obtained when the hot tube was maintained at 120, 130, 140 and 150°C respectively. At early times, the rates of increase of $u_o$ to the maximum is higher as $\Delta T_w$ is increased.

In Fig. 5.13, the forces required to maintain the minimum separation between the two surfaces are presented. At higher $\Delta T_w$, more melt is produced, the forces required to expel the melt from the gap are elevated. The results reflect the combination of an increase in the area of close contact with time and increasingly larger viscous resistance.

The development of $\delta(\theta,t)$ at different times is presented in Fig. 5.14 for $T_w$ values of 120 and 150°C respectively. The deformation rate of the melting interface is much faster while a higher driving potential ($T_w - T_m$) is imposed. It requires, for example, ~300 s to develop a similar interface shape from the same starting planar surface when $T_w$ = 120°C, compared to ~60 s when $T_w$ = 150°C. The developments of the melting interface contours are shown in Fig. 5.15(a) to (c) for $T_w$ values of 120, 130 and 140°C respectively. The gap widths have been enlarged 100 times in the plots which show a faster evolution of the surfaces at higher Stefan numbers.

The same information is presented more quantitatively in the form of $\theta_c$ in Fig. 5.16. The plot illustrates the same phenomena as discussed in the previous subsection. That is, critical angles increased rapidly within ~1 second and thereafter the rates of

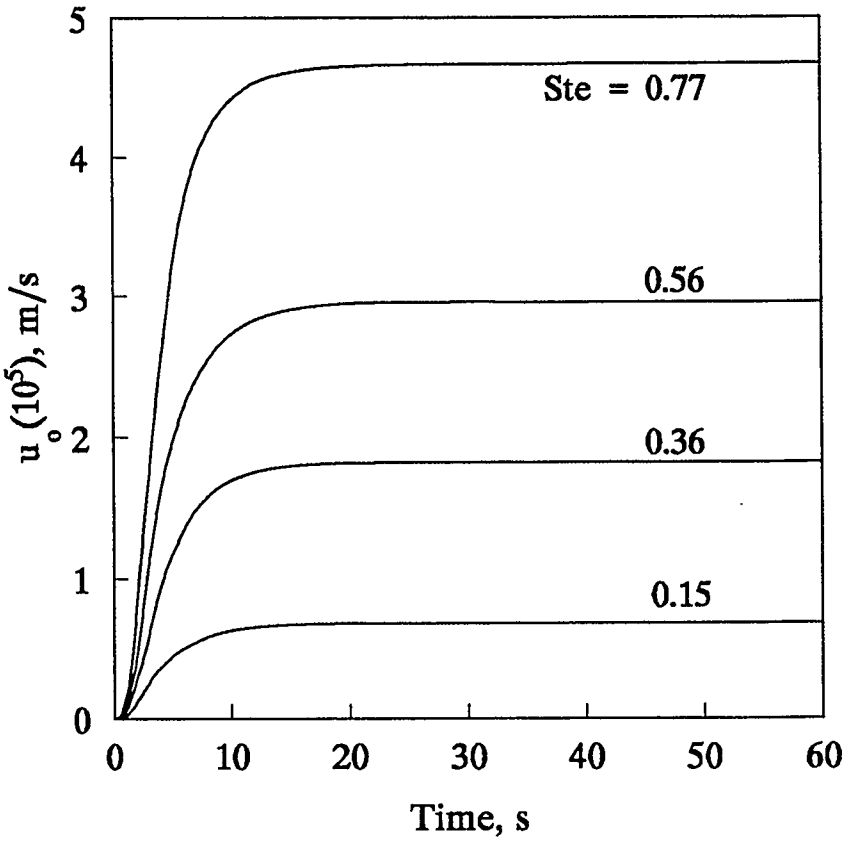


Fig. 5.12 Migration rate of the hot tube $u_o$ as function of Ste number
$\delta_o = 1.5(10^{-4})$m, $r_o = 2.5(10^{-2})$m

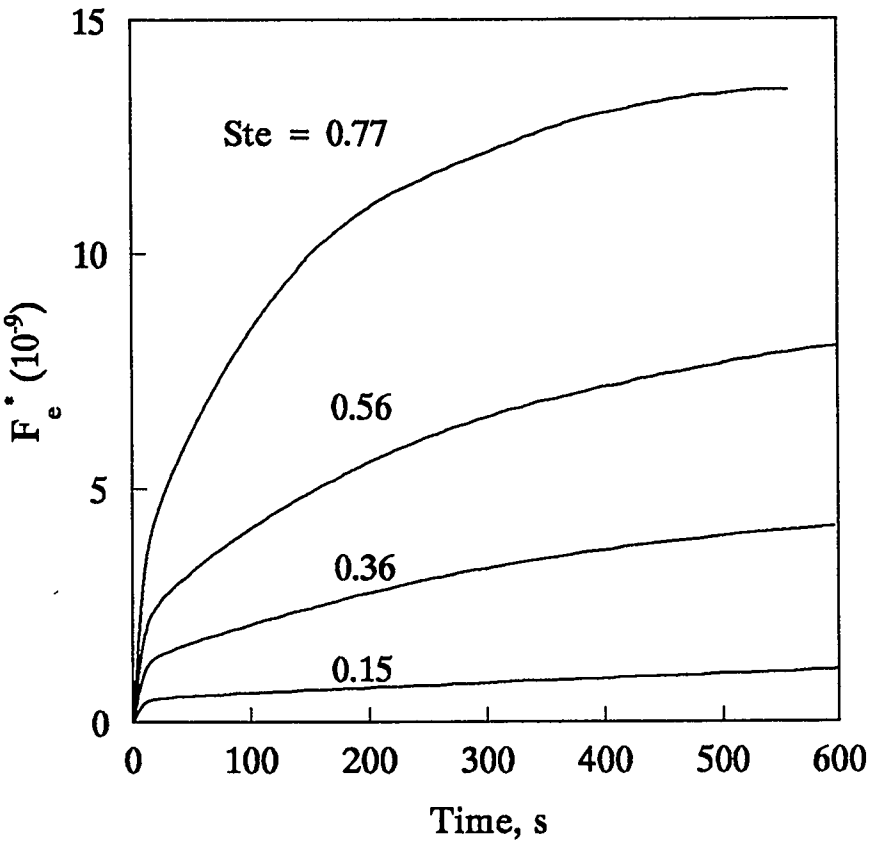


Fig. 5.13 Comparison of the applied force as function of Ste number, $\delta_o = 1.5(10^{-4})$m, $r_o = 2.5(10^{-2})$m

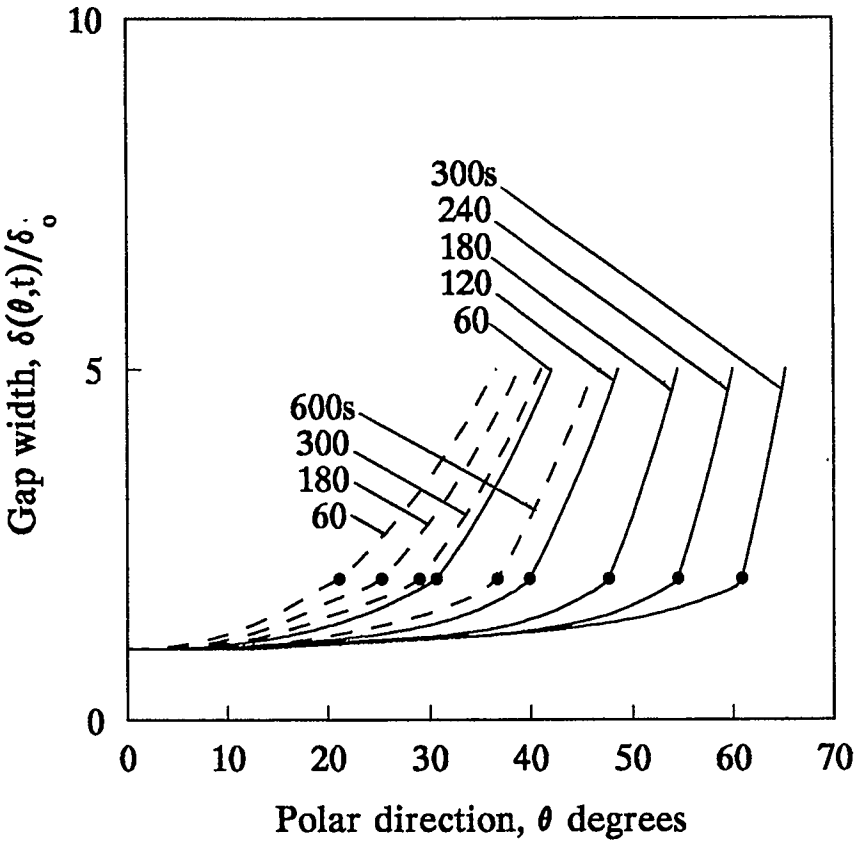


Fig. 5.14 Comparison of gap width development as function of Ste number, $T_w$ = 150°C (Ste = 0.77)(-) and 120°C(Ste = 0.15)(---), $\delta_o = 1.5(10^{-4})$m, $r_o = 2.5(10^{-2})$m

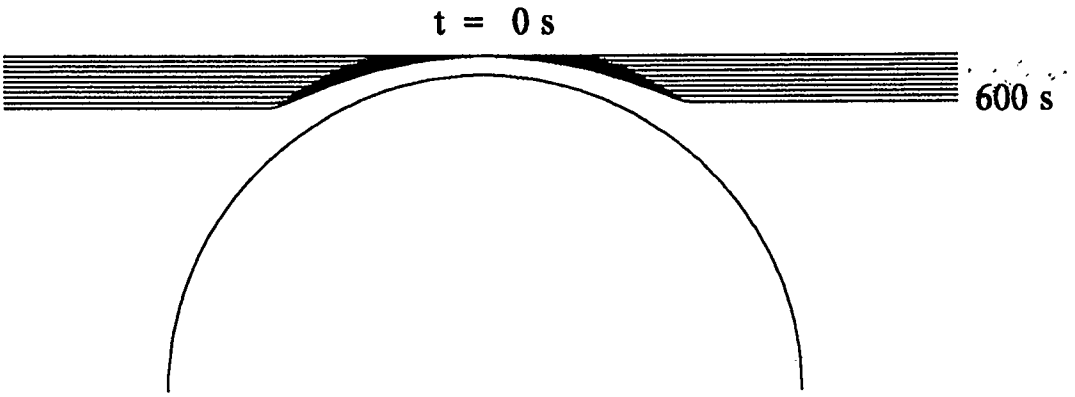


Fig. 5.15(a) Interface shape development as function of angle position;
gap width was enlarged 100 times;
time interval between two contours is 60 seconds
$T_w$ = 120°C (Ste = 0.15), $\delta_o = 1.5(10^{-4})$m, $r_o = 2.5(10^{-2})$m

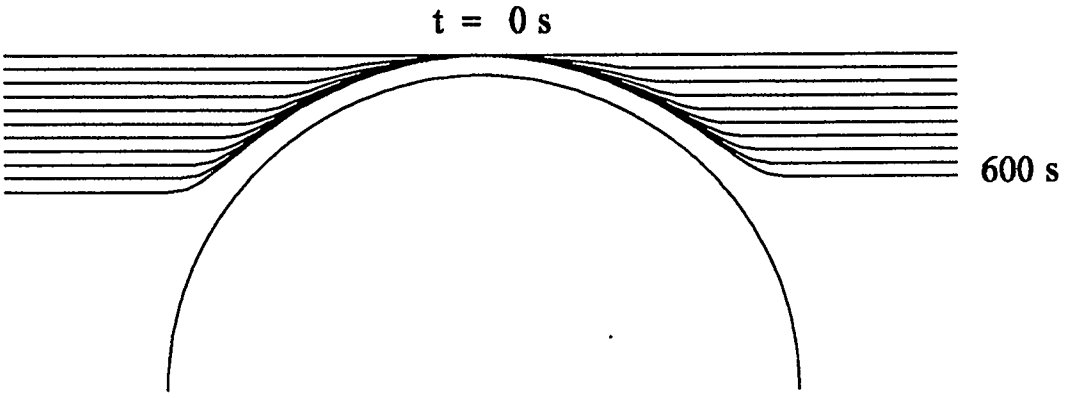


Fig. 5.15(b) Interface shape development as function of angle position;
gap width was enlarged 100 times;
time interval between two contours is 60 seconds
$T_w$ = 130°C (Ste = 0.36), $\delta_o = 1.5(10^{-4})$m, $r_o = 2.5(10^{-2})$m

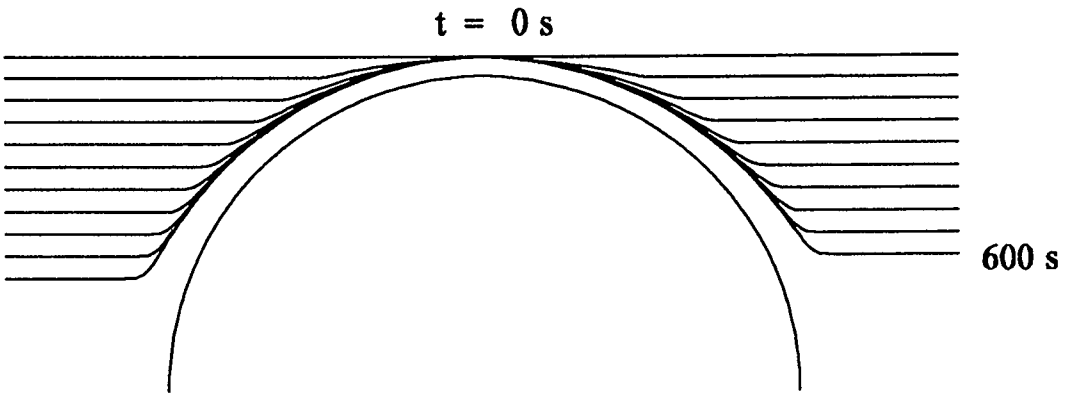


Fig. 5.15(c) Interface shape development as function of angle position,;
gap width was enlarged 100 times;
time interval between two contours is 60 seconds
$T_w$ = 140°C (Ste = 0.56), $\delta_o$ = 1.5($10^{-4}$)m, $r_o$ = 2.5($10^{-2}$)m

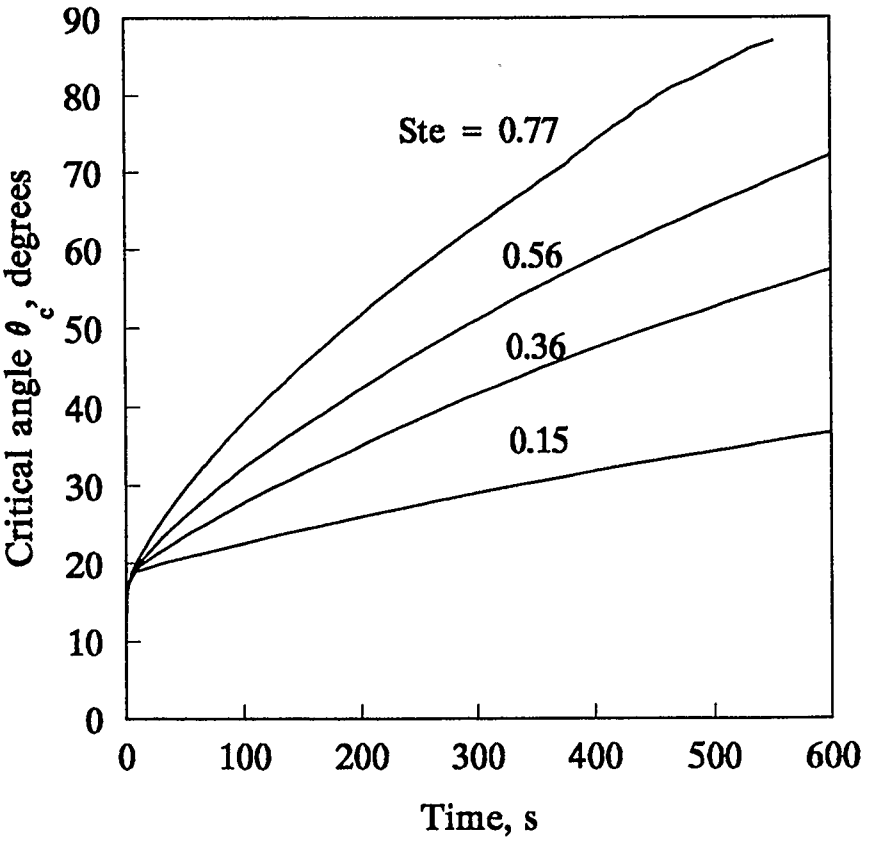


Fig. 5.16 Comparison of critical sector angle development as function of Ste number, $\delta_o = 1.5(10^{-4})$m, $r_o = 2.5(10^{-2})$m

increase for $\theta_c$ decreased. At a given instant, $\theta_c$ values increased faster under higher driving potentials $\Delta T_w$ since more melt has to be expelled and the area of close contact is larger. After ~300 seconds, for example, the melt channels stretch in the azimuthal direction to angular positions of 29°, 41°, 51°, 63° degrees when the temperatures of the hot surface are set for 120°, 130°, 140° and 150°C respectively. An increase in contact area of ~ $0.6 \bullet r_o$ per tube length has occurred when $T_w$ = 150°C, compared with $T_w$ = 120°C.

The radial temperature distributions are compared in Fig. 5.17 after 10 seconds when the $T_w$ value is set to be 120 and 150°C respectively. The temperature profiles are different when $T_w$ is different. At short melting times of 10 seconds and at higher values for $T_w$, the melt is cooler near the discharge at $\theta_c$ but warmer in the interior positions. This is due to the fact that at higher $T_w$ value, more melt is produced and the nascent liquid is at the melting point. The melt thus has not gained much sensible heat before it is expelled out of the gap. Fig. 5.18 shows a comparison of the radial temperature profiles after 60 s for the same condition of Fig. 5.17. The variations of temperature profiles at the intermediate angles are smaller. Nevertheless the profiles are not similar. The melt is always warmer when $T_w$ = 150°C to reflect the higher sensible heat convected. The temperature distributions appear closer to linear profiles when $T_w$ = 120°C probably because liquid production rates are low.

A comparison of the azimuthal velocity profiles is presented in Fig. 5.19 and Fig. 5.20 at 60 s and 300 s respectively for the same conditions as Fig. 5.17. At the same elapsed time, the profiles are not similar at the same angle values. As discussed in Section

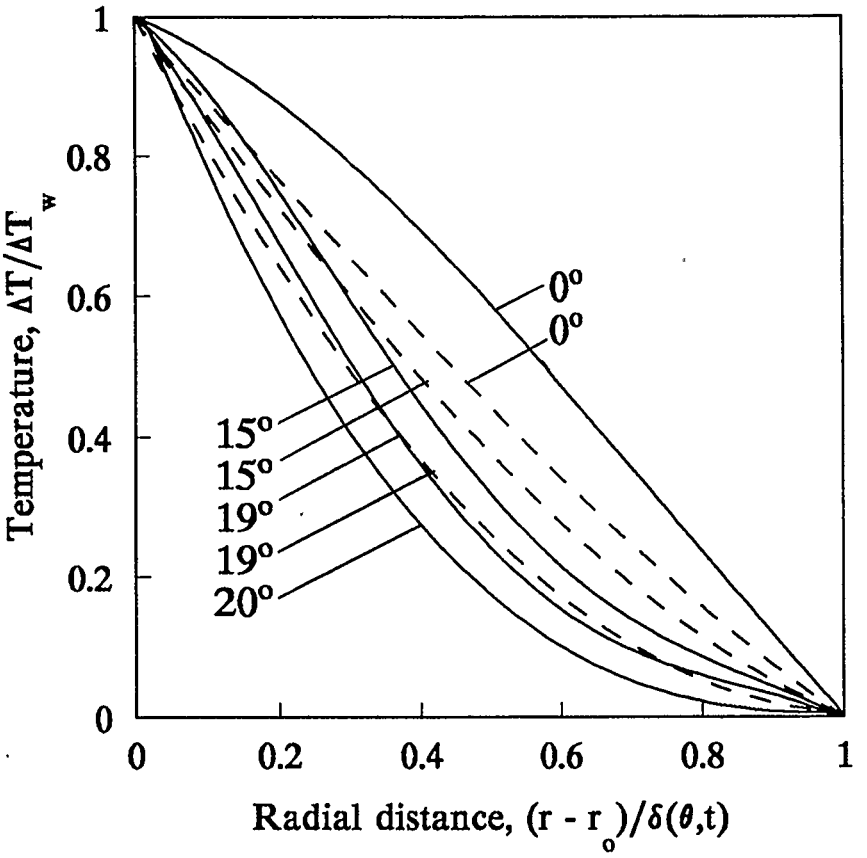


Fig. 5.17 Comparison of radial temperature profiles, at t = 10s,
$T_w$ = 150°C (Ste = 0.77)(-) and 120°C(Ste = 0.15)(---), $\delta_o = 1.5(10^{-4})$m, $r_o = 2.5(10^{-2})$m

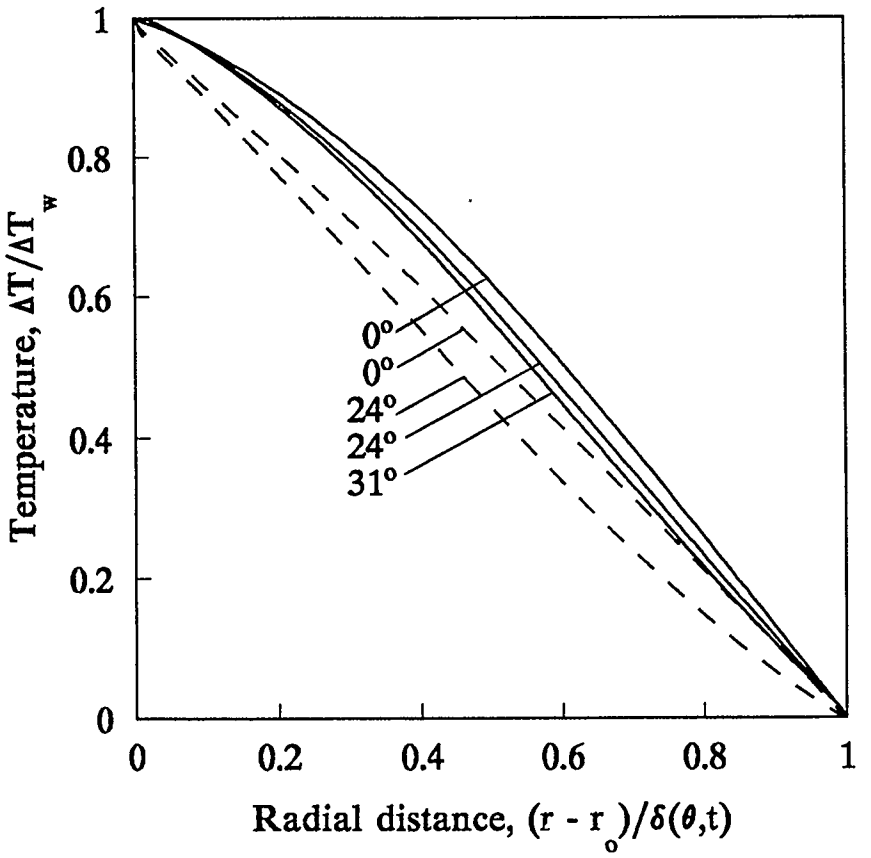


Fig. 5.18 Comparison of radial temperature profiles, at t = 60s,
$T_w$ = 150°C (Ste = 0.77)(-) and 120°C(Ste = 0.15)(---), $\delta_o = 1.5(10^{-4})$m, $r_o = 2.5(10^{-2})$m

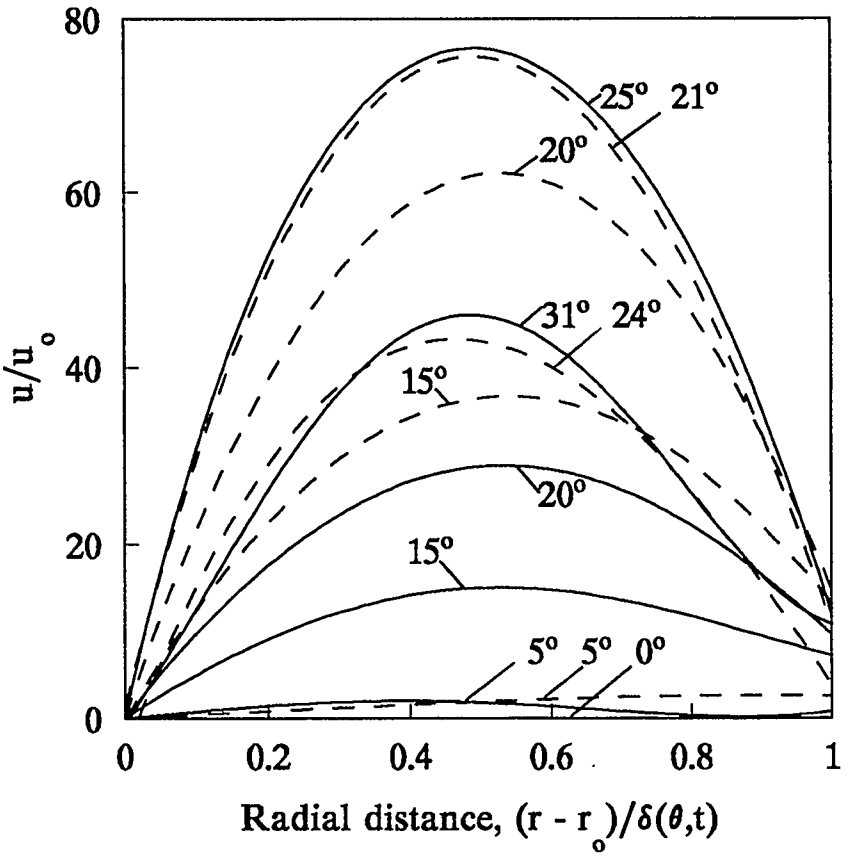


Fig. 5.19 Comparison of tangential velocity profiles, at t = 60s,
$T_w$ = 150°C (Ste = 0.77)(-) and 120°C(Ste = 0.15)(---), $\delta_o = 1.5(10^{-4})$, $r_o = 2.5(10^{-2})$m

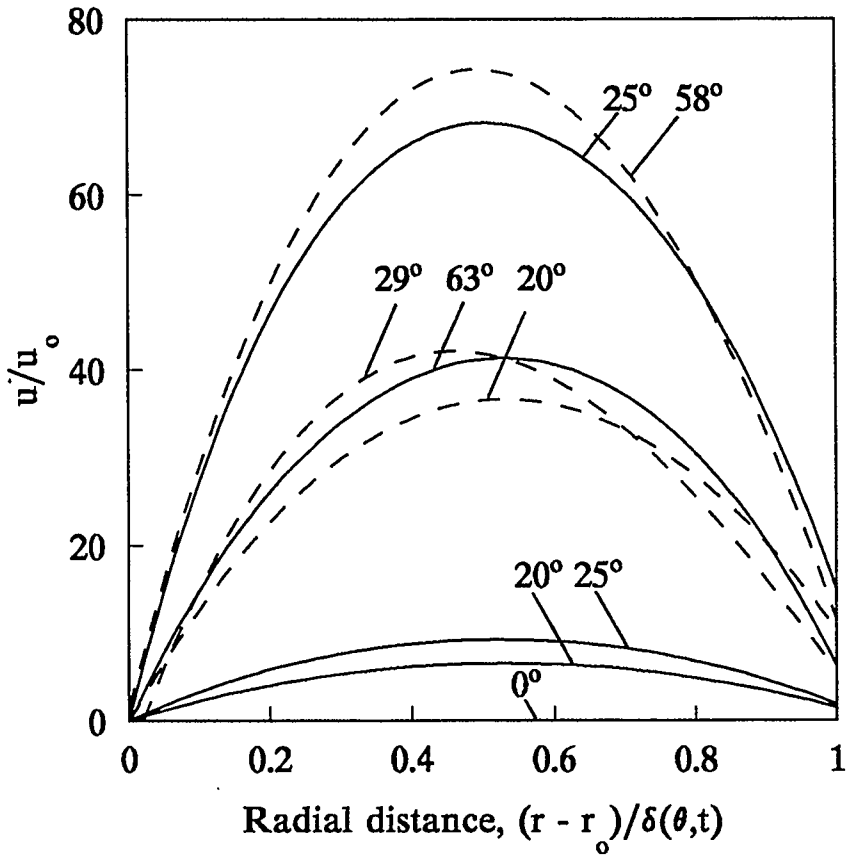


Fig. 5.20 Comparison of tangential velocity profiles, at t = 300s, $T_w$ = 150°C (Ste = 0.77)(-) and 120°C(Ste = 0.15)(---), $\delta_o = 1.5(10^{-4})$m, $r_o = 2.5(10^{-2})$m

5.1, the velocity profiles are functions of θ and melting time. They are also dependent on the $T_w$ values. At the same polar position, the normalized velocity profiles scaled by $u_o$ are located higher at lower surface temperature. As shown in Tables 5.3 and 5.4, the maximum velocities are higher with the hotter surfaces since more liquid is produced and it is expelled out of the channels with almost the same widths. The highest velocities are located at different points within the domain and they occur at larger angular positions as $T_w$ is increased.

Table 5.3 Comparison of Maximum Velocity Values at Various Angles

t = 60 s, unit for velocity, m/s, $\delta_o = 1.5(10^{-4})$m, $r_o = 2.5(10^{-2})$m

| $T_w$(°C) | 5° | 10° | 15° | 20° [1] | 21° [2] | 25° [3] | 30° [4] |
|---|---|---|---|---|---|---|---|
| 120 | $5.6(10^{-5})$ | $2.0(10^{-4})$ | $3.5(10^{-4})$ | $5.1(10^{-4})$ | $3.1(10^{-4})$ | N/A | N/A |
| 150 | $9.0(10^{-5})$ | $2.8(10^{-4})$ | $7.0(10^{-4})$ | $1.2(10^{-3})$ | $1.4(10^{-3})$ | $3.6(10^{-3})$ | $2.1(10^{-3})$ |

Notes: 1, maximum profile located at $T_w$ = 120 °C;
2, $\theta_c$ located at $T_w$ = 120 °C;
3, maximum profile located at $T_w$ = 150 °C;
4, $\theta_c$ located at $T_w$ = 150 °C.

Table 5.4 Comparison of Maximum Velocity Values at Various Angles

t = 300 s, unit for velocity, m/s, $\delta_o = 1.5(10^{-4})$m, $r_o = 2.5(10^{-2})$m

| $T_w$(°C) | 10° | 20° | 25° [1] | 29° [2] | 40° | 58° [3] | 63° [4] |
|---|---|---|---|---|---|---|---|
| 120 | $7.4(10^{-5})$ | $2.5(10^{-4})$ | $5.0(10^{-4})$ | $3.0(10^{-4})$ | N/A | N/A | N/A |
| 150 | $8.7(10^{-5})$ | $4.3(10^{-4})$ | $5.1(10^{-4})$ | $5.3(10^{-4})$ | $5.8(10^{-4})$ | $3.1(10^{-3})$ | $1.9(10^{-3})$ |

Notes: 1, maximum profile located at $T_w$ = 120 °C;
2, $\theta_c$ located at $T_w$ = 120 °C;
3, maximum profile located at $T_w$ = 150 °C;
4, $\theta_c$ located at $T_w$ = 150 °C.

### 5.2.2 *The Effect of Gap Width at* $\theta = 0$, $\delta_o$

One of the parameters fixed for the computations is the gap width at $\theta = 0°$, $\delta_o$ . The effects of its variation on the process are next considered. For the sensitivity analysis, three $\delta_o$ were chosen as $1.5(10^{-4})$, $2.0(10^{-4})$ and $2.5(10^{-4})$ m. Fig. 5.21, 5.22 and 5.23 are the plots of the migration velocity of the hot tube at $T_w$ values of 130, 140 and 150°C respectively. In general, as $\delta_o$ is increased, the migration rate of the tube decreases. The migration rate also requires a longer time to attain a plateau at higher $\delta_o$ (Table 5.5). These results are consistent with a longer path length for heat transfer across the gap to the surface at which the melt is produced.

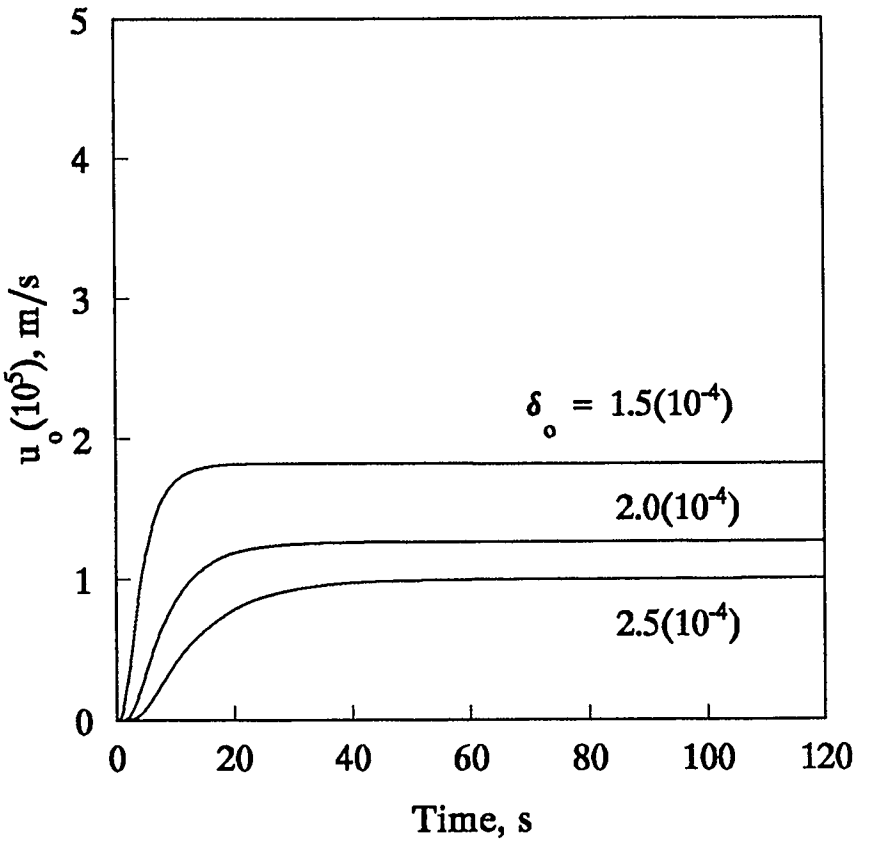


Fig. 5.21 Migration rate of the hot tube $u_o$ as function of gap width at $\theta = 0$, $\delta_o$
$T_w = 130°C$ (Ste = 0.36), $r_o = 2.5(10^{-2})$m

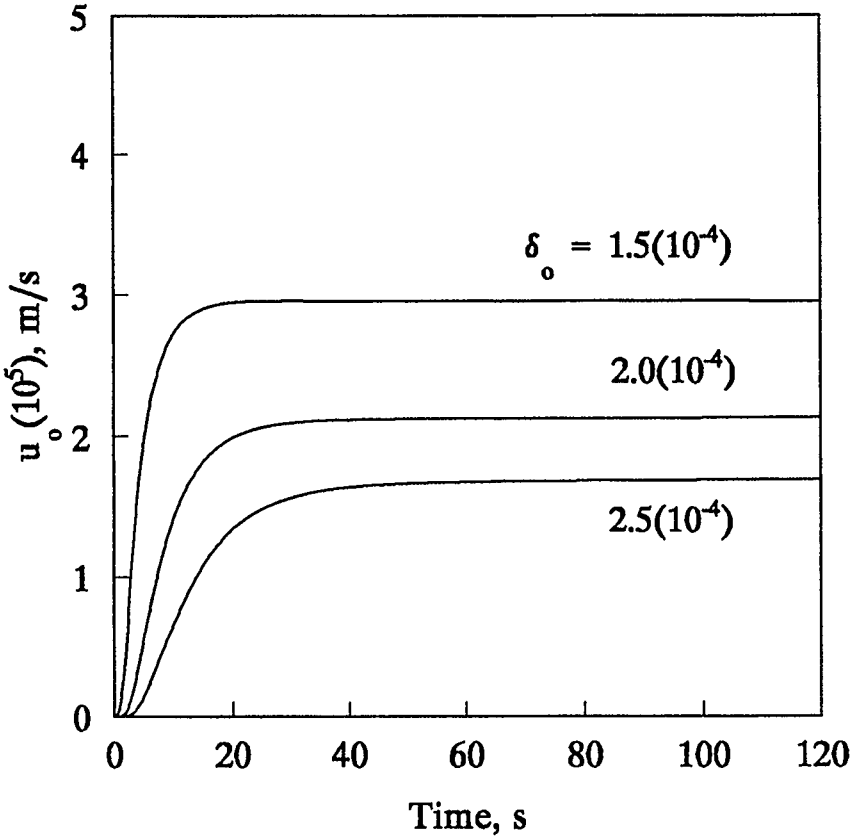


Fig. 5.22 Migration rate of the hot tube $u_o$ as function of gap width at $\theta = 0$, $\delta_o$
$T_w = 140°C$ (Ste = 0.56), $r_o = 2.5(10^{-2})$m

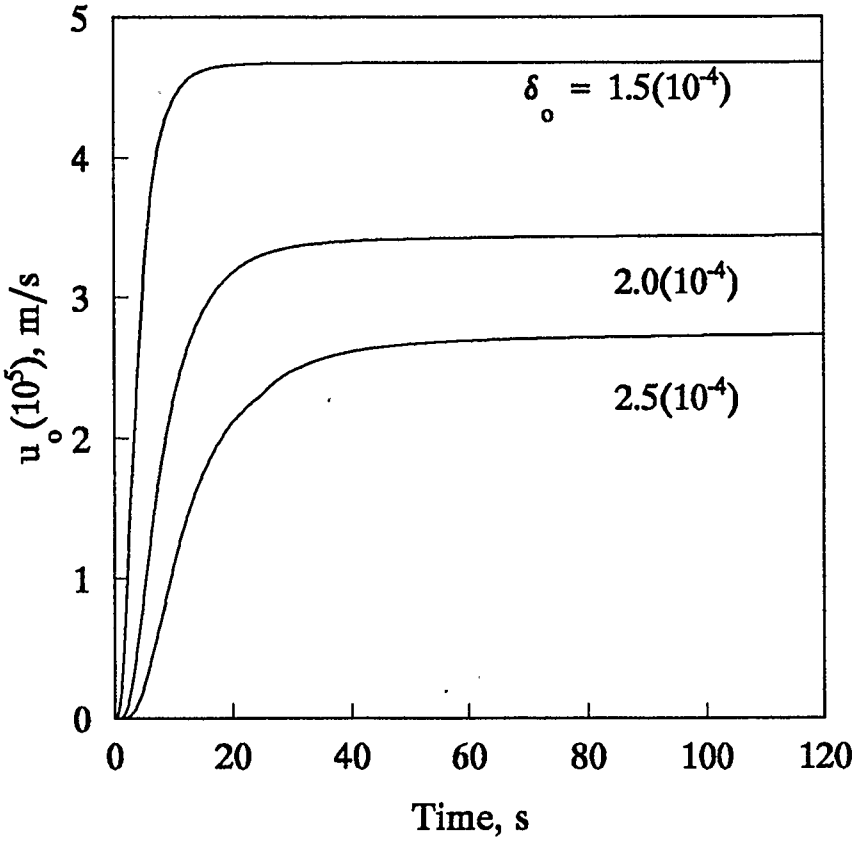


Fig. 5.23 Migration rate of the hot tube $u_o$ as function of gap width at $\theta = 0$, $\delta_o$
$T_w = 150°C$ (Ste = 0.77), $r_o = 2.5(10^{-2})$m

Table 5.5 Comparison of Migration Rates
at Different $\delta_o$ Values

| $T_w$ (°C) | $\delta_o(10^4)$, (m) | $u_o$ (m/s) | $t^*$ (s) |
|---|---|---|---|
| 120 | 1.5 | $6.80(10^{-6})$ | 19.4 |
| 120 | 2.0 | $5.12(10^{-6})$ | 34.9 |
| 120 | 2.5 | $4.08(10^{-6})$ | 76.5 |
| 130 | 1.5 | $1.82(10^{-5})$ | 22.2 |
| 130 | 2.0 | $1.26(10^{-5})$ | 46.4 |
| 130 | 2.5 | $9.97(10^{-6})$ | 108.0 |
| 140 | 1.5 | $2.96(10^{-5})$ | 25.8 |
| 140 | 2.0 | $2.12(10^{-5})$ | 47.9 |
| 140 | 2.5 | $5.12(10^{-6})$ | 130.0 |
| 150 | 1.5 | $4.70(10^{-5})$ | 27.6 |
| 150 | 2.0 | $3.42(10^{-5})$ | 54.5 |
| 150 | 2.5 | $2.74(10^{-5})$ | 143.5 |

Note: $t^*$ is the time to attain the plateau value for $u_o$.

The coupled effects of $T_w$ and $\delta_o$ on $u_o$ are reflected in Table 5.5. The velocity $u_o$ is proportional to $\Delta T_w$ and inversely proportional to $\delta_o$, or $u_o \propto (\Delta T_w, 1/\delta_o)$. To obtain the same migration velocity of the tube, one can either raise the wall temperature $T_w$ or decrease $\delta_o$. It is suggested that the migration rate of the tube $u_o$ is more sensitive to changes in $\Delta T_w$ than to $\delta_o$.

The forces applied to maintain the minimum gap separation ($\delta_o$) are plotted as functions of time in Figs. 5.24(a-c) for $T_w$ values of 130°, 140° and 150°C respectively. The forces increased with decreasing $\delta_o$ and increasing $T_w$. Both effects are complementary. A narrower gap and a higher wall temperature both promote a higher rate

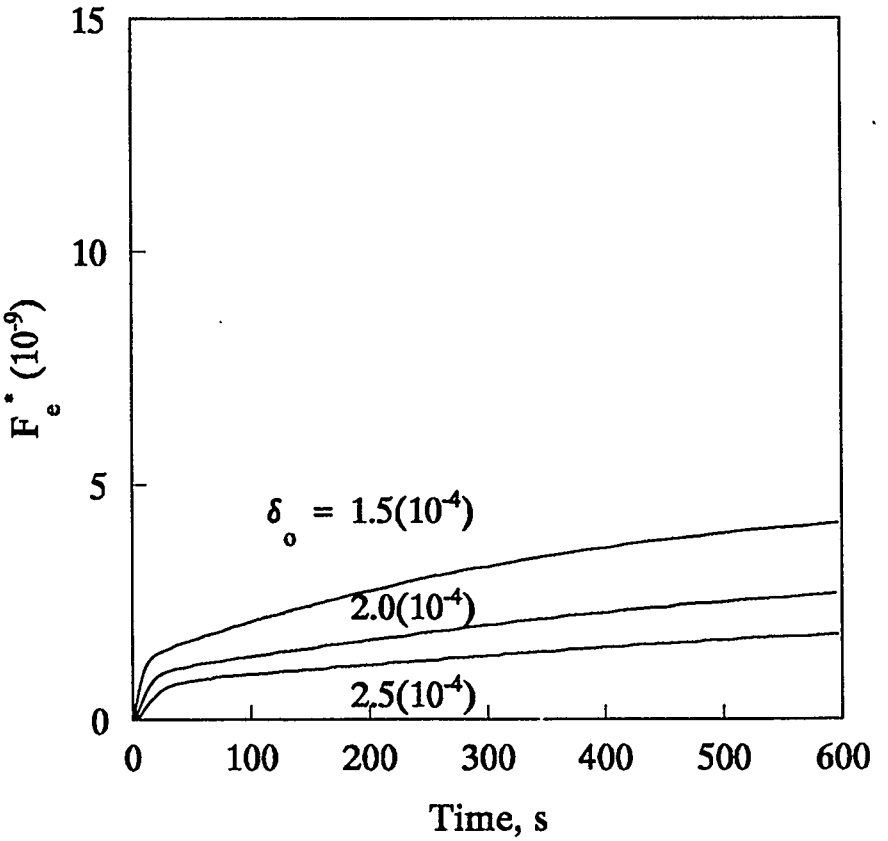


Fig. 5.24(a) Comparison of applied force as function of $\delta_o$, $T_w$ = 130°C (Ste = 0.36), $r_o$ = 2.5$(10^{-2})$m

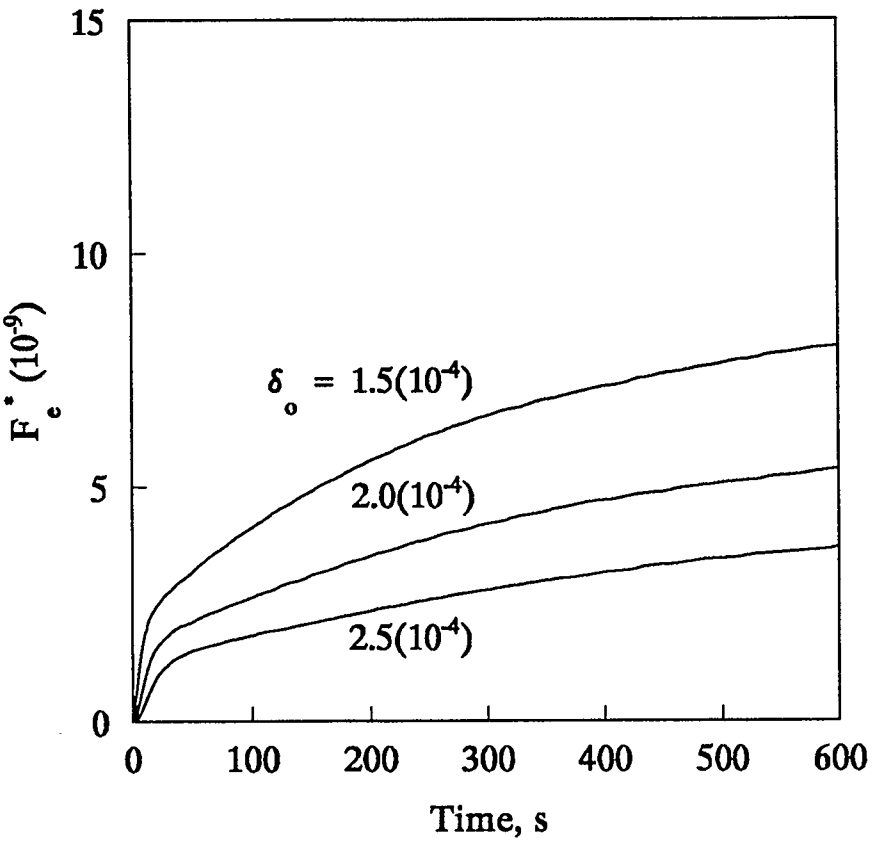


Fig. 5.24(b) Comparison of applied force as function of $\delta_o$, $T_w$ = 140°C (Ste = 0.56), $r_o$ = 2.5($10^{-2}$)m

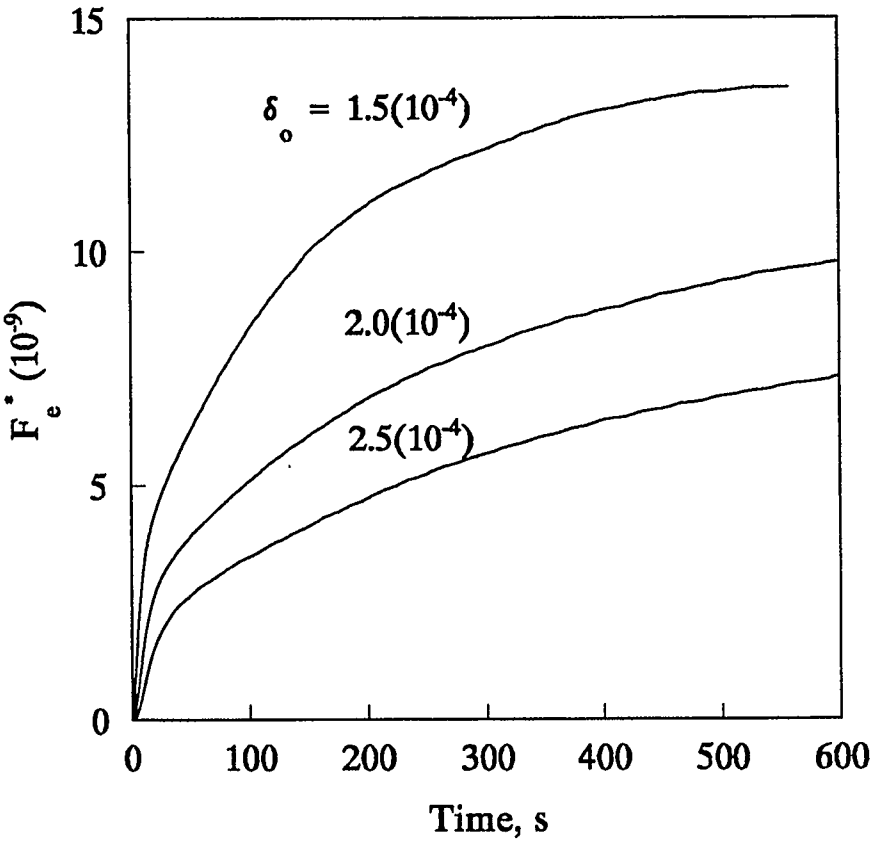


Fig. 5.24(c) Comparison of applied force as function of $\delta_o$, $T_w$ = 150°C (Ste = 0.77), $r_o$ = 2.5$(10^{-2})$m

of melt production. More work is required to displace the liquid from the narrow gap.

With regards to changes in gap width in relation to $\delta_o$, Figs. 5.25(a-c), the arrangements with larger $\delta_o$ show larger normalized discharge areas at $\theta_c$. This might be anticipated since heat has to be transported over a longer path and the corresponding rate of change of the curvature at the $\theta = 0$ will be slower compared to the arrangement with a closer approach between the surfaces. The surface, at $\theta_c$, should not be further displaced because of a higher melting rate and higher heat conduction to the boundary in the neighbourhood of $\theta_c$.

The rate at which the edge of the curved surface, the line which represents the physical (not material) intersection between the melting and the planar (unheated) walls, is displaced around the tube varies with the prescribed minimum separation distance $\delta_o$ as shown in Figs. 5.26(a-c). At a fixed elapsed time of 300 s, in Fig. 5.26(a), for example, $\theta_c$ is over 40° when $\delta_o \sim 1.5(10^{-4})$ m while it is ~22° when $\delta_o = 2.5(10^{-4})$ m. This displacement rate is significantly affected by the temperature of the hot tube wall. A comparison of the results at 130 and 150°C in Fig. 5.26(a) and (c), for example, when $\delta_o = 1.5(10^{-4})$ m and time = 300 s, shows a difference of ~25° in $\theta_o$ values. An explicit relationship for $\theta_c(\delta_o, T_w)$ has not been determined.

Changes in the temperature profiles within the gap for different $\delta_o$ are shown in Fig. 5.27 and 5.28 for elapsed times of 10 and 60 s respectively. The angles for the lower curves in the plot are the corresponding $\theta_c$ values. Therefore the temperature profiles for intermediate angles are within zones bounded by curves at 0° and $\theta_c$. The average temperatures are cooler for the gaps with wider $\delta_o$ and the gradients at the melting

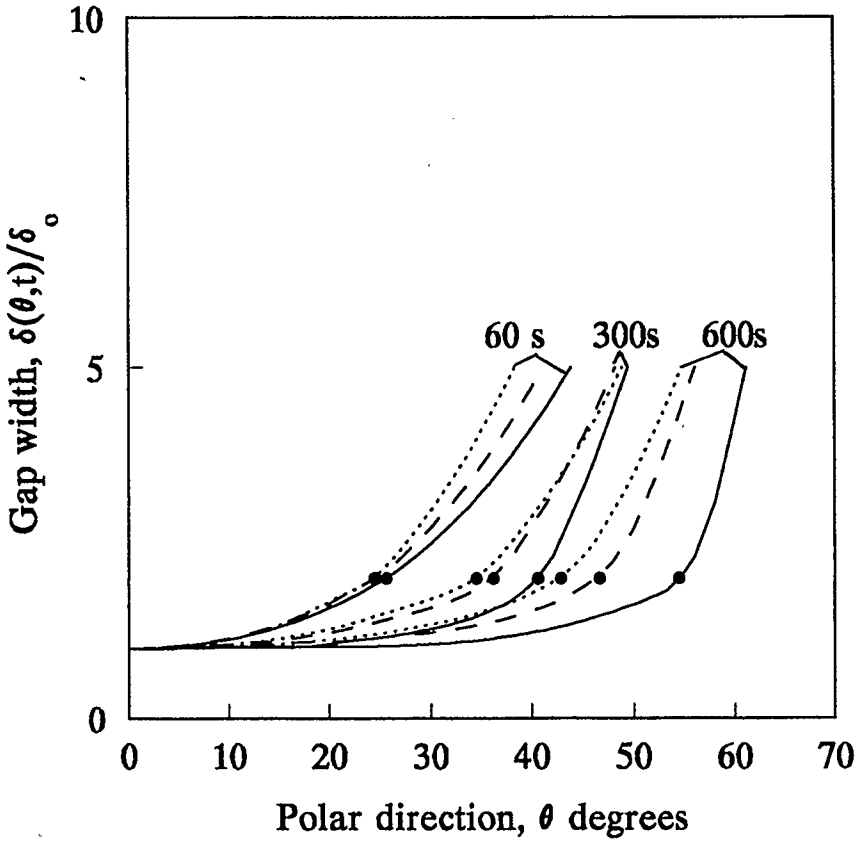


Fig. 5.25(a) Comparison of gap width development as function of $\delta_o$, $\delta_o = 1.5(10^{-4})$m(-), $2.0(10^{-4})$m(---) and $2.5(10^{-4})$m(.....), $T_w = 130°C$ (Ste = 0.36), $r_o = 2.5(10^{-2})$m

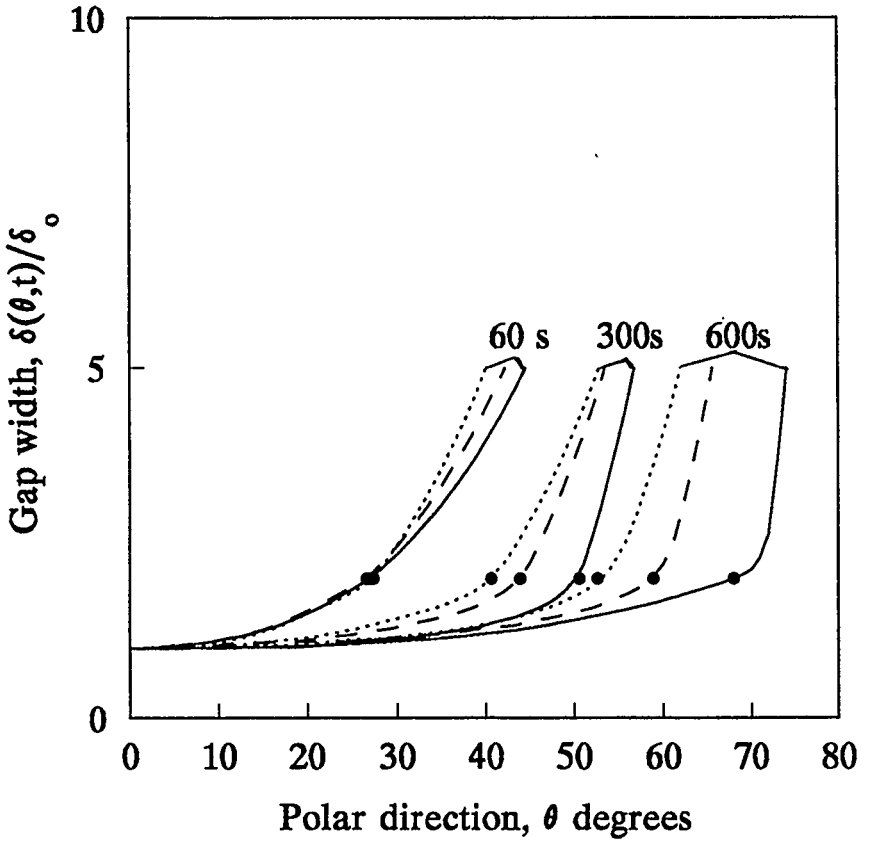


Fig. 5.25(b) Comparison of gap width development as function of $\delta_o$, $\delta_o$ = 1.5($10^{-4}$)m(-), 2.0($10^{-4}$)m(---) and 2.5($10^{-4}$)m(.....), $T_w$ = 140°C (Ste = 0.56), $r_o$ = 2.5($10^{-2}$)m

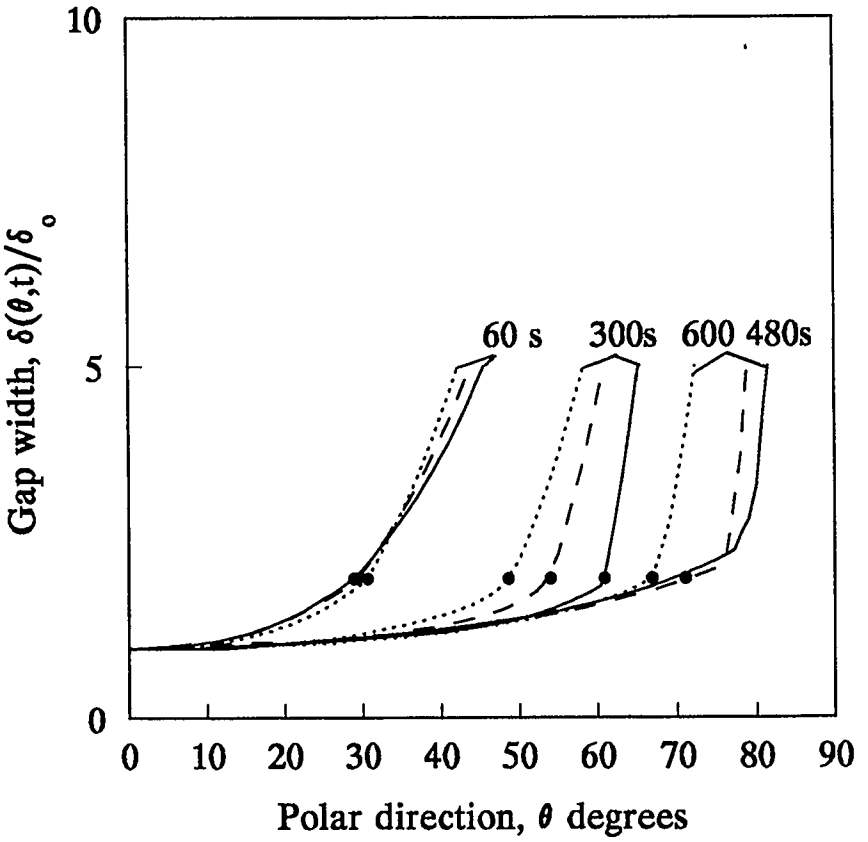


Fig. 5.25(c) Comparison of gap width development as function of $\delta_o$, $\delta_o = 1.5(10^{-4})$m(-), $2.0(10^{-4})$m(---) and $2.5(10^{-4})$m(.....), $T_w = 150°C$ (Ste = 0.77), $r_o = 2.5(10^{-2})$m

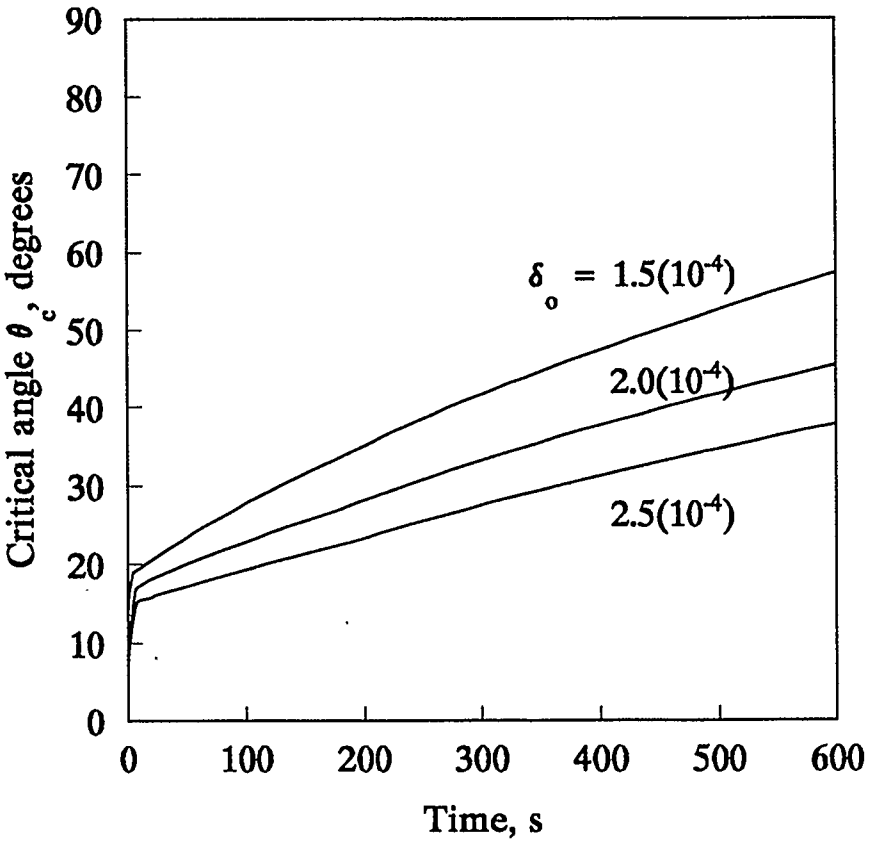


Fig. 5.26(a) Comparison of critical sector angle development as function of $\delta_o$, $T_w$ = 130°C (Ste = 0.36), $r_o$ = 2.5(10$^{-2}$)m

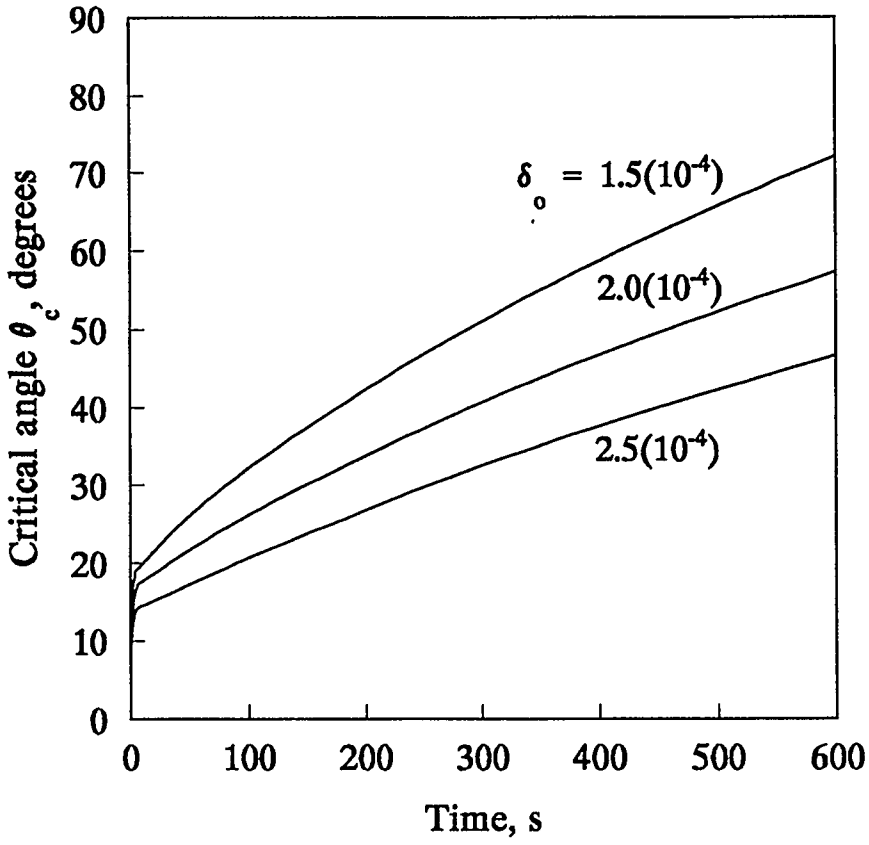


Fig. 5.26(b) Comparison of critical sector angle development as function of $\delta_o$, $T_w$ = 140°C (Ste = 0.56), $r_o$ = 2.5(10$^{-2}$)m

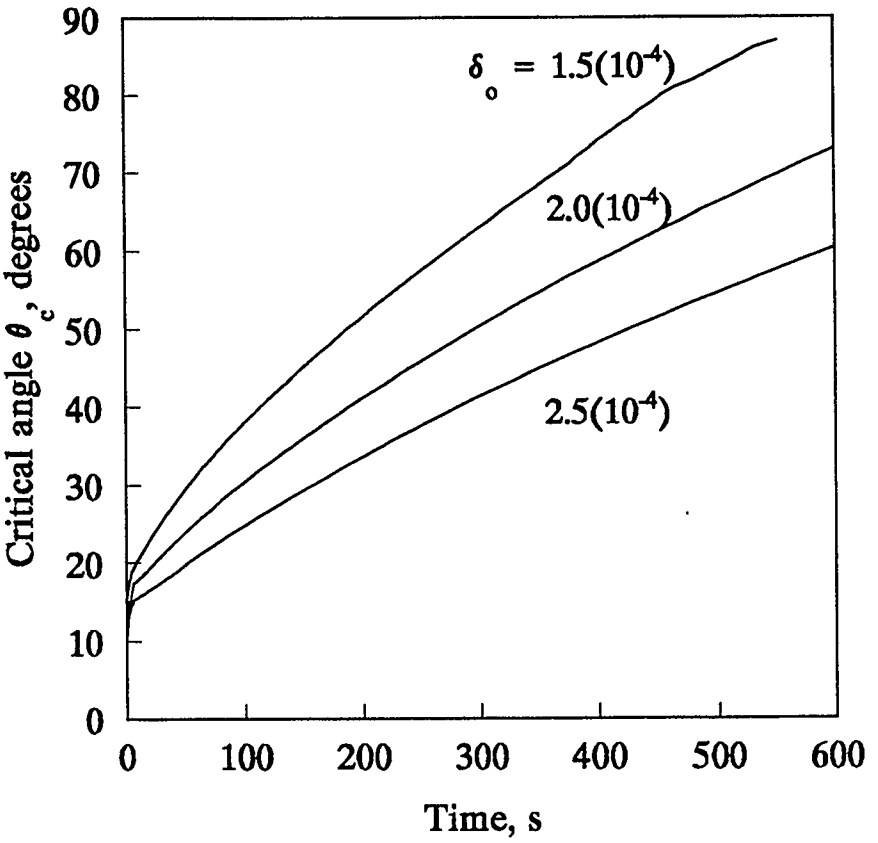


Fig. 5.26(c) Comparison of critical sector angle development as function of $\delta_o$, $T_w$ = 150°C (Ste = 0.77), $r_o$ = 2.5(10$^{-2}$)m

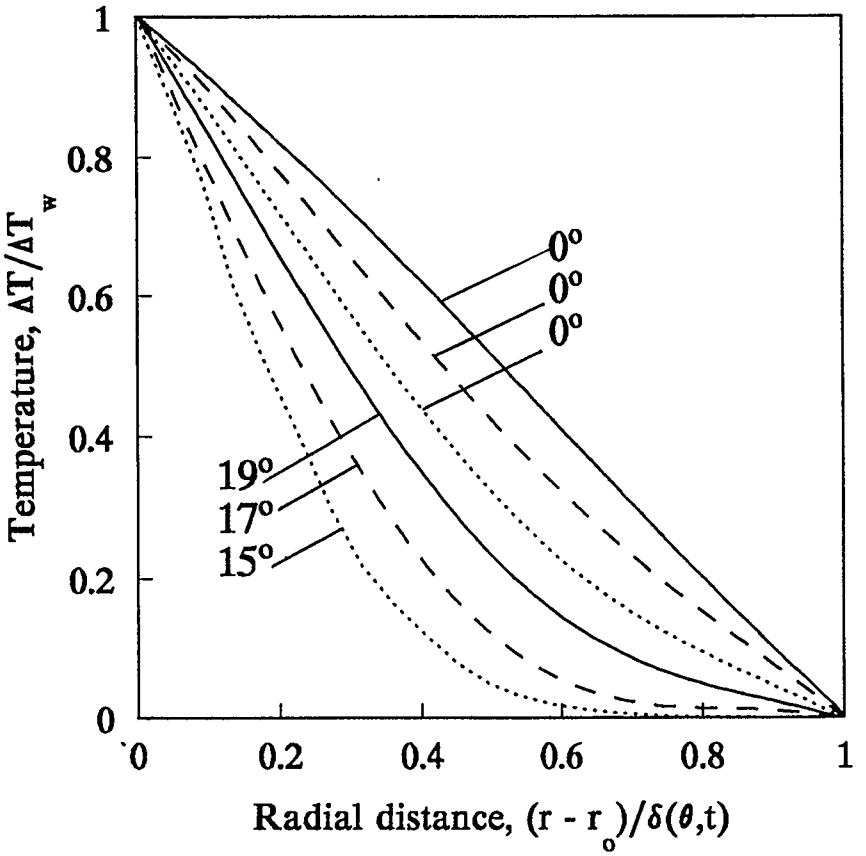


Fig. 5.27 Comparison of radial temperature profiles, at t = 10s, $\delta_o$ = 1.5($10^{-4}$)m(-), 2.0($10^{-4}$)m(---) and 2.5($10^{-4}$)m(.....), $T_w$ = 130°C (Ste = 0.36), $r_o$ = 2.5($10^{-2}$)m

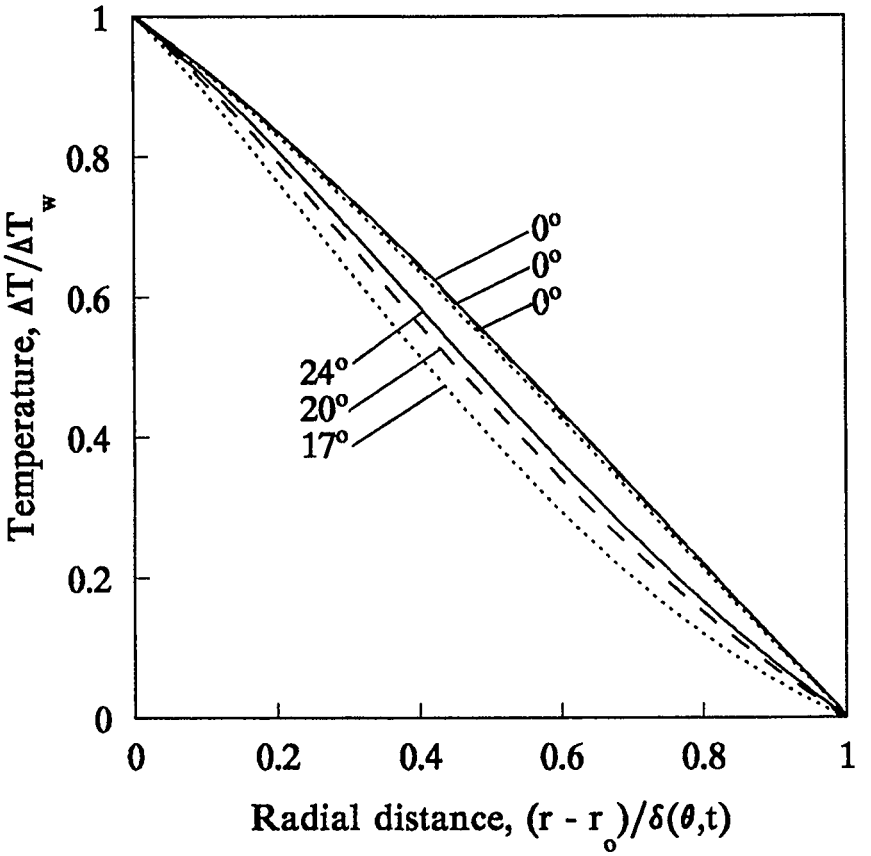


Fig. 5.28 Comparison of radial temperature profiles, at t = 60s, $\delta_o$ = 1.5($10^{-4}$)m(-), 2.0($10^{-4}$)m(---) and 2.5($10^{-4}$)m(.....), $T_w$ = 130°C (Ste = 0.36), $r_o$ = 2.5($10^{-2}$)m

boundary indicate lower heat fluxes for phase change. In Fig. 5.27, no appreciable heat appears to be used for melting for the widest gap at $\theta = 15°$, i.e., any heat input by the tube at this angle $\theta$ is entirely convected in the melt at 10 s. This situation is not static and by t = 60 s, the profiles and heat flux patterns had changed.

As might be anticipated from the temperature fields with regards to the melt production rates, the velocity profiles in the gap also depend on $\delta_o$. Although the general shapes of the profiles for velocity for different $\delta_o$ look alike at various $\theta$, they are not similar as shown in Fig. 5.29. Except for the profiles at 10°, two other sets of velocity profiles are at $\theta$ values where the velocity attains peak values within the domain and at corresponding $\theta_c$ values. Peak velocities for the three calculated examples are presented in Tables 5.6 and 5.7 for comparison. These show increases in the azimuthal direction and a sudden drop near $\theta_c$ for each of the $\delta_o$ values. An increase of $\delta_o$ by 60% also results in a 4 fold lowering of the velocity at certain angles - 16° at 10 s and 17° after 60 s when $T_w = 130°C$.

Table 5.6 Comparison of maximum velocity values at various angular positions

t = 10 s, $T_w = 130°C$, unit for velocity, m/s, for $\delta_o$, m

| $\delta_o(10^4)$ | 10° | 14° | 15° | 16° | 17° | 18° | 19° |
|---|---|---|---|---|---|---|---|
| 1.5 | $5.8(10^{-4})$ | $7.7(10^{-4})$ | $8.0(10^{-4})$ | $8.1(10^{-4})$ | $8.2(10^{-4})$ | $8.4(10^{-4})$ | $4.9(10^{-4})$ |
| 2.0 | $4.0(10^{-4})$ | $4.5(10^{-4})$ | $4.6(10^{-4})$ | $4.8(10^{-4})$ | $4.0(10^{-4})$ | N/A | N/A |
| 2.5 | $3.6(10^{-4})$ | $2.3(10^{-4})$ | $2.5(10^{-4})$ | $2.2(10^{-4})$ | N/A | N/A | N/A |

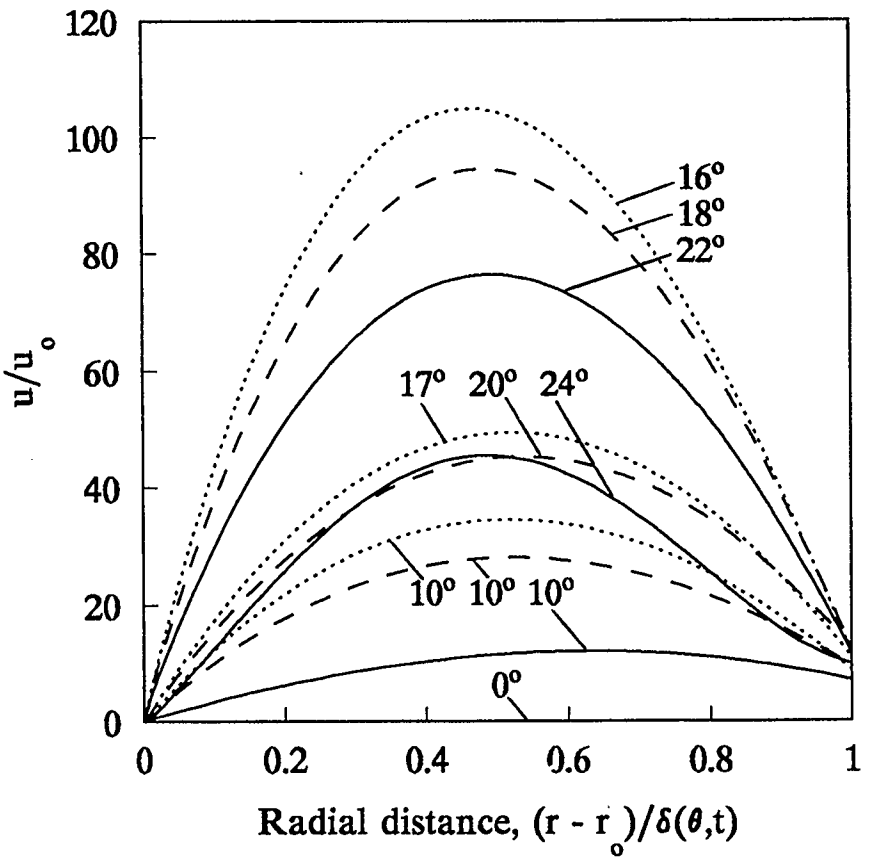


Fig. 5.29 Comparison of tangential velocity profiles, at t = 60s, $\delta_o$ = 1.5($10^{-4}$)m(-), 2.0($10^{-4}$)m(---) and 2.5($10^{-4}$)m(.....), $T_w$ = 130°C (Ste = 0.36), $r_o$ = 2.5($10^{-2}$)m

Table 5.7 Comparison of maximum velocity values at various angular positions

t = 60 s, $T_w$ = 130°C, unit for velocity, m/s, for $\delta_o$, m

| $\delta_o(10^4)$ | 10° | 16° | 17° | 18° | 20° | 22° | 24° |
|---|---|---|---|---|---|---|---|
| 1.5 | $3.4(10^{-4})$ | $7.4(10^{-4})$ | $8.1(10^{-4})$ | $8.9(10^{-4})$ | $1.0(10^{-3})$ | $1.3(10^{-3})$ | $7.9(10^{-4})$ |
| 2.0 | $3.5(10^{-4})$ | $6.8(10^{-4})$ | $7.5(10^{-4})$ | $8.5(10^{-4})$ | $5.7(10^{-4})$ | N/A | N/A |
| 2.5 | $3.4(10^{-4})$ | $6.5(10^{-4})$ | $2.3(10^{-4})$ | N/A | N/A | N/A | N/A |

### 5.2.3 *The Effect of Radius of the Hot Tube $r_o$*

The effect of changes in the tube radius on the melting characteristics was also examined. The theoretical analysis in chapter 3 suggests that the tube radius is a parameter which has a weak effect on the melting rate. To confirm this, three radii were used in the simulation. They are $1.25(10^{-2})$, $2.5(10^{-2})$ and $5.0(10^{-2})$ m. The surface temperature of the hot tube was kept at 130°C and the $\delta_o$ value was fixed as $1.5(10^{-4})$ m.

The calculated migration velocities are presented in Fig. 5.30 when $T_w$ equals 130°C. The results show that the displacement rates of the tubes attain the same steady value after ~15 seconds. Only at the initial acceleration phase do very small differences appear. The larger tubes exhibit a reduced "induction" time during which the melting surface became indented but melt flow had not been initiated. The implication is that more melt is produced per tube over a given period and this is in direct proportion to the tube diameter.

The forces required to maintain $\delta_o$ constant are compared in Fig. 5.31. The dimensionless forces are directly proportional to the tube radius. However, according to

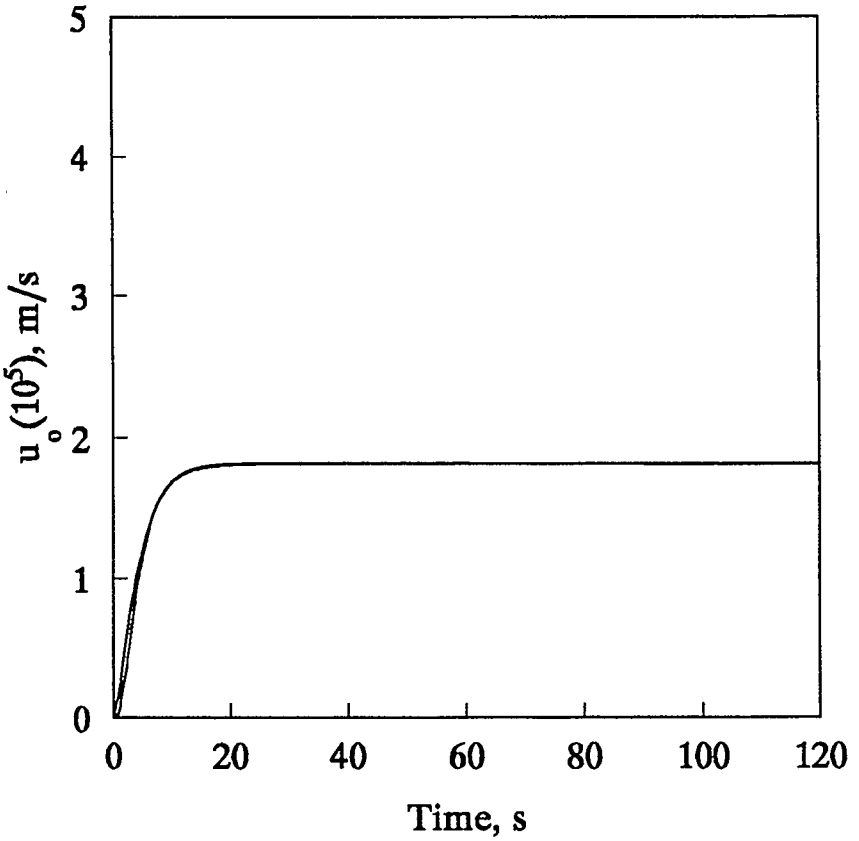


Fig. 5.30 Migration rate of the hot tube $u_o$ as function of tube radius $r_o$ (1.25, 2.5, $5.0\times10^{-2}$ m), $T_w$ = 130°C (Ste = 0.36), $\delta_o = 1.5(10^{-4})$m

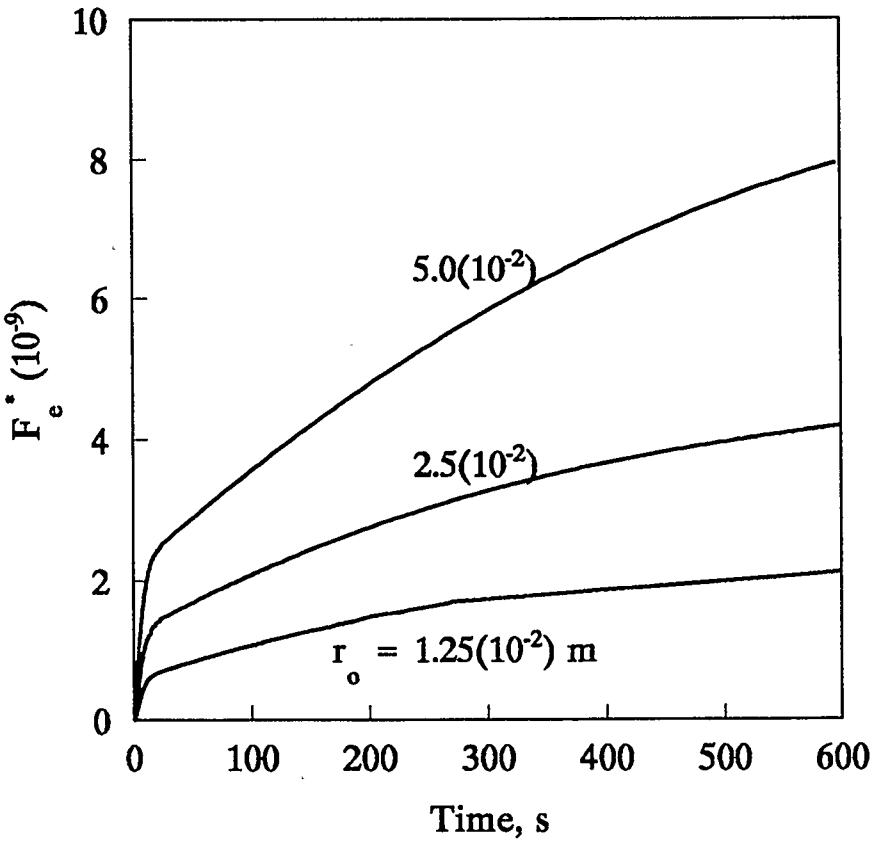


Fig. 5.31 Comparison of applied force as function of $r_o$, normalized by corresponding $r_o$ values
$T_w$ = 130°C (Ste = 0.36), $\delta_o$ = $1.5(10^{-4})$m

the definition of $F_e^*$, which is $F_e \bullet r_o/\rho\kappa_m L$, the actual forces were not increased even though $r_o$ was increased. Three dimensionless forces normalized by using the same $r_o$ value (i.e. $2.5(10^{-2})$ m) appeared to be the same except the infinitesimal differences at the initial phase of melting, as was shown in Fig. 5.32.

Changes of the liquid gap width with regards to $r_o$ are presented in Fig. 5.33. The melting interface was deformed faster when $r_o$ was smaller. A larger discharge area at $\theta_c$ was noted when the tube diameter became bigger.

Variations in the critical sector angles with time are also plotted in Fig. 5.34. At a given time of 300 s, for instance, $\theta_c$ is ~54° when $r_o = 1.25(10^{-2})$ m, while it is ~29° when $r_o$ was increased 4 fold to $5.0(10^{-2})$ m.

Temperature distributions for different $r_o$ values after 10 s elapsed time have been compared in Fig. 5.35 when $T_w = 130°C$. The lower curves are at corresponding $\theta_c$. The average temperature of the melt was higher at smaller $r_o$. When $r_o$ was increased to $5.0(10^{-2})$ m, the temperature gradient at the melting interface was very low as no appreciable heat was used for the phase change. But this situation was changed after ~ 60 s of elapsed time, as shown in Fig. 5.36. Even though the flow domain was longer along the azimuthal direction when $r_o$ was smaller, the melt produced were almost at the same average temperatures.

Fig. 5.37 shows the velocity profiles at different $r_o$ values at t = 60 s. Except for the profiles at 10°, the peak velocity profiles and those at $\theta_c$ values have also been presented. At the same angular position, the velocity profiles are different. The maximum velocity is almost tripled, for example, at 10°, with a quadruple increase for $r_o$. A 4 fold

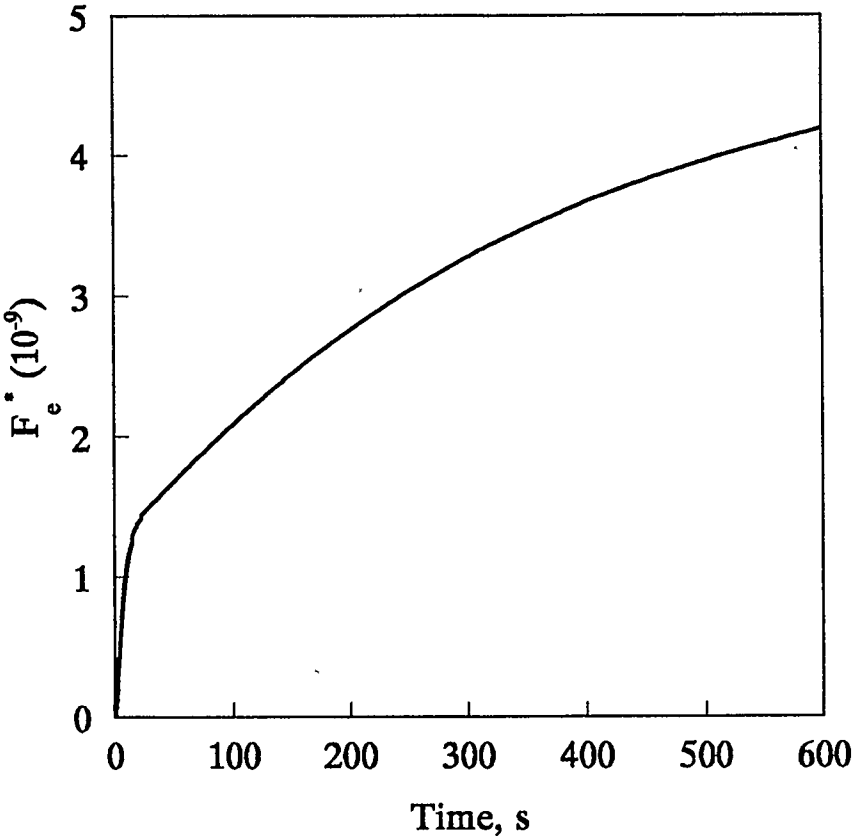


Fig. 5.32 Comparison of applied force as function of $r_o$,
$r_o$ (1.25, 2.5, 5.0×$10^{-2}$ m),normalized by the same $r_o$ value (2.5×$10^{-2}$ m)
$T_w$ = 130°C (Ste = 0.36), $\delta_o$ = 1.5($10^{-4}$)m

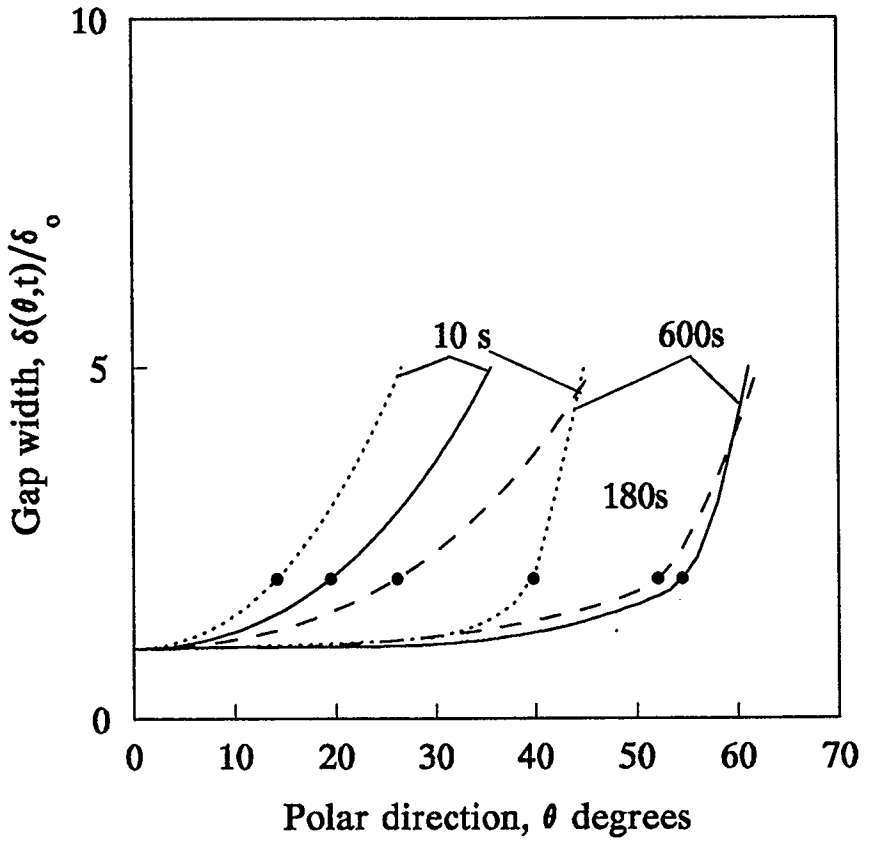


Fig. 5.33 Comparison of gap width development as function of $r_o$, $r_o = 2.5(10^{-2})$m(-), $1.25(10^{-2})$m(---) and $5.0(10^{-2})$m(.....), $T_w = 130°C$ (Ste = 0.36), $\delta_o = 1.5(10^{-4})$m

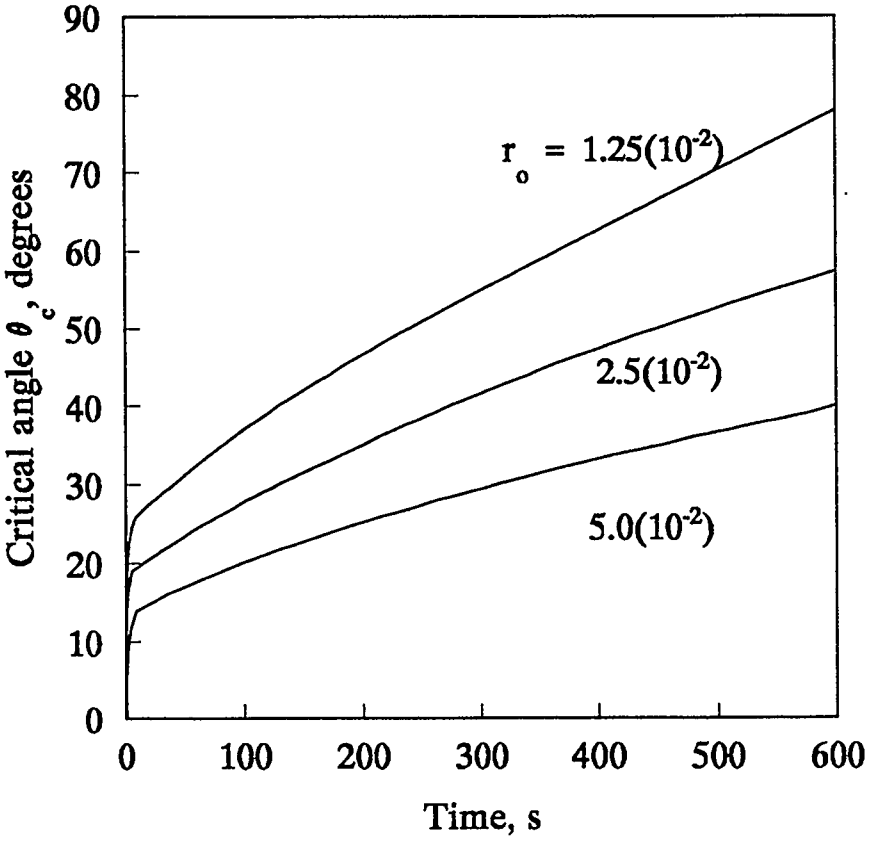


Fig. 5.34 Comparison of critical sector angle development as function of $r_o$, $T_w$ = 130°C (Ste = 0.36), $\delta_o$ = 1.5(10$^{-4}$)m

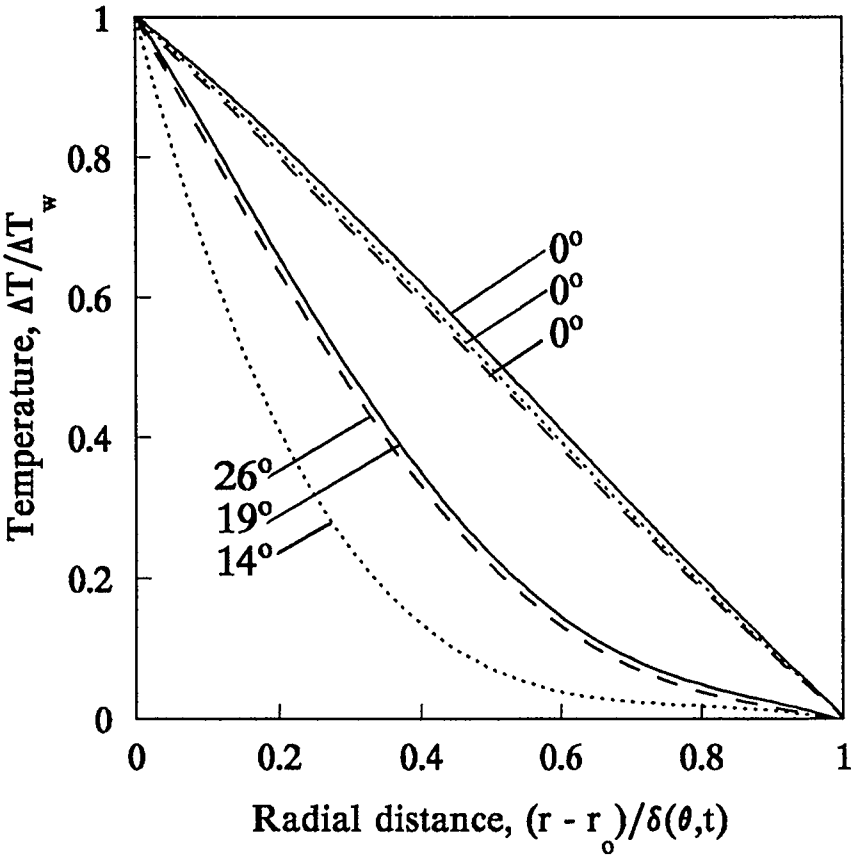


Fig. 5.35 Comparison of radial temperature profiles, at t = 10s, $r_o = 2.5(10^{-2})$m(-), $1.25(10^{-2})$m(---) and $5.0(10^{-2})$m(.....), $T_w = 130°C$ (Ste = 0.36), $\delta_o = 1.5(10^{-4})$m

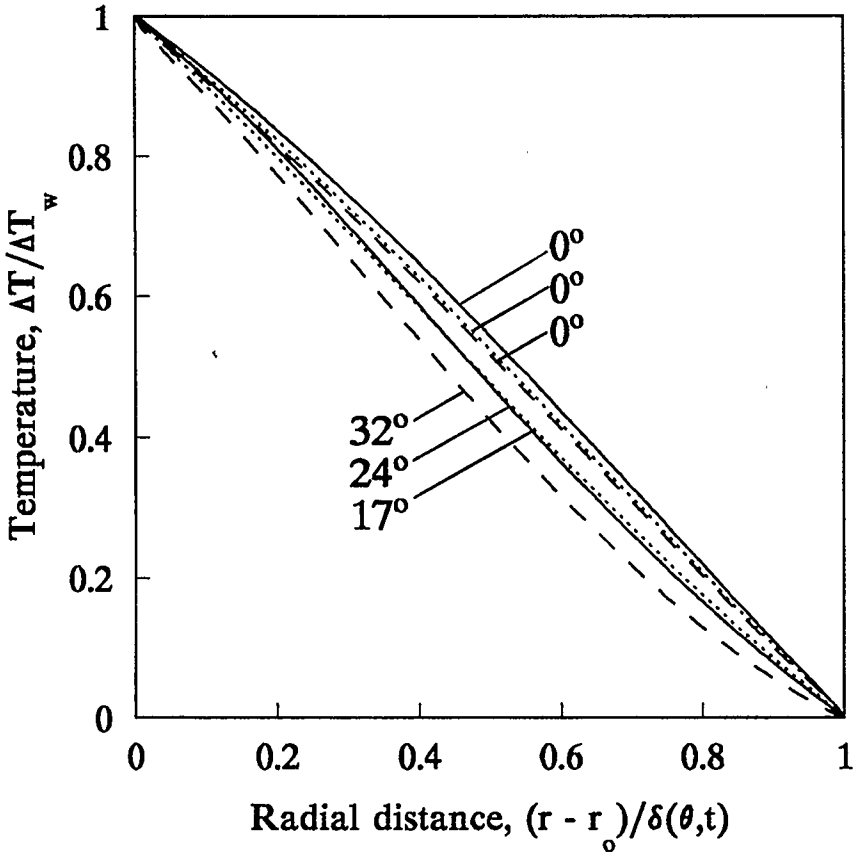


Fig. 5.36 Comparison of radial temperature profiles, at t = 60s, $r_o$ = 2.5($10^{-2}$)m(-), 1.25($10^{-2}$)m(---) and 5.0($10^{-2}$)m(.....), $T_w$ = 130°C (Ste = 0.36), $\delta_o$ = 1.5($10^{-4}$)m

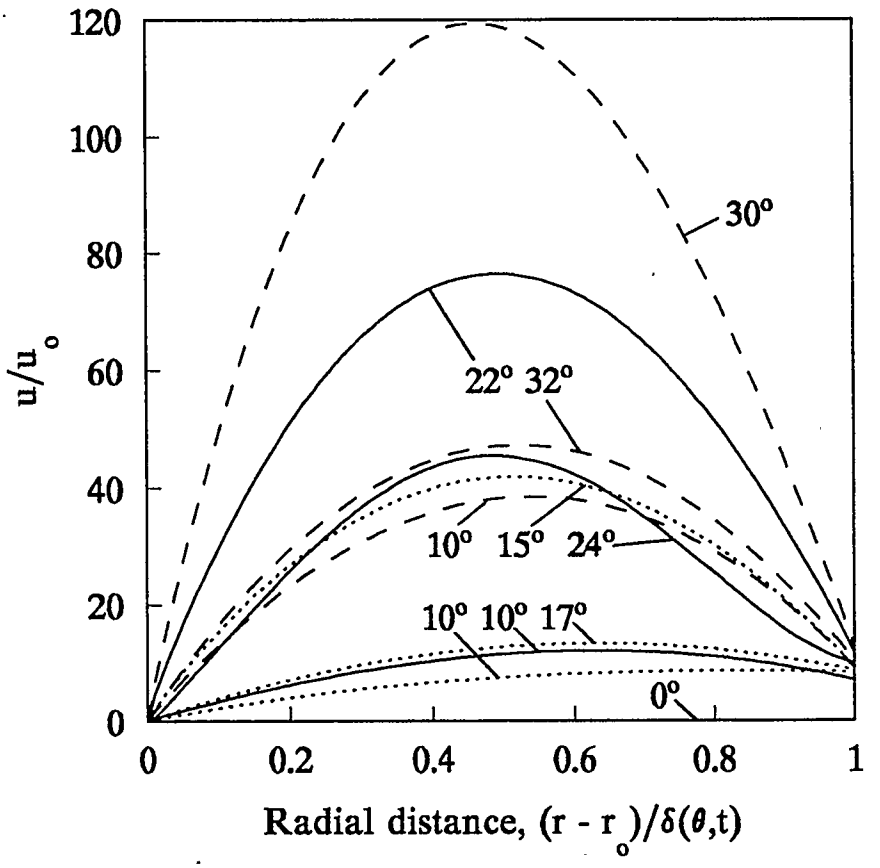


Fig. 5.37 Comparison of tangential velocity profiles, at t = 60s, $r_o$ = 2.5($10^{-2}$)m(-), 1.25($10^{-2}$)m(---) and 5.0($10^{-2}$)m(.....), $T_w$ = 130°C (Ste = 0.36), $\delta_o$ = 1.5($10^{-4}$)m

increase in the peak velocity is noted at ~60 s as presented in Table 5.8.

Table 5.8 Comparison of Maximum Velocity Values at Various Angles

t = 60 s, $T_w$ = 130°C, unit for velocity, m/s, for $r_o$, m

| $r_o(10^2)$ | 10° | 15° | 17° | 22° | 24° | 30° | 32° |
|---|---|---|---|---|---|---|---|
| 1.25 | $7.8(10^{-4})$ | $1.2(10^{-3})$ | $1.3(10^{-3})$ | $1.7(10^{-3})$ | $1.8(10^{-3})$ | $2.2(10^{-3})$ | $8.6(10^{-4})$ |
| 2.5 | $3.4(10^{-4})$ | $6.7(10^{-4})$ | $8.1(10^{-4})$ | $1.3(10^{-3})$ | $7.9(10^{-4})$ | N/A | N/A |
| 5.0 | $2.4(10^{-4})$ | $4.4(10^{-4})$ | $3.8(10^{-4})$ | N/A | N/A | N/A | N/A |

## 5.3 Computer Efficiency

The algorithm was executed with a main program and 30 subroutines. Thirty-five two-dimensional variables (size 181×101), 50 one-dimensional variables (size 181) and about 420 other variables were employed to generate the program with about 6000 lines of Fortran code. The memory size of the program is about 25 MB. The calculation included time-marching in increment of two milliseconds simulated time. Vector calculations were involved in solving the non-linear algebraic equations of the discretized PDEs. Numerous iterations exist in each time level calculation. Consequently, the simulation was time consuming and high CPU demanding. It took 2 - 4 weeks, for example, to advance through approximately 5 minutes of simulation on a time-shared IBM RISC 6000 (AIX) system at the University of Calgary. For accelerated calculations, the program was modified and transferred to the high performance Fujitsu VPX/240 system which is operated by the Fujitsu Canada High Performance Computing Centre in

Downtown Calgary.

From an analysis of the computing performances on the two systems (Wu, Jeje and Phillips, 1994), it was found that the calculations of velocity ($\boldsymbol{u}$), pressure (P) and the interface location $G\ (r_i,\ \theta,\ t)$ consumed most of the CPU time. Respectively, the CPU time consumption percentages for $u$, $P$ and $G$ were 14%, 35%, 42% on the AIX, and 19%, 25%, 53% on the Fujitsu systems. The results in Fig. 5.38 show how, for identical input conditions, the CPU times changed in relation to the simulation time on the AIX and Fujitsu systems. An inspection of the scale of the plots shows, that the Fujitsu system is faster than AIX system by an order of magnitude. The relative proportion of time to calculate $\boldsymbol{u}$, $P$ and $G$ were also different for the two hardware systems. Calculation times of the pressure and locating the melting boundary consumed similar amounts of CPU on the AIX but pressure values were determined at a faster rate than $G$ $(r_i,\ \theta,\ t)$ on the Fujitsu. The elapsed times for AIX and Fujitsu are shown in Fig. 5.39 for the identical parameter conditions. It also shows that the Fujitsu system saved 7-9 times of calculation time compared with the AIX system.

The results shown in Fig. 5.38 and 5.39 corresponded to a version of the program in which the overall vectorisation percentage is very low, only about 3%. Efforts to improve and optimize the code have been made. As mentioned earlier, due to the irregular calculation domain, the grid numbering in the r-direction is function of azimuthal angle $\theta$. This prevented certain types of optimization, which might otherwise improve vectorisation, such as interchanging certain nested loops. To overcome this difficulty, we have considered an indirect addressing scheme to reduce the nested loops to single loops

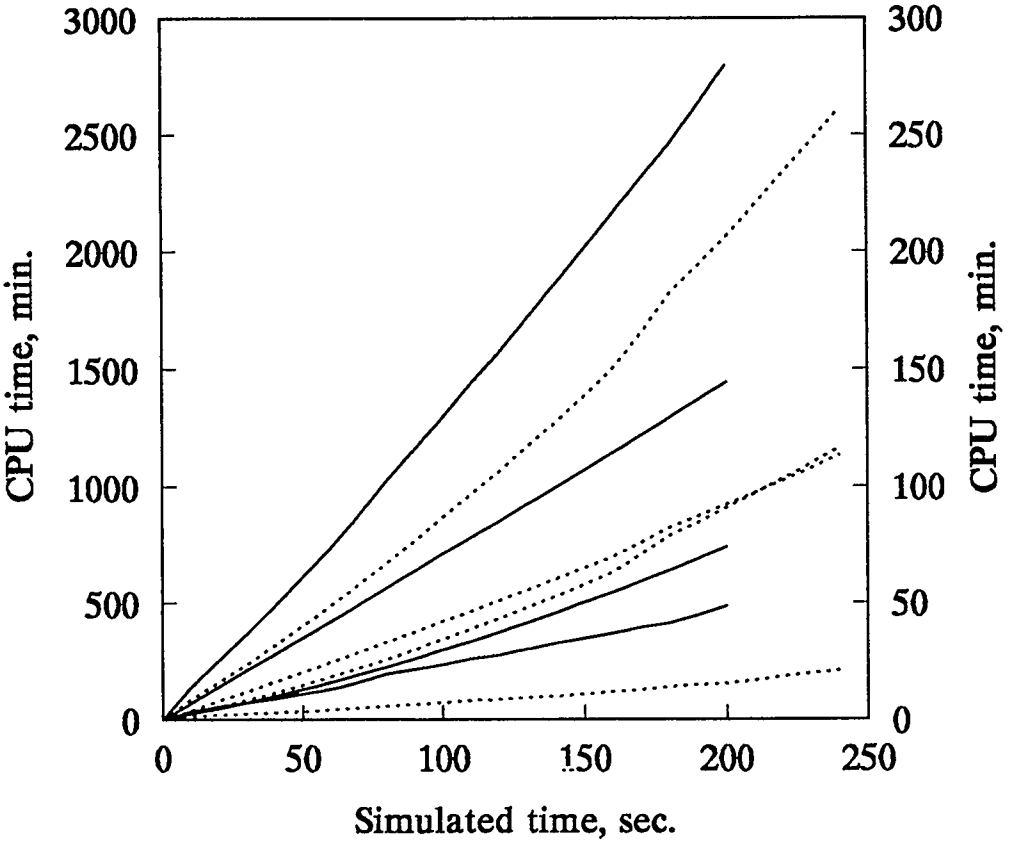


Fig. 5.38 Comparison of CPU time on both systems, AIX(-) and Fujitsu(---)

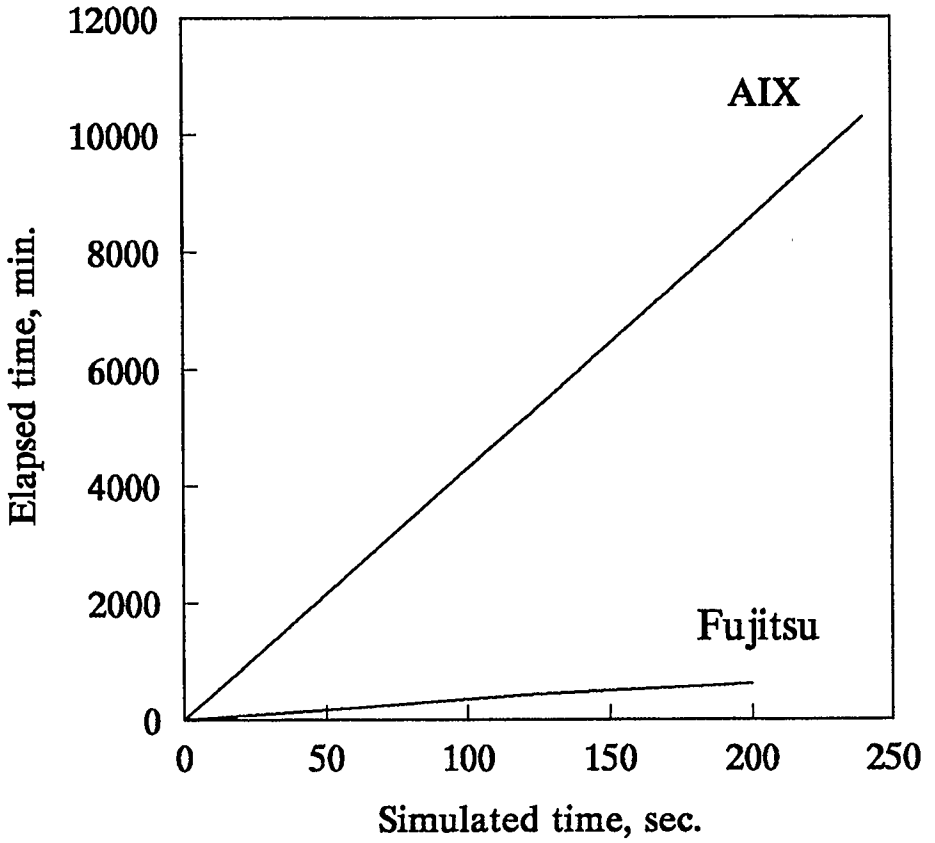


Fig. 5.39 Comparison of elapsed time on both systems, AIX(-) and Fujitsu(---)

over the angle variable. Secondly, due to the dynamic nature of the calculation, a grid much bigger than the actual calculation domain was generated. It is expected that much of the CPU and elapsed time would be saved if the calculation is always based on the actual melting region rather than on the whole mesh. The data in Fig.5.38 and 5.39 were collected using a version of the program in which the calculations involved the whole grid. A new test was done in which the calculation was restricted to the real melting domain. It was found that the CPU time was reduced by factors of 5 and 8 on the AIX and Fujitsu systems respectively. The average vectorisation percentage increased to 38-40%. With this change, the code ran about 15 times faster on the Fujitsu system compared to the AIX.

# Chapter 6

# Conclusions and Recommendations

## 6.1 Conclusions

A simplified model of the Ellithorpe remelter, for producing liquid from solid mounds of sulphur, has been numerically simulated. It was assumed that only orthorhombic sulphur ($T_m$ ~ 113°C) is present. The process involves close-contact melting and the liquid produced is continuously squeezed out of a narrow gap. The system is a hot cylinder forced into close proximity with a wall of sulphur which was initially flat and at its melting point. As latent heat was supplied, the wall was progressively deformed while the tube migrated inwards. The hydrodynamic and energy equations were solved simultaneously using a time-marching procedure based on a combined finite difference and finite element scheme in a fixed grid domain. Moreover, a volume of liquid fraction (VOF) method was used to track the moving boundary front. The shape or contour of the interface and the displacement rate of the moving heat source were determined as part of the solution. The numerical algorithm was validated by comparing the numerical simulation results with analytical solutions for a ice-making process, migration rate of the hot tube in the sulphur melting process at lower Ste values. It was also verified by

simulating the contact melting process of n-octadecane in a migrating horizontal hot tube under constant wall surface temperature and constant heat flux conditions. The numerical results are in good agreement with the experimental measurements conducted by Moallemi and Viskanta (1985b, 1986). Based on the results, the following conclusions are arrived at:

1. The migration rate of the tube was most rapid at early times, ~15 s, then the rate attained almost steady values under a typical set of system parameters and operating conditions. Radial temperature profiles developed very quickly at the early stages of the melting and the variations between the profiles at most intermediate angles became very small after ~ 60 s. The non-linearity of the temperature distribution across the channel is obvious even though the gap width is very narrow $\delta_o/r_o << 1$. The tangential velocity profiles are different at different polar angles. Maxima in the velocity distributions are more often not located midway within the liquid gap. The highest velocities were at different polar positions as melting progressed. The radial flows of the melt produced were found to be quickly re-directed azimuthally. The velocities dropped rapidly within 0.15 of the gap width from the melting boundary. The force applied to maintain a constant minimum gap separation increased rapidly at the initial stage while the displacement rate of the heat source increased rapidly from zero. Thereafter, the displacement occurred at a slower but still increasing rate. The critical melting sector angle rose quickly from 0 to nearly 20° within 5 s and then changed to a slower pace. The gap thickness also increased monotonically in the azimuthal direction. The interface was progressively deformed around the hot tube and the travel path of the melt from $\theta$

= 0 increased with time.

2. A simple pseudo-steady state analysis suggested that the surface temperature of the tube $T_w$ and the externally applied force are the principal variables which regulate the steady state melting process. The critical sector angle was a function of Ste and applied force. Its value varied from 36° to 90° depending on the process conditions. In the transient numerical analysis, the wall temperature $T_w$, the minimum spacing at $\theta = 0$, $\delta_o$ (which is related to the applied force), and the radius of the hot tube were the three primary variables. The applied force $F_e$ and the critical sector angle $\theta_c$ were calculated while $\delta_o$ was prescribed in numerical calculations.

3. The analytical model presented in chapter 3 was a simplified steady state situation with constant properties. The model is valid at small Ste numbers. Two solutions were found for f(Ste) which are expressed in eqs.(3.48b) and (3.48c). Most of the discussion in chapter 3 pertains to consequences of eq.(3.48c) while the conclusions do not change for very low Stefan number, they should be different for Stefan's number beyond 0.0132 when the results diverge and f(Ste) from eq.(3.48b) has larger values than those from eq.(3.48c) as Ste increases. The follow-up change due to the other solution (3.48b) will be done in subsequent research.

4. While other conditions/variables were maintained constant, changes in the surface temperature $T_w$ had significant effects on the melting rates. The initial and asymptotic rates of migration of the tube were higher as the driving potential ($T_w$ - $T_m$) was increased. Temperature profiles across the channel deviated more from a linear pattern as the heating surface became hotter. At a given angular position such as 20°, for

example, the profiles of the azimuthal velocity, scaled with the approach velocity between the hot tube and the sulphur block $u_o$, were higher at lower driving potentials than at higher temperature differences. However, the absolute values for the velocity were larger when the $T_w$ was higher. Both the gap width and its length along the tube wall gradually increased as the tube became enveloped. The contour of the interface was curved more towards the tube at higher $T_w$. Larger applied forces were also required to maintain $\delta_o$ as $T_w$ was increased.

5. When larger minimum separation gap widths $\delta_o$ were chosen, the migration rates of the hot tube were, as expected, lower and it required longer periods for the system to attain steady state. The applied force was correspondingly reduced compared with the configuration with smaller $\delta_o$ values. The flow field also developed faster with smaller $\delta_o$. The variations of the temperature profiles in the intermediate angles became smaller after initial stage developments, when $\delta_o$ was smaller.

6. The migration rate of the hot tube and the corresponding applied force were not affected by the hot tube radius $r_o$. Three $r_o$ values were used in the calculations. The largest $r_o$ was four times the smallest one. It was found that the steady migration rates for the tubes were the same. The only variations involved the "induction" times which were smaller for the larger tubes. All the tubes attained the steady migration rate phase at about the same time. Applied forces required to maintain the minimum separation of constant $\delta_o$ showed the same magnitudes as they were not affected by the tube diameters. The temporal development of the flow field and changes in the gap width over the same interval of melting, however, varied for the different $r_o$ values. With smaller $r_o$, the tube

surface was enveloped by the melt more quickly and the flow domain expanded faster along the azimuthal direction. The latter means that the critical angle was displaced faster around the tube. At a given angular position, The melt discharge area was narrower, the maximum velocity larger and the melt was warmer when $r_o$ was lower.

7. The program code for the simulation was written in Fortran, developed first on an IBM RISC 6000 system (AIX) and then adapted for the high performance Fujitsu VPX/240 system. Comparisons were made for the CPU time, the elapsed time and vectorisation CPU time for both systems. Results show that the Fujitsu system consumed about 7% CPU and 16% total time as for the AIX. The overall vectorisation percentage was about 40% and the calculations were not in the Fujitsu's best computing performance zone due to the short vector length in the current code.

## 6.2 Recommendations

The work presented in this thesis was focused on the transient simulation of the early development of a close-contact sulphur melting process from an initial flat wall of solid mound. There was no previous work from the literature with which it could be compared, neither were any experimental data available. More work is, hence, required on this subject as outlined in this section.

1. A longer simulation time should be attained for each calculation to observe the development of the shape of the melting interface, In particular, it is of interest to examine when the critical sector angle exceeds 90°, where a singularity may arise for the flow and temperature fields. The interface contour in this case is important in deciding

how far away the next steam tube should be positioned.

2. The simulation was confined to the situation when the solid sulphur is pure and in the orthorhombic habit form. The heating surface temperature was also maintained below 158°C such that liquid sulphur existed in the single ring structure and no polymerization occurred. As discussed in chapter 2, both the viscosity and heat capacity of a liquid change almost in a discontinuous manner at certain temperatures. Viscosity changes by a factor of $\sim 10^3$ around 160°C. Such temperature dependence may cause the system of equations to be ill-conditioned. The present work emphasized more the effects of variations in the geometric parameters and the temperature of the hot tube. A lower emphasis was placed on variations in $\eta$. The latter should be investigated because, in the current industrial melting process, operators prefer to keep the steam temperature at ~200°C.

3. Analogous experimental work should be done to validate the numerical simulation results.

4. More effort should be invested to optimize the simulation code, when it is running on the high performance computing Fujitsu VPX/240 system since the current vector length has not been in the best performance range of the machine. Vector lengths are short in some parts of the calculation because grid points in the radial direction number only 15-30. Collapsing some double loops into single ones through the use of an indirect addressing scheme to locate grid cells along the liquid-solid interface may help solve the problem.

# References

Arpaci, V. 1966, *Conduction Heat Transfer*, Addison-Wesley Publishing Company.

Bacon, R.F. & Fanelli, R. 1943, The Viscosity of Sulphur, *J. Am. Chem. Soc.*, **65**, 639 - 648.

Bahrami, P.A. & Wang, T.G. 1987, Analysis of gravity and conduction-driven melting in a sphere, *Trans. ASME, J. of Heat Transfer*, **109**, 806 - 809.

Bareiss, M. & Beer, H. 1984, An Aalytical Solution of the Heat Transfer Process During Melting of an Unfixed Solid Phase Change Material Inside a Horizontal Tube, *Int. J. Heat Mass Transfer* **27**, 739 - 746.

Bejan, A. 1989, The Fundamentals of Sliding Contact Melting and Friction, *Trans. ASME, J. of Heat Transfer*, **111**, 13 - 20.

Bejan, A. 1993, Comments on " Analysis of close-contact melting for octadecane and ice inside isothermally heated horizontal rectangular capsule", *Int. J. Heat Mass Transfer*, **36(3)**, 832.

Birch, F.S. 1975, Conduction Heat Flow Anomalies Over a Hot Spot in a Moving Medium, *J. of Geophysical Research*, **80**, 4825 - 4827.

Bird, R.B., Stewart, W.E. & Lightfoot, E.N. 1960, Transport Phenomena, J. Wiley & Sons, New York.

Brent, A.D., V.R. Voller, V.R. & Reid, K.J. 1988, Enthalpy-Porosity Technique for

Modeling Convection-Diffusion Phase Change: Application to the Melting of a Pure Metal, *Numerical Heat Transfer*, **13**, 297 - 318.

Burden, R.L. & Faires, J.D. 1985, Arpaci, V. 1966, *Numerical Analysis*, Prindle, Weber & Schmidt, Boston.

Carslaw, H.S. & Jeager, J.C. 1959, *Conduction of Heat in Solids (2nd Ed.)*, Oxford University Press, New York.

Cho, S.H. & Sunderland, J.E. 1974, Phase Change Problems with Temperature-Dependent Thermal Conductivity, *Trans. ASME, J. Heat Transfer*, **96**, 214 - 217.

Crank, J. 1981, How to deal with moving boundaries in thermal problems, Chapter 9, *Numerical Methods in Heat Transfer*, John Wiley & Sons Ltd.

Crank, J. 1984, *Free and Moving Boundary Problem*, Clarendon Press, Oxford.

Currell, B.R. et al., (1975): In: New Uses of Sulphur, West, J.R.(ed), *Adv. Chem. Ser.* **140**, 1-17.

Date, A.W. 1991, A strong enthalpy formulation for the Stefan problem, *Int. J. Heat Mass transfer*, **34**, 2231 - 2235.

Emerman, S.H. & Turcotte, D.L. 1983, Stokes's problem with melting, *Int. J. Heat Mass transfer*, **26**, 1625 - 1630.

Eckert, E.R.G. & Drake Jr., R.M. 1987, Analysis of Heat and Mass Transfer, Hemisphere Publication Corp., New York.

Findlay, A. 1945, *The Phase Rule and It's Application*, 8th edition, Dover Publications, New York.

Hale Jr., N.W. & Viskanta, R. 1978, Photographic observation of the solid-liquid interface

motion during melting of a solid heated from an isothermal vertical wall, *Lett. Heat Mass Transfer*, **5**, 329 - 337.

Hale Jr., N.W. & Viskanta, R. 1980, Solid-liquid phase-change heat transfer and interface motion in materials cooled or heated from above or below, *Int. J. Heat Mass Transfer*, **23**, 283 - 292.

Hastaoglu, M. A. 1987, Numerical solution of three - dimensional moving boundary problems: melting and solidification with blanketing of a third layer, *Chemical Engineering Science*, **42**, 2417 - 2423.

Hatch, L.F. 1972, What Makes Sulphur Unique?, *Hydrocarbon Processing*, **July**, 75 - 78.

Hirata, T., Makino, Y. & Kaneko, Y. 1991, Analysis of close - contact melting for octadecane and ice inside isothermally heated horizontal rectangular capsule, *Int. J. Heat Mass Transfer*, **34**, 3097 - 3106.

Hirt, C.W. & Nichols, B.D. 1981, Volume of Fluid ( VOF ) method for the dynamics of free boundaries, *J. of Computational Physics*, **39**, 201 - 225.

Hong, H. & Saito, A. 1993, Numerical method for direct contact melting in transient process, *Int. J. Heat Mass Transfer*, **36**, 2093 - 2103.

Hsu, C.F., Sparrow, E.M. & Patankar, S.V. 1981, Numerical solution of moving boundary problems by boundary immobilization and a control-volume-based finite-difference scheme, *Int. J. Heat Mass Transfer*, **24**, 1335 - 1343.

Hyman, J. 1984, Numerical Mehtods for tracking Interfaces, *Physica*, **12D**, 369 - 407.

Hyne, J.B. 1981/2, *The Quarterly Bulletin of ASRL*, **XVIII(2-4)**, 63 - 85.

Hyne, J.B. 1989, The forming, handling and transportation of elmental sulphur, *The*

*Quarterly Bulletin of ASRL*, **XXVI(1)**, .

Hyne, J.B. 1990, *The Quarterly Bulletin of ASRL*, **XXVII(1)**, 16 - 36.

Hyne, J.B. & Schwalm, W.J. 1982/1983, *The Quarterly Bulletin of ASRL*, **XIX(3,4)**, 1 - 23.

Hyne, J.B. & Schwalm, W.J. 1983, *The Quarterly Bulletin of ASRL*, **XX(1)**, 1 - 12.

Jackson, F. 1965, Moving heat sources with change of phase, *Trans. ASME, J. of Heat Transfer*, **87**, 329 - 332.

Jeje, A.A. & Wu, C. 1994, Contact melting of Sulphur With Continuous Drainage, *The 10th International Heat Transfer Conference*, Brighton, England, August 14-18, 1994.

Johnson, W.E. 1970, Development and application of computer programs related to hypervelocity impact, *System Science and Software report*, **3SR-353**.

Katayama, K., Saito, A., Utaka, Y., Saito, A., Matsu, H., Mae Kawa, H. & Saifullah, A.Z.A., 1981, Heat transfer characteristics of the latent heat thermal energy storage capsule, *Solar Energy*, **27**, 91 - 97.

Kuehn, T.H. & Goldstein, R.J. 1976, An experimental and theoretical study of natural convection in the annulus between horizontal concentric cylinders, *J. of Fluid Mechanics*, **74**, 695 - 719.

Kirk and Othmer, 1984, Sulphur, In *Encyclopedia of Chemical Technology*, Interscience Publishers, Vol. 19.

Lacroix, M. & Voller, V.R. 1990, Finite difference solutions of solidification phase change problem: transformed versus fixed grids, *Numerical Heat Transfer ( Part*

*B* ), **17**, 25 - 41.

Landau, H. G. 1950, Heat Conduction in a Melting Solid, *Quarterly of Applied Mathematics*, **8(1)**, 81 - 94.

Lea, J.F. & Stegall, R.D. 1973, A Two-Dimensional theory of Temperature and Pressure Effects on Ice Melting Rates with a Heated Plates, *Trans. ASME, J. Heat Transfer*, 95, 571 - 573.

Lewis, G.N. & Randall, M. 1991, The Heat Content of Various Forms of Sulphur, *J. Am. Chem. Soc.*, **33**, 476 - 488.

Li, X. & Durbetaki, P. 1992, The Conjugate Formulation of a Radiation Induced Transient Natural Convection Boundary Layer, *Int. J. for Numerical Methods in Engineering*, **35**, 853 - 870.

Logan, S.E. 1974, Deep delf-burial of radioactive wastes by rock-melting capsule, , *Nuclear Technology*, **21**, 111 - 124.

Moallemi, M.K. 1985, Melting around a migrating heat source, *Ph.D. Dissertation*, Purdue University, West Lafayatte, IN., U.S.A.

Moallemi, M.K. & Viskanta, R. 1985a, Melting heat transfer around a migrating heat source, *Trans. ASME, J. of Heat Transfer*, **107**, 451 - 458.

Moallemi, M.K. & Viskanta, R. 1985b, Experiments on fluid flow induced by melting around a migrating heat source, *J. of Fluid Mech.*, **157**, 35 - 51.

Moallemi, M.K. & Viskanta, R. 1986, Analysis of close - contact heat transfer, *Int. J. Heat Mass Transfer*, **29**, 855 - 867.

Moallemi, M.K., Webb, B.W. & Viskanta, R. 1986, An experimental and analytical study

of close-contact melting, *Trans. ASME, J. of Heat Transfer*, **108**, 894 - 899.

Mollere, P.D. 1989, From Calcasieu to Caminada: a brief history of the Louisiana sulphur industry, *Chemical Engineering Porgress*, **March**, 73 - 78.

Moore, F.E. & Bayazitoglu, Y. 1982, Melting within a spherical enclosure, *Trans. ASME, J. of Heat Transfer*, **104**, 19 - 23.

Morega, AL.K., Filip, A.M. & Bejan, A. 1993, Melting around a shaft rotating in a phase - change material, *Int. J. Heat Mass Transfer*, **36**, 2499 - 2509.

Negiz, A. 1991, Freezing Inside a Buried Pipe, *M.Sc. Thesis*, The University of Calgary, Calgary, Alberta, Canada.

Nichols, B.D., Hirt, C.W. & Hotchkiss, R.S. 1980, Volume of fluid (VOF) method for dynamics of free boundaries, *Los Alamos Scientific Laboratory report*, **LA-8355**.

Nusselt, W.Z. 1916, Die Oberflachenkondensation des Wasserdampfes, *Ver. Deut. Ing.*, **60**, 541 - 569.

Ogawa, M., Schubert, G. & Zebib, A. 1991, Numerical Simulation of Three-Dimensional Thermal Convection in a Fluid With Strongly Temperature-Dependent Viscosity, *J. Fluid Mech.*, **233**, 290 - 328.

Oliver, D.L. & Sunderland, J.E. 1987, A phase change problem with temperature-dependent thermal conductivity and specific heat, *Int. J. Heat Mass Transfer*, **30**, 2657 - 2662.

Ozisik, M.N. 1978, A Note on the General Formulation of Phase Change Problem as Heat Conduction Problem with a Moving Source. *Tran. ASME, J. Heat Transfer*, **100**, 370 - 371.

Ozisik, M.N. 1980, *Heat Conduction*, Wiley Interscience Publications, Toronto.

Patankar, S.V., 1980, *Numerical Heat Transfer and Fluid Flow*, McGraw - Hill/Hemisphere, New York.

Patankar, S.V. in Minkowycz, W.J. et al. 1988, *Handbook of Numerical Heat Transfer*, Wiley, New York.

Patel, P.D. 1968, Interface Conditions in Heat-Conduction Problems with Change of Phase, *AIAA J.*, **6**(12), 2454.

Pfeiffer, J.B. 1975, *Adv. Chem. Ser.*, **139**, ACS, Washington.

Platou, J. 1972, Use sulphur in fertilizers, *Hydrocarbon Processing*, **July**, 86 - 88.

Prakash, C., Samonds, M. & Singhal, A.K. 1987, A fixed grid numerical methodology for phase change problems involving a moving heat source, *Int. J. Heat Mass Transfer*, **30**, 2690 - 2694.

Prasad, A. & Sengupta, S. 1987, Numerical investigation of melting inside a horizontal cylinder including the effects of natural convection, *Trans. ASME, J. of Heat Transfer*, **109**, 803 - 806.

Raymont, M.E.D. & Hyne, J.B. 1983, 10 years experience in sulphur forming, *The Quarterly Bulletin of ASRL*, **XX(2)**, 24 - 72.

Roberts, B., Turner, C., Hyne, J.B. 1987, *The Quarterly Bulletin of ASRL*, **XV(2)**, 1-25.

Rosenthal, D. 1946, Theory of moving source of heat transfer and its application to metal treatments, *Trans. ASME*, **68**, 849 - 866.

Roy, S.K. & Sengupta, S. 1987, The melting process within spherical enclosures, *Trans. ASME, J. of Heat Transfer*, **109**, 460 - 462.

Saito, A., Utaka, Y., Akiyoshi, M. & Katayama, K. 1985a, On the contact heat transfer with melting ( 1st Report, Experimental study ), *Bulletin of JSME*, **28**, 1142 - 1149.

Saito, A., Utaka, Y., Akiyoshi, Y. & Katayama, K. 1985b, On the contact heat transfer with melting ( 2nd Report, Analytical study ), *Bulletin of JSME*, **28**, 1703 - 1709.

Saito, A., Utaka, Y., Shinoda, K. & Katayama, K. 1986, Basic Research on the latent heat thermal energy storage utilizing the contact melting phenomena, *Bulletin of JSME*, **29**, 2964 - 2952.

Saito, A., Utaka, Y. & Tokihiro, Y. 1988, On Contact Heat Transfer with Melting ( The Melting on the Inner Surface of a Horizontal Cylindrical Tube ), *JSME of International Journal*, **Series II, 31, NO. 1**, 58 - 65.

Saitoh, T. & Hirose, K. 1982, High Rayleigh number solutions to problems of latent heat thermal energy storage in a horizontal cylindrical capsule, *Trans. ASME, J. of Heat Transfer*, **104**, 545 - 553.

Samarskii, A.A., Vabishchevich, P.N., Iliev, O.P. & Churbanov, A.G. 1993, Numerical simulation of convection/diffusion phase change problem - a review, *Int. J. Heat Mass Transfer*, **36**, 4095 - 4106.

Schlichting, H. 1979, Boundary-Layer Theory, *McGraw-Hill, New York*, 112 - 116.

Schwalm, W.J. & Hyne, J.B. 1983, *The Quarterly Bulletin of ASRL*, **XX(2)**, 1 - 9.

Schwalm, W.J. & Hyne, J.B., 1984, *The Quarterly Bulletin of ASRL*, **XXI(1,2)**, 37 - 46.

Schwalm, W.J., Dowling, N.J. & Hyne, J.B., (1987/8), *The Quarterly Bulletin of ASRL*, **XXIV(3,4)**, 1 - 15.

Shamaundar, N. & Sparrow, E.M. 1975, Analysis of multidimensional conduction phase change via the enthalpy model, *Trans. ASME, J. of Heat Transfer*, **97**, 333 - 340.

Sheen, S. & Hayakawa, K. 1991, Finite difference simulation for heat conduction with phase change in an irregular food domain with volumetric change, *Int. J. Heat Mass Transfer*, **34**, 1337 - 1346.

Sparrow, E.M. & Geiger, G.T. 1986, Melting in a horizontal tube with the solid either constrained or free to fall under gravity, *Int. J. Heat Mass Transfer*, **29**, 1007 - 1019.

Sparrow, E.M. & Miriam, T.A. 1985, Inclination - inclined direct - contact melting in a circular tube, *Trans. ASME, J. of Heat Transfer*, **107**, 533 - 540.

Sparrow, E.M. & Myrum, T.A. 1985, Inclination - inclined direct - contact melting in a circular tube, *Trans. ASME, J. of Heat Transfer*, **107**, 533 - 540.

Sparrow, E.M., Patankar, S.V. & Ramadhyani, S. 1977, Analysis of melting in the presence of natural convection in the melt region, *Trans. ASME, J. of Heat Transfer*, **99**, 520 - 526.

Stefan, J. 1890, Uber die theorie der Eisbildung, insbes ondere uber die eisbildung in Polarmeere, *Sitzungsberichie der Kaiserlichen Akademie Wiss Wien*, Mathinaturnsiss KL **98(22)**, 965 - 973.

Tamma, K.K. & Namburu, R.R. 1990, Recent advances, trends and new perspectives via enthalpy-based finite element formulation problems, *Int. J. for Numerical Methods in Engineering*, **30**, 803 - 820.

Thom, A. & Apelt, C.J. 1961, *Field Computations in Engineering Physics*, D. Van

Nostrand Company Ltd.

Thomas, G. B. & Finney, R. L. 1980, *Calculus and Analytical Geometry*, fifth edition, Addison-Wesley Publishing Company.

Thompson, J. F. 1982, *Numerical Grid Generation*, Editor: Thompson, J. F., North-Holland.

Tong, L.S. 1968, Core cooling in a hypothetical loss of coolant accident estimate of heat transfer in core meltdown, *Nuclear Engineering and Design*, **8**, 309 - 312.

Vemuri, V. & Karplus, W.J. 1981, *Digital Computer Treatment of Partial Differential Equations*, Prentice-Hall, New York.

Vroom, A.H. 1972, New uses for sulphur: the Canadian Viewpoint, *Hydrocarbon Processing*, **July**, 79 - 85.

Voller, V.R. & Prakash, C. 1987, A fixed grid numerical modeling methodology of convection/diffusion mushy phase change problems, *Int. J. Heat Mass Transfer*, **30**, 1709 - 1719.

Voller, V.R. & Swaminathan, C.R. 1993, Treatment of discontinuous thermal conductivity in control-volume solutions of phase-change problems, *Numerical Heat Transfer,Part B*, **24**, 161 - 180.

Warsi, Z. U. A. & Thompson, J. F. 1982, A noniterative method for the generation of orthogonal coordinates in doubly-connected region, *Mathematics and Computation*, **38**, 501 - 516.

Wassink, B. & Hyne, J.B. 1993, Fugitive dust generation and mearsurement during handling of formed solid elmental sulphur, *The Quarterly Bulletin of ASRL*,

**XXX(1&2)**, 1 - 10.

Webb, B.W., Moallemi, M.K. & Viskanta, K. 1987, Experiments on melting of unfixed ice in a horizontal cylindrical capsule, *Trans. ASME, J. of Heat Transfer*, **109**, 454 - 459.

West, J.R. 1975, *Adv. Chem. Ser.*, **140**, ACS, Washington.

Wu, C., Phillips, D. & Jeje, A.A. 1994, Numerical Simulation of A Transient Close - Contact Melting Problem, *Proceedings of Supercomputing Symposium '94, Canada's 8th Annual High Performance Computing Conference and Exhibition*, pp.70-77, Toronto, Canada, June 6-8, 1994.

# Appendix A-1

## Governing Equations in Non-inertial Coordinate System

The Navier-Stokes equations are applicable to the inertial coordinate system the origin of which does not have any motion. If the body is in acceleration, however, it is straightforward and convenient to formulate the conservation equations with respect to body-fixed coordinate system which is non-inertial. Therefore, it is necessary to transform the inertial coordinate system to the non-inertial one in order to obtain the conservation equations in body-fixed coordinate system. The boundary conditions and the energy balance equations at the melting interface also have to be transferred in the new non-inertial body-fixed coordinate system.

Conservation Equations

A coordinate system $x_i$ whose origin has a pure translational motion ( no rotation ) with velocity $\mathbf{U}_o(t)$ with respect to a fixed coordinate system $X_i$ , i = 1, 2, 3, is shown in Fig. A-1. A point p(**X**) which moves with velocity **U** with respect to the fixed system becomes p(**x**) in the moving coordinate system and moving at the velocity $\mathbf{u} = \mathbf{U} - \mathbf{U}_o(t)$ with respect to the new non-inertial system. The non-inertial set of variables are related to the inertial ones by

$$x_i = X_i - \int_0^t U_{oi}\, dt \qquad i = 1, 2, 3 \tag{A-1}$$

Time variables are the same for both systems. If the motion is purely translational and $\mathbf{U}_o$ is only a function of time, then the derivatives respect to the coordinate spaces are the

same in both systems except for the derivatives with respect to time. That is,

$$\frac{\partial}{\partial x_i} = \frac{\partial}{\partial X_i} \tag{A-2}$$

and

$$\frac{\partial}{\partial t}\Big|_I = \frac{\partial}{\partial t}\Big|_{NI} + \frac{\partial x_i}{\partial t}\frac{\partial}{\partial x_i} \tag{A-3}$$

where subscripts I and NI indicate inertial and non-inertial frames respectively.

With $\frac{x_i}{t} = - U_{oi}(t)$ , Eq.(A-3) can be simplified as:

$$\frac{\partial}{\partial t}\Big|_I = \frac{\partial}{\partial t}\Big|_{NI} - \boldsymbol{U}_o \cdot \nabla \tag{A-4}$$

where $\nabla$ is the divergence operator in $x_i$ - frame.

With Eq.(A-2) and the pure translational motion of the non-inertial frame which means the principal unit vectors of the system are identical. It is inferred that,

$$\nabla|_I = \nabla|_{NI} \tag{A-5}$$

$$\nabla^2|_I = \nabla^2|_{NI} \tag{A-6}$$

The total substantial derivative vector in the inertial frame can be expressed as:

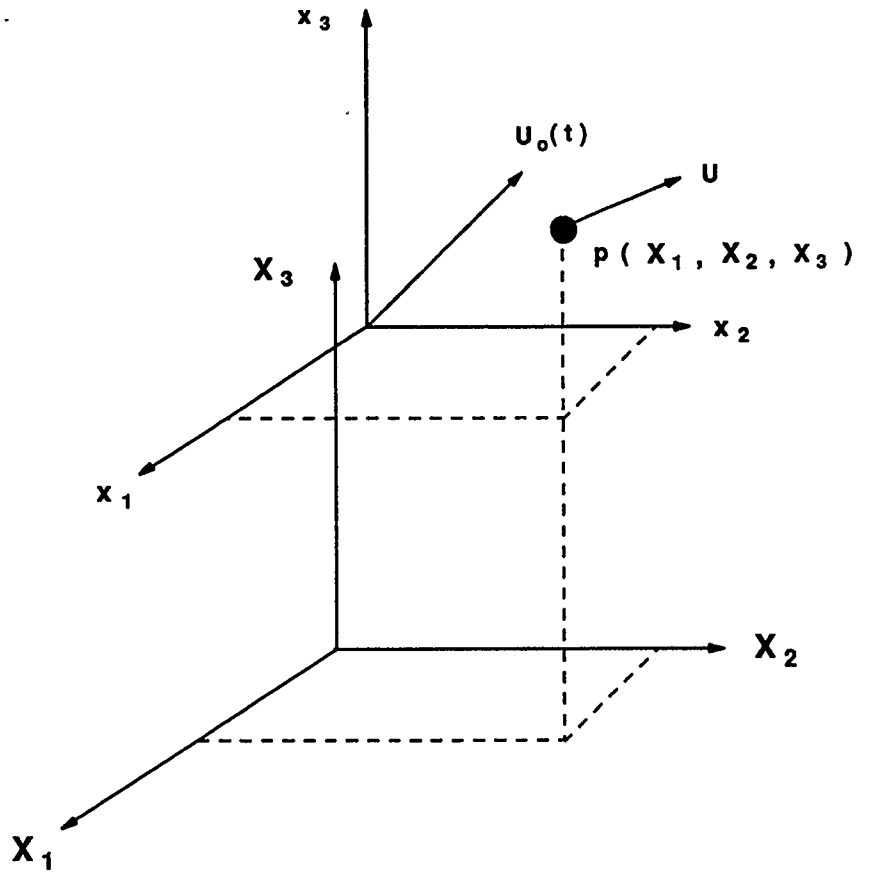


Fig. A-1 Schematic of inertial and moving frames of reference

$$\frac{D}{Dt}|_I = \frac{\partial}{\partial t}|_I + \boldsymbol{U}\cdot\nabla \qquad \text{(A-7)}$$

After substituting Eq.(A-4) into (A-7), one obtains

$$\frac{D}{Dt}|_I = \frac{\partial}{\partial t}|_{NI} + ( \boldsymbol{U} - \boldsymbol{U}_o ) \cdot \nabla \qquad \text{(A-8)}$$

While the substantial derivative in the non-inertial frame is

$$\frac{D}{Dt}|_{NI} = \frac{\partial}{\partial t}|_{NI} + \boldsymbol{u} \cdot \nabla \qquad \text{(A-9)}$$

From Eq.(A-8) and (A-9) with $\mathbf{u} = \mathbf{U} - \mathbf{U}_o$, it can be seen that

$$\frac{D}{Dt}|_{NI} = \frac{D}{Dt}|_I \qquad \text{(A-10)}$$

Therefore the conservation equations can be written with respect to the new non-inertial coordinate system by applying the above conclusions.

CONTINUITY EQUATION:

In $X_i$ - coordinate system,

$$\frac{\partial \rho}{\partial t}|_I + \nabla|_I \cdot (\rho \boldsymbol{U}) = 0 \qquad \text{(A-11)}$$

Substituting Eq.(A-4) and (A-5) into Eq.(A-11), one can get,

$$\frac{\partial \rho}{\partial t}|_{NI} - \boldsymbol{U}_o \cdot \nabla \rho + \nabla|_{NI} \cdot (\rho \boldsymbol{u}) = 0 \qquad \text{(A-12)}$$

For the reason that $\mathbf{U}_o$ is a function of time only, therefore, $\rho \nabla \cdot \mathbf{U}_o = 0$, the Eq.(A-12) can be written as:

$$\frac{\partial \rho}{\partial t}|_{NI} + \nabla|_{NI} \cdot [\rho( \boldsymbol{U} - \boldsymbol{U}_o )] = 0 \qquad \text{(A-13)}$$

With $\mathbf{u} = \mathbf{U} - \mathbf{U}_o$, the velocity vector with respect to the non-inertial coordinate remains the same form as in the inertial one. That is,

$$\frac{\partial \rho}{\partial t}|_{NI} + \nabla|_{NI} \cdot (\rho \boldsymbol{u}) = 0 \qquad \text{(A-14)}$$

MOMENTUM EQUATIONS:

In the fixed coordinate $X_i$ - system, the momentum equation can be written as

$$\rho \frac{DU}{Dt}|_I = \rho \boldsymbol{g} - \nabla_I p + \nabla_I( \tau_I ) \qquad \text{(A-15)}$$

According to Eq.(A-5) and (A-10), the above equation can be transformed to

$$\rho \frac{DU}{Dt}\Big|_{NI} = \rho g - \nabla_{NI} p + \nabla_{NI}( \tau_{NI} ) \qquad \text{(A-16)}$$

With $\mathbf{U} = \mathbf{u} - \mathbf{U}_o$ and $\mathbf{U}_o$ is the function of time only, this, combined with Eq.(A-16), and yields

$$\rho \frac{Du}{Dt}\Big|_{NI} = \rho g - \nabla_{NI} p + \nabla_{NI}( \tau_{NI} ) - \rho \frac{\partial U_o}{\partial t} \qquad \text{(A-17)}$$

ENERGY CONSERVATION EQUATION:

In $X_i$ - system, the energy conservation equation is

$$\frac{D}{Dt} ( \rho C_p T)\Big|_I = \nabla_I ( \lambda \nabla_I T ) + \Phi \qquad \text{(A-18)}$$

The viscous dissipation term $\Phi$ is same as in both frames, which is the stress tensor. With the aid of Eq.(A-4) and (A-10), the energy equation in non-inertial coordinate system can be transformed to the form of

$$\frac{D}{Dt}( \rho C_p T)\Big|_{NI} = \nabla_{NI}( \lambda \nabla_{NI} T ) + \Phi \qquad \text{(A-19)}$$

In the liquid phase, the velocity with respect to the moving frame is $\mathbf{U} = \mathbf{u} - \mathbf{U}_o$ , the energy equation (A-19) can be written as

$$\frac{\partial}{\partial t}\left(\rho_f C_{pf} T\right) + \left(\boldsymbol{u} \cdot \nabla_{NI}\right)\left(\rho_f C_{pf} T_f\right) = \nabla_{NI}\left(\lambda \nabla_{NI} T\right) + \Phi \qquad \text{(A-20)}$$

In concluding, the governing equations in a moving frame of velocity $\mathbf{U}_o(t)$, with respect to the body-fixed coordinates should be transformed. With substantial derivative not changing (Eq. A-10) and partial derivative respect to time t having an extra term in right-hand side (Eq. A-4), the continuity and energy conservative equations remain unchanging in the non-inertial frame as shown in Eq. (A-14) and (A-20), the momentum equation, however, deserves an extra term, which is $-\rho\frac{\partial \boldsymbol{U}_o}{\partial t}$, on the right-hand side as shown in Eq. (A-17).

# Appendix A-2

## Melt Velocity at the Solid-liquid Interface

The solid-liquid interface can be expressed using an implicit function as Eq.(3.10) which is

$$G(r_i\ ,\ \theta,\ t)\ =\ 0 \tag{A-21}$$

If a unit vector **n** normal to the interface $G(r_i,\theta,t)$ is defined, then

$$\boldsymbol{n}\ =\ \frac{\nabla\ G}{|\nabla\ G|} \tag{A-22}$$

It is assumed that **n** is pointing into the liquid phase. The magnitude of the interface normal velocity $\mathbf{u}_n$ can be expressed as

$$\boldsymbol{u}_n\ =\ \boldsymbol{V}\cdot\boldsymbol{n}\ =\ \frac{\boldsymbol{V}\cdot\nabla G}{|\nabla G|} \tag{A-23}$$

where **V** is the interface velocity vector.

The total derivative of the interface position function gives

$$\left[\ \frac{\partial G}{\partial t}\ dt\ +\ \frac{\partial G}{\partial r}\ dr\ +\ \frac{1}{r}\frac{\partial G}{\partial \theta}\ d(r\theta)\ \right]\ =\ 0 \tag{A-24}$$

or

$$\frac{\partial G}{\partial r} v_r + \frac{1}{r}\frac{\partial G}{\partial \theta} v_\theta = - \frac{\partial G}{\partial t} \qquad \text{(A-25)}$$

On the other hand, the interface velocity vector **V** can be written as

$$\boldsymbol{V} = \hat{i} \frac{\partial G}{\partial r} + \hat{j}\frac{1}{r}\frac{\partial G}{\partial \theta} \qquad \text{(A-26)}$$

therefore

$$\boldsymbol{V} \cdot \nabla G = \frac{\partial G}{\partial r} v_r + \frac{1}{r}\frac{\partial G}{\partial \theta} v_\theta = -\frac{\partial G}{\partial t} \qquad \text{(A-27)}$$

Substituting Eq.(A-27), (A-23) yields

$$\boldsymbol{u}_n = \boldsymbol{V} \cdot \boldsymbol{n} = - \frac{\partial G/\partial t}{|\nabla G|} \qquad \text{(A-28)}$$

The interface velocity with respect to a non-inertial frame moving with velocity $\mathbf{U}_o$ may be obtained by substituting Eq.(A-4) into Eq.(A-28), or

$$u_n = - \frac{\partial G/\partial t - \boldsymbol{U}_o \cdot \nabla G}{|\nabla G|} \qquad \text{(A-29)}$$

The boundary condition for the fluid next to the interface is the same as $u_n$ expressed in eq. (A-29).

# Appendix A-3

## Local Energy Balance Equation at the Interface

The energy balance equation at the solid-liquid interface has been expressed in Eq. (3.11), which is

$$\lambda_s \frac{\partial T_s}{\partial n} - \lambda \frac{\partial T}{\partial n} = \rho\, h_{sl} \boldsymbol{u}_n \tag{A-30}$$

As the temperature field at the melting interface possesses the same properties as the isothermal surface function G, defined in Eq.(3.10), **n** at the melting interface can also be expressed as:

$$\boldsymbol{n} = \frac{\nabla G}{|\nabla G|} = \frac{\nabla T_i}{|\nabla T_i|} = \frac{\nabla T_s}{|\nabla T_s|} = \frac{\nabla T}{|\nabla T|} \tag{A-31}$$

The derivatives in the **n** direction become

$$\frac{\partial T_i}{\partial n} = \nabla T_i \cdot \boldsymbol{n} = \frac{\nabla T_i \cdot \nabla G}{|\nabla G|} \tag{A-32}$$

Substituting Eqs.(A-32) and (A-29) into (A-30), one obtains

$$(\lambda_s \nabla T_s - \lambda \nabla T) \cdot \nabla G = -\rho\, h_{sl} \left[ \frac{\partial G}{\partial t} - \boldsymbol{u}_o \cdot \nabla G \right] \tag{A-33}$$

This yields, in the non-inertial frame with $T_s = T_m$ (a constant)

$$\nabla G \cdot \nabla T = \frac{\rho\, h_{sl}}{\lambda} \left[ \frac{\partial G}{\partial t} - \boldsymbol{u}_o \cdot \nabla G \right] \tag{A-34}$$

which is Eq.(3.12).

# Appendix B-1

## Curvature of the Melting Interface $G(r_i,\theta,t) = 0$

The interface curve described by Eq.(A-21) also can be expressed as function of liquid gap width, which is

$$G(r_i\ ,\ \theta,\ t) = r_i - r_o - \delta\ (\theta,\ t\ ) = 0 \tag{B-1}$$

or

$$r_i = r_o + \delta\ (\theta,\ t\ ) \tag{B-2}$$

where $\delta(\theta,t)$ is the liquid gap width.

Any point p(x,y) at the curve has coordinates $(r_i,\theta)$ in polar system as shown in Fig.B-1. Their relationships can be expressed as

$$x = r_i \sin\ \theta = (r_o + \delta)\ \sin\ \theta = f(\theta) \tag{B-3}$$

and

$$y = r_i \cos\ \theta = (r_o + \delta)\ \cos\ \theta = g(\theta) \tag{B-4}$$

The curvature k of G can be calculated from the formula (Thomas & Finney, 1980),

$$k = \frac{|\ f'(\theta)\ g''(\theta) - g'(\theta)\ f''(\theta)|}{\left[\left(\ f'(\theta)\ \right)^2 + \left(\ g'(\theta)\ \right)^2\right]^{3/2}} \tag{B-5}$$

since

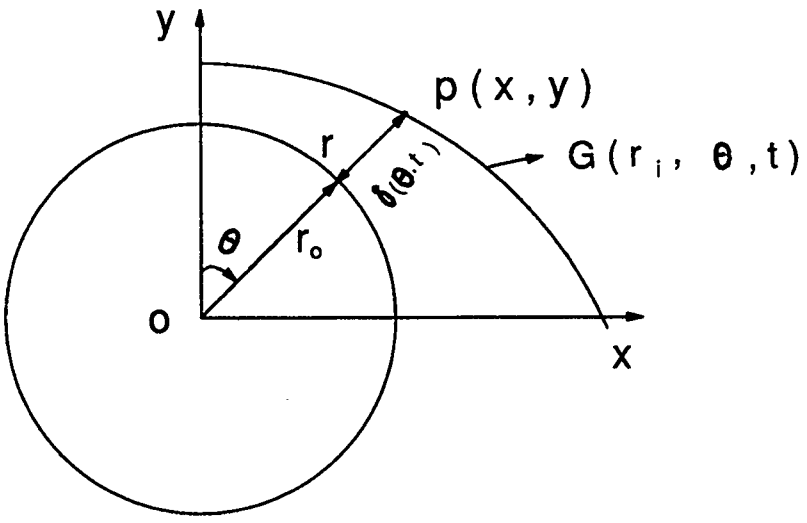


Fig. B-1 Expression of a point on the interface at both cartesian and polar systems

$$f'(\theta) = (r_o + \delta)\cos\theta + \frac{\partial\delta}{\partial\theta}\sin\theta$$

$$f''(\theta) = -(r_o + \delta)\sin\theta + 2\frac{\partial\delta}{\partial\theta}\cos\theta + \frac{\partial^2\delta}{\partial\theta^2}\sin\theta \qquad \text{(B-6)}$$

and

$$g'(\theta) = -(r_o + \delta)\sin\theta + \frac{\partial\delta}{\partial\theta}\cos\theta$$

$$g''(\theta) = -(r_o + \delta)\cos\theta - 2\frac{\partial\delta}{\partial\theta}\sin\theta + \frac{\partial^2\delta}{\partial\theta^2}\cos\theta \qquad \text{(B-7)}$$

therefore

$$\left(f'(\theta)\right)^2 = (r_o + \delta)^2\cos^2\theta + \left(\frac{\partial\delta}{\partial\theta}\right)^2\sin^2\theta + 2(r_o + \delta)\frac{\partial\delta}{\partial\theta}\sin\theta\cos\theta \qquad \text{(B-8)}$$

$$\left(g'(\theta)\right)^2 = (r_o + \delta)^2\sin^2\theta + \left(\frac{\partial\delta}{\partial\theta}\right)^2\cos^2\theta - 2(r_o + \delta)\frac{\partial\delta}{\partial\theta}\sin\theta\cos\theta \qquad \text{(B-9)}$$

and

$$\left(f'(\theta)\right)^2 + \left(g'(\theta)\right)^2 = (r_o + \delta)^2 + \left(\frac{\partial\delta}{\partial\theta}\right)^2 \qquad \text{(B-10)}$$

where

$$term\ 1 = -(r_o + \delta)\frac{\partial \delta}{\partial \theta} \sin\theta \cos\theta + (r_o + \delta)\frac{\partial^2 \delta}{\partial \theta^2} \cos^2\theta$$

$$- \left(\frac{\partial \delta}{\partial \theta}\right)^2 \sin^2\theta + \frac{\partial \delta}{\partial \theta}\frac{\partial^2 \delta}{\partial \theta^2} \sin\theta \cos\theta$$

$$term\ 2 = -(r_o + \delta)\frac{\partial \delta}{\partial \theta} \sin\theta \cos\theta - (r_o + \delta)\frac{\partial^2 \delta}{\partial \theta^2} \sin^2\theta$$

$$+ \left(\frac{\partial \delta}{\partial \theta}\right)^2 \cos^2\theta + \frac{\partial \delta}{\partial \theta}\frac{\partial^2 \delta}{\partial \theta^2} \sin\theta \cos\theta$$

so that

$$\begin{aligned} & f'(\theta)\, g''(\theta) - g'(\theta)\, f''(\theta) \\ &= -\left[ (f'(\theta))^2 + (g'(\theta))^2 \right] + term1 - term2 \\ &= (r_o + \delta) - 2\left(\frac{\partial \delta}{\partial \theta}\right)^2 - (r_o + \delta)^2 \end{aligned} \tag{B-12}$$

Substituting Eqs.(B-10) and(B-12) into (B-5), yields

$$\begin{aligned} k &= \frac{(r_o + \delta)\frac{\partial^2 \delta}{\partial \theta^2} - 2\left(\frac{\partial \delta}{\partial \theta}\right)^2 - (r_o + \delta)^2}{\left[(r_o + \delta)^2 + \left(\frac{\partial \delta}{\partial \theta}\right)^2\right]^{3/2}} \\ &= \frac{(1 + \delta^*)\frac{\partial^2 \delta^*}{\partial \theta^2} - 2\left(\frac{\partial \delta^*}{\partial \theta}\right)^2 - (1 + \delta^*)^2}{\left[(1 + \delta^*)^2 + \left(\frac{\partial \delta^*}{\partial \theta}\right)^2\right]^{3/2} \cdot r_o} \end{aligned} \tag{B-13}$$

which is Eq.(4.9).

# Appendix B-2

## Expression of Local Energy Balance Equation at the Melting Interface With Gap Width $\delta(\theta,t)$

The temperature gradient at the melting interface in θ-direction can be expressed in terms of the gradient in the r-direction, or

$$\frac{\partial T}{\partial \theta} = \frac{\dfrac{\partial G}{\partial \theta}}{\dfrac{\partial G}{\partial r}} \frac{\partial T}{\partial r} \tag{B-14}$$

The substitution of Eq.(B-14) into (A-34) results in the following expression for interface condition

$$\left[1 + \frac{1}{r^2}\left(\frac{\partial G/\partial \theta}{\partial G/\partial r}\right)^2\right] \frac{\partial T}{\partial r} = \frac{\rho\, h_{sl}}{\lambda} \left[\frac{\partial G}{\partial t} - \boldsymbol{u}_o \cdot \nabla G\right] \tag{B-15}$$

As the interface curve also can be expressed as Eq.(B-1), therefore

$$\frac{\partial G}{\partial r} = 1, \quad \frac{\partial G}{\partial \theta} = -\frac{\partial \delta}{\partial \theta}, \quad \frac{\partial G}{\partial t} = -\frac{\partial \delta}{\delta t} \tag{B-16}$$

The velocity $\mathbf{u}_o$ can be written as a vector

$$\boldsymbol{u}_o = -u_o\,(\cos\theta\,\hat{i} - \sin\theta\,\hat{j}) \tag{B-17}$$

and

$$\nabla G = \hat{i}\,\frac{\partial G}{\partial r} + \hat{j}\,\frac{1}{r}\,\frac{\partial G}{\partial \theta} \tag{B-18}$$

Substitution of Eqs.(B-16), (B-17) and (B-18) into (B-15), one obtains

$$\left( 1 + \frac{1}{r^2} \left( \frac{\partial \delta}{\partial \theta} \right)^2 \right) \frac{\partial T}{\partial r} = \frac{\rho \, h_{sl}}{\lambda} \left( u_o \left( \cos \theta + \frac{1}{r} \frac{\partial \delta}{\partial \theta} \sin \theta \right) - \frac{\partial \delta}{\partial t} \right) \tag{B-19}$$

The above equation can be non-dimensionlized into Eq.(4.11), which is

$$\frac{\partial \delta^*}{\partial t^*} = u_o^* \left( \cos \theta + \frac{1}{r^*} \frac{\partial \delta^*}{\partial \theta} \sin \theta \right) - Ste \left( 1 + \frac{1}{r^{*2}} \left( \frac{\partial \delta^*}{\partial \theta} \right)^2 \right) \frac{\partial T^*}{\partial r^*} \Big|_{r^* = 1 + \delta^*} \tag{B-20}$$